Polymer-Ceramic Composites for 3D Inkjet Printing

Dissertation zur Erlangung des Doktorgrades der
Technischen Fakultät der
Albert-Ludwigs-Universität Freiburg im Breisgau

Dennis Graf
2022

IMTEK – Institut für Mikrosystemtechnik
Professur für Werkstoffprozesstechnik

A dissertation submitted in partial fulfillment of the requirements for the degree of

Doktor-Ingenieur
in
Microsystems Engineering

according to the examination regulations at the University of Freiburg for
Ph.D. in Microsystems Engineering
of May 10, 2000.

Author	Dennis Graf
Institute	Department of Microsystems Engineering - IMTEK

Dean	Prof. Dr. Roland Zengerle
Referees	Prof. Dr. Thomas Hanemann *Laboratory for Materials Processing* Prof. Dr. Margit Zacharias *Laboratory for Nanotechnology* Prof. Dr. Jürgen Wilde *Laboratory for Assembly and Packaging Technology*
Chairperson	Prof. Dr. Jürgen Wöllenstein *Laboratory for Gassensors*
Date of defense	September 26, 2022

Declaration according to §5(2f) of the examination regulations:

I hereby confirm to have written the following thesis on my own, not having used any other sources or resources than those listed. All passages taken over literally or correspondingly from published sources have been marked accordingly. Additionally, this thesis has not been prepared or submitted for another examination, neither partially nor completely.

Freiburg, May 6, 2022

Dennis Graf

"*Unless you are very lucky, life is not a bowl of cherries."*

- Sir James Fraser Stoddart, Nobel prize laureate 2016.

I would like to say thank you to my mother and father for keeping me on the right path.

Abstract

As one of the few additive manufacturing methods, 3D inkjet printing enables multi-material deposition. However, there is a need for functional and structural materials. Among them, thermally conductive polymer-ceramic composites are required for thermal management applications.

In this work, three new types of Al_2O_3 particle-filled inks were fabricated and investigated. First and foremost are the thermally conductive particle filled inks. They were initially prepared without, but later with volatile solvents to increase the filling level. Furthermore, studies were made on the effect of nanoparticles on the toughness and elongation at break of composites, which resulted in solvent-free UV curable inks. During production, the ceramic was homogenized and comminuted by grinding in a planetary ball mill. Simultaneously or following grinding, dispersants in the form of the small molecules 3-(trimethoxysilyl)propylmethacrylate or 2-(2-methoxyethoxy)-ethoxy acetic acid were added to the particles. Depending on whether the grinding took place in a volatile grinding medium or directly in the organic matrix, the particles were dried in the former case and directly filled for use in the latter. The dried particles were subsequently incorporated into the organic matrix. The process was accompanied by analytical measurements that characterized the powder on the one hand and the finished composite ink on the other. Characterization of the inks included rheological measurements, stability tests, and inkjet printing tests. Printed composite test specimens were analyzed mechanically and thermally.

The nanocomposite inks showed no significant improvements in mechanical properties for the parameters studied. The second solvent-free ink led to a composite with a filling grade of 30 vol% and thermal conductivity of 0.6 W/(m·K). The investigation of the solvent-containing inks resulted in a material with a filler content of 50 vol% and thermal conductivity of 1 W/(m·K), unprecedented for this technology. Mechanical properties showed Young's modulus of 2.4 GPa, tensile strength of 40 MPa, elongation at break of 1 %, and toughness of 1.3 J/m³. Both the solvent-free and solvent-containing inks were used to make components for demonstration purposes.

Zusammenfassung

Als eine der wenigen additiven Fertigungsmethoden ermöglicht der 3D-Tintenstrahldruck die Multimaterialabscheidung. Es besteht jedoch ein Bedarf an Funktions- und Strukturmaterialien. Unter anderem werden thermisch leitfähige Polymer-Keramik-Komposite zur thermischen Regulierung benötigt. In dieser Arbeit wurden drei neue Arten von Al_2O_3-Partikel gefüllten Tinten hergestellt und untersucht. Allen voran sind es die thermisch leitfähigen, Partikel gefüllten Tinten, die anfänglich ohne, später aber mit volatilen Lösungsmitteln hergestellt wurden, um den Füllgrad zu steigern. Des Weiteren wurden Untersuchungen zu der Auswirkung von Nanopartikeln auf die Zähigkeit und Bruchdehnung von Kompositen angestellt, welche in lösungsmittelfreien UV härtbaren Tinten mündeten. Bei der Herstellung wurde die Keramik in einer Planetenkugelmühle homogenisiert und zerkleinert. Zeitgleich oder im Anschluss an die Mahlung wurden den Partikeln die Dispergatoren 3-(Trimethoxysilyl)propylmethacrylat oder 2-[2-(2-Methoxyethoxy)ethoxy]essigsäure hinzugegeben. Je nachdem, ob die Mahlung in einem volatilen Mahlmedium oder direkt schon in der organischen Matrix stattfand, wurden die Partikel im ersteren Fall getrocknet und im letzteren direkt für die Verwendung abgefüllt. Die getrockneten Partikel wurden im Anschluss in die organische Matrix eingearbeitet. Der Prozess wurde von Analysemessungen begleitet, welche zum einen das Pulver und zum anderen die fertige Komposit-Tinte charakterisierten. Die Charakterisierung der Tinten umfasste rheologische Messungen, Stabilitätsuntersuchungen und Tintenstrahl-Drucktests. Gedruckte Komposit-Prüfkörper wurden mechanisch und thermisch analysiert. Die Nanokomposit-Tinten zeigten keine nennenswerten Verbesserungen der mechanischen Eigenschaften bei den untersuchten Parametern. Die zweite lösungsmittel-freie Tinte führt zu einem Komposit mit einem Füllgrad von 30 Vol% und einer thermischen Leitfähigkeit von 0.6 W/(m·K). Die Untersuchung der lösungsmittel-haltigen Tinten ergab ein Material mit einem Füllgrad von 50 Vol% und einer thermischen Leitfähigkeit von 1 W/(m·K), ein bisher unerreichtes Ergebnis. Die mechanischen Eigenschaften zeigten einen E- Modul von 2.4 GPa, eine Zugfestigkeit von 40 MPa, eine Bruchdehnung von 1 % und eine Zähigkeit von 1.3 J/m³. Sowohl die lösungsmittelfreie als auch lösungsmittelhaltige Tinte wurden für die Herstellung von Komponenten zu Demonstrationszwecken verwendet.

Contents

Nomenclature

Latin letters

Variable	Description
$[I]$	Initiator concentration
$[M]$	Concentration of double bonds
$[M_n \bullet]$	Total radical concentration
a	Characteristic length or diameter of the nozzle
A	Hamaker constant
A_g	Cross-section of the sample gauge
a_K	Kapitza radius
a_n	Area one nitrogen molecule occupies
c	Speed of light
c_s	Concentration of the scattering/absorbing species
C_D	Drag coefficient of a sphere
c_i	Specific heat capacity
d_m	Minimal resolvable feature
d	Particle diameter
d_{LS}	Distance of the sample surface from the light source
dl_t	Sample gauge length change
D_p	Optical penetration depth
dQ	Applied heat flux
d_{st}	Sample thickness
dT	Temperature change
E	Youngs's modulus
E_c	Young's modulus of the composite
E_f	Young's modulus of the filler
E_I	Impact energy
E_{kin}	Kinetic energy
E_m	Young's modulus of the matrix
E_{max}	Maximum energy released from light source
E_{th}	Threshold energy for polymerization initiation
E_z	Energy absorption at the location z
f	Efficiency of photo-polymerization
F	Force
$f(R)$	Function of the surface roughness
g	Acceleration of gravity
G_{IC}	Fracture energy of the composite
$G_{IC,m}$	Fracture energy of the matrix
$G_{IC,S}$	Fracture energy of shear banding
$G_{IC,V}$	Fracture energy of void growth
h	Planck's constant
I_0	Initial light intensity
$I_{abs,z}$	Attenuated light intensity

k	Empirical prefactor
k_{apex}	Principal curvature at the apex
k_b	Boltzmann constant
k_p	Propagation rate constant
k_t	Termination rate constant
K_V	Von Mises stress concentration factor
$K_{\varphi_{max}}$	Empirical factor for monomodal spheres
l	Distance between two spherical particles
l_0	Equilibrium distance
l_{0t}	Original gauge length
l_i	mean free path of the phonon
m	Sample mass
m_0	Rest mass of an electron
m_1	Mass of grinding ball 1
m_2	Mass of grinding ball 2
M_2^R	Molecular weight
M_r	Torque
N_A	Avogadro constant
n_{mono}	Nitrogen molar quantity per particle mass
p	Pressure
P	heat-flowrate
p_0	Pressure at atmospheric conditions
P_{LS}	Power of the light source
R	Radius between two spherical particles
r	Radius of the cone
r_1	Principal radius of a droplet 1
r_2	Principal radius of a droplet 2
R_{Bd}	Thermal surface resistance
R_i	Initiation rate of photo-polymerization
R_p	Propagation reaction
r_{pz}	Radius of the plastic zone in unmodified matrix
R_t	Termination reaction rate
r_y	Radius of the plastic zone in nanoparticle laden matrix
T	Temperature
$t_{0.5}$	Time at half maximum
t_{LS}	Illumination duration from light source
W_{sl}^{AB}	Polar part of the work of adhesion
x	Distance transversed by an inkjet drop
x^*	Quotient of x/a
Z	Inverse of the Ohnesorge number
z	Coordination of P at the z-axis
ΔG	Total free energy
$\Delta G_{l_0}^{AB}$	Polar part of the free energy interaction at l_0
$\Delta G_{l_0}^{vdW}$	Nonpolar part of the free energy interaction at l_0
ΔG_l^{AB}	Polar part of the free energy interaction
ΔG_l^{EL}	Repulsive free energy
ΔG_l^{vdW}	Nonpolar part of the free energy interaction
$\Delta G^{ST,mix}$	Free energy interaction during mixing of surface polymers
Δp	Pressure difference between drop interior and exterior

Greek letters

Variable	Description
α	Angle of inclination
α_{max}	Angle of direction alteration
δ	Organic layer thickness on a particle
$\Delta\rho$	Density difference between droplet and air
ε	Dielectric constant
ε_{abs}	Absorption coefficient
ε_m	Molar absorptivity
ε_t	Tensile elongation
ζ	Zeta potential
η	Dynamic viscosity
η_0	Solvent dynamic viscosity
η_{rel}	Relative viscosity
κ	Inverse of the Debye length
λ	Wavelength of electromagnetic radiation
λ_c	Thermal conductivity of the composite
λ_d	Decay length of liquid molecules
λ_F	Thermal conductivity of the filler
λ_M	Thermal conductivity of the matrix
μ_m	Constant visualizing the pressure-dependency of yield stress
ν	Drop velocity
ν^*	Quotient of ν/ν_0
ν_0	Initial drop velocity
ν_1	Molar volume of the solvent
ν_i	Velocity of the phonon
ν_s	Sedimentation velocity
ρ	Density
ρ_2	Density of adsorbed polymer
ρ_{2p}	Density of 2-propanol
ρ_{air}	Density of the air
ρ_{ink}	Density of the ink
ρ_p	Particle density
ρ_s	Solvent density
σ	Applied stress
σ_{yc}	Plane-strain compressive true yield stress
τ	Shear stress
υ	Impact velocity
γ	Surface tension
γ^-	Non-additive parameter for electron-donation
$\dot{\gamma}$	Shear rate
γ^+	Non-additive parameter for electron-acceptance
γ^{AB}	Polar part of surface tension
γ_f	True fracture strain of the unmodified matrix
γ_l	Surface tension of the liquid
υ_{min}	Minimum drop velocity
γ_s	Surface energy of the solid
γ_{sl}	Surface tension between solid and liquid

γ^{vdW}	Nonpolar part of surface tension
φ	Angle between the tangent at point P and the x-axis
φ_2^R	Average volume fraction of segments in attached organic layers
φ_c	Filler content
φ_{max}	Maximum filler content
φ_q	Quantum yield
χ	Flory-Huggings parameter
ψ_0	Surface potential of a particle
ω	Angular velocity

Abbreviations

Short form	Full form
2PP	Multiphoton polymerization
3DBP	3D bio plotting
3DP	Binder jetting
A240	Commercial Al_2O_3 particles CT3000SG
A240 [m²]	Surface area of A240
A240 [wt%]	Weight percentage of A240
AB	Polar
ABS	Acrylonitrile butadiene styrene
Abs1638	Absorbance at 1638 cm^{-1}
Abs1734	Absorbance at 1734 cm^{-1}
ACMO	Acryloyl morpholine
Al_2O_3 [g/ml]	Density of the Al_2O_3 filler
Al_2O_3 [nm]	Average particle diameter
$Al_2O_{3\ dehyd}$ [g]	Mass of the dehydrated fillers
$Al_2O_{3\ dehyd}$ [ml]	Volume of the dehydrated fillers
$Al_2O_{3\ dehyd}$ [wt%]	TGA derived weight percentage of the dehydrated fillers
$Al_2O_{3\ hyd}$ [g]	Initial particle weight before thermogravimetric analysis
$Al_2O_{3\ hyd}$ [wt%]	Initial particle weight percentage amounting to 100 wt%
AM	Additive manufacturing
b-Al_2O_3 [wt%]	Weight percentage of Al_2O_3 with strongly reduced water content
BET	Brunauer-Emmett-Teller
CAD	Computer-assisted design
CAM	Computer-aided manufacturing
CIJ	Continuous inkjet printing
CTFA	Cyclic trimethylolpropane formal acrylate
DED	Directed energy deposition
DEGMEE	Diethylene glycol monoethyl ether
DLP	Digital light processing
DOD	Drop-on-demand inkjet printing
DPGMME	Dipropylene glycol monomethyl ether
DSC	Differential scanning calorimetry
EBM	Electron beam melting
EIJ	Electrostatic inkjet printing
ES	Electrostatic
FDM	Fused deposition modeling
FFF	Fused filament fabrication
FTIR	Fourier transform infrared spectroscopy

H_2O [wt%]	Weight percentage of water on Al_2O_3 particles
H_2O_{chem} [g]	Mass of the chemically bound surface water
H_2O_{chem} [ml]	Volume of the chemically bound surface water
H_2O_{phys} [wt%]	Weight percentage of physisorbed water
HexylAc	Hexyl acetate
HRSEM	High-resolution scanning electron microscope
IBOA	Isobornyl acrylate
Inorg. [wt%]	Weight percentage of b-Al_2O_3 and Si
LFA	Laser flash analysis
LP	Dilauryl peroxide
LS	Laser sintering
MPS	3 - (trimethoxysilyl)propylmethacrylate
$MPS_{coating}$ [mg/m²]	Mass of MPS attached to Al_2O_3 particles surface area
MPS_{hyd} [mg]	Mass of hydrolyzed MPS
MPS_{hyd} [wt%]	Weight percentage of hydrolyzed MPS
Org. [wt%]	Weight percentage of organic MPS components
Org.H_2O [wt%]	Weight percentage of organic MPS components and water
PBM	Planetary ball milling
PDMS	Polydimethylsiloxane
Pe	Peclet number
PGMMEA	Propylene glycol monomethyl ether acetate
PP	Polypropylene
PSD	Particle size distribution
PTFE	Polytetrafluoroethylene
Re	Reynolds number
RP	Rapid prototyping
SA	Stearic acid
SFF	Solid free form fabrication
Si [wt%]	Weight percentage
Sil0-A240	PBM grinded powder without MPS addition
Sil6-A240	MPS coated A240
Sil6-TEC170	MPS coated TEC170
SL	Sheet lamination
SLA	Stereolithography
SLS	Selective laser sintering
SLSC	Static light scatting
SSA	Specific surface area
STEM	Scanning transmission electron microscope
TGA	Thermogravimetric analysis
TMPEO3TA	Trimethylolpropane (EO) 3-triacrylate
TODA	2-[2-(2-methoxyethoxy)ethoxy]acetic acid
TPGDA	Tripropylene glycol diacrylate
TPO	Diphenyl(2,4,6-trimethylbenzoyl)phosphinoxid
USB	Ultrasonic bath
UT	Hand-held dispersing device
UTS	Ultimate tensile strength
vdW	Van der Waals electrodynamic
VOC	Volatile component
We	Weber number

1. Introduction

In the 21st century, the world faces challenges on many fronts. Among others, the need for a rising living standard collides with an increasing global population, sharper competition for natural resources and a constraint on the natural balance of the globe. The major economies, global industries and the international scientific community are increasingly aware of the problems and try to counteract by rethinking current concepts in a multitude of areas [1–3]. Manufacturing is one example, which was always subjected to change throughout time, geared towards greater complexity at a steadily accelerating output. It is a tendency, which can only be kept up if the current manufacturing methods become even more efficient. This can be achieved by utilizing the synergies in the different sectors of modern technology [4–6]. Additive manufacturing (AM) is one great example where competence in computer science, mechanical engineering and material science meet. It is a way of production, which is expected to revolutionize manufacturing, not by replacing current methods but by complimenting them [7–9]. In the following subchapters an introduction to the topic of this work will be given and it is going to be explained what additive manufacturing is. Furthermore, 3D inkjet printing will be presented as one important technology in the effort for more efficiency in production. Finally, the overall scope of this work will be illuminated.

1.1. Additive Manufacturing

In the 1980s AM, also known as 3D printing, experienced a gradual introduction. It harnessed the possibilities of the upcoming computer-assisted design (CAD) technology to produce sophisticated models and unraveled the upcoming trend of rapid prototyping (RP). It was possible to produce components with a high degree of freedom and customization from metal, ceramic and polymers without the need for molds or the established machining methods [9–12]. By now 3D printing has turned into a widely spread way of production, even at home, with commercial desktop machines being easily accessible [13]. Similarly, as 2D printing heavily influenced the

sphere of communication and information technology, AM in connection with the "internet of things" can transform the production of highly complex and multifunctional structures. It is not bound to the limiting rules of mass manufacturing, which on the one hand allows the turn out of high volumes of goods at a significantly low cost, but on the other hand lacks flexibility of fast product redesign. Consequently, the development of small-scale batches is not profitable [14–16]. The concept of AM involves the CAD based modelling of structures, partly with a high degree of complexity. The designed object is then digitally sliced into layers and transferred to the printer often as a STL file. Using its freedom of movement in xyz-direction the 3D printer arranges the material in one layer after the other, which is termed computer-aided manufacturing (CAM) [17,18]. Depending on the AM method, the layer thickness can vary between 15 µm to 500 µm. Very elaborate prints make it necessary to utilize support structures or materials, which necessitate post processing. Compared to traditional manufacturing methods like injection molding and CNC machining, AM is a slow production method. However, given its above stated properties to produce increasingly multifunctional and extraordinarily complex structures, the positive aspects often outweigh the drawbacks. In addition to that, in the last decades great strides have led to a gradual increase in printing speeds and user-friendliness of the devices. This moves AM from limited use to a wider audience [19–21].

In 2009, the ASTM International Committee F42 on Additive Manufacturing Technology sought to arrange the established AM methods to give a cleared overview of their different possibilities and to differentiate them from other production methods. They enumerated the methods as follows [22–26] :

Material extrusion is the targeted deposition of highly viscose material through a nozzle. Examples of this category are fused deposition modeling (FDM), fused filament fabrication (FFF), solid free form fabrication (SFF) and 3D bio plotting (3DBP)

Material jetting is the targeted drop vise deposition of liquid material like photopolymers and other pre-polymers. This technology is synonymously called 3D inkjet printing.

Binder jetting (3DP) involves the dispensing of a liquid bonding agent for the targeted fusing of powdered materials.

Sheet lamination (SL) uses layers of sheets, which bond using intermediate adhesive to form 3D objects.

Vat photo-polymerization involves a container or vat filled with UV curable resin, which selectively solidifies. This category encompasses generally lithography-based approaches like multiphoton polymerization (2PP), digital light processing (DLP), and stereolithography (SLA).

Powder bed fusion uses thermal energy, generated for example by lasers or an electron beam, for the targeted fusing of a powder bed of polymers, ceramics or metals. This technology involves laser sintering (LS), selective laser sintering (SLS) and electron beam melting (EBM).

Directed energy deposition (DED) also utilizes thermal energy, using for example lasers or a plasma arc, to melt and fuse materials, in particular metals, during deposition.

1.2. 3D Inkjet Printing

Inkjet printing was one of the first methods adjusted for additive manufacturing, when Sachs et al develop binder jetting in 1992. Besides binders, the range of printable commercial materials was broadened and encompasses direct 3D deposition of organic inks without the need for a powder bed. The method differed from most of the other AM methods, for it allowed the deposition of several materials in one printing process [9,27–29]. It is an advantage when it comes to rapid manufacturing, which ideally aims at the production of ready to use components. It could address the challenge that even a part of a potential device or machinery frequently fulfills numerous functions and is composed of more than one and often several materials. Most of the AM methods are limited to one material and the extension of the materials choice means conducting significant changes to the method itself [30–32]. Nowadays, commercial material

jetting or 3D inkjet printing devices are equipped with print heads moveable in xyz-direction [28,33]. They incorporate up to 450 nozzles [34] and allow multi-material deposition-rates in the area of 1.5 kg/h, depending on the used parameters [35]. The print head emits droplets with a volume of 1 pL to 200 pL, which allows precise drop placement with an accuracy of around 50 µm [34–36]. The requirements for the liquid materials, often denoted as inks, are strict. During jetting the viscosity at printing temperature is limited to values between 8 mPa·s to 40 mPa·s and the surface tension should be between 25 N/m and 35 N/m. After deposition, the ink must readily solidify through physical or chemical transformation enabling the placement of one material layer over the other. This happens by either employing a volatile component (VOC), which evaporates after deposition, or a phase changing material, such as a wax, which increases its viscosity upon cooling [35,37–39]. In addition, UV and/or thermally curable inks are progressively coming up, as they combine the properties of solidification within a millisecond, efficient material usage under omittance or reduction of VOCs and mechanical properties, which go beyond wax-based composites. The current variety of commercial UV curable formulations for 3D inkjet printing ranges from flexible to comparatively stiff materials after polymerization. The materials show similar properties to established polymers like polypropylene (PP) or acrylonitrile butadiene styrene (ABS) [40,41]. Furthermore, biocompatible polymers are available for dental applications [32]. New materials are constantly in development so that in the foreseeable future additional functionalities and properties will be accessible like increased thermal resistance, magnetization and electrical conductivity [42–44]. Also, 3D inkjet-printed electronics could become a reality [45,46]. However, as it is with current electronic devices, such newly developed designs will likely also suffer heat induced shortenings of the service-life. The necessity for heat management might remain an issue to be dealt with [47–49]. Conventionally produced electronics often utilize thermally conductive but electrically insulating ceramic materials or polymer ceramic composites for dissipation of excess heat [50–52]. Similar approaches have shown that the addition of ceramic particles to UV and/or thermally curable materials for 3D inkjet printing could yield comparable results [53–55]. However, the size of employable particles is limited due to the narrow diameter of inkjet print heads, which is around 20 µm to 80 µm. A rule of thumb prohibits the particle size to go beyond the 100^{th} to 20^{th} of the nozzle diameter [35][56]. Furthermore, the suspended particulate systems, whether these are primary particles

or aggregated structures, must be stable and not form agglomerates during printing [35].

1.3. Scope of this Work

The purpose of this work was arranged according to the EU project DIMAP [57], which strived to develop an array of novel inks for multi-material 3D inkjet printing. These materials should demonstrate their capabilities within a 3D printed and functional luminaire and an industrial robot arm. One development branch should formulate up to two kinds of ceramic inks for structural and thermal management applications, in part, by utilizing volatile solvents. A systematic evaluation assessed the range of performance possibilities for these inks. The development chain trialed parameters within the domains of particles, dispersants, organic matrix and solvents to yield an ink, which performs close to the physical possibilities defined by the deposition technology. To our knowledge, these boundaries were not broadly assessed so far within this technology, particularly in the area of thermal management.

Process Development

A process should be developed, which enables the production of ink quantities up to 1 L.

Material Selection

The process should use widely available commercial materials and devices from established vendors.

Material Characterization

The inks and the resulting composites should be characterized with methods, which show their qualification for 3D inkjet printing as well as for the final application.

Ink Requirements

The inks should be jetable with established inkjet systems. The printability with the Fujifilm Dimatix DMP-2831 is seen as representative for these systems. The ink

viscosity should be between 8 mPa·s and 25 mPa·s at printing temperature. The surface tensions should be between 25 N/m and 35 N/m.

Composite Requirements

The development of the thermally conductive materials should aim for values between 1 W/(m·K) and 4 W/(m·K), which are the benchmark characteristics of established pastes for thermal management. The structural material should reach values of 7.0 J/m³ for the tensile toughness and 10 % for the elongation at break. Furthermore, the material should have a Young's modulus of 4000 GPa and a tensile strength of 80 GPa.

It must be noted that the material requirements are very ambitious and are, in part, not possible to achieve under the prerequisite to use established commercial materials. Instead, the values should be seen as an ideal to strive for.

2. Working Principle

The introduction chapter presented 3D inkjet printing as a method combining the flexibility of AM with multi material printing, which fosters new material development. Particle filled composites are one class, which is suitable to convey needed physical properties. The increase of thermal conductance is the focus of this thesis and requires careful adjustment of the material to the boundaries of the deposition technology. To do so, it is important to understand the physical and chemical principles governing the method and the material. The subsequent chapter will deal, among others, with material aspects. This chapter aims at illuminating the 3D inkjet technology and in particular the jetting process itself. During 3D inkjet printing, a print head, which is moveable in xyz-direction, dispenses layer vice material over a build plate (**Figure 1a**) [28]. After each layer the material is dried and/or UV cured, depending on its composition. Often print head mounted IR and UV lamps, as well a heated build plate are utilized [58–60]. In this work, the inkjet printer Fujifilm Dimatix (DMP-2831, Fujifilm Dimatix Inc., Santa Clara, CA, USA) saw employment as a laboratory sized machine for material development (**Figure 1b**). Its DMC-11010 cartridge allowed the testing of materials and examining the four important phases of material deposition (**Figure 1c**), which contribute to the overall quality of the AM. These are the drop generation, morphology, flight and deposition [61,62].

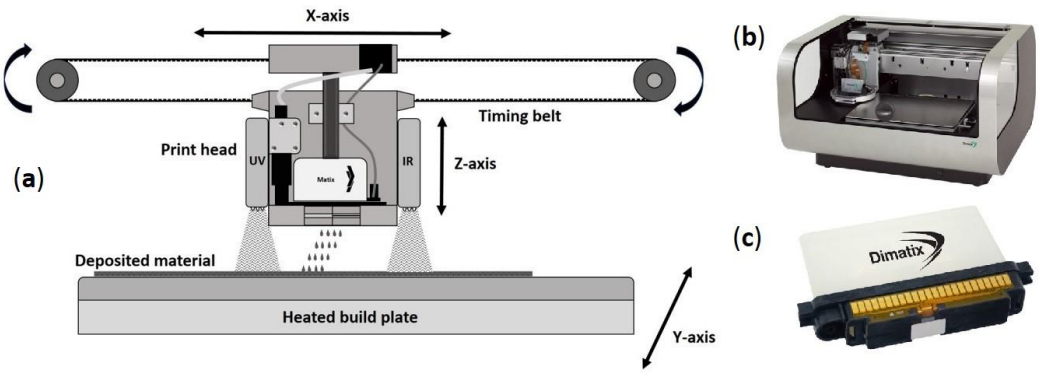

***Figure 1**: **(a)** Schematic depiction of the 3D inkjet printing setup with the print head moveable in xz-direction and the build plate moveable in y-direction. The deposited material is solidified via head mounted UV and IR lamps as well as with a heated build plate. **(b)** DMP-2831 Fujifilm Dimatix inkjet printer* [63]. ***(c)** DMC-11010 cartridge for the inkjet printer* [64].

2.1. Drop Generation

Predominately three established technologies govern the process of drop formation and ejection. These are continuous inkjet printing (CIJ), electrostatic inkjet printing (EIJ), and drop-on-demand inkjet printing (DOD). The first two arrangements are limited in their application. CIJ is the most inaccurate and at the same time most maintenance intensive, while EIJ is a new approach and therefore rarely employed [35,61]. Hence, further discussions in this work are going to be limited to the DOD set up. For over 40 years DOD exhibited increased deployment as the prevalent inkjet technology with most publications revolving around piezoelectric actuated droplet ejection (**Figure 2a**). It allows the generation of 1 pL to 1000 pL droplets with the corresponding diameters of 10 µm to 100 µm [34,35,65]. The application of a voltage onto the piezoelectric actor enables its controlled bending at a predefined frequency of up to 20 kHz. The piezo waveform describes the bending regime of the piezo membrane (**Figure 2b**). The bending happens in phases, where first ink is pumped into the chamber. Second it is emitted from the chamber. Third and fourth, the piezo membrane relaxes stepwise to prevent air suction [35,66,67].

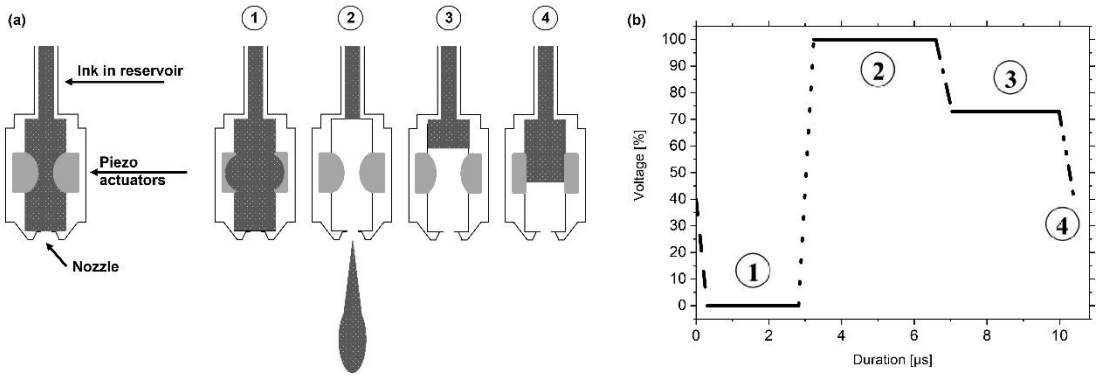

***Figure 2**: **(a)** Schematic representation of the piezoelectrically actuated droplet generation* [67]. ***(b)** Waveform describing respective piezo conditions.*

2.2. Drop Morphology

The inkjet printing process bears several requirements for the successful deposition of materials [35,67]. Among others, the ink and the dispensing arrangement must bear properties to enable the repeatable generation of droplets with a targeted standard and

an adequate rate. **Figure 2a** shows a schematic depiction of the drop formation process in a DOD nozzle. The resulting droplet exhibits a DOD characteristic tail. During flight, the surface tension of the ink causes the tail to retract under formation of a spherical droplet. In the course of this process parts of the ligament can break off under formation of satellite droplets. Since the print head is in motion over the substrate, satellite droplets can cause a decrease in resolution due to their altered trajectory relative to the main droplet [68]. Consequently, satellites must be prevented by adjusting the physical properties of inks. Also, the ink must show compatibility with the initial substrate as well as with the previously deposited layer. Ideally, the droplets get immobilized upon impact, assume a stable sessile drop configuration and interact with adjacent material to form the intended structure [69]. Early investigations on the mechanism of drop generation introduced the parameter $Z = \frac{1}{Oh}$ [70], with Oh being the Ohnesorge number:

$$Z = \frac{1}{Oh} = \frac{\rho \cdot v \cdot a}{\eta} \cdot \sqrt{\frac{\gamma}{\rho \cdot v^2 \cdot a}} = \frac{Re}{\sqrt{We}}, \quad (1)$$

where ρ, η, γ and v are the density, dynamic viscosity, surface tension and drop velocity of the fluid, respectively. The characteristic length a is the diameter of the nozzle. Z

is also described by the Reynolds (Re) and Weber (We) numbers. Further experimental investigations set the boundaries for successful drop ejection and effective satellite droplet prevention, which were within the limits $1 < Z < 10$ [71]. These findings are also relevant for particle-based systems, which were confirmed experimentally [37,72]. An increasing ink viscosity with decreasing Z contributes to a stable droplet tail under the prevention of satellite formation [73]. The area of ink printability is further limited by two other boundaries. On the one hand there is the minimum drop velocity v_{min} needed to overcome the ink surface tension at the nozzle [74]. This value is represented by a minimum Weber number:

$$We_{min} = v_{min}\left(\frac{\rho a}{\gamma}\right)^{1/2} = 4\,, \quad (2)$$

On the other hand, the drop velocity is limited to prevent the onset of splashing upon drop impact on the substrate [75]. A formulated threshold defines the limit as follows:

$$(We)^{1/2}(Re)^{1/2} = f(R), \tag{3}$$

with f(R) being a function of the surface roughness. An experimentally derived value for flat surfaces with a low roughness is f(R) ≈ 50 [76]. The introduced equations 1 to 3 describe an area of printability in a parameter space of Re and We for inks with a DOD inkjet system (**Figure 3**). This system is compatible with a wide range of particle filled inks where Z was a useful parameter for material adjustment. However, it applies particularly to Newtonian inks, with investigations on non-Newtonian materials being lower in number.

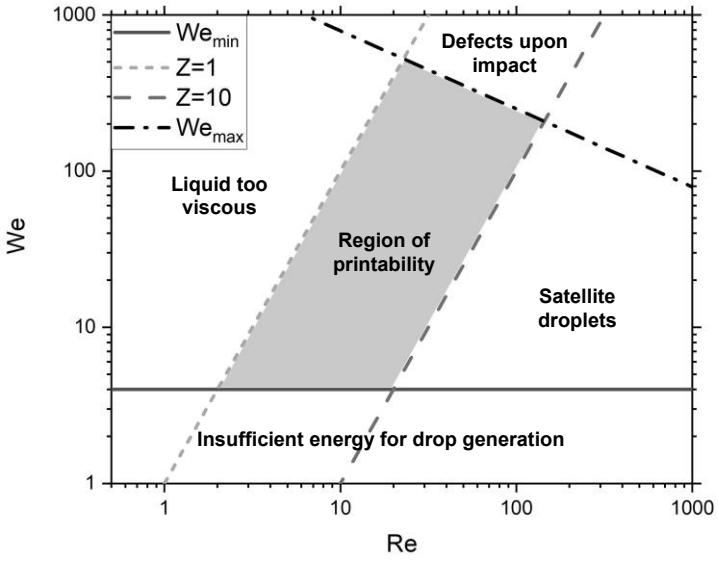

***Figure 3**: The area of printability of Newtonian inks suitable for DOD inkjet printing. The parameter space is a function of the Re and the We number. The image was redrawn from* [61].

In literature the problem with satellite droplets was addressed. Fluids with inadequate properties improved after addition of low concentrations of polymers. Thereby molecular weight of more than 300000 g/mol showed the most benefits and contributed to a repeatable retraction of the droplet tail during flight [77,78]. In addition to that, the waveform of the piezoelectric actuator has an influence on the

satellite formation and on the stability and repeatability of the droplet. Especially at drop generation rates beyond 1 kHz careful adjustment is necessary [73,79–81].

2.3. Drop Flight

The droplet tail shown schematically in **Figure 2** retracts steadily to form a spherical droplet. To enable enough time for the process the print head substrate distance should be 1 mm to 3 mm. Distances, which are too long, however, can contribute to the misplacement of droplets during flight due to air resistance. A modified Stokes' formula describes the procedure using air as the fluid. It adjusts the drag coefficient of a sphere C_D to the Reynolds number range of $2 < \mathrm{Re} < 50$, which are values characteristic of inkjet drop sizes and velocities [74]:

$$C_D = \frac{24}{Re} + 4(Re)^{1/3} . \tag{4}$$

The equation allows establishing a relation between the dimensionless velocity of the drop v^* and the dimensionless distance from the printhead to the substrate x^*:

$$x^* = \frac{\rho_{ink}}{\rho_{air}}\left[(Re_0)^{1/3}\left(1 - v^{*1/3}\right) + \sqrt{6}tan^{-1}\left(\frac{1}{\sqrt{6}}Re_0^{1/3}v^{*1/3}\right) - \sqrt{6}tan^{-1}\left(\frac{1}{\sqrt{6}}Re_0^{1/3}\right)\right] \tag{5}$$

with $x^* = x/a$, x being the distance covered by the drop and a the diameter of the nozzle. The term $v^* = v/v_0$, contains v being the drop velocity and v_0 the initial drop velocity. Re_0 describes the initial Reynolds number of the drop right after ejection from the nozzle. The terms ρ_{ink} and ρ_{air} are the respective densities of the ink and air in standard conditions. The equation visualizes that the resolution can be limited by drag. However, decreasing the distance between the print head and the substrate counteracts that tendency for drop sizes of 10 µm and larger. Smaller dimensions cannot be countered by printhead substrate vicinity.

2.4. Drop Deposition

The object fabrication in 3D inkjet printing relies on the conversion of the deposited liquid to a solid. With a volume of 1 pL to 1000 pL the drops have a diameter of 10 µm to 120 µm. Ideally, they form a sessile drop upon landing, resembling a spherical cap. The droplets coalesce with other droplets nearby creating a continuous structure. The transformation to a solid occurs either through solvent evaporation or phase change. In turn the phase change can be triggered by temperature or polymerization, induced thermally or through irradiation.

The inkjet drop speed upon arrival onto the substrate is normally 1 m/s to 10 m/s. When the drop hits the surface, its properties are best described as a function of initial velocity u_0. The inks behave according to a dynamic process, during which the droplet initially spreads and converts kinetic energy into surface energy [82]. Although unlikely for inkjet printing, during this step, large droplets, at large velocities can disintegrate into pieces by splashing. After the spreading event, the droplet retracts to minimize surface energy again, followed by oscillatory energy dissipation before being stabilized by capillary forces in an equilibrium shape. The whole process takes place on a timescale of µs.

3. Materials and Methods

This chapter focuses on the materials for 3D inkjet printing, their chemical and physical background as well as the methods involved in their fabrication and characterization. As previously explained the main target of this thesis is the production and testing of inkjet printable polymer ceramic composites for thermal management applications. Furthermore, investigations on nanocomposites gave insight into the area of structural materials. The utilized components are pre-polymers, which polymerize into thermosets, alumina particles and molecules for stabilization of the organic and inorganic phases.

3.1. Thermosets

Highly cross-linked materials gained importance in recent decades due to their advantageous properties in comparison to other materials. These include thermal stability, mechanical strength, lightweight, low cost and manufacturing time [83,84]. Due to their network structure, they do not change their shape once manufactured. Therefore, they often serve as a substitute for metals and alloys in areas like aerospace, medicine and energy [83–85]. Since the first commercial thermoset, the Bakelite, in 1909 [86] several manufacturing techniques like wet lay-up, spray-up and resin transfer molding have established themselves [87–90]. They have in common that the liquid or powdered precursors react due to heat or chemical initiation. The time, energy and monetary investment to produce complex parts are high while the process remains rigid and not easily adaptable to changes [84,91,92]. 3D printing is an emerging way of production to allow the necessary flexibility while still providing high performance results [93]. The possibility to microstructure the print often results in the simplification of the design by reduction of unnecessary components. This is an advantage for example in lightweight applications. Moreover, it allows for cutting costs, energy and material expenses. Elaborate structural planning also allows increasing the mechanical properties of components [92,94]. New materials for 3D inkjet printing have also better rheological properties, which eases their handling and exhibit better pot life in comparison to established materials [95].

With some newly formulated 3D printing inks, such as bulk polymerizable acrylates and methacrylates, the in-situ curing process is complete in the order of seconds via frontal polymerization, compared with many hours or days by the conventional method [94]. The following subchapter deals with the aforementioned material group and examines its polymerization mechanism.

3.1.1. Bulk Polymerization

Bulk polymerized materials are often highly cross-linked thermosets, which result from (meth-) acrylate precursors (**Figure 4**) in a photo- or thermally induced reaction. These possess advantageous properties, which set them apart from other, mostly linear polymers. The educts react energy efficiently in solvent free and ambient conditions whilst allowing, in case of photo-polymerization, to control the timing and location of conversion [96–98]. This led, besides their utilization in additive manufacturing, to a widespread adoption in areas like dentistry, optics, coatings, lithography, microfluidics and tissue engineering [96,97,99–102].

However, bulk polymerization still suffers from a range of problems, which limits its usage. During conversion, materials experience volume shrinkage, which leads to stress development and compromises their mechanical integrity [103]. Oxygen inhibition and other factors contribute to an incomplete conversion of the educts so that they remain in the material, decrease the structural properties of the polymer and leach out from the material with time [104,105].

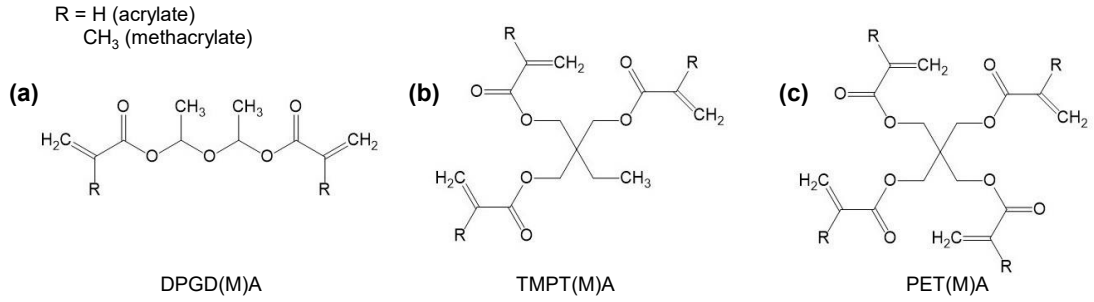

***Figure 4**: Widely used commercially available polyfunctional acrylate (R=H) and methacrylate (R=CH3) monomers often utilized as reactive diluents in mass polymerization reactions. With (**a**) being dipropylene glycol di(meth)acrylate, (**b**) trimethylolpropane-tri(meth)acrylate and (**c**) pentaerythritol tetraacrylate. The image was redrawn from* [106].

The bulk polymerization proceeds via radicals, which originate from photo- or thermal initiators upon light irradiation or thermal activation. As shown in **Figure 5**, the reaction follows the scheme of initiation, propagation and termination [107]. The materials transform from a liquid into a highly cross-linked network in a fraction of a second. This has dramatic implications on the polymer properties as the reaction becomes highly complex due to diffusion dependencies, postponed equilibria, gradients in concentration, light intensity, and temperature, as well as increased network heterogeneities [108–111]. It leads to the situation that the conditions during the polymerization have a massive influence on the resulting material characteristics. The understanding and control of the reaction are necessary to generate a wanted outcome for the material since, as opposed to linear polymers, it is not possible to restructure cross-linked polymers once they have set. Additionally, targeted adjustments of monomers at the molecular level and alterations of the polymerization mechanism offer further options to influence the reaction. The reaction presented in **Figure 6** shows schematically the traditional radical generation. It starts, in case of photo-initiation, via a Norrish type I reaction or Norrish type II reaction. The former mostly initiates via UV triggered reactions by cleaving upon irradiation and the latter often uses visible light, which results in the abstraction of a hydrogen atom from an amine synergist [112,113]. In case of thermal initiation, the reaction is started via thermal decomposition of organic peroxide [114]. The initiator (*I*) transforms into two equally reactive primary radicals (*R*•), which then interact with the monomer based double bonds to form polymers.

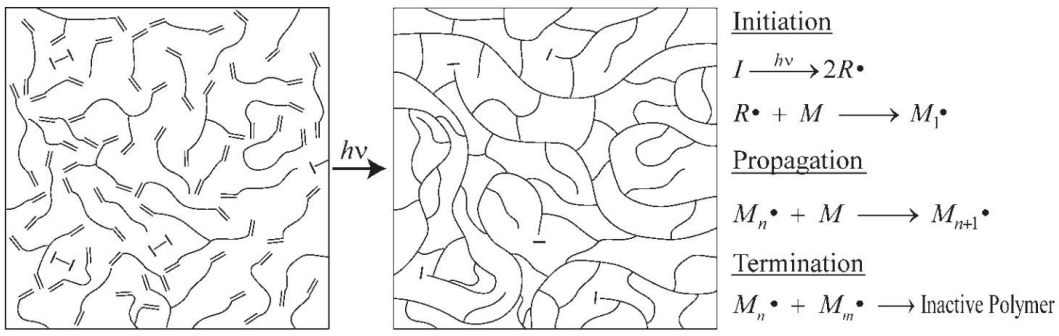

Figure 5*: Schematic representation of the light induced polymerization. An initiator and monomers form a conjugated network in the three steps initiation, propagation and termination. The image was reprinted from* [115] with kind permission from the AIChE Journal.

The light induced decay of the photoinitiators is the only light dependent step during photo-polymerization. However, factors like the strong absorption of the radical forming molecules, thick monomer films, dyes or pigments can result in a light intensity gradient within the materials [116], which leads to locally different initiation rates (R_i) described by:

$$R_i = 2f\varphi_q\varepsilon_m[I]I_0, \tag{6}$$

with f being the efficiency, φ_q the quantum yield, ε_m the molar absorptivity, $[I]$ the initiator concentration and I_0 the light intensity.

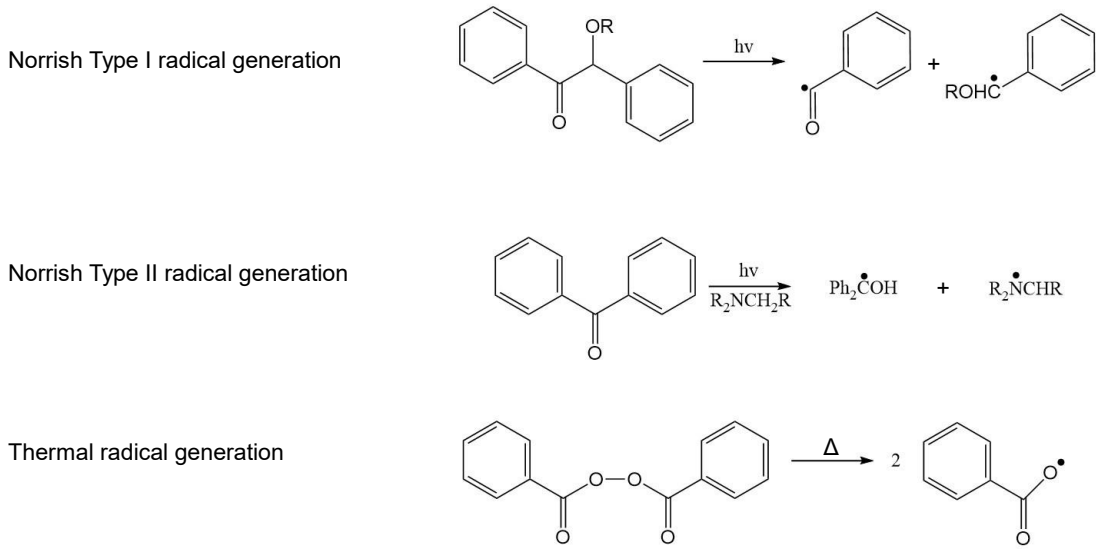

***Figure 6**: Radical generation via Norrish Type I initiator with cleavage upon UV light irradiation. Radical generation via Norrish Type II initiators with abstraction of hydrogen from an amine synergist during irradiation with visible light. Radical generation via thermal decomposition of an aryl peroxide initiator. In part, the image was redrawn from* [106].

As the reaction proceeds, the description of the initiation rate becomes more complicated since equation 6 mentioned efficiency decreases due to a higher likelihood of recombination reactions [117,118].

Similarly, the propagation reaction rate (R_p) shows significant changes as well. The radicals and double bonds attached to the growing polymer exhibit chain length dependent reactivity [119,120]. The increasing interconnectivity of the polymer further limits the progression of the double bond conversion and causes vitrification

as well as diffusional limitations. Under these circumstances, the propagation reaction rate has the following formulation:

$$R_p = k_p[M][M_n\bullet], \tag{7}$$

where k_p is the propagation rate constant, $[M]$ is the concentration of double bonds and $[M_n\bullet]$ is the total radical concentration. The equation describes a multitude of reactions encompassing the interaction of radicals with pendant and monomeric double bonds as well as with chain transfer reinitiated radicals [121,122]. During the conversion, the constant k_p accounts for all of these reaction participants, which exist at different times and locations within the material.

The theoretical description of the termination reaction rate (R_t), where two radicals recombine, is given by:

$$R_t = 2k_t[M_n\bullet]^2, \tag{8}$$

with k_t being the termination rate constant. The term does not include chain length variations, polymer heterogeneity and radical entrapment. However, these diffusional limitations heavily influence the polymerization termination and lead to the auto-acceleration or gel effect [123,124]. It manifests itself when the reduced mass transfer causes increased radical concentration with consequently high polymerization rates despite a shrinking double bond concentration [121]. Because of the high crosslinking at some point, radicals are completely unable to move and remain potentially active for significant amounts of time.

Since the concentration of radicals is hard to evaluate a pseudo steady state assumption has been established to modify equation 7,

$$R_p = k_p[M](R_i/2k_t)^{1/2}. \tag{9}$$

Besides the described polymerization processes, simultaneous side reactions occur, which significantly influence the conversion. One such major event is oxygen inhibition, where the air derived molecules chemically interact with free radicals under the formation of peroxy-based radicals. These in turn do not show meaningful

propagation polymerization and therefore prevent the conversion reaction [125,126]. Once the monomer dissolved oxygen is consumed and no further molecules diffuse into the location of reaction, the polymerization can resume. This can be observed in thicker monomer films, where the oxygen exposed surface does not solidify but deeper layers do.

The bulk polymerization network is very heterogeneous with significant variations in the crosslinking density and glass transition temperature differences of 150°C [127,128]. Upon the formation of radicals after light irradiation a high degree of polymerization can be observed locally with a large proportion of the propagating chains binding intramolecularly in a primary cyclisation, which fosters the formation of microgels [129,130]. Since this behavior delays the formation of a network, which spans the whole polymer, vitrification starts not at a theoretically predicted conversion of 1 %, but at 5-10 %. Due to the depletion and binding of the initiators within the microgel, nanoscale regions of unreacted monomer remain trapped after the polymerization propagation has been finished.

During photopolymerization the conversion rate can be adjusted by the energy density of the UV light. At values of around 0.7 W/cm² the propagation of the double bonds can outpace the shrinkage of the polyacrylate allowing for a higher conversion of an otherwise unaltered material. In turn, curing with the same energy dose but for a longer time prevents the movement of radicals.

3.1.2. Physical Properties

Polymerized polyfunctional acrylates possess advantages over other polymers and even other thermosets for being readily bulk polymerizable from pre-polymers within seconds. This property makes them suitable for additive manufacturing. However, depending on the area of application, further beneficial characteristics are important. Often, these are mechanical properties, thermal properties, stability towards UV irradiation and toxicity. To this day, polyacrylates show weaknesses in all these areas and often do not live up to the expectations and necessities of the application [109,115,131–133]. As explained in the previous subchapter, the crosslinking density of polyacrylates is very heterogeneous with highly connected areas, the microgels, and loosely connected or unpolymerized nano areas of educts. Hence, the materials possess build-in breaking points, which compromised the mechanical properties

[106,134,135]. Polyacrylates are often mixtures of monomer diluents with one, but mostly two acrylate functionalities and higher functional monomers. Furthermore, they incorporate oligomers with urethane, polyester or epoxy core segment structures, a molecular weight of 500 g/mol to 2500 g/mol and two to six acrylate functionalities [35]. The smaller monomers are particularly prone to circular cross-linking and therefore to low mechanical properties with high brittleness. These tendencies complicate the measurement of mechanical properties leading to few literature-derived results [135,136]. Contrary to that, oligomers possess well-documented characteristics as some examples in **Table 1** show. Depending on the chemical structure the Young's modulus may reach values up to 2.8 GPa, the ultimate tensile strength 85 MPa and the elongation at break 17 % [137]. Reasons for that are the higher length and stiffness of the molecules, which limits the formation of circular cross-linking and allows for a more homogeneous mesh formation. However, oligomers have a very high viscosity in the area of 1000 mPa·s to 100000 mPa·s [35,138]. For their utilization in inkjet printing, reactive diluents are necessary, which mitigates the positive aspects of oligomers. Manufacturers of commercial materials for 3D inkjet printing have solved the challenge by creating elaborate combinations of acrylate monomers and oligomers with further components, which allow them to significantly reduce the ink viscosity at printing temperatures, in part, beyond 100°C [139–141]. For example, the companies 3D Systems and Stratasys show materials with a wide array of mechanical properties [142,143]. Some of their mechanically most durable materials are depicted in **Table 1**. As can be seen, their characteristics reach and partly exceed the values of the oligomers. Their composition is proprietary and therefore not known. Publications and patents on commercial materials in general, hint at the utilization of cationic polymerizeable materials and waxes besides acrylates [139–141].

The thermal properties of polyacrylates are governed by their thermoset nature. They show no melting point instead the mobility of the cross-linked chains increases with increasing temperature, which is marked by the glass transition temperature (T_g). Otherwise, they stay in the shape they were brought before setting [144]. The degradation temperature reaches values up to 200 °C for some polyacrylates [145].

***Table 1**: Youngs's modulus (E), ultimate tensile strength (UTS) and elongation at break (ε_{max}) of commercial materials after UV and/or thermal curing, which can be utilized for structural applications.*

Product name	E [MPa]	UTS [MPa]	ε_{max} [%]	Supplier
Genomer 3364	1072	17	5	Rahn [137]
Genomer 4247	2809	28	8	Rahn [137]
Genomer 2281	2785	85	17	Rahn [137]
Digital ABS Plus	2800[a]	58[a]	33[a]	Stratasys [146]
VisiJet M2R-CL	1750[a]	40[a]	9[a]	3D Systems [147]
VisiJet M2S-HT90	2750[a]	75[a]	7[a]	3D Systems [148]

[a]Average value.

Like most polymers, the thermal conductance is poor and revolves around 0.17 *W/(m·K)* to 0.20 *W/(m·K)*. Although chain order and proximity were observed to improve the thermal conductance in certain highly engineered epoxides and semi crystalline thermoplastics, both strategies are currently outside the scope of UV curable materials [149–151]. A more thorough explanation of the physics behind thermal conductance in polymers will be discussed in subchapter 3.3.4. UV stability is another topic, which is often addressed when it comes to polyacrylates as the materials are vulnerable to molecular decay by irradiation. The application of UV blocking and absorbing agents, like particles is often utilized to reduce the sensitivity towards UV [132]. Toxicity is also a topic, which is relevant for the handling of polyacrylates. Since the remaining monomers in the polyacrylate leach out over time from the material, they can be regarded as a safety risk. The monomers can cause skin irritation and allergic reaction when it comes in contact with the human body. In the case of dental applications, the molecules can even be toxic due to ingestion, which is one of the reasons that has prevented their broader use up to now [115,133].

3.2. Ceramics

Ceramics are one of the first materials to be used by men predominantly as a structural material in pottery, for buildings and as refractory materials. With time, the functional aspects gained importance so that today the utility of ceramic is manifold [152]. It is used as dielectric material in capacitors, as piezo active material in electromechanical systems, as a catalyst for the generation of hydrogen and for thermal management in

electronic devices [153–156]. The addition of ceramics to polymers translates their properties in part onto the created composite, a process, which is going to be discussed in subchapter 3.3.

Thereby the composite properties strongly depend on the physical properties of the incorporated ceramic as well as on the surface property of it as it influences the quality of the polymer ceramic interface [157].

3.2.1. Surface Characteristics

The surface of a ceramic, for example aluminum oxide, differs from its volume by the high amount of not terminated oxygen atoms, which adsorb water upon contact with atmospheric moisture. Due to the extraordinary chemical reactivity of the ceramic oxygen towards its surrounding, the surface bound water splits heterolytically to form two hydroxyl groups per adsorbed water molecule. These hydroxyl groups then attract other water molecules, which attach physically under the formation of a hydrate layer. The amount of adsorbed water is governed by the thermodynamics of the system [158–160]. Under specific circumstances, for example during soaking in water, alumina can incorporate structural water forming transitional alumina, hydroxides and oxyhydroxides [161].

3.2.2. Physical Properties

Aluminum oxide, Al_2O_3, is one of the most frequently used ceramics due to its low price and advantageous physical properties. Technical bulk alumina with a grain size of 5 µm shows a Young's modulus of 370 GPa and an ultimate tensile strength of 260 MPa [162,163]. Depending on its purity bulk alumina has thermal conductance up to 32 (W/m·K) [164]. Its transitional states change with temperature starting at 750 °C, when γ-Al_2O_3 is transformed into δ-Al_2O_3. α-Al_2O_3 is thermodynamically the most stable state having a melting point of 2072 °C [165,166]. However, this is not always the case in nanoparticular alumina. When the surface area surpasses 100 m^2/g γ-Al_2O_3 becomes more stable than α-Al_2O_3 [167–169].

3.3. Composite Materials

Under optimal conditions, the incorporation of ceramic particles into an organic matrix enables the combination of their positive aspects [170]. In the case of acrylates for 3D inkjet printing, these are the instantaneous ability to form solid polyacrylates under UV irradiation and further cross-link with thermal treatment. However, as described in subchapter 3.1.2, their drawbacks are, among others, the limited mechanical integrity and the low thermal conductance. The focus of this work was to improve these two properties by incorporation of alumina fillers as a second phase, since they show significantly superior values in those areas (3.2.2) and therefore, can, in part, transfer these onto the composite. In the following subchapters, the relevant theoretical background of polymer-ceramic composites for 3D Inkjet printing is going to be covered. This addresses the stabilization of ceramic particles in the organic matrix, the rheological properties of the liquid composite, the mechanical properties of the solidified composite and its thermal conductivity.

3.3.1. Stabilization

Stabilization of the ceramic particles in the liquid organic matrix is important for optimal compounding. The term describes the process, during which the separation of the organic and inorganic phases is prevented by thermodynamic and entropic means [157]. The particle-particle and particle-matrix interactions dictate the state of stabilization and for it to be successful, the former must be as low as possible and the latter has to be as high as possible [171]. This is important as long as the ceramic ink is liquid. Upon polymerization the requirements may change if intense particle-particle interactions are needed, as it is the case in thermal conductance, where the thermal energy transport depends on percolated pathways. Contrary to that, for a positive influence on the mechanical properties, a homogeneous particle distribution is advantageous when the polymer-ceramic interface is at its highest [172–174]. The topics on mechanical properties and thermal conductance in composites are going to be covered in detail in the subchapters 3.3.3 and 3.3.4, respectively. In general, ceramic particle surfaces are highly energetic in a thermodynamic sense when compared with the bulk properties of the same material. The reasons for that lie in their imperfect nature with numerous protruding micro-facets of different crystallographic planes the

edges of which consist of low-coordinated atoms [168,175,176]. This contributes to characteristic electronic states being in the gap region between the bulk valence band and the bulk conduction band. It causes the surface oxygen to exhibit a more basic and the surface cations a more acidic nature in comparison to the bulk material, which is a source of the increased surface reactivity. While particles are remarkably energetic, oxides as a whole exhibit the potential to readily interact with their surroundings. A property, which can be explained by electrostatic instability. This occurs when ceramic material dipole moments in the repeating crystallographic units, which are arranged perpendicular to the surface, create a divergence of poles with the surface bearing a net negative or net positive partial charge [177,178].

The theoretical foundation for the description of forces between particles was developed as classical DLVO theory by Derjaguin and Landau in 1941 as well as by Verwey and Overbeek in 1948, which was developed with water as solvent [179–181]. Their model incorporated electrostatic (ES) and van der Waals electrodynamic (vdW) forces. The ES forces between particles are repulsive and arise from unsatisfied electronic charges caused by structural ion substitution when submerged in a polar solvent. The formerly particle-based ions float around the charged surface as counterions under the formation of an equilibrium. The situation is described in the double layer theory (**Figure 7**), according to which the counterions and solvent molecules near the particle surface are strongly limited in their movement being the quasi-static Stern layer or the inner-Helmholtz plane. Further away from the surface and adjacent to the Stern layer is the outer-Helmholtz plane, which contains hydrated counter ions and solvent molecules, which can orient themselves more freely. With increasing distance from the surface, the electrostatic potential decreases. The direct measurement of the potential, however, is not possible. Instead, the electrophoretic or Zeta potential (ζ) is measured at the slipping plane, which is the interface between the strongly bound and freely moveable solvent molecules [182,183].

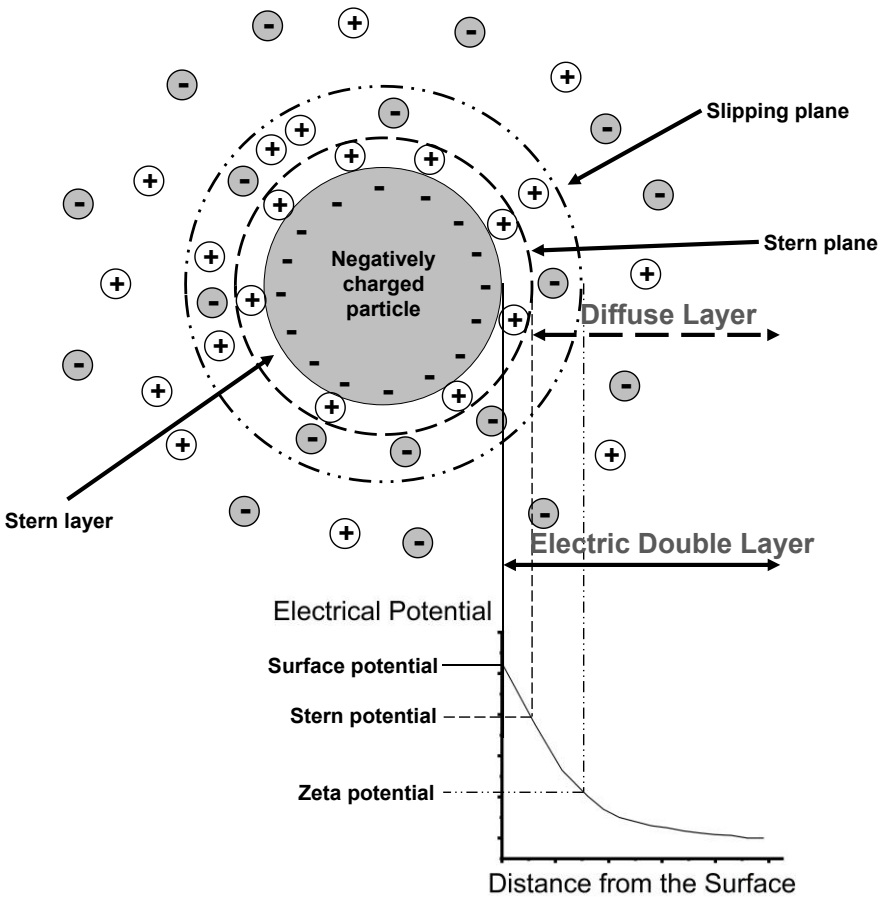

***Figure 7**: Double layer model with a schematic depiction of a negatively charged particle surrounded by ions in a liquid medium. The image is juxtaposed to a diagram showing the electrical potential as a function of the distance from the surface. This image was inspired by* [182].

Following the equations a1 to a3 in A.1.1, the repulsive free energy ΔG_l^{EL} or the electrostatic interaction energy can be formulated, which behaves roughly exponential with distance. When ζ is between 10 mV and 60 mV the interaction energy between two spherical particles with the radius R and the distance l is expressed as follows:

$$\Delta G_l^{EL} = 0.5\varepsilon R\psi_0^2 ln[1 + exp(-\kappa l)], \tag{10}$$

with ε being the dielectric constant of the bulk fluid, ψ_0 the surface potential of the particle in eV and κ the inverse of the Debye length, being the thickness of the double layer. Varying κ by changing the specific salt concentration of the solution, in which particles are suspended, controls the range of the double-layer repulsion and strength. In the case of water-based systems, the salt influences the pH of the suspension and regulates proton association and dissociation with surface hydroxyl groups.

The attractive component of the DLVO theory, the Lifshitz-van der Waals nonpolar electrodynamic forces are composed of: First, randomly oriented permanent dipole-permanent dipole interactions, termed orientation forces, second, randomly oriented permanent dipole-induced dipole interactions, termed induction forces and third, fluctuating dipole-induced dipole interactions, termed dispersion forces [178,184]. The interactions have a small reach and decline with l^{-6} .

The nonpolar part of the free energy interaction ΔG_l^{vdW} between two equal spherical particles can be expressed by:

$$\Delta G_l^{vdW} = -AR/12l = \Delta G_{l_0}^{vdW}(Rl_0)/12l, \tag{11}$$

with l_0 being the equilibrium distance and R the radius of the spheres >> l. A is the Hamaker constant and l is the distance between the surfaces. $\Delta G_{l_0}^{vdW}$ is the nonpolar part of the free energy interaction at the equilibrium distance. For liquids, this can be assessed using contact angle measurements. The theoretical foundation alluding to this is described in A.1.2 showing the equations a4 and a5.

Since the DLVO theory does not suffice to describe the behavior of ceramic particles in a liquid the extended DLVO theory was introduced by complementing the ES and vdW forces with polar (AB) forces. Also, at smaller gaps of 10 Å to 50 Å between the particles the absolute value for the AB forces can surpass the ES and vdW forces by up to 10 to 100 times. The AB surface-energy parameters encompass all Lewis electron-acceptor-electron-donor, or Lewis acid-base interactions. These also incorporate hydrogen-donor, hydrogen-acceptor and consequently hydrogen bonding interactions [185,186]. To describe the decay of the AB free energy with the distance of the two spheres, the following equation is to be used:

$$\Delta G_l^{AB} = \pi R \lambda_d \Delta G_{l_0}^{AB} e^{(l_0 - l)/\lambda_d}, \tag{12}$$

where R is the radius of curvature of the particles, λ_d is the decay length of the liquid molecules, with $\lambda_d \approx 10$ Å for water. $\Delta G_{l_0}^{AB}$ is the free energy of interaction in the parallel flat plate conformation at the minimum equilibrium distance l_0, as measured

by contact angle determinations, where $\Delta G_{l_0}^{AB} = -2\gamma^{AB}$, being the surface tension between the two materials A and B. The subchapter A.1.3 in the appendix describes the assessment of the surface energy term with the equations a6 to a8.

As described previously the extent of the repulsive electrostatic forces can be tuned by directly or indirectly adjusting the pH in water-based systems. Yet, the attractive forces are harder to control. It can be achieved by coating the particles with an organic surfactant with lower dielectric properties [187–189]. Surfactants or "surface-active agents" are molecules with the ability to adsorb to surfaces in solution due to their amphiphilic character. The molecules have a polar hydrophilic "head" and a nonpolar "tail". In case the surface is polar, as it is in ceramics like Al_2O_3, and the solvent is the opposite, the adsorption is particularly strong. The surfactant tails protrude into the solvent, cap the van der Waals forces and prevent the particle agglomeration [178,190]. However, in solvents with increasing polarity the attachment strength of surfactants declines. In addition to that, the molecules, which attach anyway, may render the particle surface hydrophobic relative to the solvent. This worsens the suspension stability as surrounding solvent molecules start to associate more with each other than with the particles [187].

Besides shielding the attractive forces, surfactants may provide steric stabilization by preventing particle surfaces from approaching each other and entering proximity where van der Waals forces are strongest. Nevertheless, due to their small size steric hindrance seems to be the minor stabilizing effect for surfactants. Here polymers may offer improvement as shown in **Figure 8** [188,191]. In comparison to the short-chained surfactants, polymers can form a denser and thicker coating on the particle surface with parts of the polymer extending further into the solvent. Thereby, homopolymers are frequently used. The macromolecules attach to the particle surface with their train segments, while the loop and tail segments extend into the lumen. The large molecular body provide good adherence to the particle surface even if the attraction of the single monomer segments is low. Further possible dispersants encompass molecules like diblock copolymers and comb-like copolymers with engineered segments for higher affinity to the particle and segments for increased interaction with the solvent [192,193].

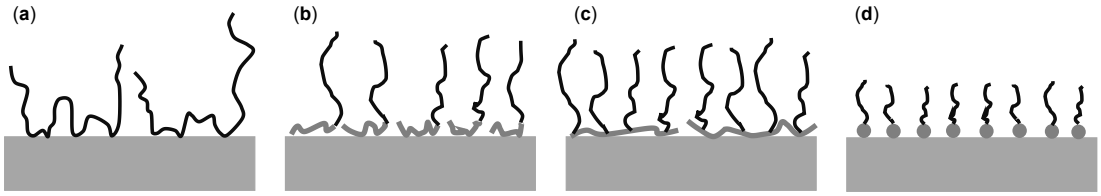

***Figure 8**: Schematic depiction of varying organic coatings on an idealized ceramic surface. (**a**)Homopolymers, with segments, forming tail, loop, and train arrangements. (**b**) Diblock copolymers, with a short anchor segment for surface attachment and an elongated tail segment. (**c**) Comblike copolymers, with protruding tail segments on a surface attached backbone. (**d**) Short-chained surfactants, with the head group anchored to the particle surface and a short protruding tail. This image was redrawn from* [188].

For the theoretical description of the steric repulsion in polymer coatings, empirical models exist for the different molecular configurations of the dispersants. However, this subchapter has not the intention to deliver an exhaustive overview of the models presented in the literature. Instead, two established model cases for homopolymers should exemplify the calculation of the steric repulsion. Thereby, particle surfaces approach each other having a distance l, which is closer than the double of the attached organic layer thickness δ. The pseudo-homopolymer model illuminates the situation $\delta < l < 2\,\delta$, where the surface polymers start to mix with each other causing steric repulsion [192,194] given by:

$$\Delta G^{ST,mix} = \frac{32\pi R k_b T \varphi_2^a (0.5-\chi)}{5 v_1 \delta^4}\left(\delta - \frac{l}{2}\right)^6, \tag{13}$$

with φ_2^R being the average volume fraction of segments in the attached organic layer with the empirical value of 0.37 and k_b being the Boltzmann constant. The Flory–Huggins parameter χ is a measure of solvent quality, v_1 is the molar volume of the solvent, and l is the interparticle distance.

The uniform segment model describes the situation when $l < \delta$. The polymer layers densify during the particle approach so that the main contribution to the repulsive force is elastic in nature while the chain mixing force is subordinate [192,194]. The total force is the sum of the contributors:

$$\Delta G^{ST,mix} = \frac{4\pi R \delta^2 k_b T \varphi_2^a (0.5-\chi)}{v_1}\left(\frac{l}{2\delta} - \frac{1}{4} - ln\frac{l}{2\delta}\right), \tag{14}$$

$$\Delta G^{ST,el} = \frac{2\pi R\delta^2 k_b T \rho_2 \varphi_2^a}{M_2^R}\left\{\frac{l}{\delta} ln\left[\frac{l}{\delta}\left(\frac{3-l/\delta}{2}\right)^2\right] - 6ln\left(\frac{3-l/\delta}{2}\right) + 3\left(1-\frac{l}{\delta}\right)\right\}, \tag{15}$$

with ρ_2 being the density of the adsorbed polymer and M_2^R is its molecular weight.

By combining all introduced forces, it is possible to construct a total free energy vs. distance curve [181,188] given by:

$$\Delta G = \Delta G^{EL} + \Delta G^{vdW} + \Delta G^{AB} + \Delta G^{ST}, \tag{16}$$

which incorporates the electrostatic EL, the nonpolar vdW, the polar AB and the steric forces. **Figure 9** shows example curves composed of the four forces. The used parameters represent homopolymer coated Al_2O_3 particles in a polar solvent. It has to be mentioned that the Born repulsion was not used in the calculation as the particle distance was set to be not smaller than 1.5 Å.

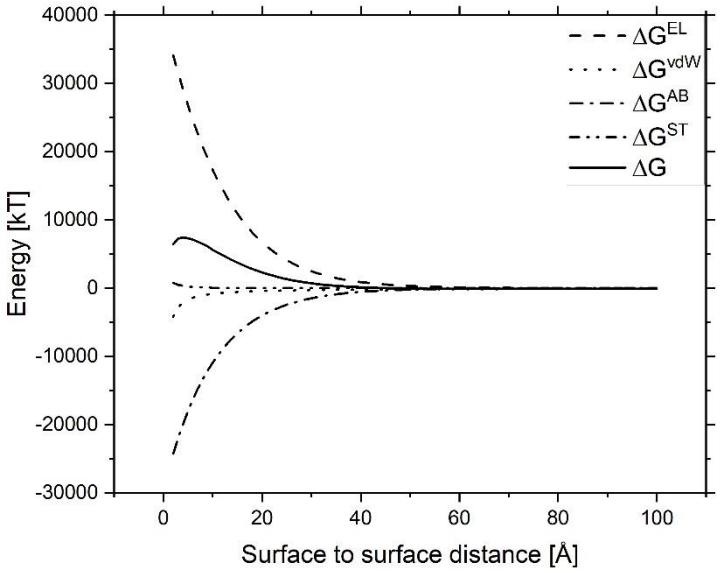

***Figure 9**: Total free energy ΔG in dependency of the particle surface distance. The curve is a combination of the attractive van der Waals and polar forces as well as the repulsive electrostatic and steric forces. The Born repulsion was not used in the calculation due to the closest particle distance being 1.5 Å. It represents a polymer stabilized particle system in a polar solvent.*

3.3.2. Rheology

In 3D inkjet printing rheology is a crucial property and is decisive for successful material deposition. Colloidal systems often have complex rheologies so that a proper understanding of the underlying mechanics is necessary to adjust the material characteristics to the application. Rheology measurement devices track changes in the flow behavior in response to the applied stress or strain according to the Newton equation [195] for an ideal fluid:

$$\tau = \eta\dot{\gamma}, \tag{17}$$

with τ being the shear stress, η the dynamic viscosity and $\dot{\gamma}$ the shear rate.

This measurement can uncover the coherence, structure and consequently the stability of the investigated suspension. Depending on the nature of the suspension, several types of flow behavior occur as a function of shear rate (**Figure 10**) [188,195]. When a fluid is independent of the shear rate it is Newtonian, while a decreasing viscosity at an increasing shear rate hints at pseudoplastic or shear-thinning behavior. When both cases show additionally a yield stress τ_y, caused by internal particle network formation, the respective designations are Bingham plastic and pseudoplastic with yield. If the viscosity increases with the shear rate the behavior is called dilatant or shear thickening. Concentrated particle suspensions often exhibit a time dependent rheology. When the viscosity decreases with time during shear application but slowly establishes its original values after cessation of the stress, it is Thixotropy. Rheopexy is a similar phenomenon, during which however time dependent shear thickening instead of thinning occurs.

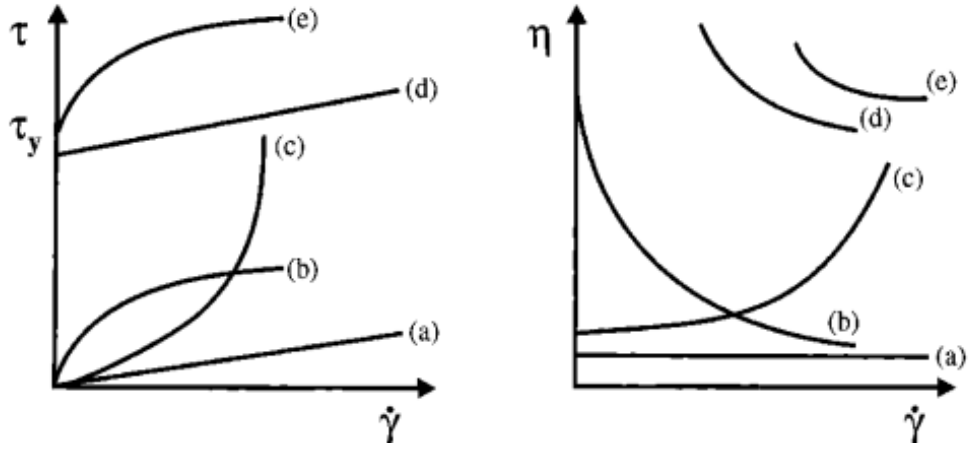

***Figure 10**: Variations of particle suspension rheology depicted as shear stress (left) and dynamic viscosity (right) in dependency of the shear rate. (**a**) Newtonian behavior, (**b**) shear thinning, (**c**) shear thickening, (**d**) Bingham plastic and (**e**) pseudoplastic with yield. The image is adjusted and reprinted from* [188] *with kind permission from the Journal of the American Ceramic Society.*

The suspension matrices used in this thesis were mostly short-chained molecules, which show a Newtonian behavior during measurement. Deviations of this regime mostly arise due to the interactions of the particulate fillers. The simplest situation in such systems is when the particles act like "hard spheres". This means the particles have no inter particle interaction, until their surfaces touch each other and create infinite repulsion (**Figure 11**). There, solely hydrodynamic forces and Brownian motion govern the suspension rheology [196–198]. Only a few model systems live up to this idealized case. However, hard sphere systems serve as a means to assess more complicated situations, where inter particle forces are present. The relative viscosity ($\eta_{rel} = \eta/\eta_0$) is proportional to the Peclet number (Pe):

$$Pe = \frac{R^3 \eta_0 \dot{\gamma}}{k_b T}, \tag{18}$$

with R being the radius of the particles, η_0 the solvent dynamic viscosity, $\dot{\gamma}$ the shear rate, k_b the Boltzmann's constant and T the temperature of the system. Pe shows the energy relation between the hydrodynamic and Brownian interactions. At a Pe value of about 1 the former surpasses the latter, which is accompanied by a beginning shear-thinning behavior. In hard-sphere systems Newtonian behavior remains at low ceramic concentrations of $\varphi < 0.3$. At $\varphi > 0.3$ shear thinning occurs framed by areas of Newtonian flow at low and high shear rates. The shear thinning sets in due to rotating

doublets, hydrodynamic interactions, which disintegrates during the shear rate increase leading to viscosity reduction [199]. On the contrary, shear thickening can occur at higher solid loadings due to order-disorder transitions or cluster formations [200,201]. When the filler content approaches φ_c = 0.6 yield stress can occur because of structural disruption upon shear caused movement initiation. The viscosity of hard-sphere systems is governed by hydrodynamic forces and Brownian motion for φ > 0.05. The empirical Krieger-Dougherty model [199] describes this relationship:

$$\eta_{rel} = \left(1 - \frac{\varphi_c}{\varphi_{max}}\right)^{-K_{\varphi max}}, \tag{19}$$

with $K_{\varphi_{max}}$ being 2.5 for monomodal spheres and φ_{max} is the maximum filler content. The latter is 0.60 to 0.64 for such systems, however, by adjusting the particle size distribution the content can be further increased.

As **Figure 11** describes it, in soft-sphere systems the repulsive interactions start at an inter particle distance l > 0 nm. The electric double-layer and or the organic coating defines the extent of the distance. Such systems are either repulsive or weakly attractive depending on the extent of the van der Waals forces. In case the repulsive forces dominate, the rheological properties of soft-sphere systems are akin to hard-sphere systems if the stabilizing layer is small in comparison to the particle radius [188].

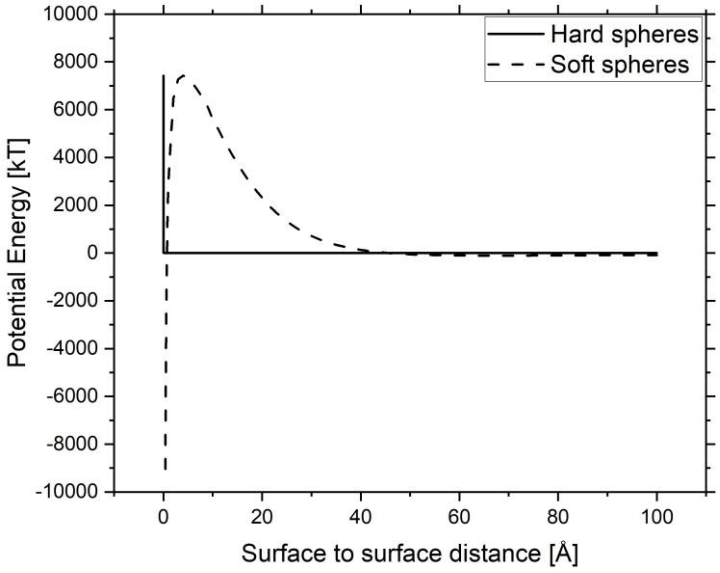

***Figure 11**: Potential interaction energies of model hard and soft sphere systems. The image is redrawn from* [188].

With decreasing particles sizes into the submicron and nano range the proportion of the surface area increases and with it the influence of surface forces. This leads to a stronger interaction between the particles and the matrix. The consequence is, among others, increased agglomerate formation, matrix immobilization (**Figure 12**) and viscosity increase proportional to the surface energy difference of the involved components [106,202].

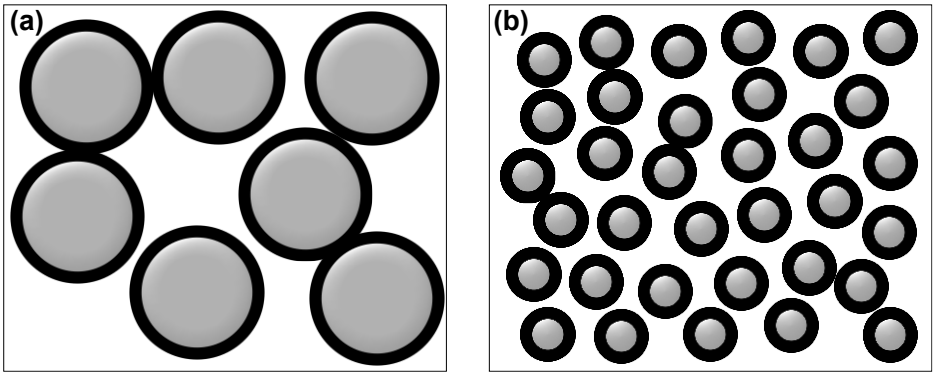

***Figure 12**: Schematic depiction of spherical (**a**) micro particles and (**b**) nanoparticles with a layer δ of immobilized matrix* [202].

3.3.3. Mechanical Properties

The addition of particles to highly cross-linked thermosets changes the thermo-mechanical properties of the materials [170]. A high ceramic content is often advantageous for the thermal conductance. Subchapter 3.3.4 is going to cover this topic. The influence on the mechanical properties depends on the concentration and the characteristics of the filler. This subsection deals with the influence of ceramic fillers on the composite Young's modulus (E_c), ultimate tensile strength (UTS), elongation at break (ε_{max}) and tensile toughness (U_T).

The Young's modulus of a composite is a result of the involved component properties. Notable models following concepts like the law of mixtures [203], the Hashin-Shtrikman bounds [204], and the general self-consistent scheme [205] can predict the development in dependency of the filler concentration. However, their accuracy is very limited for highly concentrated systems.

Newer concepts [206], derived from the rule of mixture, focus on descriptions of higher filled systems considering the particle size distribution:

$$\left(\frac{E_c}{E_m}\right)\left(\frac{E_c - E_f}{E_m - E_f}\right)^{-2.5} = e^{2.5\varphi_c}, \tag{20}$$

with E_m and E_f being the Young's modulus of the matrix and filler, respectively. φ_c is the filler content. The model shows that the stiffness of a composite increases, with increasing ceramic content as the proportion of the flexible organic components decreases. Thereby, the particle size does seem to have only a minor and often negligible influence on the Young's modulus.

Regarding the ultimate tensile strength, literature results show that composites based on highly cross-linked thermosets rarely profit from nano and submicron particle addition [207–210]. Since the ideal ceramic particle acts as a linker bridging parts of the polymer, it attaches, depending on the surface property of the particle, either physically or covalently to the network. Theoretical enforcement of the composite relative to the unfilled polymer would take place if the cross-linking density of equivalent strength and homogeneity increases. This can be achieved with fillers small enough to bridge the voids between the polymer networks. According to literature, simple diacrylate formulations show cross-link densities of around 1200 mmol/cm³ [211–213]. As opposed to that, commercially available spherical mono modal 10 nm particles [207], to name a common example, allow only values of $6.2 \cdot 10^{-4}$ mmol/cm³. Hence, increasing the tensile strength with particles is not a promising approach for composites. In turn, large particles of micrometer size, agglomerates of nanoparticles and high ceramic concentrations of particles were shown to deteriorate the UTS. Micro particles cause areas of increased tension within the material when exposed to stress. These micro dimensional areas are often of the same size as typical cracks, which fosters their initiation [202]. In their entirety, agglomerates of nanoparticles often resemble microstructures and therefore share the similar adverse effects as micro particles [209]. While high ceramic concentrations beyond 30 vol% may contribute to agglomeration in the first place due to particle percolation, even higher concentrations beyond 65 vol% may foster the entrapment of air [199].

In thermosets, the elongation at break and toughness have an indirect relationship to the Young's modulus and to the cross-link density of the material. Stiff thermosets show only a little elastic and almost no plastic deformation with values around 1 % to 17 % (**Table 1**). This consequently leads to a decrease in toughness [106,214,215]. The addition of ceramic fillers can further exacerbate the tendencies due to the increase in stiffness [216]. Despite the fact, ceramic fillers can also initiate mechanisms to toughen the composite. Micro particles do that among others by triggering crack deflection, crack pinning, particle pullout and micro cracking, while nanoparticles below a size of 40 nm rather involve particle debonding, plastic void growth and shear banding [217]. A more detailed description of the mechanisms is in the appendix in A.2 showing the equations a9 to a14.

Recently, the influence of nano and submicron particles was extensively investigated in highly crosslinked epoxy matrix composites. In part, the materials showed significant improvement with regard to Young's modulus and toughness. With ceramic contents of 30 vol%, the values showed increases of up to 50 % and 130 % relative to the unfilled matrix, respectively [207]. While no improvement of the UTS was reported, the ε_{max} of the composites improved by around 64 % in composites with 2.5 Vol% filler content [207,210]. However, materials akin to 3D inkjet-printed particles filled composites were investigated less frequently. When it comes to the Young's modulus, the addition of 30 vol% of ceramic fillers increased the value up to 30 % relative to the unfilled matrix [218]. The toughness improves by 8 %, while no information on elongation at break and UTS could be gathered [218].

3.3.4. Thermal Properties

In polymer ceramic composites thermal conductance takes place via vibrations of atoms, which propagate throughout the polymer chain networks and ceramic lattices (**Figure 13a**) [174,219]. These vibrations are called phonons and are mathematically described in the Peierls model [220]:

$$\lambda = \frac{1}{3}\sum_{i} c_i \, v_i l_i \, , \tag{21}$$

with c_i being the specific heat capacity at constant volume, v_i the velocity of the phonon and l_i it's mean free path. The thermal conductance is higher in ceramic materials due to their crystallinity, which positively influences the thermal properties of composites. The overall lower conductivity of composites compared to the pure fillers is the result of the poor polymer properties on the one hand [221]. On the other hand, the interface between the two phases is a source of phonon scattering [222] and increases with higher thermal surface resistance (R_{Bd}):

$$R_{Bd} = \frac{a_K}{\lambda_M}, \tag{22}$$

with a_K being the Kapitza radius and λ_M the thermal conductivity of the matrix material. The Kapitza radius resembles the particle radius at which no net increase in thermal conductivity of the composite relative to the matrix material is achievable due to the interfacial resistance [223].

Further parameters, which influence the thermal conductivity of composite materials, are the thermal conductivity of the matrix and the filler as well as the concentration of the filler (**Figure 13b**) [174,219]. The latter has the biggest impact on the composite especial at filling grades which exceed 30 vol%, a threshold where percolation takes place [224]. It is possible to predict the thermal conductivity of a composite based on the respective data of the matrix and the fillers using suitable models. The Bruggeman model [174,225] has established itself as a reliable means for predicting composite properties at elevated ceramic contents:

$$1 - \varphi_c = \frac{k \cdot \lambda_F - \lambda_C}{k \cdot \lambda_F - \lambda_M} \cdot \left(\frac{\lambda_M}{\lambda_C}\right)^{\frac{1}{3}}, \tag{23}$$

with φ_c being the filler content, λ_F the thermal conductance of the filler and λ_C the thermal conductance of the composite. However, the model does not consider the thermal surface resistance R_{Bd}, which is a source of error and has to be accounted for. We adjusted this circumstance by adding an empirically derived dimensionless prefactor k, which takes the surface resistance of the utilized fillers into consideration. In literature the thermal conductivity of 3D inkjet-printed particle filled composites was not investigated according to our knowledge. However, a sufficient number of

publications dealt with Al_2O_3 particles in polymer matrices. Since the thermal conductivity of polymers has a comparatively low variation, these values can be regarded as representative of inkjet printable materials. The thermal conductivity of respective composites is in the range of 1 W/(m·K) at a filler content of 50 vol% [226–228].

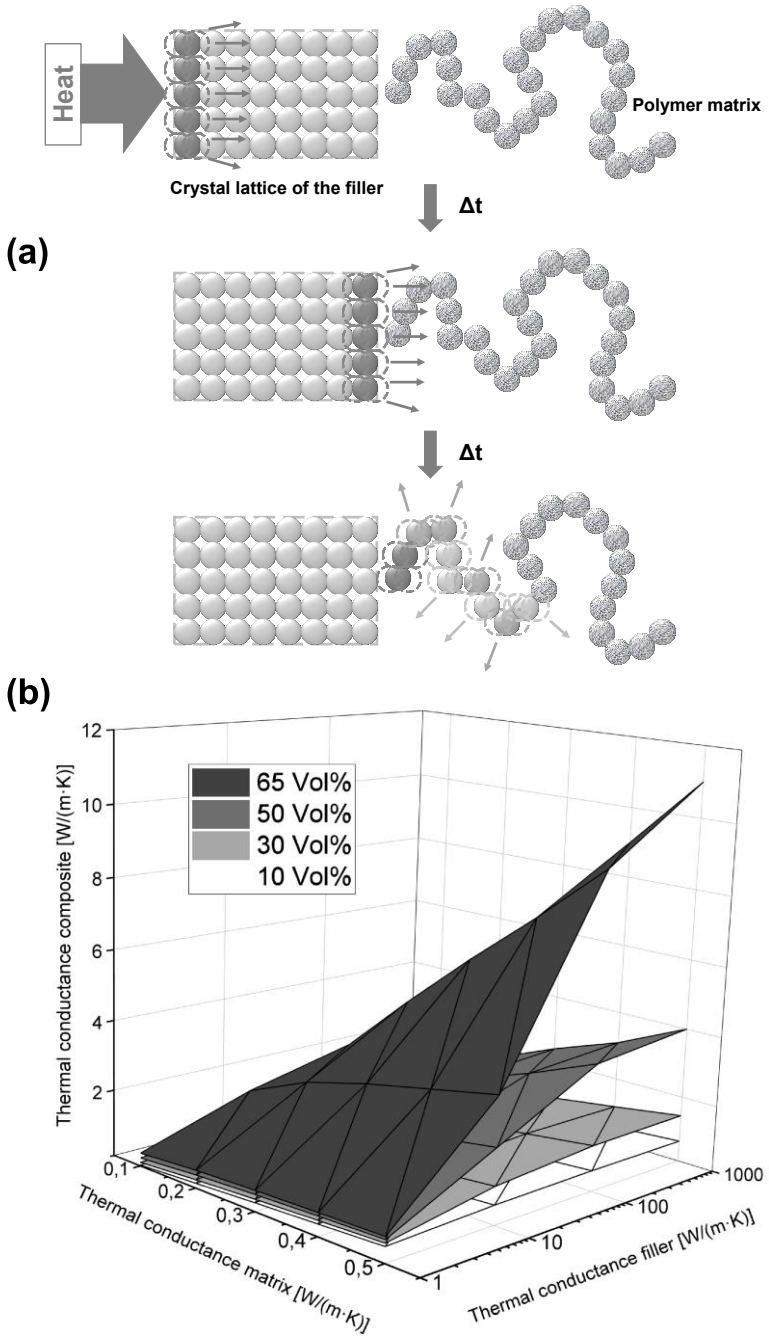

***Figure 13**: (**a**) Schematic depiction of thermal conductance in a composite material with phonons propagating from the ceramic lattice to the polymer network. The image was redrawn from* [174]. ***(b)** Bruggeman model of the composite thermal conductance as a function of the matrix thermal conductance and the filler thermal conductance* [174].

3.4. Manufacturing and Analysis

The subchapter lists the basic functional principles of the methods utilized in this work. It encompasses the analysis of the ceramic particle morphology and size, the processes of particle homogenization and stabilization and the rheological characterization of formulated inks. Consequent method introductions illuminate the analysis of substrate wetting and the conversion efficiency measurements of cured inks. Investigations on the thermal properties of produced composites involved thermogravimetric analysis as well as methods to assess the glass transition temperature and the thermal conductance. Finally, the tensile test introduces a way to analyze the mechanical properties.

3.4.1. Morphology

This work utilized alumina particles of varying sizes with stabilizing organic coatings. The morphologies of these particles differ, which has an influence on the thermal conductance and the mechanical properties of the resulting composite. Visualization using microscopic imaging is a viable option. However, due to the small features of the powder electron-based microscopy was preferred to gain a sufficient resolution according to the Abbe diffraction limit [229]:

$$d_m \approx \frac{\lambda}{2NA}, \tag{24}$$

with d_m being the minimal resolvable feature, λ the wavelength of the employed electromagnetic radiation and NA is the numerical aperture, a dimensionless number to characterize the maximum angle over which the optical system can emit or accept the radiation. The wavelength of an electron depends on its kinetic energy (E_{kin}):

$$\lambda = \frac{h}{\sqrt{2m_0E_{kin}\left(1+\frac{E_{kin}}{2m_0c^2}\right)}}, \tag{25}$$

with h being Planck's constant, m_0 the rest mass of the electron and c the speed of light [230].

This work utilized two devices working in transmission mode, a high-resolution scanning electron microscope (HRSEM) and a scanning transmission electron microscope (STEM). Both machines work according to similar principles. **Figure 14** shows a generic set up of a STEM in imaging and diffraction mode. Electrons are emitted from an electrically heated cathode, pass a magnetic condenser lens, aperture and penetrate through the sample bearing the sample information. Depending on whether the device is run in imaging and diffraction mode, the position of a further aperture is adjusted between two magnetic lenses. Finally, a magnetic projector lens transmits the image onto a detector for visualization. The whole setup is employed in a vacuum, so that a sample, once it is positioned onto a specialized copper grid is inserted through an airlock into the device [230].

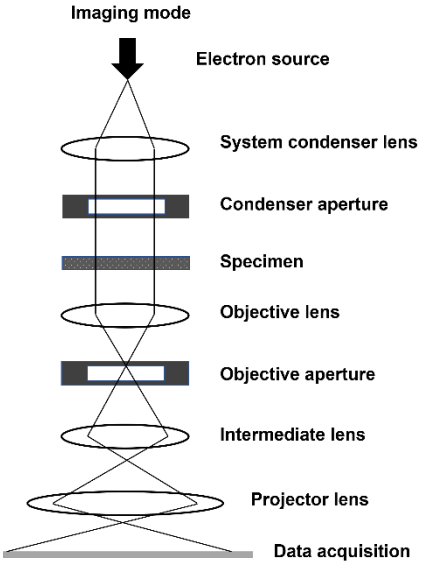

***Figure 14**: Schematic depiction of a transmission electron microscopy setup in imaging mode* [230].

3.4.2. Filler Size

The determination of the particle size indirectly bears information about the stability and degree of agglomeration. This work utilized two techniques, the sedimentation test and the static light scattering. The former method allows only qualitative assessment of the size of particle systems compared relative to each other. Thereby, particles sediment in solvents being exposed to gravitational, drag and buoyancy forces

(**Figure 15a**), which lead to a net sedimentation velocity described by the Stokes equation [231]:

$$v_s = \frac{g(\rho_p - \rho_s)d^2}{18\eta}, \tag{26}$$

with g being the acceleration of gravity, ρ_p the particle density, ρ_s the solvent density, d the particle diameter and η the dynamic viscosity.

The latter method allows a quantitative assessment of the particle size by exposing the floating particle to laser light with wavelengths of 475 nm, 613 nm and 900 nm. In addition to that, the light is horizontally as well as vertically polarized [232]. Using the Mie-theory [233] the device establishes a particle size distribution using the simplified assumption that all particles are spherical. It utilizes the phenomenon that larger particles scatter light at a lower angle than smaller particles, which deliberately placed detectors can receive and attribute to respective particle sizes (**Figure 15b**). Moreover, the light polarization allows further differentiation of particle diameters below 20 nm by comparing signal differences between the two regimes. The measurement works with liquid particle suspensions, which are pipetted into a 2 - propanol filled chamber where the laser light passes through.

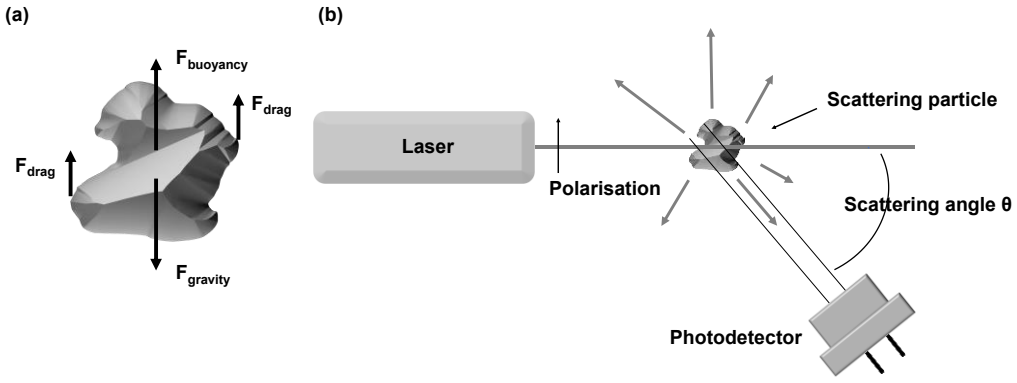

***Figure 15**: (**a**) Sedimenting particle experiences gravity, buoyancy and drag forces in solvent. (**b**) Schematic depiction of the static light scattering principle. Polarized light hits a particle and exhibits absorption, diffraction and refraction* [231,234].

3.4.3. Specific Surface Area

Knowledge about the surface area per gram of powder mass is important for the development of ink formulations. As subchapter 3.3.1 points out, surfaces strongly interact with their environment. They affect rheology and define the number of coating molecules necessary for stabilization. The Brunauer-Emmett-Teller (BET) method [235] is an established technique for the specific surface area (SSA) assessment. It uses the adsorption desorption isotherm of nitrogen, which condensates onto the particle surface at a reduced relative pressure of 0.05 p/p_0 to 0.3 p/p_0 (**Figure 16**).

In this regime, the amount of the attached nitrogen monolayer allows the calculation of the SSA:

$$SSA = n_{mono} \cdot N_A \cdot a_n \,, \tag{27}$$

With n_{mono} being the nitrogen molar quantity per particle mass, N_A is the Avogadro constant and a_n is the area one nitrogen molecule occupies.

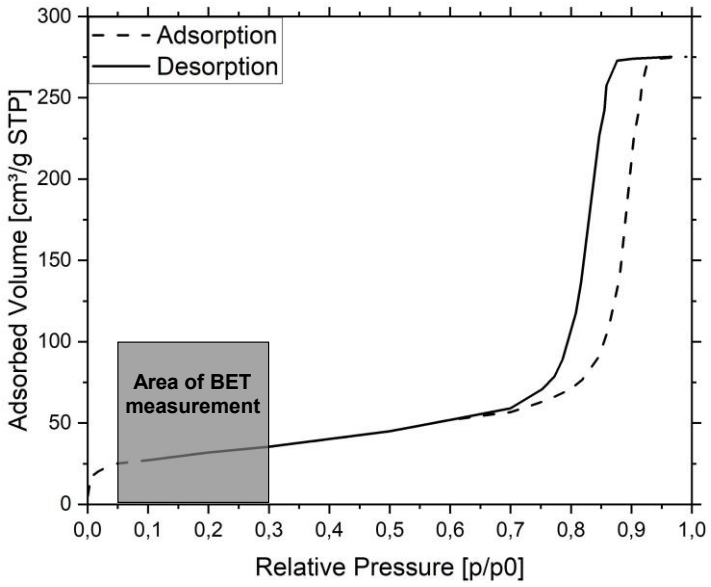

***Figure 16**: Isotherm with highlighted area for BET measurement* [235].

3.4.4. Attrition

In this work, two procedures of deagglomeration and stabilization of ceramic particles were employed for the ink formulation. A hand-held device from IKA enabled quick ink preparation. However, most approaches relied on planetary ball milling (PBM) due

to its higher attrition potential. The device enabled the size reduction of agglomerated powders in solvent and allowed their mechano-chemical stabilization with the silane MPS in some instances. The device contains two grinding jars with 2 mm grinding balls positioned on a spinning platform (**Figure 17a**). In addition to that, the jars themselves spin around their own axis. The tossing of the grinding balls inside the vessels during grinding creates mechanical and thermal energy, which acts upon the sample. The frequency of the grinding process and the content of the grinding jars influences the grinding ball motion. The mode with the highest energy infusion is the catarcting, a movement when after every half revolution the balls change their position onto the opposite beaker site (**Figure 17b**) [236]. The calculation of the energy (E_I) released during each impact is:

$$E_I = \frac{v^2 m_1 m_2}{2(\mathrm{m}_1 + m_2)}, \tag{28}$$

with v being the impact velocity and m_1 and m_2 are the masses of two colliding grinding balls. In addition to that, the energy and the grinding result depend on further parameters, such as the physical and chemical properties of the particles, solvent and surfactant. Furthermore, the ratios of grinding balls, particles, solvent and surfactant to each are relevant, as well [237,238].

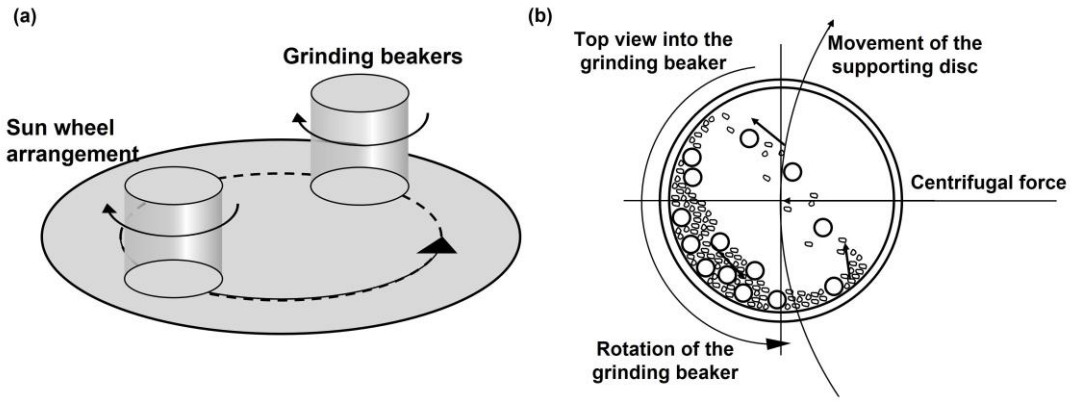

***Figure 17**: (**a**) Schematic depiction of the planetary ball milling process. (**b**) Schematic representation of grinding ball movement in the grinding beaker. The Figure was redrawn from* [239,240].

3.4.5. Rheology

Ink formulations developed in this work had to meet the stringent requirements of inkjet printing. Their rheology had to be measured and if necessary, adjustments to their composition were made. Subchapter 3.3.2 deals with the theory of rheology, which is the study of the deformation and flow of matter. Upon application of stress, matter develops a velocity gradient. equation 29, shows the relation of these two terms:

$$\eta = \frac{\tau}{\dot{\gamma}}, \tag{29}$$

The proportionality factor is denoted as the dynamic viscosity (η).

In this work, the cone-plate rheometer was employed to track η (**Figure 18**) [241]. The device uses roughly 2 ml of sample volume between a stationary bottom plate and a rotating top cone. For the measurement a cone was used with a diameter of 60 mm and an angle of inclination (α) of 2°. The knowledge of the angular velocity (ω) of the rotating plate allows the determination of the shear rate:

$$\dot{\gamma} = \frac{\omega}{\sin \alpha}. \tag{30}$$

The calculation of the shear-stress is as follows:

$$\tau = \frac{3M_r}{2\pi r^3}, \tag{31}$$

with M_r being the torque and r the radius of the cone.

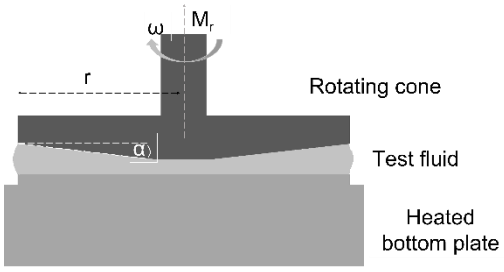

***Figure 18**: Schematic depiction of the cone-and-plate rheometer* [241].

3.4.6. Wetting Behavior

Measuring the contact angle using the Krüss device enabled the assessment of the substrate surface energy. It served the characterization of the PDMS surface and the surfaces of cured ink intending to achieve homogeneous wetting during ink deposition. Subchapter 3.3.1 introduced the surface energy as a combination of the van der Waals and polar forces, which contribute to the agglomeration process in particle suspensions. However, the surface energy of the substrate, together with the surface tension of the ink, also define the wetting behavior. Good wetting can be observed when the surface energy of the substrate is higher than the surface tension of the liquid. **Figure 19a** shows schematically the principle of the surface tension assessment [184,242]. The liquid ink protrudes from a needle tip forming a pendant drop. A camera records the contours of the drop and the device software calculates the surface tension (γ), provided the drop is in a hydromechanical equilibrium. The software uses the Laplace pressure, which describes the pressure difference between the drop interior and exterior:

$$\Delta p = \gamma \cdot \left(\frac{1}{r_1} + \frac{1}{r_2}\right), \tag{32}$$

with r_1 and r_2 being the principal radii of the droplet which are positioned over each other. The drop is rotationally symmetrical in the z-direction. This allows the geometrical description of the curvature and calculation of γ utilizing the following equation:

$$\frac{d\phi}{ds} = 2k_{apex} - \frac{z \cdot \Delta\rho \cdot g}{\gamma} - \frac{sin\,\phi}{x}, \tag{33}$$

where ϕ is the angle between the tangent at point P and the x-axis, which is the tangent of the cross section between the z-axis and drop apex, being the tip/lowest point of the hanging drop (**Figure 19a**). The parameter s is the arc length along the drop profile, k_{apex} is the principal curvature at the apex, z is the coordination of P on the z-axis, $\Delta\rho$ is the density difference between the droplet and air, g is the earth acceleration and x is the coordination of P on the x-axis.

Figure 19b shows schematically the assessment of the surface energy using contact angle measurements of a sessile drop on a substrate. The theoretical background differs from the calculations introduced in 3.3.1, in that it uses two instead of three liquids. The approach orients itself on the method of Fowkes, which determines successively the disperse and the polar fraction of the surface energy using diiodomethane and water, respectively. Thereby, the disperse and polar parts of the liquid surface tensions are known. The calculation starts with the Fowkes equation:

$$\gamma_{sl} = \gamma_s + \gamma_l - 2\sqrt{\gamma_s^D \cdot \gamma_l^D} - 2\sqrt{\gamma_s^P \cdot \gamma_l^P}, \tag{34}$$

With γ_{sl} being the surface tension between solid and liquid, γ_s is the surface energy of the solid, γ_l surface tension for the liquid, and γ_s^D, γ_l^D, γ_s^P and γ_l^P the respective values for the dispersive and polar components.

The utilization of the Young and Dupré equation allows the calculation of the total surface energy γ_s, which is described in A.3 using equations a15 and a16.

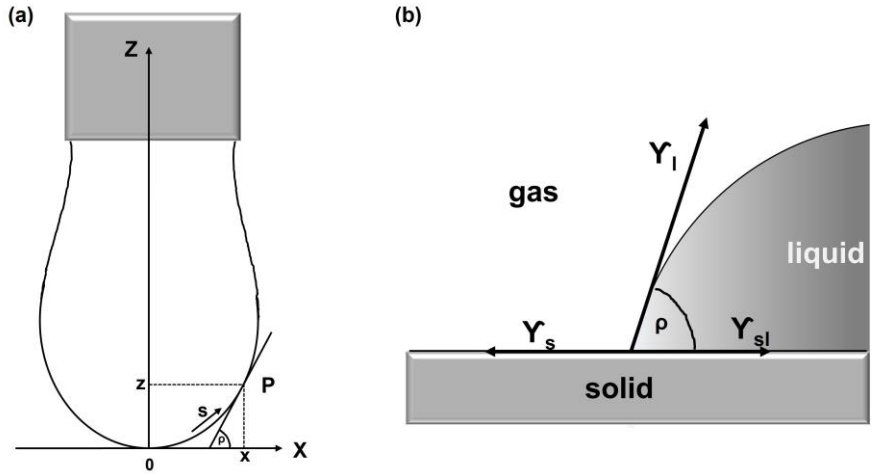

***Figure 19**: (**a**) Schematic depiction of the pendant drop setup for the surface tension measurement with parameters for the geometrical description of the curvature and calculation of the surface energy. (**b**) Schematic depiction of a contact angle measurement using a sessile drop on a substrate* [184,242].

3.4.7. Conversion Efficiency

Measuring the polymerization degree relative to the original formulation allows the adjustment of the process relevant curing modalities. This work utilizes the Fourier transform infrared spectroscopy (FTIR) [243]. It allows the quantitative determination of converted vinyl (C=C) bonds in UV and thermally cured ink formulations. The device collects spectral data over a wide range of wavelengths simultaneously at a high-resolution using a Fourier-transformed interferogram. One of the main components of the device is the Michelson-interferometer (**Figure 20a**), an arrangement of mirrors, which divide the light ray coming from a source into two and direct one onto a static mirror and the other onto a mobile mirror. After that, the two beams recombine again. Depending on their frequency and the distance of the mobile mirror the characteristic interferences emerge (**Figure 20b**). During the measurement, a constant nitrogen flow prevents oxygen from accumulating in the sample chamber, which would falsify the resulting spectrum. The data resembles the absorbance as a function of the wavenumber in cm^{-1}. For the work, the absorbance at 1638 cm^{-1} (Abs^{1638}) and 1734 cm^{-1} (Abs^{1734}) were relevant, which correspond to the peaks of the C=C bond and the C=O bond, respectively. By dividing the value for the vinyl bond by the value of the carbonyl bond a normalization takes place. The calculation of the sample conversion utilizes the absorbance values in the following manner:

$$Conversion\ [\%] = \left(1 - \frac{Abs_s^{1638}/Abs_s^{1734}}{Abs_r^{1638}/Abs_r^{1734}}\right) \cdot 100\ , \tag{35}$$

with the indices s and r being the designation for sample and for reference, respectively. The reference is the uncured sample material with the maximum amount of C=C bonds [244].

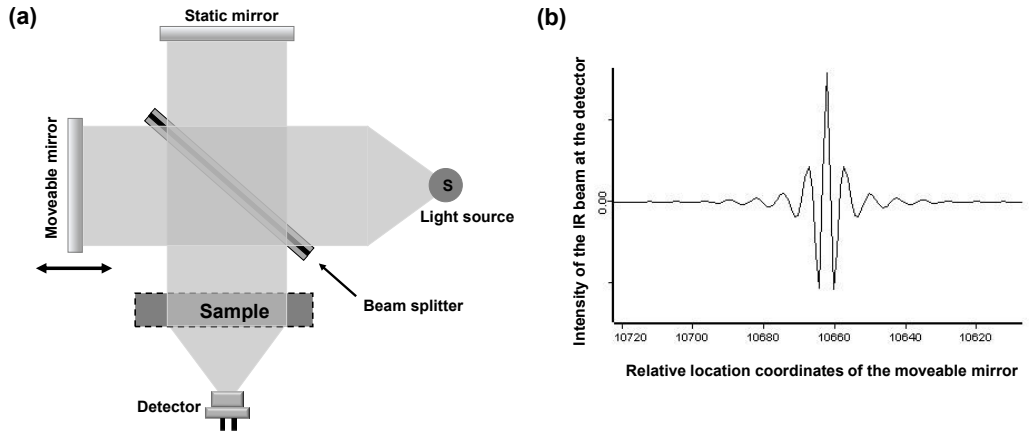

***Figure 20**: (**a**) Schematic depiction of the FTIR based Michelson Interferometer. (**b**) Interferogram of a FTIR measurement* [243], [245]. *Butenbremer 16:54, 14th September 2006 (UTC) (https://commons.wikimedia.org/wiki/File:Ftir-interferogram.png), „Ftir-interferogram“, Color from Dennis Graf , https://creativecommons.org/licenses/by-sa/3.0/legalcode.*

3.4.8. Curing Procedure

The curing of inkjet-printed inks involved irradiation with UV light and often a thermal post-treatment. The thermal curing allows a homogeneous polymerization throughout the samples regardless of the ceramic content. Contrary to that, the presence of ceramic may serve as an obstacle to UV curing. The scattering of light by particles in addition to light adsorption by the matrix components leads to a depth dependent energy absorption governed by extinction. Starting out with the Lamber-Beers law (equation 36), this behavior can be described as follows [34]:

$$\mathrm{I}_{abs,z} = \mathrm{I}_0 e^{-\varepsilon_{abs} c_s z}\,, \tag{36}$$

with I_0 being the initial light intensity, ε_{abs} the absorption coefficient, c_s the concentration of the scattering/absorbing species, e.g. ceramic fillers, and z the thickness of the layer to be cured. The maximum energy input from the light source is:

$$\mathrm{E}_{max} = \frac{\mathrm{P}_{LS} t_{LS}}{d_{LS}}\,, \tag{37}$$

whereby P_{LS} is the power of the light source, t_{LS} is the duration of illumination and d_{LS} is the distance of the sample surface from the light source.

This allows to ascertain what the local energy absorption at the location z within the printed layer is:

$$\mathrm{E}_z = \mathrm{E}_{max} e^{-\frac{z}{D_p}}, \tag{38}$$

with D_p being the optical penetration depth, an intensity decay down to 1/e of the initial intensity or $1/e^2$ of the initial energy. In turn, this leads to the formulation of the equation for the accessible curing depth:

$$\mathrm{z}(\mathrm{E}_{th}) = \mathrm{D}_p \ln\left(\frac{E_{max}}{E_{th}}\right) = \mathrm{D}_p \ln\left(\frac{\mathrm{P}_{LS} t_{LS}}{d_{LS} E_{th}}\right), \tag{39}$$

with E_{th} being the threshold energy necessary to initiate the polymerization reaction.

3.4.9. Thermal Properties

The thermogravimetric analysis (TGA) determines the mass change of a sample relative to its original mass as a function of the temperature and the temperature change with time. **Figure 21** shows the composition of the device with sample and reference holders positioned on high precision balances [246]. An atmospheric controlled furnace surrounds the fixtures. During measurement, a gas inlet allows a constant stream of air to pass the sample with a flow rate of 100 ml/min. The analysis took place on 20 mg to 200 mg of powdered, liquid or bulk samples with the aim to analyze the inorganic content in the samples. The result allowed to recalculate the ratio of inorganic to organic components.

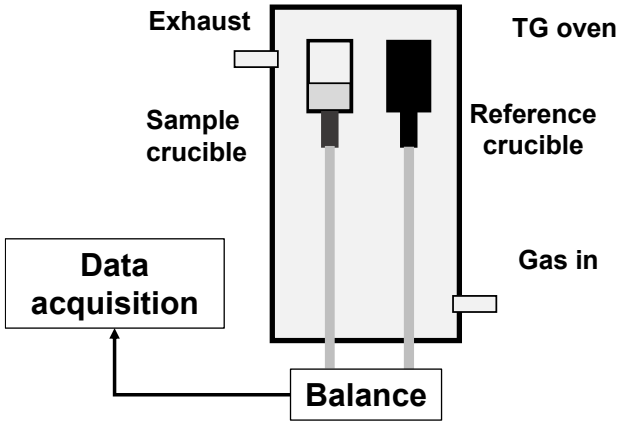

***Figure 21**: A schematic of thermogravimetric analysis apparatus.*

The assessment of the thermal conductivity (λ_c) of the 3D inkjet printed composites involved the measurement of the sample density (ρ), specific thermal capacity (c_i) and thermal diffusivity (a_i) [174]. The calculation of the term is as follows:

$$\lambda_c = \rho \cdot c_i \cdot a_i \,. \tag{40}$$

The Archimedes method serves as a simple method for density determination. It involves the acquisition of sample mass (m_{air}) in air and 2-propanol (m_{2p}) using precision scales [247]. The measured results converge as follows:

$$\rho = \frac{m_{air}}{\left(m_{air} - m_{2p}\right)} \cdot \rho_{2p} \,, \tag{41}$$

with ρ_{2p} being the density of 2-propanol at the measurement temperature.

The differential scanning calorimetry (DSC) enabled the acquisition of the specific heat capacity (c_i). The measurement records the temperature change (dT) of a pre-weighted sample mass (m) as a consequence of an applied heat flux (dQ) without the initiation of a phase change and at a constant pressure [246]. The calculation of the term is as follows:

$$c_i = \frac{dQ}{dT \cdot m}, \tag{42}$$

During measurement, a sample and a reference of known c_i reside in tin pans positioned in a pressure-controlled chamber. During the application of the heat flow, sensors in the holders track the change in temperature as a voltage signal in µV, which is recalculated into a heat flow-rate signal in mW afterwards.
Three measurements of the heat-flowrate ($P = dQ/dt$) are necessary to assess c_p of the sough for sample. The reference remains empty throughout the procedure. First and second recording is a measurement with an empty pan and one containing a calibration sapphire crystal with known c_p, respectively. The third run takes place with the sample. Using the following equation results in the specific heat capacity:

$$c_{i(s)} = c_{i(c)} \frac{m_c(P_s - P_e)}{m_s(P_c - P_e)}, \tag{43}$$

with $c_{i(s)}$, m_s and P_s being the specific heat capacity, mass and heat-flowrate of the sample, respectively. $c_{i(c)}$, m_c and P_c are the respective values for the calibration sapphire and P_e is the heat-flux-rate of the empty tin pan.

The thermal diffusivity measurement uses the laser flash analysis (LFA) method (**Figure 22**) [248]. The irradiation of a plane-parallel cylindrical sample, which has a diameter of 10 mm and a thickness of 1 mm, with short laser pulses heats up its surface. An infrared sensor detects the temperature increases on the opposite side. The higher the temperature diffusivity, denoted as a, the faster the temperature increases. One-dimensional, adiabatic conditions allow the following calculation:

$$a_i = 0.1388 \frac{{d_{st}}^2}{t_{0.5}}, \tag{44}$$

with d_{st} being the samples thickness and $t_{0.5}$ is the time at half maximum. The device uses a 1064 nm laser (max. 30 kW, 20 J), which emits trapezoid pulses of 0.3 ms to 1.2 ms detecting values of 0.001 cm²/s to 3 cm²/s. The measurement temperature reaches up to 1450 °C with a dynamically changeable atmosphere ranging from inert to vacuum. The accuracy of the device reaches 3 %.

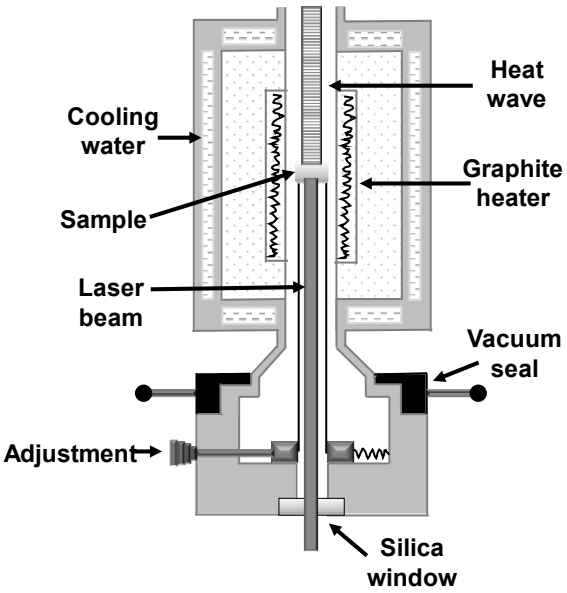

***Figure 22**: Schematic illustration of the LFA apparatus, redrawn from* [249].

3.4.10. Mechanical Properties

The tensile test should investigate the printed sample Young's modulus, ultimate tensile strength, elongation at break and tensile toughness [250]. Using the data from the measurement the calculations of the values are as follows:

$$E = \frac{\sigma}{\varepsilon_t}, \tag{45}$$

with E being the Young's modulus, σ is the applied stress and ε_t the elongation of the sample. The value for E is collected at an elongation between 0.01 % and 0.05 %. The stress is defined as:

$$\sigma = \frac{F}{A_g}, \tag{46}$$

being derived from dividing the force F applied onto a sample by the cross-section A_g of the sample gauge (**Figure 23**). The ultimate tensile strength is the stress when the sample breaks at the elongation at break.

The elongation is defined as:

$$\varepsilon = \frac{dl_t}{l_{0t}}, \tag{47}$$

with dl_t being the sample gauge length change and l_{0t} being the original gauge length. During the measurement the sample, which is positioned between two clamps, is subjected to stress. The software-controlled machine applies the stress to achieve a constant sample elongation of 1 mm/s. The resulting forces, which arise when the sample resists deformation are recorded using an extensometer with a maximum force threshold of 10 kN.

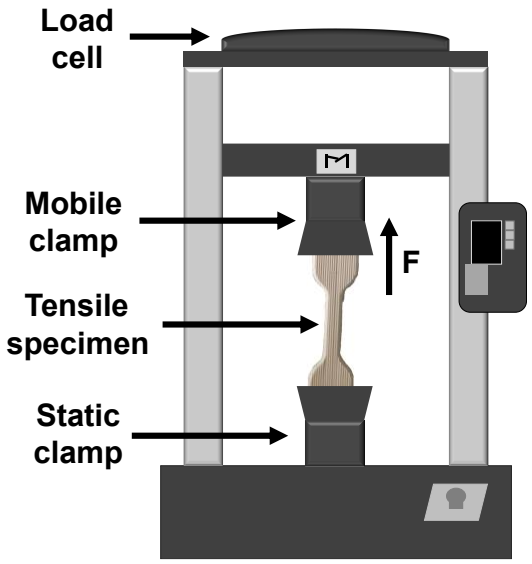

***Figure 23**: Schematic depiction of tensile testing of a 3D inkjet-printed sample. Two clamps are holding the sample during measurement. One is fixed and the other moves up with a constant velocity applying a force onto the sample.*

4. Solvent Free Inks

In this chapter solvent free ceramic inks for 3D inkjet printing were investigated for their use as composite materials with enhanced mechanical and thermal properties. This chapter is based, in part, on published results in [251]. In the subchapter "Experimental Section" the preparation of inks is shown, their characterization is illustrated and the further processing of these inks towards composites is described. The sought for properties of the composites are analyzed as well. In the subchapter "Result and Discussion" the findings of the experiments are presented, interpreted and conclusions for further actions are drawn.

4.1. Experimental Section

In this subchapter procedures and parameters are described which were used to investigate solvent free ceramic inks for 3D inkjet printing. The used materials are introduced, the sample preparation is shown and the characterization, as well as the processing, is illuminated. Thereby, the description is further divided into five subchapters titled "Nanocomposites", "Ceramic Stabilization", "Monomer Selection", "Ceramic Attrition" and "Inkjet Ink". In "Nanocomposites" nanoparticles were used to test their ability to improve the structural properties of 3D inkjet printed composites. Furthermore, submicron particles were investigated for their property to increase the thermal conductance of 3D inkjet printed composites by strongly increasing the ceramic content. Therefore, in "Ceramic Stabilization" ways were tested to lower the viscosity of highly filled ceramic suspensions. Their stability was further improved in the subchapter "Monomer selection". Then after the most fitting components were chosen the ink preparation was further enhanced in "Ceramic Attrition". At last, in "Ink characterization" the aptitude of the ink for the application as a thermally conductive composite was investigated. Thereby inkjet tests have been performed, the polymerization properties were assessed, the thermal conductance of the ink was measured and a component for the purpose of demonstration was printed.

4.1.1. Materials

The **Table 2** and **Table 3** summarizes the materials which were utilized in this chapter. The alumina particles introduced in **Table 2** differ in density, primary particle diameter and SSA. Depending on their size a varying amount of chemisorbed and physisorbed water is attached onto their surface. While physisorbed water may detach from the surface by heating, in vacuum or displacement, chemisorbed water is less likely to do so and therefore influences the density of the particle. The density has been assessed using TGA (STA 409C, Netzsch Group, Selb, Germany). Thereby the fillers were heated to 1200°C at a heating rate of 10 K/min, held at this temperature for 30 min and cooled down to 25°C at a rate of 10 K/min. The received heating profile was used for the following calculations:

$$Al_2O_3\ [g/ml] = \frac{Al_2O_{3\,dehyd}\ [g] + H_2O_{chem}\ [g]}{Al_2O_{3\,dehyd}\ [ml] + H_2O_{chem}\ [ml]} \tag{48}$$

The density of the fillers *Al₂O₃ [g/ml]* is composed of the mass of the dehydrated fillers *Al₂O₃ dehyd* $[g]$ and chemically bound surface water *H₂O_chem* $[g]$ divided by the volume of the two terms.

$$Al_2O_{3\,dehyd}\ [g] = \frac{Al_2O_{3\ dehyd}\ [wt\%] \cdot Al_2O_{3\ hyd}\ [g]}{Al_2O_{3\ hyd}\ [wt\%]} \tag{49}$$

Al₂O₃ dehyd $[g]$ can be expressed as the product of *Al₂O₃ dehyd* $[wt\%]$ and *Al₂O₃ hyd* $[g]$. The former is the weight percentage of the dehydrated fillers which was measured in the TGA. The latter is the initial particle weight for the thermogravimetric analysis. The product is then divided by *Al₂O₃ hyd* $[wt\%]$ which accounts to 100 wt%.

$$H_2O_{chem}[g] = \frac{(Al_2O_{3\ hyd}\ [wt\%] - H_2O_{phys}\ [wt\%] - Al_2O_{3\ dehyd}\ [wt\%]) \cdot Al_2O_{3\ hyd}\ [g]}{Al_2O_{3\ hyd}\ [wt\%]} \tag{50}$$

H₂O chem $[g]$ can be similarly described by the product between the weight percentage of the chemisorbed water and the initial particle mass divided by *Al₂O₃ hyd* $[wt\%]$, which accounts to 100 wt%. Thereby, the weight percentage of the chemisorbed water

is the difference between the weight percentages of the initial particles, the physiosorbed water and the completely dehydrated alumina.

$$Al_2O_3\left[\frac{g}{ml}\right] = \frac{Al_2O_{3_{dehyd}}\,[g] + H_2O_{chem}\,[g]}{1/(3.95\,[g/ml]) \cdot Al_2O_{3_{dehyd}}\,[g] + 1/(1\,[g/ml]) \cdot H_2O_{chem}\,[g]} \quad (51)$$

Since the dehydrated alumina is regarded as bulk α-Al_2O_3 the density of which is 3.95 (g/ml) and the density of water is 1 (g/ml), the respective terms in the divisor can be expressed in [ml]. Consequently, the particle density can be calculated by inserting equation 49 and 50 into 51.

***Table 2**: Al_2O_3 fillers utilized during the experiments conducted in this chapter. The density was calculated according to equation 51, the SSA was measured using the BET method and the diameter was calculated with equation 52. All materials have been used as received.*

Product name	Density [g/cm³]	SSA [m²/g].	Diameter [nm].	Supplier
TEC14[a]	3.68	118.6	14	Tecnan
TEC50[a]	3.58	30.1	56	Tecnan
TEC170[a]	3.91	8.7	176	Tecnan
CT3000SG (A240)	3.90	6.4	239	Almatis

[a] The product does not have a product name since it was an experimental batch produced in the scope of the EU project DIMAP. The shown name is an internal designation.

The measurement of the average particle diameter and SSA [m²/g] has been done with a Gemini VII 2390 (Micromeritics, Norcross, Georgia, USA). The analysis is based on BET method introduced in subchapter 3.4.3. The particles are degassed in a vacuum and are exposed to nitrogen afterwards. Using the adsorption/desorption isotherm, calculations of the SSA could be made. The calculation of the average particle diameter Al_2O_3 [nm] can be done according to:

$$Al_2O_3\,[nm] = \frac{6000}{SSA[m^2/g] \cdot Al_2O_3[g/ml]}\,. \quad (52)$$

All materials utilized in this chapter were used as received without further purification.

***Table 3**: Organic materials utilized during the experiments done in this chapter. All materials have been used as received.*

Chemical name (product name)	CAS. No.	Supplier
Ethanol	64-17-5	Carl Roth
2-propanol	67-63-0	Carl Roth
2-[2-(2-methoxyethoxyethoxy)ethoxy] acetic acid	16024-58-1	Merck
Isobornyl acrylate	5888-33-5	Merck
Tripropylene glycol diacrylate	42978-66-5	Arkema
Trimethylolpropane (EO) 3-triacrylate	28961-43-5	KPX
Di(trimethylolpropane) tetraacrylate	94108-97-1	Merck
(Genomer 3364)	-	Rahn
Diphenyl(2,4,6-trimethylbenzoyl)phosphine oxide	75980-60-8	TCI
Dilauroyl peroxide	105-74-8	Merck
Elastosil RT 602 A/B	-	Wacker
Acryloyl morpholine	5117-12-4	Rahn
Stearic acid	57-11-4	Carl Roth
(Disperbyk-168)	-	Rahn
(Disperbyk-2152)	-	Rahn
(Disperbyk-2205)	-	Rahn
(Disperbyk-22124)	-	Rahn
(Disperbyk-22144)	-	Rahn
(Disperbyk-22146)	-	Rahn
(Disperbyk-22552)	-	Rahn
Cyclic trimethylol-propane formal acrylate	94108-97-1	Arkema

4.1.2. Structural Composites

When produced in a bulk reaction, UV cured polyacrylates have shown heterogeneous chainmesh distributions, which causes mechanical instability such as brittleness. Under the right circumstances, improvement can be achieved by adding alumina nanoparticles and submicron particles, which evidently increase Young's modulus and toughness in thermosets. This subchapter describes the sample preparation and characterization of 3D inkjet-printed composites to investigate their mechanical properties.

4.1.2.1. Matrix Selection

For the described composite, an acrylate matrix has been formulated influenced by recipe examples in Magdassi et al [35]. It consists of isobornyl acrylate (IBOA), a monoacrylate with a high T_g after polymerization, as well as tripropylene glycol diacrylate (TPGDA) and trimethylolpropane (EO) 3-triacrylate (TMPEO3TA), which both polymerize into flexible networks. Thereby, the triacrylate shows a better curing

rate at a higher viscosity. Furthermore, the highly viscose di(trimethylolpropane) tetraacrylate was added (DTMPTA), which has a high curing velocity. Also, to increase the toughness the highly reactive difunctional oligomer Genomer 3364 was employed, which possesses a low viscosity relative to other oligomers from the Genomer product family. For radical polymerization, the photo initiator diphenyl(2,4,6-trimethylbenzoyl)phosphine oxide (TPO) was chosen. The chemical structures of the materials are shown in **Figure 24**.

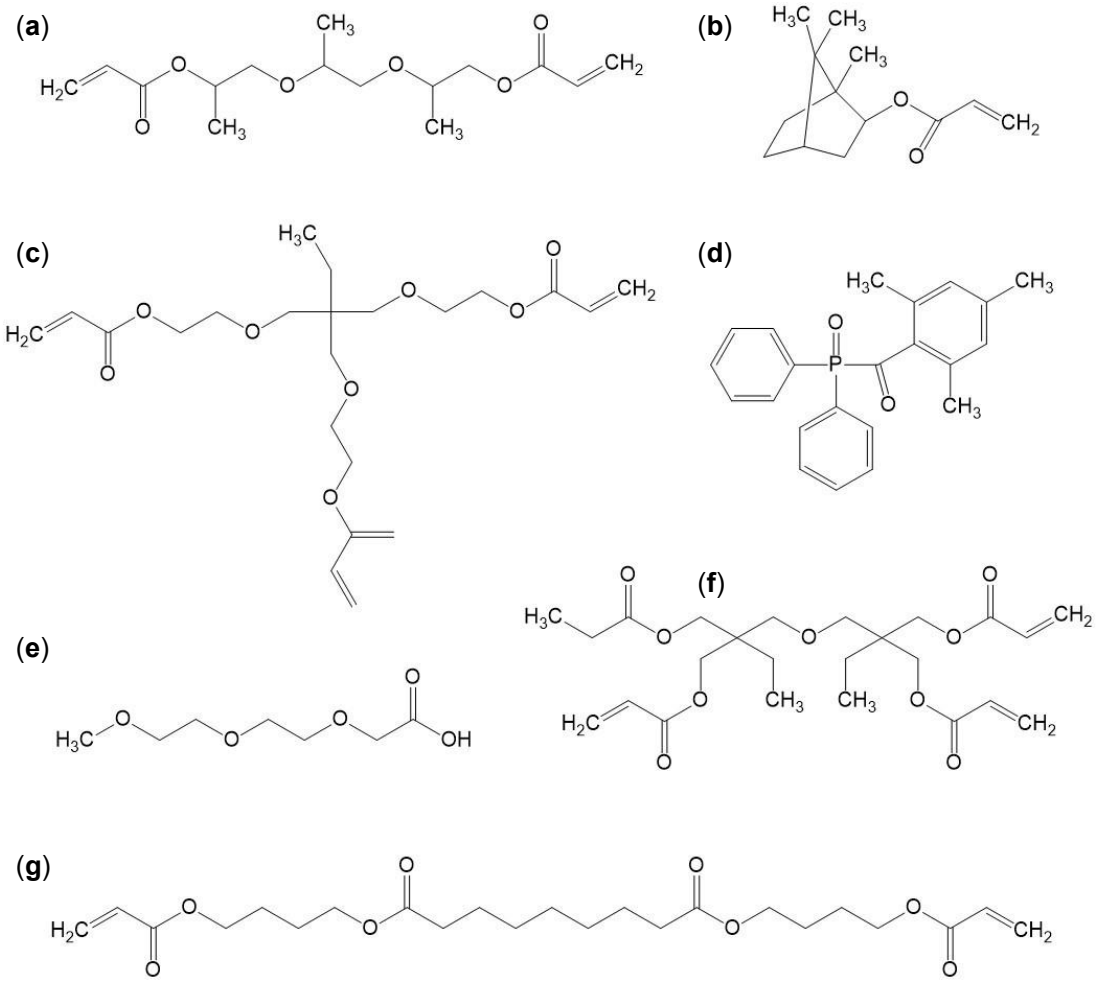

***Figure 24**: Chemical structures of the organic ink components (a) tripropylene glycol diacrylate (TPGDA), (b) isobornyl acrylate (IBOA), (c) trimethylolpropane-(EO)3 triacrylate (TMPEO3TA), (d) diphenyl(2,4,6-trimethyl-benzoyl)phosphine oxide (TPO), (e) 2-(2-methoxyethoxy)ethoxy acetic acid (TODA) (f) di(trimethylolpropane)-tetraacrylate (DTMPTA) and (g) polyester acrylate representative for Genomer 3364. The actual structure of Genomer 3364 is confidential and property of the Rahn AG.*

4.1.2.2. Ceramic Conditioning

As inorganic composite components, three kinds of nanofillers have been utilized TEC14, TEC50 and TEC170 with a primary particle size of 14 nm, 56 nm and 176 nm, respectively. These nanoparticles were produced via flame-spray pyrolysis which yields agglomerated materials. However, poorly distributed particles in inkjet inks compromise the jetting process. Furthermore, the presence of agglomerated particles in composites can decrease their mechanical properties instead of improving them. Therefore, to assess the degree of agglomeration, the morphologies were analyzed via high-resolution scanning electron microscopy (Nova NanoSEM with EDAX EDX, FEI, Hillsboro, OR, USA) in STEM mode. For the measurement, a diluted suspension of each of the as received particles was prepared in ethanol with a concentration of 100 µg/ml. Each suspension was then placed on one carbon-coated TEM grid, which dried overnight.

After the imaging, the agglomerated particles were deagglomerated via planetary ball milling (PBM) (PM400, Retsch GmbH, Haan, Germany) and coated with 2- [2- (2- methoxyethoxy)ethoxy]acetic acid (TODA), shown in **Figure 24e,** for a better dispersion in the acrylate matrix. As a preparation for this procedure, the fillers were dried to get rid of physisorbed water from the particle surface to ease the adsorption of TODA. TEC14 and TEC170 were heated at 200 °C for 24 h in an oven (LHT 6/60, Carbolite Gero GmbH & Co. KG, Neuhausen, Germany). For TEC50, however, the drying step was altered according to the heating profile shown in **Figure 25**, due to a different crystallography of the surface, which has more incorporated water than the other fillers. The particles were heated to 260°C at a rate of 10 K/min (1), held at the temperature for 24 h (2), subsequently heated to 400 °C at a heating rate of 5 K/min (3) and then to 500 °C at 10 K/min (4). Finally, the powder was cooled down to room temperature at a rate of 10 K/min (5).

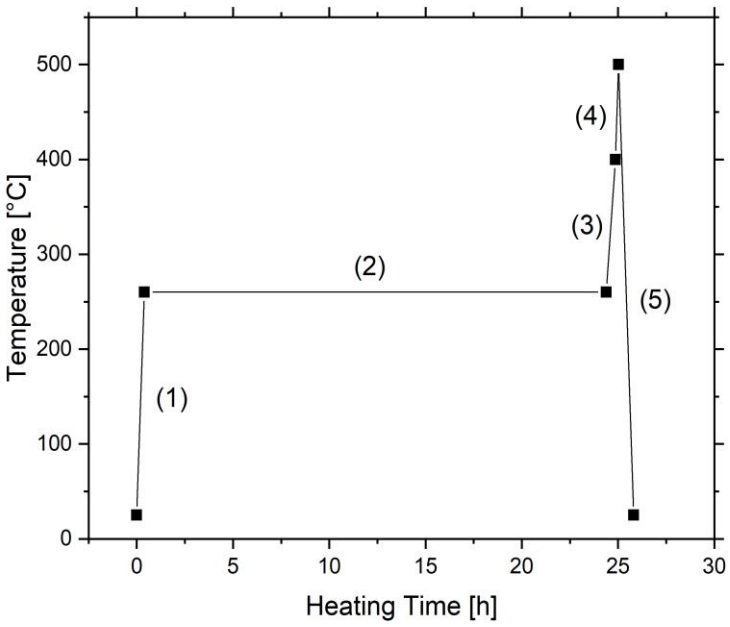

***Figure 25**: Heat treatment of TEC50 nanoparticles. (1) The temperature program was increased to 260°C with a heating rate of 10 K/min and (2) was held there for 24 h. (3) After that the temperature was raised to 400°C with a heating rate of 5 K/min and upon reaching it, (5) it was further increased to 500°C with 10 K/min.*

The grinding was conducted in 125 ml grinding beakers with yttrium stabilized ZrO_2 inner cladding and with grinding balls of the same material with a diameter of 2 mm. The ratio of grinding balls to ceramic particles is 10:1 and the grinding time was 8 h. For the attrition of the TEC14 fillers 11 g were suspended with 110 g of ZrO_2 grinding balls in 58 ml 2-propanol. The parameters for TEC50 and TEC170 are similar. 20 g of both powders were each dispersed in 60 ml 2-propanol with 200 g ZrO_2 grinding balls. During the mechanical treatment subsamples of 0.1 g were taken from the beakers after 5 min, 1 h and 8 h to measure the degree of particle attrition. The subsamples were then dispersed in 5 g of 2-propanol by shaking and analyzed by static light scattering (Beckmann Coulter LS-230, Beckmann-Coulter Inc., Brea, CA, USA). Each measurement was conducted three times. After the grinding time of 8 h was elapsed TODA was added in an amount of 2 mg/m² of the particle surface. Thereby 2.8 g were added to the TEC14 based sample, 1.4 g to the sample with TEC50 and 0.4 g to the TEC170 based sample. The particles were then further ground with the surfactant for 15 min, retrieved from the beakers by pouring the content through a sieve to separate the grinding balls. Then drying was conducted in a rotary evaporator (Laborota 4003 digital, Heidolph Instruments, Schwabach, Germany) for 1 h at 175 mbar and 50 °C. The coated particles were thermogravimetrically analyzed (STA 409C, Netzsch

Group, Selb, Germany) to investigate whether TODA desorbed from the particle surface during rotary evaporation. The measurement took place in an air atmosphere by heating to 1200 °C at a rate of 10 K/min, holding the temperature for 30 min and then cooling to room temperature at 10 K/min.

4.1.2.3. Ink Characterization

As shown in **Table 4**, the conditioned particles were subsequently resuspended at a nominal concentration of 1.0 vol%, 1.5 vol% and 2.0 vol% in the previously described matrix the components of which are shown in **Figure 24**. The process was done with a hand-held dispersing device (T10 basic Ultra-Turrax, IKA GmbH, Staufen, Germany) at 14560 rpm for 5 min with subsequent ultrasonication (Sonorex Super RK103H, Bandelin electronic GmbH and Co. KG, Berlin, Germany) with a power of 560 W for 15 min. The prepared inks were then filtered with a polytetrafluoroethylene (PTFE) filter with a pore diameter of 5 µm (Rotilabo®, Carl Roth, Karlsruhe, Germany).

***Table 4**: Sample description of liquid inks with and without particle filling. The particles are coated with TODA.*

Composition	Matrix [wt% (vol%)]	14-I/50-I [wt% (vol%)]	14-II/50-II [wt% (vol%)]	14-III/50-III [wt% (vol%)]
TEC14 or TEC50	0.0 (0.0)	3.4 (1.0)	5.0 (1.5)	6.6 (2.0)
TODA	0.0 (0.0)	0.9 (0.8)	1.3 (1.2)	1.7 (1.6)
IBOA	44.7 (46.8)	42.8 (45.9)	41.8 (45.5)	41.0 (45.1)
TPGDA	26.0 (25.8)	24.9 (25.4)	24.4 (25.1)	23.9 (24.9)
TMPEO3TA	10.9 (10.2)	10.4 (10.0)	10.2 (9.9)	10.0 (9.8)
DTMPTA	3.7 (3.5)	3.5 (3.4)	3.5 (3.4)	3.4 (3.3)
Genomer 3364	11.8 (11.1)	11.3 (10.9)	11.1 (10.8)	10.9 (10.7)
TPO	2.91 (2.68)	2.79 (2.64)	2.73 (2.61)	2.67 (2.59)

Composition	170-I [wt% (vol%)]	170-II [wt% (vol%)]	170-III [wt% (vol%)]
TEC170	3.7 (1.0)	5.5 (1.5)	7.2 (2.0)
TODA	0.9 (0.9)	1.4 (1.3)	1.8 (1.7)
IBOA	42.6 (45.9)	41.6 (45.5)	40.6 (45.0)
TPGDA	24.8 (25.3)	24.2 (25.1)	23.7 (24.9)
TMPEO3TA	10.4 (10.0)	10.1 (9.9)	9.9 (9.8)
DTMPTA	3.5 (3.4)	3.4 (3.4)	3.4 (3.3)
Genomer 3364	11.3 (10.9)	11.0 (10.8)	10.8 (10.7)
TPO	2.78 (2.63)	2.71 (2.61)	2.65 (2.59)

The filtering of the inks removes potential agglomerates, which were not broken up by the mechanical treatment of the samples. However, excessive agglomeration, which may take place after the ink preparation due to particle collisions could lead to ceramic content reduction during filtering. Thus, to assess the extent of ceramic retention in the filter, the filtered suspensions were analyzed thermogravimetrically in an air atmosphere at a temperature of up to 1200 °C and a heating rate of 10 K/min. Furthermore, to determine whether the viscosity was in the right range for inkjet printing, the dynamic viscosity of the filtered inks was measured using an automated dynamic shear rheometer (CVO 50, Malvern Instruments, Malvern, UK) with a cone-plate design. The cone had a diameter of 60 mm and an angle of inclination of 2 °. The measurement was done in two regimes, first, at a constant shear rate of 500 s^{-1} and a temperature variation between 20 °C and 60 °C, second, at a constant temperature of 60 °C and a shear rate variation between 2 s^{-1} and 500 s^{-1}. Moreover, the surface tension was evaluated to test whether the ink is in the required range of 25 (mN/m) to 35 (mN/m). The measurement was conducted with a drop shape analyzer (DSA 100, Krüss GmbH, Hamburg, Germany). To assess the inkjet capabilities of the materials the Dimatix Materials Printer (DMP-2831, Fujifilm Dimatix Inc., Santa Clara, CA, USA) was used with the DMC-11610 cartridge using a drop volume of roughly 10 pl. The firing voltage was adjusted to 30 V and the waveform was set as displayed in **Figure 26**. It is subdivided into four phases, during which the piezo-electric actor in the printhead initiates drop formation by bending. Initially, the firing voltage decreases from 40 % to 20 % at a slew rate of 0.66. Thereby, in 2.8 µs the ink is pulled from the ink reservoir into the firing chamber. During the second phase, the curve rises in 3.8 µs to 100 % at a slew rate of 1.90 and the ink is pushed out of the nozzle. In the third phase, the piezoelectric membrane rectifies partially to prevent air suction into the firing chamber so that the curve sinks only slightly from 100 % to 73 % at a slew rate of 0.60 in 3.4 µs. During the fourth phase, which lasts 0.8 µs, the curve returns from 73 % to 40 % with a slew rate of 0.80, the membrane straightens and the ink drop, which until now remained pendant, separates from the nozzle. The ink characterization involved the analysis of the drop shape, velocity, weight and volume of the samples unmodified, 14-III, 50-III and 170-III by using the drop view of the printer.

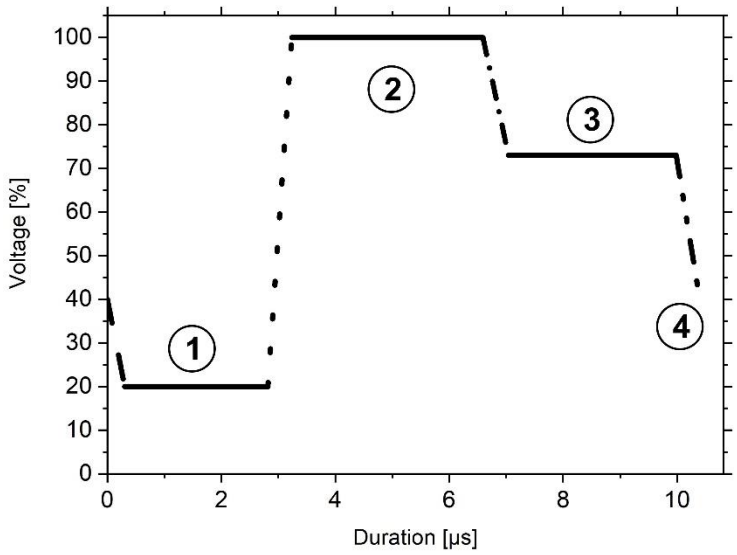

***Figure 26**: Waveform for the printing of UV curable inks with and without ceramic-filling. The waveform is divided into four segments: (1) Ink filling, (2) ink firing, (3) initial piezo recovery and (4) complete piezo recovery.*

For the assessment of the mechanical properties the formulated inks were used to produce tensile specimens according to DIN EN ISO 527-2 type A5 standard with the same parameter setup described above. Five specimens were printed at once into a polydimethylsiloxane (PDMS) mold. This was previously cast using Elastosil RT 602 A/B and DIN EN ISO 527-2 type A5 standard shaped aluminum specimens. After five jetted layers the mold was retrieved from the printer and irradiated with a UV light source (LED Spot 100 IC/HP IC, Dr. Hönle AG, Gräfelfing, Germany) at a wavelength of 405 nm and specific power of 540 mW/cm² in ambient atmosphere. The process was repeated until the mold was filled with cured material. The number of cured layers necessary to do so is enumerated in **Table A3**. The cross-section of the finished specimens was measured three times using a caliper gauge according to the standard DIN EN ISO 527-2 type A5 in the gauge section of the sample. The tensile tests were conducted using a universal testing machine (Zwick Z010, ZwickRoell GmbH & Co. KG, Ulm, Germany). Per sample five specimens were measured with a preload of 10 N and a strain rate of 1 mm/min with a 2500 N load cell. During printing inhomogeneous ceramic distribution can lead to a reduction of the ceramic content in the printed specimen. To assess the difference to the initial ink TGA measurements have been conducted up to a temperature of 900°C at a heating rate of 10 K/min. The temperature was kept for 15 min and was reduced thereafter with 10 K/min. For each sample, three subsamples were taken from the entire cross-section of the length segment.

Furthermore, for the samples 14-III, 50-III and 170-III subsamples were retrieved from the grip cross-section, the lower and the upper part of the grip. The glass transition temperature of all samples was analyzed with the differential scanning calorimetry (Netzsch Group, DSC 204 F1 Phoenix, Netzsch Group, Selb, Germany) at a temperature range between -80 °C and 200 °C with a heating rate of 10 K/min. For each sample three subsamples were measured and evaluated with the Netzsch thermal analysis software.

4.1.3. Thermally Conductive Composites

Besides the improvement of the mechanical properties, solvent-free UV curable inkjet inks enable the printing of thermally conductive composites. However, the filler size and their content must be higher than in the previous subchapters. Beyond a ceramic content of 30 vol% a marked improvement can be measured. The necessity of high filling grades requires the formulation of inks with adequate viscosity at printing temperature and suitable particle size distribution for successful ink jetting.

4.1.3.1. Surfactant Selection

In this subchapter the investigation of surfactants for the stabilization of suspensions is described. The viscosity of 9 surfactants and a reference was measured in a suspension of 20 vol% CT3000SG (A240) of the alumina particles in the hydrophilic and low viscose matrix acryloyl morpholine (ACMO). The surfactants stearic acid (SA) and TODA, shown in **Figure 27a** and **Figure 27b**, were added with a concentration relative to the ceramic surface area of 2 (mg/m²). The same was done with the polymeric surfactants Disperbyk-168, Disperbyk-2152, Disperbyk-2205, Disperbyk-22124, Disperbyk-22144, Disperbyk-22146 and Disperbyk-22552, the chemical structure of which is confidential and therefore not known. For the preparation of each suspension the particles, matrix and surfactant were weighted according to **Table 5**. The homogenization was conducted with a hand-held dispersing device (T10 basic Ultra-Turrax, IKA GmbH, Staufen, Germany) at 14560 rpm for 5 min with subsequent ultrasonication (Sonorex Super RK103H, Bandelin electronic GmbH and Co. KG, Berlin, Germany) with a power of 560 W for 15 min. The viscosity was recorded with an automated dynamic shear rheometer (CVO 50, Malvern Instruments, Malvern, UK) with a cone-plate design. The cone had a diameter of

60 mm and an angle of inclination of 2 °. The measurement took place at 32°C and a shear rate between 2 s^{-1} and 500 s^{-1}.

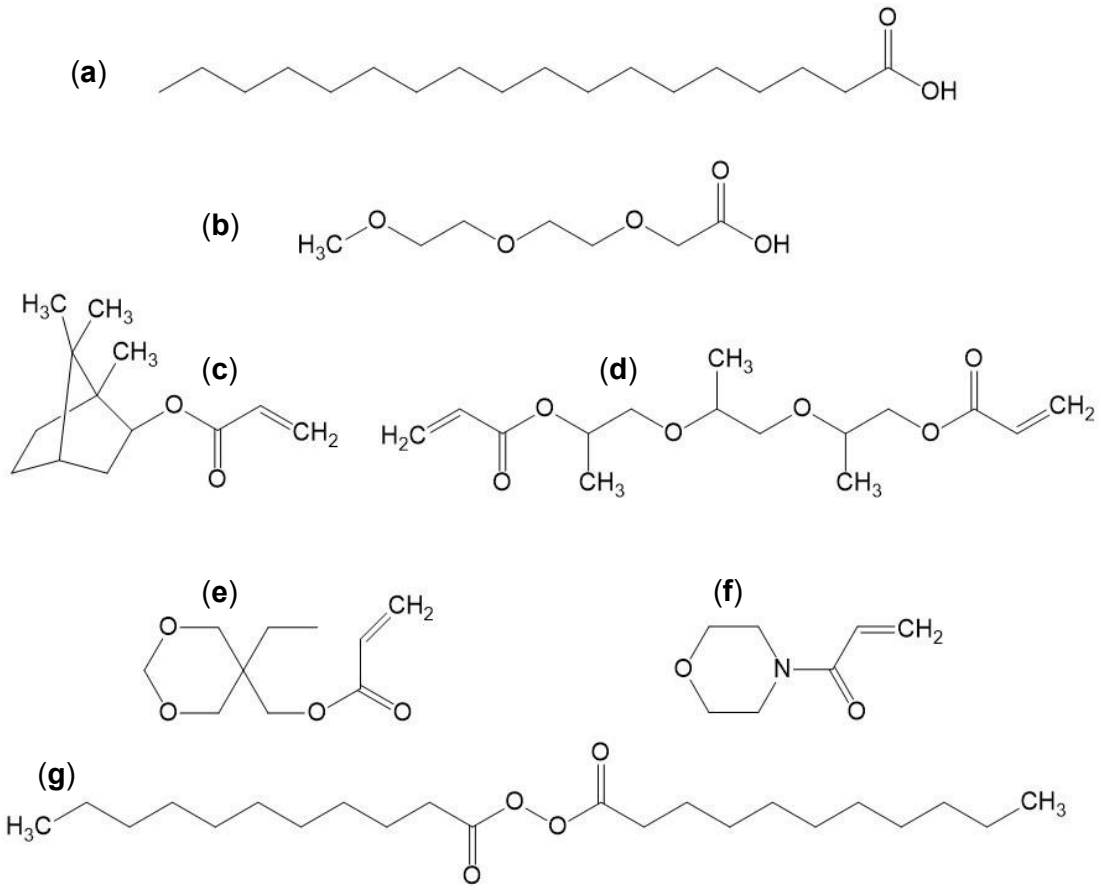

***Figure 27**: Chemical structures of the employed surfactants (**a**) stearic acid and (**b**) TODA, as well as of the monomer acrylates (**c**) IBOA, (**d**) TPGDA, (**e**) cyclic trimethylolpropane formal acrylate (CTFA), (**f**) acryloyl morpholine (ACMO) and the thermal initiator(**g**) dilauroylperoxide (LP).*

The same surfactants with 0.1 vol% A240 as fillers and ACMO as matrix were investigated for their property to influence the sedimentation tendency of the suspensions. Their concentration relative to the ceramic surface area was 1000 (mg/m^2). The preparation was done similarly to the rheological investigations with the hand-held dispersing device and subsequent ultrasonication using the same parameters. **Table 5** shows the respective weight of the components used for the samples. The suspensions were prepared in vials, which were photographed after the preparation and 72 h later to track the sedimentation progress.

***Table 5**: Suspension composition of surfactant modified A240 in the hydrophilic matrix ACMO for the investigation of the viscosity and the sedimentation tendency. The respective reference suspensions do not contain surfactants. The suspension samples for the rheology tests are denoted "Rheology" and "Rheology reference". "Sedimentation" and "Sediment. reference" are the suspension references for the sedimentation tests.*

Sample	Surfactant [g]	A240 [g]	ACMO [g]
Rheology	0.10	7.90	8.84
Rheology reference	0.00	7.90	8.94
Sedimentation	0.25	0.04	10.94
Sediment. reference	0.00	0.04	10.94

4.1.3.2. Acrylate Selection

The juxtaposition of suspensions with IBOA, TPGDA or cyclic trimethylolpropane formal acrylate (CTFA) to ACMO based suspensions allowed the comparison of the matrix materials. It employed rheological measurements and sedimentation tests. For the rheology each suspension contained 50 vol% TODA stabilized A240 (**Table 6**). For the sedimentation examination, the suspensions incorporated 0.1 vol% TODA stabilized A240 (**Table 7**).

***Table 6**: Suspensions based on varying acrylate monomers with a ceramic content of 50 vol% for rheological measurements.*

Matrix name	TODA [wt% (vol%)]	A240 [wt% (vol%)]	Matrix [wt% (vol%)]
IBOA	3.1 (6.5)	79.7 (50.0)	17.3 (43.5)
TPGDA	3.0 (6.5)	78.9 (50.0)	18.1 (43.5)
CTFA	3.0 (6.5)	78.1 (50.0)	18.9 (43.5)
ACMO	3.0 (6.5)	77.8 (50.0)	19.2 (43.5)

Their preparation involved the hand-held dispersing device (T10 basic Ultra-Turrax, IKA GmbH, Staufen, Germany), running at 14560 rpm for 5 min, and ultrasonication (Sonorex Super RK103H, Bandelin electronic GmbH and Co. KG, Berlin, Germany) with a power of 560 W for 15 min. The rheology investigation of the concentrated suspensions was done at a temperature of 32°C and a varying shear rate between 2 s^{-1} and 500 s^{-1}. Similarly, to the previous subchapter, the sedimentation tests for the diluted samples were prepared in vials to observe the sinking ceramic front. A photo was taken right after the preparation and after 72 h.

***Table 7**: Suspensions based on acrylate monomers with varying polarity and a ceramic content of 0.1 vol% for the investigation of the ceramic sedimentation behavior.*

Matrix name	TODA [wt% (vol%)]	A240 [wt% (vol%)]	Matrix [wt% (vol%)]
IBOA	2.5 (2.2)	0.4 (0.1)	97.1 (97.7)
TPGDA	2.4 (2.2)	0.4 (0.1)	97.2 (97.7)
CTFA	2.3 (2.2)	0.4 (0.1)	97.3 (97.7)
ACMO	2.3 (2.2)	0.4 (0.1)	97.4 (97.7)

For the investigation of the ceramic content influence, suspension with varying degrees of A240 in CTFA were prepared with the handheld dispersing device (T10 basic Ultra-Turrax, IKA GmbH, Staufen, Germany) at 14560 rpm for 5 min with subsequent ultrasonication (Sonorex Super RK103H, Bandelin electronic GmbH and Co. KG, Berlin, Germany) with a power of 560 W for 15 min. Their composition is shown in **Table 8**. The viscosities were taken three times at a temperature of 32°C and a shear rate of 500 s^{-1}. In addition to that, the viscosity of CTFA was measured with the same parameters to calculate the viscosity of the suspensions relative to the monomer matrix. Furthermore, the Krieger and Dougherty model was used to predict the theoretical viscosity of the respective suspensions. For the calculation, the equation 19 was utilized which was introduced in the theoretical section. The model shows the relative viscosity as a function of hydrodynamic forces. Finally, the prepared suspensions were subjected to filter tests with a 5 µm PTFE filter (Rotilabo®, Carl Roth, Karlsruhe, Germany). This is a prerequisite for inkjet printing to remove agglomerates from the suspension, which could otherwise occlude the nozzles.

***Table 8**: TODA stabilized suspensions with varying ceramic content in CTFA for rheological measurements.*

Sample name	TODA [wt% (vol%)]	A240 [wt% (vol%)]	CTFA [wt% (vol%)]
1	1.1 (1.3)	28.5 (10.0)	70.4 (88.7)
2	1.8 (2.6)	47.3 (20.0)	50.9 (77.4)
3	2.3 (3.9)	60.6 (30.0)	37.1 (66.1)
4	2.7 (5.2)	70.5 (40.0)	26.8 (54.8)
5	3.0 (6.5)	78.1 (50.0)	18.9 (43.5)

4.1.3.3. Ceramic Attrition

The previous subchapter has shown the preparation of A240 based suspensions at varying ceramic contents with CTFA. Due to the supposed presence of agglomerates and the potential risk of nozzle occlusion during inkjet printing, the submicro powder A240 was subjected to higher shear forces than in the previous subchapter. Three suspensions were prepared with a composition according to **Table 9**. The first samples, denoted "as received", were prepared with unaltered powder, which was combined with TODA and CTFA and homogenized with the hand-held dispersing device (T10 basic Ultra-Turrax, IKA GmbH, Staufen, Germany) at 14560 rpm for 5 min and ultrasonication (Sonorex Super RK103H, Bandelin electronic GmbH and Co. KG, Berlin, Germany) with a power of 560 W for 15 min. For the second batch of samples, denoted "2-propanol", the A240 was ground in a planetary ball mill (PBM) (PM400, Retsch GmbH, Haan, Germany) at 200 rpm for 8 h in a 125 ml grinding beaker with yttrium stabilized ZrO_2 inner cladding. The grinding medium was 2-propanol and 2 mm balls of the same material as the inner wall of the beaker. The ratio between the grinding balls and the ceramic particles was 7.4:1. Thereby, 30 g of fillers were suspended with 221 g of ZrO_2 grinding balls in 13.15 g (16.73 ml) 2-propanol. After the grinding time was elapsed 1.15 g TODA was added to the beaker and the treatment was continued for further 15 min. After that, the sample was retrieved by pouring the content through a sieve to separate the grinding balls from the suspension. The TODA coated particles were then dried in a rotary evaporator (Laborota 4003 digital, Heidolph Instruments, Schwabach, Germany) for 1 h at 175 mbar and 50 °C. Once the drying was complete the powder was suspended in CTFA with the hand-held dispersing device and ultrasonication using the same parameters as in the first sample. The third sample, denoted "CTFA", was also ground in the PBM with the same equipment and grinding balls to ceramic particles ratio. The beaker was filler with 30 g of fillers which were combined with 221 g of ZrO_2 grinding balls, 18.38 g (16.73 ml) of CTFA and 1.15 g of TODA. The attrition lasted for 8 h at a speed of 200 rpm. After the treatment, the suspension was retrieved by pouring the content through a sieve, separating the grinding balls and filling the suspension without further modification into a vial.

Each of the three samples was analyzed three times via static light scattering (Beckmann Coulter LS-230, Beckmann-Coulter Inc., Brea, CA, USA) to assess their particle sized distribution and gain insight into the agglomerate reduction potential of

the PBM. Each sample was prepared for the measurement by adding 0.1 g into 5 g of 2-propanol and ultrasonicate the diluted dispersion for 15 min. Thereafter each sample was drop by drop added into the device.

Furthermore, the samples were rheologically analyzed with an automated dynamic shear rheometer (CVO 50, Malvern Instruments, Malvern, UK) with a cone-plate design. The cone had a diameter of 60 mm and an angle of inclination of 2 °. The measurement took place at 32°C and a shear rate between 2 s^{-1} and 500 s^{-1}. In addition to that, the sample "CTFA" was measured at 60°C and a shear rate between 2 s^{-1} and 500 s^{-1}.

As a prerequisite for inkjet printing, filtering tests have been conducted with a 5 µm PTFE filter (Rotilabo®, Carl Roth, Karlsruhe, Germany). To test the amount of removed ceramic that did not pass the filter membrane due to size, the samples were analyzed via TGA (STA 409C, Netzsch Group, Selb, Germany). Thereby, 20 mg of each suspension before and after filtration was heated to 900°C at a heating rate of 10 K/min, kept for 15 min and then reduced the temperature with 10 K/min steps to 25°C. The weight reduction of the samples was recorded by the instrument software.

***Table 9**: Samples for the investigation of mechanical treatment influence on ceramic suspensions. The methods involved the usage of a hand-held dispersing device (UT), an ultrasonic bath (USB) and planetary ball milling (PBM). The sample "as received" was prepared with UT and USB. While the formulations of "2-propanol" and "CTFA" also involved the PBM.*

Sample name	TODA [wt% (vol%)]	A240 [wt% (vol%)]	CTFA [wt% (vol%)]	Preparation method
As received	2.3 (3.9)	60.6 (30.0)	37.1 (66.1)	UT, USB
2-Propanol	2.3 (3.9)	60.6 (30.0)	37.1 (66.1)	PBM, UT, USB
CTFA	2.3 (3.9)	60.6 (30.0)	37.1 (66.1)	PBM

4.1.3.4. Ink Characterization

The investigations in the previous subchapter led to the result that the ink preparation of 30 vol% TODA stabilized A240 fillers in CTFA in a one pot approach was more beneficial than the other investigated methods. In this subchapter parameters and procedures are described for assessment of the curing, jetting and thermal properties of the ink. The preparation was done in the PBM using a 125 ml steel beaker with $YZrO_2$ inner cladding and grinding balls of the same material. The beaker was filled with 30 g of A240, 18.38 g (16.73 ml) of CTFA and 1.15 g of TODA. After a grinding

time of 7 h at a speed of 200 rpm, the photo initiator TPO and the thermal initiator LP were added to the ink in a concentration of 3 wt% and 1 wt% relative to the acrylate, respectively. The latter should enable a thermally induced post polymerization. The treatment went on for another 1 h, after which the suspension was retrieved by pouring the content through a sieve for separation of the grinding balls. The ink was then used without further modifications.

UV initiated polymerization allows the layer-by-layer construction in 3D inkjet printing. A high conversion of monomer to a polymer can improve the thermal conductance of the composite. For the testing of the conversion degree one 5 mm² layer of ink was jetted onto 10 mm² silicon wafers, which were polished on both sides. The jetting was conducted with the Dimatix Material Printer (DMP-2831, Fujifilm Dimatix Inc., Santa Clara, CA, USA) using a DMC-11610 cartridge with a drop volume of roughly 10 pl. The printhead voltage was set to 30 V, the temperature to 60°C and the drop spacing to 20 µm. The waveform, which is subdivided into four phases is depicted in **Figure 28**. It describes the motion of the piezo-electric membrane in the printhead which generates and emits droplets. In the first phase, the firing voltages decreased from 40 % to 0 % at a slew rate of 0.66. In 4.2 µs the ink was sucked from the ink reservoir into the firing chamber. The second phase lasted for 5.6 µs, the curve increased to 100 % at a slew rate of 1.90 and the ink protruded through the nozzles. During the third phase, the piezo-electric membrane reversed partially its bending to prevent air suction into the firing chamber. The curve sank from 100 % to 73 % at a slew rate of 0.60 in 5.1 µs. In the fourth phase the curve returned from 73 % to 40 % in 0.8 µs, with a slew rate of 0.80. The membrane was then in its starting position and the pendant ink droplet was ejected from the nozzle. As depicted in **Table 10** a total amount of 10 samples has been produced as triplets under variation of the UV irradiation dose. In addition to that, 5 samples were heat treated at 100°C for 12 h after the irradiation. The samples were investigated via Fourier transform infrared spectroscopy (FTIR) (Excalibur series, Bio Rad, Hercules, California, USA) in rapid scan mode. During the measurement 64 scans were performed between 750 cm^{-1} and 4000 cm^{-1} with a sensitivity of 16 and a steady nitrogen flow of 11 l/min. Prior to the measurement the background signal has been recorded with a bare polished silicon wafer piece. As it was mentioned in the theoretical section, the calculation of the conversion efficiency was done using the relation between the carbonyl peak and the vinyl peak of the ink.

***Table 10**: Samples for the measurement of the conversion efficiency of 30 vol% TODA coated A240 in CTFA. The samples were UV irradiated and 5 of the samples were additionally thermally cured.*

Sample name	Irradiation dose [J/cm²]	Thermal curing [°C (h)]
1	0	0 (0)
2	1	0 (0)
3	5	0 (0)
4	10	0 (0)
5	30	0 (0)
6	0	100 (12)
7	1	100 (12)
8	5	100 (12)
9	10	100 (12)
10	30	100 (12)

Aside from the polymerization characteristics, the ink jetting properties are important for 3D inkjet printing of precise structures. For the analysis, the ink was observed in the drop watcher of the DMP-2831. The software of the printer was used to assess the drop velocity by setting the stroboscope camera to image mode, reading the position of the drop from the displayed number grid and dividing it by the time the droplet needed to reach this position. Furthermore, the weight of the droplet was determined by using the weight assessment tool. Thereby, 10 of the 16 available nozzles were chosen to jet 200000 drops into a pre weighted pan, weight the collected ink and divide the result by the number of droplets. The volume of the droplet was calculated using the density of the ink. To assess the morphology and trajectory of the droplets images were taken of their position as a function of the time at 0 µs, 20 µs, 40 µs, 60 µs, 80 µs, 100 µs and 120µs. The Weber, Reynolds and Ohnesorge numbers, which can further quantify the jetting quality of the ink, were calculated using the equations introduced in the theoretical section.

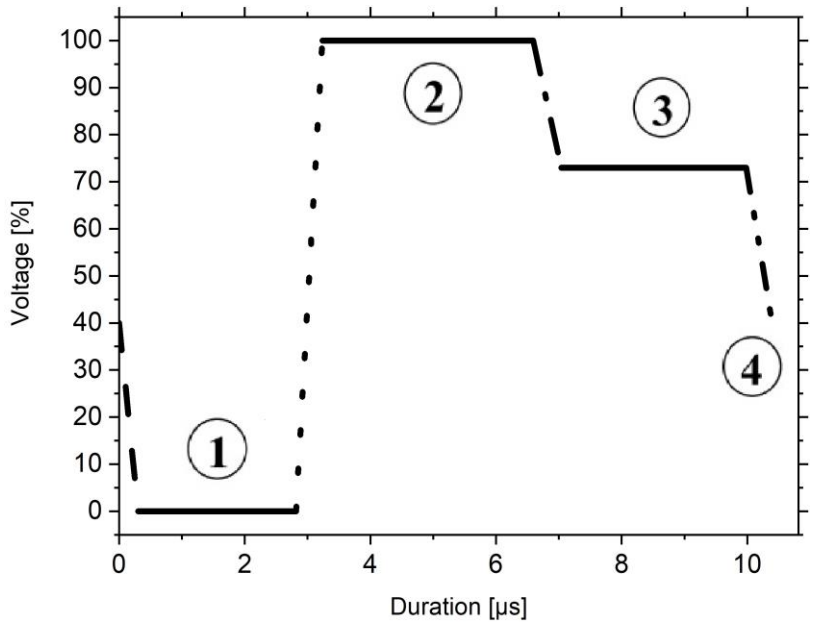

***Figure 28**: Waveform for the jetting of the UV curable ink with 30 vol% of TODA stabilized A240 in CTFA. The waveform is divided into four segments: (1) Ink filling, (2) ink firing, (3) initial piezo recovery and (4) complete piezo recovery.*

As the primary purpose of the materials is to raise the thermal conductance in the UV curable organic matrix, respective measurements have been conducted. In the theoretical section the used methods are closer explained. These involved the assessment of the density, the thermal capacitance, and the thermal diffusivity. The specimens for the analysis were printed with the DMP-2831 according to the BMP template shown in **Figure 29**. The larger specimens had a diameter of 10 mm and the smaller ones 5 mm. The substrate was an aluminum plate coated with a 100 µm thick PDMS layer using a hand-held high precision film applicator for better specimen retrieval. The printing was done using the waveform shown in **Figure 28** at a printhead voltage of 30 V, a temperature of 60°C and a drop spacing of 20 µm. Thereby, layer-by-layer a structure with a height of 1 mm was printed. After each layer, the deposited ink was UV cured with a wavelength of 405 nm and a power density of 100 mW/cm² for 10 s using a UV light source (LED Spot 100 IC/HP IC, Dr. Hönle AG, Gräfelfing, Germany) in ambient atmosphere. The density of the printed specimens was measured and calculated with the Archimedes method described in the subchapter 3.4.9 using the equation 41. This required the weighting of the 6 samples in air and in 2-propanol with the 2-propanol having a density of 0.78 (g/cm³) at a temperature of 22 °C.

The thermal capacity was assessed by DSC (DSC 204 F1 Phoenix, NETZSCH-Gerätebau GmbH, Selb, Germany) of the 5 mm specimens. While the thermal

diffusivity determination employed LFA (LFA 447, NETZSCH-Gerätebau GmbH, Selb, Germany) where two of the three 10 mm specimens were measured. Each measurement was repeated 7 times with a 1000 µs laser pulse.

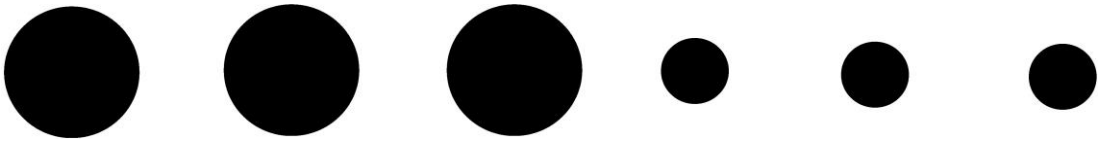

***Figure 29**: BMP template for the inkjet printing of specimens for the thermal conductance measurement.*

To demonstrate the suitability of the material to print 3D structures a demonstrator was produced with the DMP-2831 using the BMP template shown in **Figure 30**. The template is composed of a ground plate depicted on the left side and columns shown on the right side of the image. The print parameters were the same as used for the printing of the thermal specimens. At first 10 ground layers were printed with the material ACMO modified with 3 wt% of TPO as photoinitiator onto an aluminum substrate using the template of the ground plate. The purpose of that is the possibility to remove the demonstrator, which was printed onto the water solvable material, from the substrate by ultrasonication in water. The ground plate itself was printed layer-by-layer with the ceramic ink until 100 layers and a height of 1 mm were reached. Then the BMP template was switched to the columns and another 300 layers of 3 mm height were printed to form the whole structure. Between each layer UV irradiation was applied using the UV light source with the same parameters introduced for the thermal specimens.

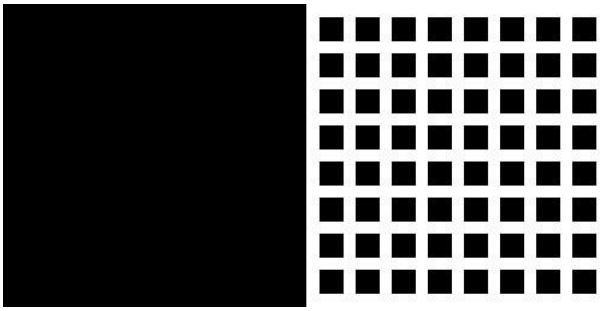

***Figure 30**: BMP template for the inkjet printing of a heat sink for the purpose of demonstration. On the left the base of the heat sink is shown and on the right side the columns are depicted, which were printed on top of the base.*

4.2. Results and Discussion

This chapter shows the results of the solvent free ceramic ink investigation for 3D inkjet printing. It is divided into the subchapters “Structural Composites” and “Thermally Conductive Composites”. In the former the possibility was investigated to inkjet print structural materials utilizing nanoparticles and submicron particles. In certain cases, such materials have shown improvement of the mechanical properties of polymers while at the same time maintaining a low material density. Furthermore, experiments have been done to raise the thermal conductance in inkjet-printed polymers, which necessitates a high ceramic content. Hence, possibilities were assessed to reduce viscosity and enable ink jetting of highly filled composites. After elucidating a suitable composition and preparation method, experiments have been conducted to test the sufficiency of the composite properties. They illuminated the printing process and the final application of thermal conductance.

4.2.1. Structural Composites

Bulk polymerized thermosets from polyfunctional acrylate precursors are prone to a heterogeneous distribution of its chainmesh. They exhibit areas of high and low crosslinking where the latter may compromise the mechanical integrity. The addition of alumina nanoparticles into the polymers can increase their tensile toughness at already small concentrations without compromising their Young’s modulus and tensile strength. In this subchapter, the possibility was investigated to improve the respective property in an UV curable acrylate mixture by adding nanoceramics with the purpose of creating a 3D inkjet printable ceramic ink. As explained in subchapter 3.3.3, to harness the full advantages of the large specific surface area of the fillers, they must be homogeneously distributed in the matrix. This increases the polymer-ceramic interface and reduces internal tensions within the composite once it solidifies. Furthermore, the introductory subchapter 1.2 has shown, that the maximum ceramic structure size must be between 210 nm and 1050 nm, which is the 100^{th} to 20^{th} of the 21 µm sized printhead nozzles of the 10 pl Dimatix materials cartridge. To achieve that, the investigation involves three kinds of alumina filler with a primary particle size of 14 nm (TEC14), 56 nm (TEC50) and 170 nm (TEC170).

4.2.1.1. Ceramic Conditioning

For the assessment of the particle morphology high-resolution scanning electron microscopy images (HRSEM), shown in **Figure 31,** have been made. The powders exhibit the fractal-like structures of combustion produced materials. TEC14 consists of spherical primary particles connected with sinter-necks. TEC50 has a similar appearance with the difference that it is a bimodal composition of spherical primary particles with one mode being in the 30 nm range and the other in the 70 nm range. The primary particles of TEC170 hint at an aspect ratio of more than 1 since, as depicted in **Figure 31c,** the longitudinal diameters of the fillers reach in some parts values of more than 1000 nm. Platelet-like shapes can improve the toughness of polymers to a larger extent. For all fillers, the images reveal their agglomerated nature, which requires their mechanical homogenization by applying strong shear forces.

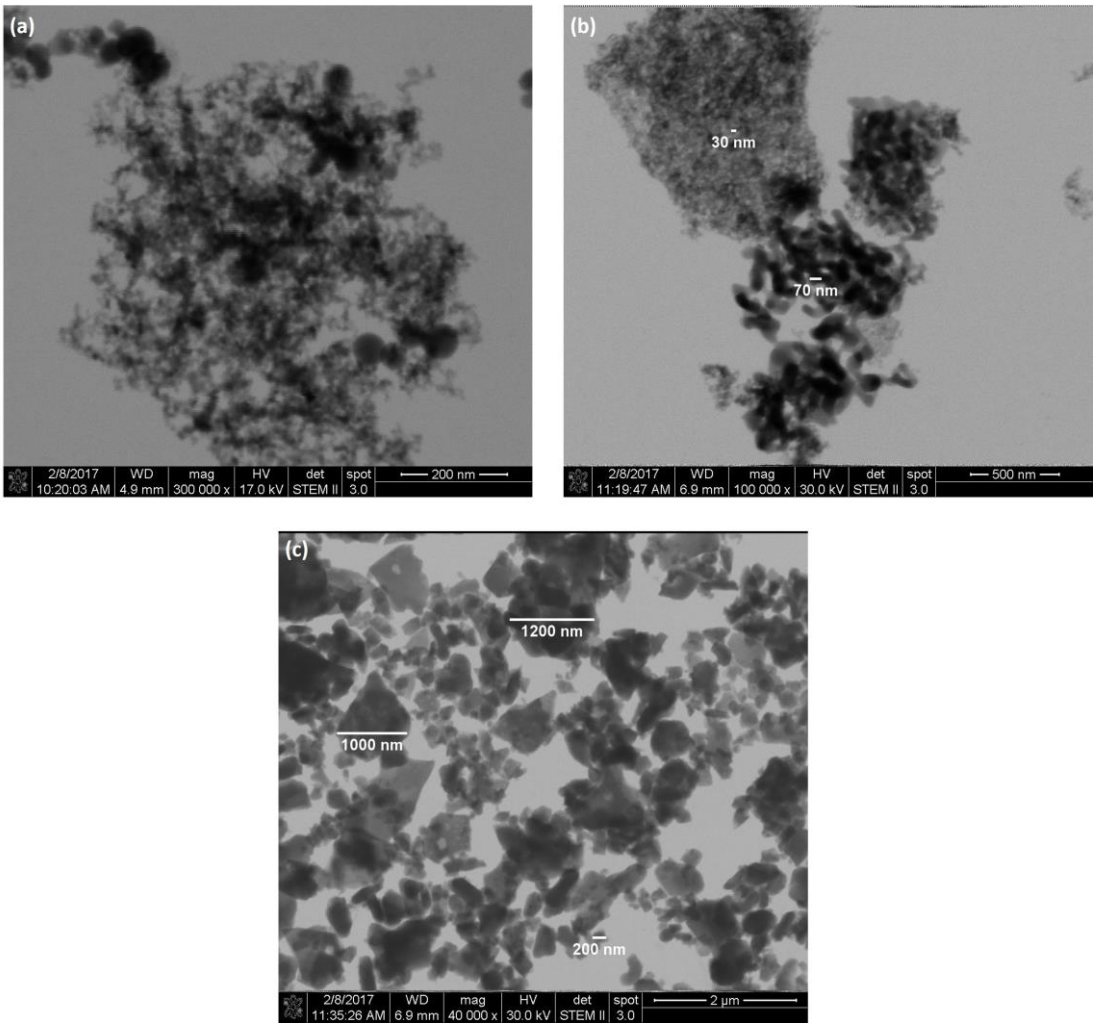

Figure 31*: HRSEM images of (a) TEC14, (b) TEC50 and (c) TEC170. All particles were analyzed as received.*

The deagglomeration of the particles took place in the PBM. But instead of grinding the ceramic in the final acrylate matrix, 2-propanol was the medium of choice. The reason for that lies in the utilization of the surfactant TODA, which prevents homogenized particles from re-agglomeration. The molecules are described to degrade while being exposed to prolonged mechanical energy. This necessitates the addition of the TODA after the grinding process. Nonetheless, without a surfactant during grinding the hydrophobic matrix material would increase the viscosity of the suspension, thus limiting the grinding efficiency. Contrary to that, 2-propanol allows low suspension viscosities due to its high polarity. Prior to grinding, physisorbed water was removed by heating the powder in an oven at 200°C for 12 h. The reduction of the hydration layer on the particles aimed at improving the TODA attachment onto the particle surface, which could otherwise compete with the adherent water. The monitoring of the size development during the 8 h milling duration allowed to identify an optimal timeframe to generate the smallest possible particle size. As **Figure 32** shows, the particles experience a noticeable reduction of the D10, D50 and D90 values in the first stage of grinding, followed by a minor reduction at most in the later stages. Thus, after 1 h TEC14 reaches its minimum size under given conditions, while TEC50 and TEC170 exhibit their lowest values after 8 h. At this point, TEC170 likely consists to a large extent of primary particles while TEC14 and TEC50 still remain fractal-like structures. The reason for that is the size reduction efficiency of the PBM with 2 mm grinding balls decreases the smaller the particles get. For a more thorough reduction in particle size, smaller grinding balls are needed. This, however, would make the separation of the sample and grinding balls significantly more complicated. As the next step in the production process, TODA was added to the suspension and 2-propanol was removed by rotary evaporation.

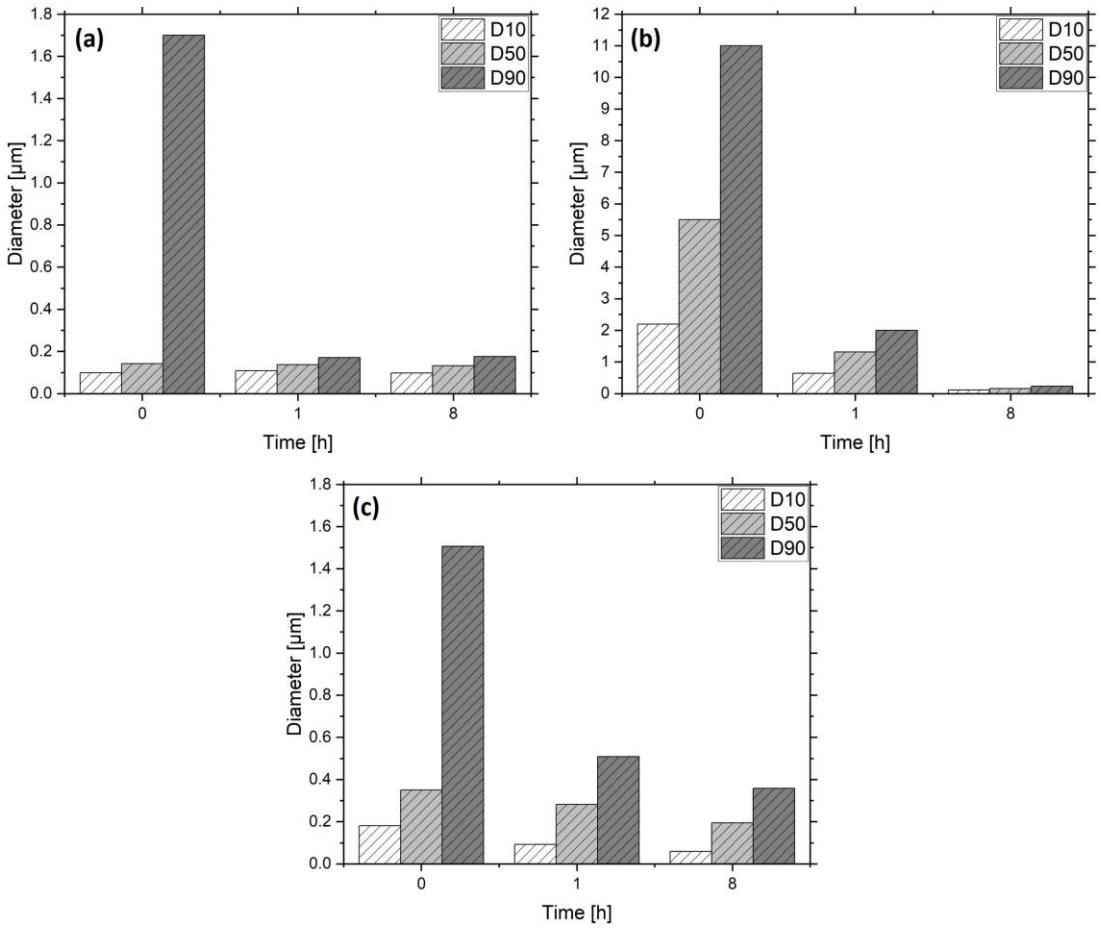

***Figure 32**: Particle size reduction in the PBM prior to TODA addition for (**a**) TEC14, (**b**) TEC50 and (**c**) TEC170 fillers over a timeframe of 8 h.*

Figure 33 exhibits the TGA curves of the untreated, heated and TODA coated powders. The measurement visualizes the extent of water removal during heating to 200 °C by comparing particles before and after the treatment. Moreover, it allows to assess the degree of TODA molecule adherence during the drying step. **Table 11** summarizes the values for the sample mass loss recorded during the TGA. The as received particles show mass reduction with increasing temperature. Between 20 °C and 200 °C physically bound water molecules evaporate. Between 200 °C and 1200 °C chemisorbed water detaches from the particles surface. The curve of the second phase differs by its lower decrease from first phase. It indicates that more physically bound water is present than chemically bound water. The former also detaches more easily from the surface than the latter, which is in accordance with observations in literature. The heated particles behave in a similar way; however, the weight reduction is lower, since drying at 200 °C prior to TGA leads to the removal of OH groups on the surface, which in turn causes lower physical water binding. Given the findings in the

subchapter 3.2.1, it is likely that TEC14 untreated is γ-Al_2O_3, while TEC170 untreated is possibly α-Al_2O_3, which are the thermodynamically stable forms for the respective particle sizes. The TEC50 untreated exhibits a step in the TGA curve between 230 °C and 250 °C, which is not visible in the other curves. It indicated that $Al(OH)_3$, e.g. bayerite, is present and starts transforming to η-Al_2O_3 at 230 °C and then to α-Al_2O_3 at 1200 °C. The examination of TEC50 heated shows no such transformation, which suggests that the powder already turned into η-Al_2O_3. The milled and TODA coated powders exhibit a weight reduction of 25.9 wt% (TEC14), 8.9 wt% (TEC50) and 2.9 wt% (TEC170). Their TGA curves in **Figure 33** start to decline at 150 °C, which resembles the boiling point of the TODA. At around 400 °C the molecules are most likely evaporated. The curves indicate that the surfactant can replace the physically adsorbed water on the particle surface. Therefore, in **Table 11** the depicted dispersant concentrations, denoted as "measured TODA" is the difference between the weight reduction of coated and heated particles without the surface-bound moisture. The results are in good agreement with the "weighted TODA", being the surfactant amount added during ball milling. This implies that the desorption of TODA during drying in the rotary evaporator is negligible. Also, it suggests that drying prior to grinding and coating of the particles is not necessary because TODA seems to outcompete water during attachment on the surface.

***Table 11**: Thermogravimetric mass loss of as received, heated and TODA coated fillers. "Weighted TODA" is the surfactant amount relative to the total mass of the coated particles added during ball milling. "Measured TODA" is the concentration deduced from the mass loss.*

Nanoparticles	Total Mass Loss (wt.%)	Weighted TODA (wt.%)	Measured TODA (wt.%)
TEC14 as-received	6.3	-	-
TEC14 heated	5.4	-	-
TEC14 coated	25.9	23.6	23.5
TEC50 as-received	3.7	-	-
TEC50 heated	3.2	-	-
TEC50 coated	8.9	7.1	7.6
TEC170 as-received	1.2	-	-
TEC170 heated	0.8	-	-
TEC170 coated	2.9	2.0	2.4

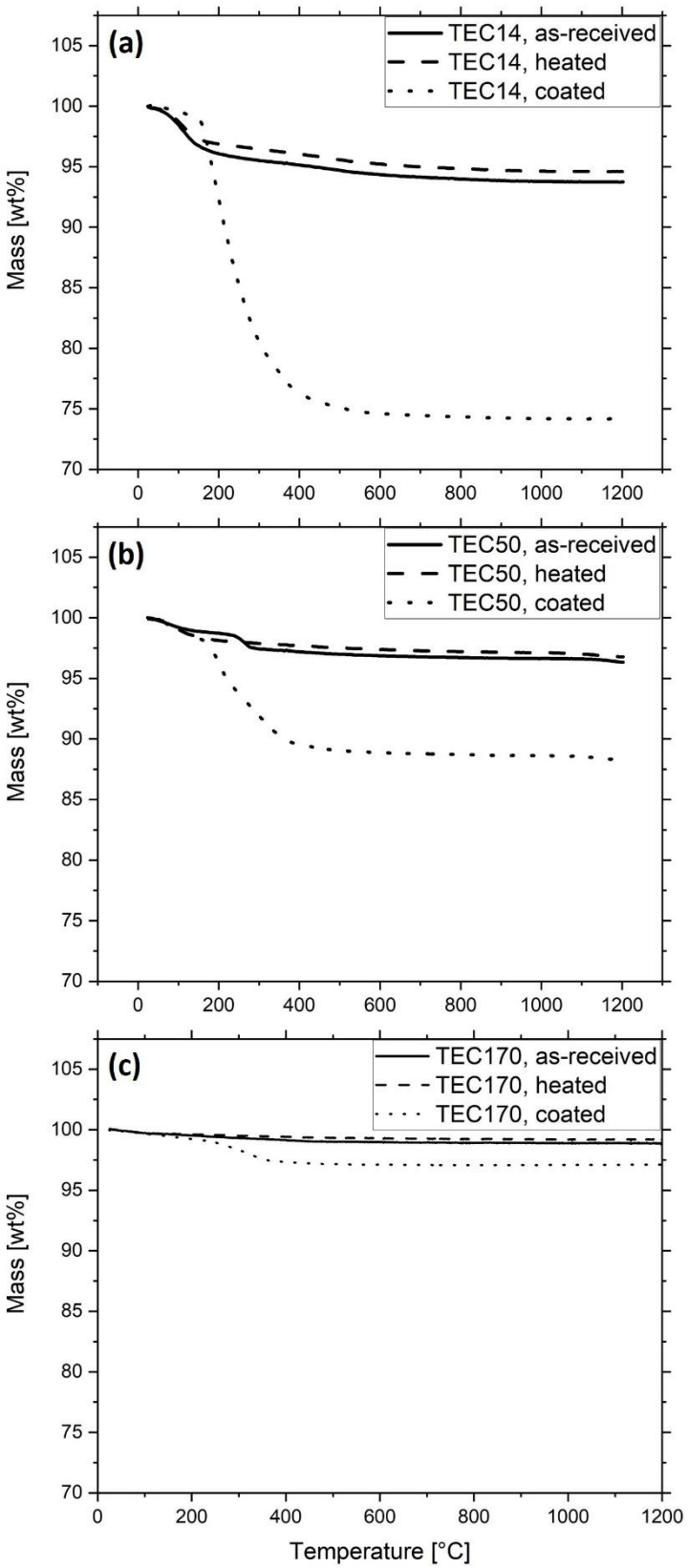

***Figure 33**: Thermogravimetric investigation of (**a**) TEC14, (**b**) TEC50 and (**c**) TEC170 as received, heated and TODA coated filler particles.*

4.2.1.2. Ink Characterization

Once successfully coated and homogenized, solvent free and UV curable ink formulations 14-I to 170-III incorporated the treated nanoparticle in varying concentrations. The experimental subchapter 4.1.2 describes the compositions of the inks. After formulation, the inks were filtered with 5 µm PTFE filters to remove larger agglomerates before inkjet printing. These would otherwise clog the printhead nozzles. To correlate the amount of agglomerated and thus removed particles, the reduction of the ceramic mass after filtering was measured using TGA. But the retention of agglomerates might also occur during printing so that **Figure 34a**, **Figure 34b** and **Figure 34c** display the ceramic content of the inks 14-I to 170-III before and after filtration as well as after printing. For the filtration of 5 ml TEC14 based inks one 5 µm PTFE filter for each ink was used while for 5 ml of the TEC50 and TEC170 based inks three filters for each ink were necessary. Their higher tendency to agglomeration is supposedly caused by the larger size of the fillers and the lower TODA content, relative to TEC14 based inks, which might contribute to lower stability. During filtering and printing ceramic retention can be observed for the inks. Thereby, TEC50 based inks lose the most particles, which differ structurally from the surfaces of the other particles by their η-Al_2O_3 phase. In general, despite the low ceramic content in all inks, their filtering properties further declined when filtering volumes of more than 5 ml. The low polarity of the organic matrix might be the main reason for this behavior.

Figure A1 and **Table A1** in the appendix show the viscosity of the liquid matrix material and the inks 14-I to 170-III at 60°C as a function of the shear rate. All inks are between 5 mPa·s and 7 mPa·s and exhibit a Newtonian behavior, which is advantageous for the printing process. Since only moderate shear forces affect the ink in the printhead before the actual jetting. Depending on the printing system, this means that the transport of the ink to the piezo actuators relies on a constant low viscosity. A non-Newtonian ink, which exhibits a suitable viscosity only at high shear forces, would obstruct the periphery of the printer. The influence of the nanoparticles on the viscosity is negligible due to their low volume percentage.

The fillers moderately increase the surface tension of the inks with the powder SSA being seemingly not an influencing factor, as depicted in **Table A1**. Jetting tests of the inks are shown in **Figure A2** in the appendix. With the Fujifilm Dimatix it was possible to assess the drop morphology, velocity, volume and weight. The inks exhibit an elongated ligament with no visible satellite droplet formation. With a velocity

between 8 m/s and 11.5 m/s (**Table A2**) the drops lie in the optimal range for inkjet printing. The average drop volume is 8.3 pL and the average drop weight is 9 ng. It was possible to maintain the same constant quality of the jetting for more than 10 min.

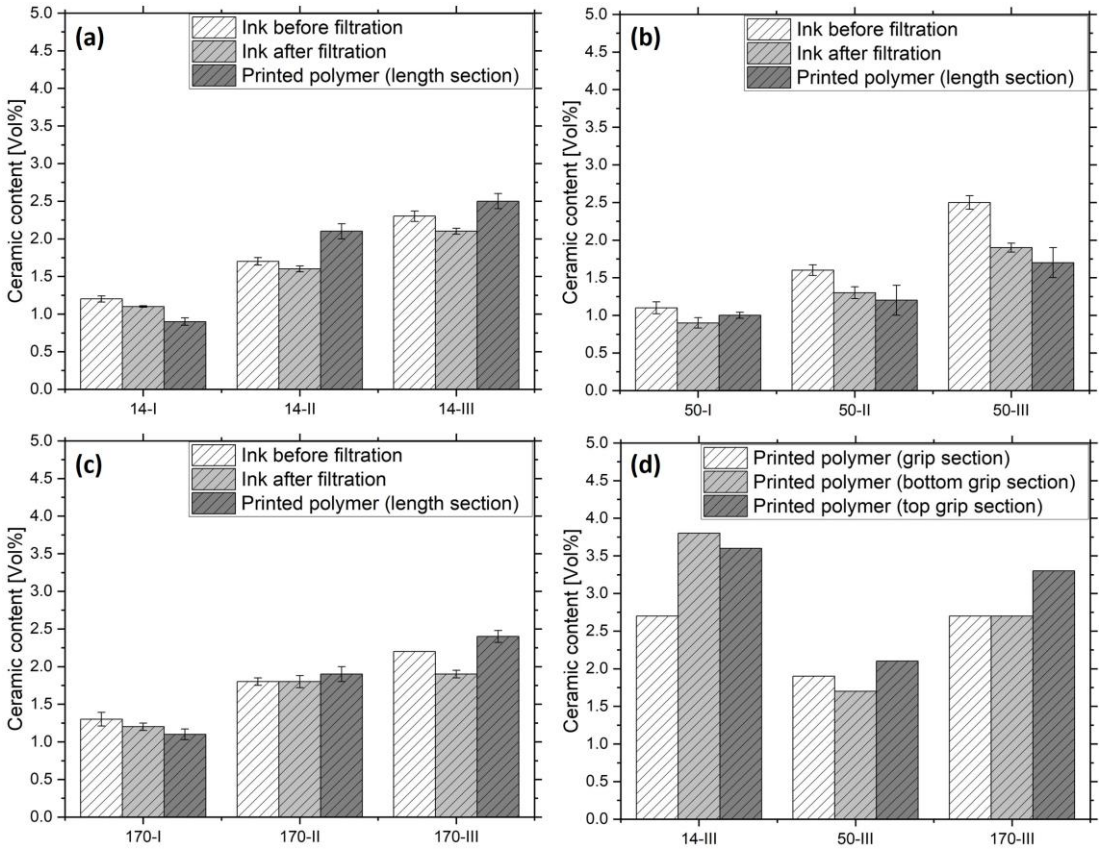

***Figure 34**: Ceramic content of the ink samples before and after filtration with a 5 µm filter as well as after printing and polymerization. The samples are (**a**) 14-I, 14-II, 14- III, (**b**) 50-I, 50-II, 50-III and (**c**) 170-I, 170-II, 170-III. The subsamples for the polymerized samples were taken in the longitudinal section, the gauge section, of the tensile specimen. In (**d**) the ceramic content of samples 14-III, 50-III and 170-III is shown after printing and polymerization. The subsamples were taken in the cross-section of the grip, on the bottom of the grip and on top of the grip of the tensile specimen.*

The formulated inks allowed the printing of tensile specimens for mechanical analysis by jetting the ink into a PDMS mold, a measure to accelerate the printing procedure in comparison to layer-by-layer building. The polymerization of the material happened after every five layers of printed ink. As opposed to layer-wise curing, the adoption of this printing approach allowed a faster production of tensile specimens. **Figure 35a** shows printed tensile specimens of sample 170-III and **Figure 35b** exhibits the cross-section of one of the specimens after the tensile test. The printing into the PDMS form

gave the top of the specimen a concave curvature, which is due to the interaction of the initially liquid ink with the PDMS sidewalls. In addition to that the sides of cross section are rounded, which is caused by the form of the PDMS mold. Examination of the ceramic content in the tensile specimens after printing suggest that the composition of the material changed during the printing process (**Figure 34)**. The ceramic content relative to the filtered inks decreased slightly in sample 14-I, while samples 14-II and 14-III had a significant increase. For the samples 50-I, 50-II and 50-III only minor deviations are visible. In 170-I, 170-II and 170-III, only the last sample exceeded the ceramic content of the liquid precursor.

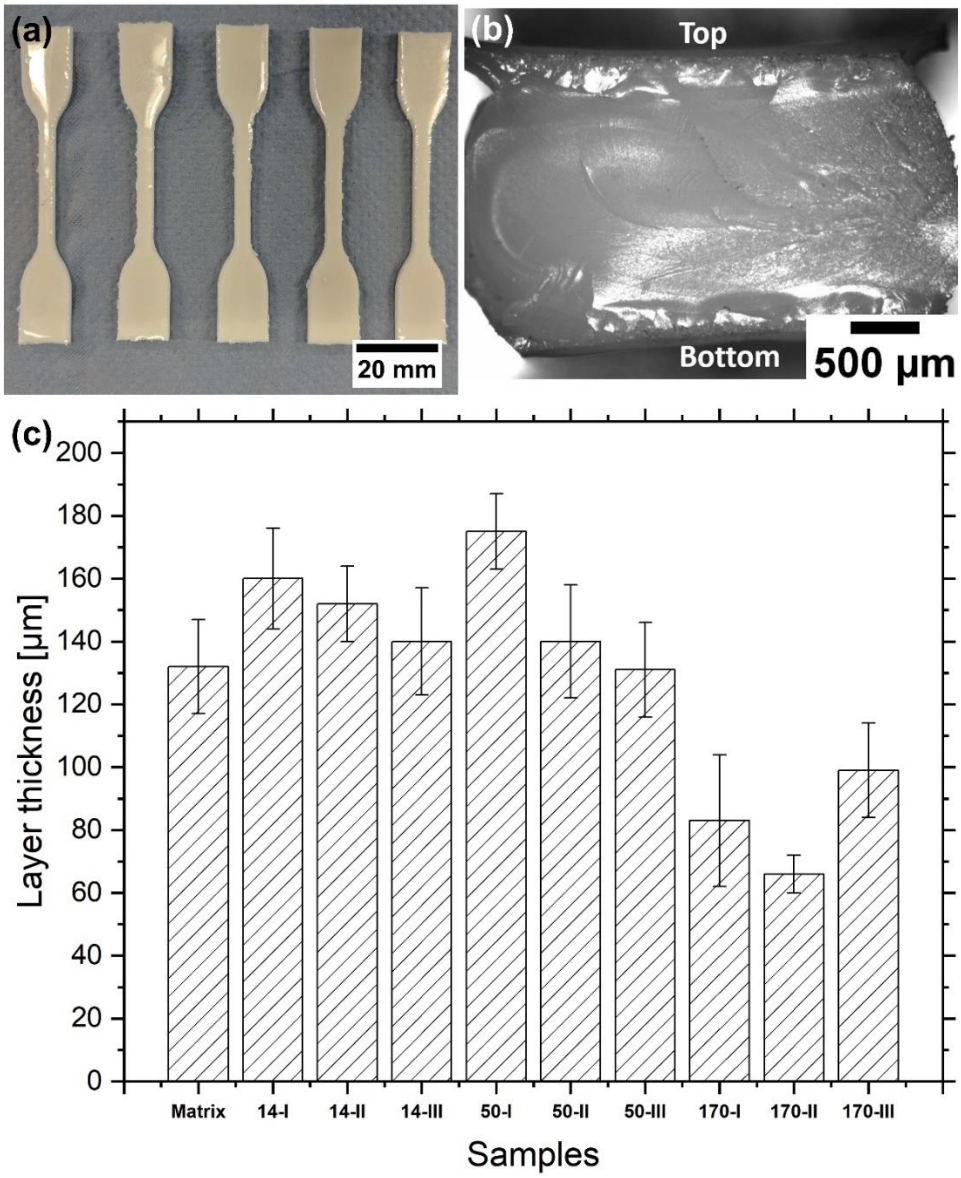

***Figure 35**: (**a**) Printed tensile specimens of 170-III, (**b**) Cross-section of one of the specimens. (**c**) Layer thickness of five subsequently printed layers with a UV curing step after their deposition for all printed inks.*

Agglomeration and occlusion of the print head nozzles could be one reason for the ceramic content reduction. Yet a more likely cause might be the uneven distribution of ceramic within the specimens, which might explain not only ceramic reduction, but also its increase. **Figure 34d** illustrates the variances in ceramic content in the grip section. The results give evidence for a possible interaction of the ceramic with the PDMS mold walls and therefore phase separation as a cause of the heterogeneity. Moreover, evaporation of acrylate components during printing and curing might cause a ceramic increase as well.

Crosslinked structural polymers are suitable for load bearing positions. But these materials may exhibit a reduction in stiffness when it exceeds the glass transition temperature. The knowledge about this value is important for materials like the investigated samples. The unfilled polyacrylate reaches a glass transition temperature of 66 ± 7 °C (**Table 12**). Ceramic addition does not lead to any significant change in the value, probably due to the low ceramic content.

***Table 12**: Characteristics of the tensile samples after printing: Glass transition, Young's modulus, ultimate tensile strength and tensile toughness.*

	T_g [°C]	E [MPa]	UTS (MPa)	U_T (J/m²)
Matrix	66 ± 7	516 ± 51	33 ± 6	1.1 ± 0.2
14-I	59 ± 4	447 ± 43	26 ± 4	0.8 ± 0.2
14-II	58 ± 4	367 ± 34	32 ± 7	1.4 ± 0.6
14-III	55 ± 5	369 ± 87	21 ± 7	0.6 ± 0.3
50-I	64 ± 8	409 ± 103	20 ± 6	0.5 ± 0.2
50-II	62 ± 1	456 ± 42	28 ± 6	0.8 ± 0.3
50-III	63 ± 1	484 ± 94	28 ± 10	0.9 ± 0.5
170-I	66 ± 5	458 ± 46	27 ± 6	0.8 ± 0.3
170-II	64 ± 5	433 ± 78	29 ± 6	0.8 ± 0.3
170-III	66 ± 3	517 ± 33	35 ± 2	1.2 ± 0.2

As stated at the beginning of this subchapter, the question arises, whether already low amounts of nanoparticles can improve certain mechanical properties. Tensile tests of the unfilled polyacrylate show Young's modulus of 516 ± 51 MPa, which is the second-best result (**Figure 36**, **Figure A3**, **Table 12**). The elastic moduli of the other samples, except for 170-III, show lower values, which could stem from the scattering effect of the fillers, limiting monomer conversion and indirectly reducing the degree of polymer crosslinking. In 170-III the stiffness of 517 ± 33 MPa coincides with the lowest cured layer thickness of all samples (**Figure 35** c), which might have reduced

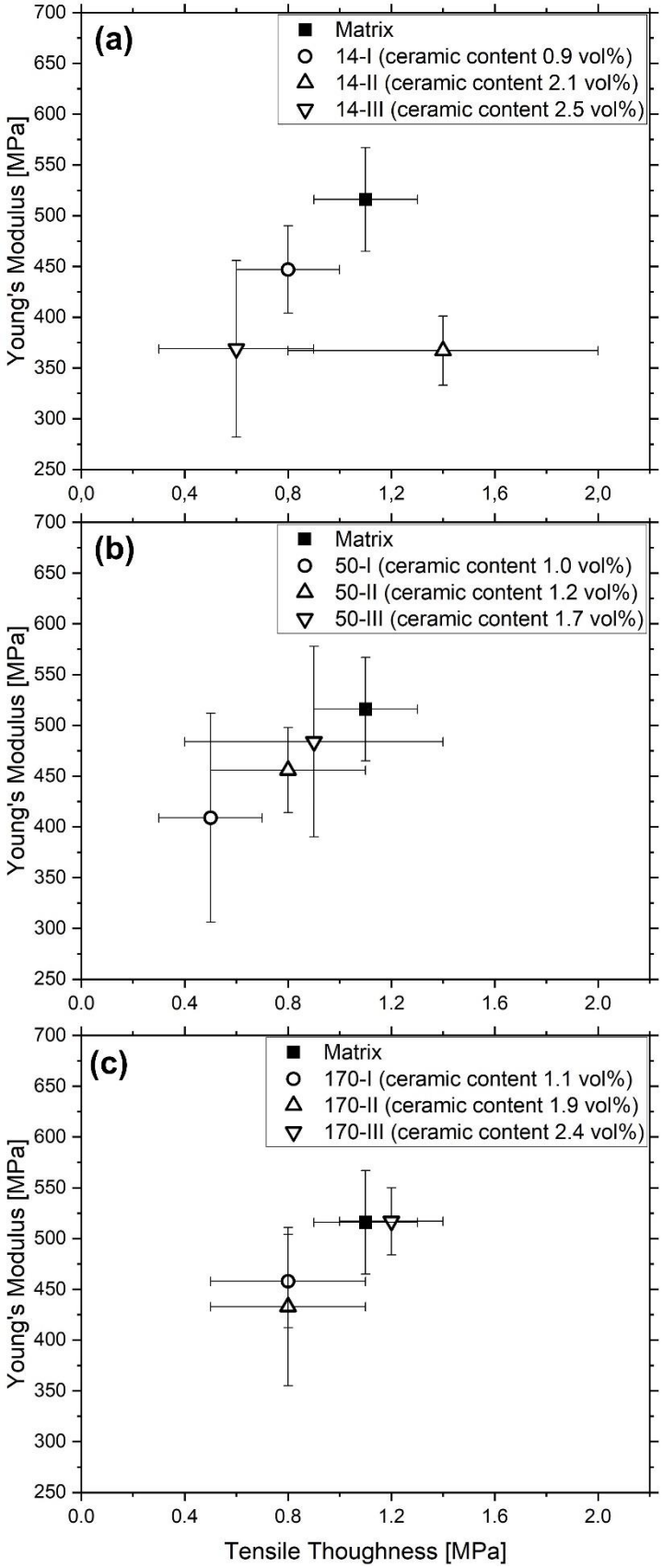

***Figure 36**:Stiffness/tensile toughness relationship of the printed (**a**) TEC14, (**b**) TEC50 and (**c**) TEC170 filled samples with varying ceramic content.*

the influence of UV light scattering. The tensile strength and toughness of all samples are subjected to minor fluctuations (**Figure 36**, **Figure A4** to **Figure A6**, **Table 12**). However, similarly to the results of the stiffness measurement, the filled samples show slightly lower values, except for 14-II and 170-III.

In the current chapter it was shown that low nanoparticle contents did not enhance the mechanical properties of the investigated polymer-ceramic composites in any significant manner. Instead, the results mostly hint at a decrease in the mechanical properties, which is especially attributed to the increased UV light scattering of the particles. The improvement of the toughness, described in literature, could possibly be reached if the influence of particle scattering was mitigated and more particle homogeneity, especially in the TEC14 based inks, was achieved.

4.2.2. Thermally Conductive Composites

As opposed to the previous subchapter, which dealt with mechanical improvement of 3D inkjet-printed UV curable ceramic inks, the following set of investigations deals with the increase of the thermal conductance in composites for 3D inkjet printing. As described in subchapter 3.3.4, the introduction of ceramic fillers, for example submicro alumina particles, increases the thermal conductance significantly at a ceramic content beyond 30 vol%. At these concentrations the fillers start to percolate and form interconnected pathways throughout the ceramic material. This makes it necessary to produce inks, which are on the one hand highly concentrated, but on the other hand still exhibit a viscosity, which is sufficient for ink jetting at printing temperature.

4.2.2.1. Surfactant Selection

In this subchapter, surfactants have been investigated to stabilize the particle surface and to reduce the viscosity of the ceramic inks. **Figure 37a** shows the viscosity of 10 suspensions with 20 vol% A240 in the hydrophilic matrix ACMO at a shear rate of 2 s^{-1} and 500 s^{-1} and a temperature of 32°C. With its high polarity, ACMO enables good wetting of the ceramic surface. In **Figure 37b** there are the respective sedimentation setups of the suspensions, diluted to a ceramic content of 0.1 vol%.

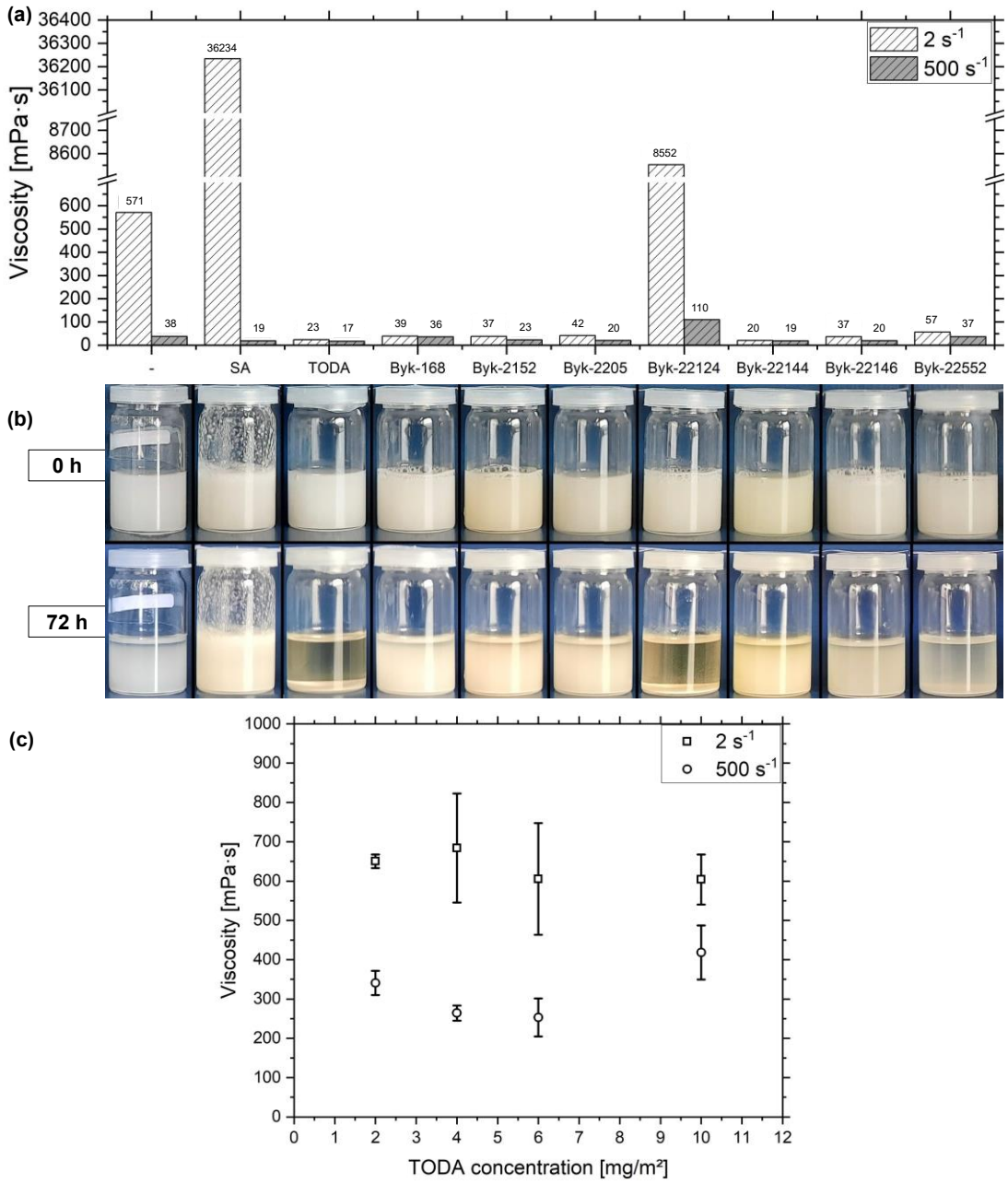

***Figure 37**: (**a**) Viscosity of 20 vol% A240 as received in ACMO without surfactant and with added 2 mg/m² of the surfactants SA, TODA, Disperbyk-168, Disperbyk-2152, Disperbyk-2205, Disperbyk-22124, Disperbyk-22144, Disperbyk-22146 and Disperbyk-22552 at a temperature of 32°C. (**b**) Sedimentation of the diluted suspensions during a course of 72 h. (**c**) Viscosity of 50 vol% A240 as received in ACMO in dependency of the TODA concentration at a temperature of 32°C.*

With exception of the reference, each suspension contains surfactants with a concentration relative to the particle surface area of 2 mg/m² for the former and 1000 mg/m² for the latter experiment. The surfactant concentration relative to the total volume, however, remained the same.

All suspensions exhibit a shear thinning behavior, which however differs in strength. Without stabilizing molecules, the reference has one of the highest discrepancies between the viscosities at 2 s^{-1} and 500 s^{-1}. In the sedimentation setup the particle front sedimented by 5 % relative to the suspension surface after 72 h. The dispersion stabilized with SA shows a viscosity of 36234 mPa·s at 2 s^{-1}, which is the highest value of all the suspensions. At 500 s^{-1} the viscosity drops to 18 mPa·s, which is among the lowest values. This could be explained by the hydrophobicity of the SA covered particles. It might cause the ACMO molecules to interact more with each other and forces the coated fillers to agglomerate, a tendency also described in [187]. While the high viscosity at low shear rates hints at particle network formation, the interaction between the particle is seemingly low and results in the viscosity drop at high shear forces. At diluted concentrations, this effect does not lead to a visible sedimentation. Part of the reason is, SA is not easy to dissolve in ACMO. Therefore, a certain amount of surfactant remains as a solid powder in suspension and prevents proper assessment of the SA effectiveness.

TODA leads to the lowest viscosity at the shear rate of 500 s^{-1}, with the second lowest shear thinning effect. The suspension rheology is in the allowed range for inkjet printing. However, the particles are unstable so that after 72 h the powder completely sediments. Due to the polarity of ACMO there is the assumption, that electrostatic stabilization acts upon the particle, possibly further enhanced by TODA. Steric stabilization by the surfactant is also conceivable, as the surface energy of the fillers attracts the surfactant molecules more than the, although polar but less energetic, ACMO. The reason for faster sedimentation relative to the reference, might lie in the decrease of the polarity of the coated particle to a value lower than in the matrix, as suggested in [187]. Disperbyk-168, Disperbyk-2152 and Disperbyk-2205 show viscosities between 41 mPa·s and 20 mPa·s being slightly worse than TODA. The particle front of the three suspensions sediments by 6 % relative to the surface after 72 h. It is supposed that the polymeric surfactants provide steric and electrostatic stabilization. The compatibility of the polymer coated particles with the matrix is seemingly better than in TODA. On the one hand, an explanation might be, that the polymer coatings have energetic characteristics akin to ACMO. On the other hand, the Disperbyk additives might be not more favorable than TODA but attach less efficiently to the particles thereby rendering them more compatible with the matrix. Disperbyk 22124 shows elevated viscosities between 8552 mPa·s and 109 mPa·s for

shear rates of 2 s^{-1} and 500 s^{-1}, respectively. In addition to that the suspension is not stable for 72 h. Similarly, to TODA, one possible explanation could be hydrophobization of the particle surface due to a strong attachment of the polymer, which results in sedimentation. Furthermore, such polymers are known to bridge several particles at once, which might have contributed to the increase in viscosity due to network formation. Disperbyk-22144 has similar characteristics to TODA when it comes to the viscosity. However, the sedimentation properties are better, with the particle front sinking by 4 % after 72 h. Disperbyk-22146 and Disperbyk-22552 show viscosities between 56 mPa·s and 19 mPa·s with the former being more stable than the latter. Their particle fronts decrease by 3 % and 75 %, respectively. The behavior of the three Disperbyk additives in the suspensions might be again the interplay of their attachment efficiency, surface energy and the resulting energetic compatibility of the polymer particle system to ACMO.

When the ceramic content of the 10 suspensions was increased from 20 vol% to 50 vol%, the preparation was not possible for all but the suspension with TODA due to a sharp viscosity increase. Hence, despite the seemingly insufficient stability further experiments were conducted with this surfactant. **Figure 37c** shows the viscosity of 50 vol% A240 in ACMO with differing TODA concentrations relative to the particle surface. It suggests that the viscosity at a shear rate of 2 s^{-1} and 500 s^{-1} is lowest at 6 mg/m².

4.2.2.2. Acrylate Selection

The stability of suspensions with TODA as a surfactant was shown to be low in ACMO. As discussed in the previous subchapter, polar fluids seemingly tend to increase agglomeration in combination with a certain type of surfactant. A possible explanation is the hydrophobization of particles relative to the matrix. Reducing the matrix polarity can improve the stability of these suspensions. In **Figure 38a** the viscosities of 50 vol% TODA stabilized A240 are shown in IBOA, TPGDA, CTFA and ACMO. At a shear rate of 500 s^{-1} the viscosity of the IBOA based suspension starts at 27043 mPa·s and decreases to 1503 mPa·s. This is caused by the low polarity of the IBOA, which may lead to a strong interaction between the particles. The viscosities of the other monomers are significantly lower. At 2 s^{-1} the TPGDA based suspension has the lowest viscosity followed by the CTFA and ACMO based suspensions. At 500 s^{-1} the ACMO based suspension has the lowest value followed by

the CTFA and then by the TPGDA based suspension. The results allow the interpretation that in TPGDA the TODA contributes to a better energetic compatibility to the matrix. Hence, the low viscosity under quasi static conditions. At elevated shear rate the electrostatic stabilization is better in CTFA and more so in ACMO, which might decrease shear induced viscosity increase. **Figure 38b** shows the respective sedimentation tests of the suspensions with a ceramic concentration of 0.1 vol% and a surfactant concentration of 1000 mg/m². Thereby, the surfactant amount relative to the total volume is the same for the rheological and for the sedimentation experiments. After 72 h the ceramic level in the IBOA based suspensions sinks by 45 % relative to the surface, which again is attributed to the lower polarity of the matrix relative to the coated particle surface. The TPGDA and CTFA suspensions sink by roughly 4 % relative to the surface highlighting their comparatively high stability. The ACMO based suspension sediments completely after 72 h, which may be attributed to the higher polarity of the matrix relative to the coated particle surface. The extent of the sedimentation in the samples might be proportional to the energetic difference of the involved suspension components. Consequently, for further experiments CTFA was chosen as the matrix. **Figure 38c** juxtaposes the relative viscosity of CTFA based suspensions with varying ceramic contents to the empirical Krieger and Dougherty model. The relative viscosity of the suspensions was taken at a temperature of 32°C and a shear rate of 500 s^{-1}. The purpose of the model is to show the relative viscosity as a function of hydrodynamic forces between particles and to visualize an ideal system, where inter-particular forces are not involved. In the investigated suspensions a part of the component interactions can be attributed to van der Waals and electrostatic forces. Furthermore, the TODA, which accounts for 13 vol% relative to the particle volume and which is in part attached to the particle surface, could increase the effective volume fraction of the fillers and raise the viscosity. Consequently, the model suggests that suspensions with a high ceramic content of up to 50 vol% could be viable for inkjet printing in terms of viscosity if a sufficiently low viscous matrix is chosen. Nonetheless, the fact that, despite the utilization of a seemingly efficient surfactant, particle interactions raise the viscosity stronger than predicted, necessitates lower filled inks than theoretically possible. Some of the suspensions, which were prepared by using a hand-held high-power stirrer for 5 min could be filtered with a 5 µm PTFE filter. Filtering of a suspension before printing is a prerequisite to prevent

agglomeration. However, beyond a concentration of 20 vol% filtering was not possible probably due to large agglomerates, which were not broken up during stirring.

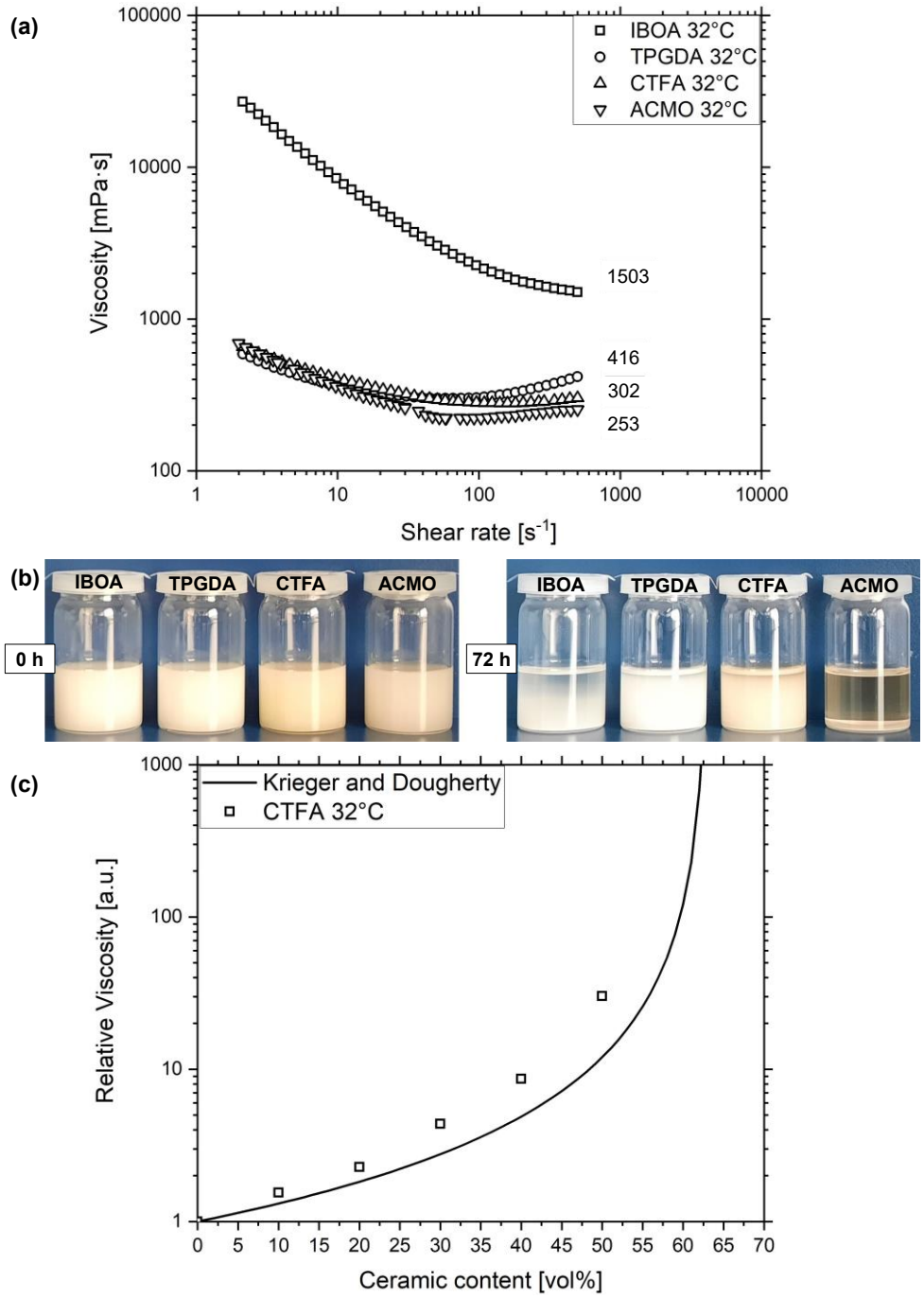

***Figure 38**: (**a**)Viscosity of 50 vol% of A240 in IBOA, TPGDA, CTFA and ACMO as a function of the shear rate. (**b**) Sedimentation of A240 in the monomers with TODA as surfactant. (**c**) Comparison of the theoretical Krieger and Dougherty model with relative viscosity values of CTFA based inks with varying contents of A240 with TODA as a surfactant at a temperature of 32°C and a shear rate of 500 s^{-1}.*

4.2.2.3. Ceramic Attrition

The previous subchapter introduced the preparation CTFA based inks with TODA stabilized A240 using a hand-held high-power stirrer. Yet, the filterable ceramic content was limited to 20 Vol%. Probably large agglomerates were still present in the suspensions after the stirring, which occluded the 5 µm PTFE filter. Consequently, more and longer application of shear forces was necessary to reduce the agglomerate size. In this subchapter the influence of ceramic attrition on the preparation of inkjet inks has been investigated based on three samples. Two were mechanically processed in the PBM for 8 h. The production of the third one just involved the hand-held high-power stirrer as a reference, denoted "as received" in **Figure 39**. The PBM grinded samples differed in their grinding medium. One sample was treated in 2-propanol with the ink being finalized only after the grinding and drying. The preparation of the other sample happened completely in the PBM. To visualize the difference in production method, **Figure 39a** shows the PSD of the three samples, measured using static light scattering. While the reference has a bimodal distribution with one mode being between 1 µm and 2 µm, the other two samples have a mono modal PSD significantly below 1 µm. Hence, the grinding in the PBM has led to a left shift of the PSD by attrition of agglomerates. **Figure 39b** exhibits the viscosity of the three samples as a function of the shear rate. The reference and the 2-propanol sample show similar viscosities between 66 mPa·s and 45 mPa·s at 32 °C. Yet, the value of the CTFA sample, is between 85 mPa·s and 55 mPa·s at 32 °C. Possibly this is the influence of partial TODA degradation due to high mechanical energy exposure during grinding. The viscosity rise of the CTFA sample might be detrimental for inkjet printing. Although, elevating the ink temperature to 60 °C reduces the values to between 34 mPa·s and 22 mPa·s, which is more suitable for ink deposition. **Figure 39c** summarizes preliminary 5 µm PTFE filter tests to probe for ceramic retention. Due to agglomerates the filtration of the reference was not possible. Yet the others two samples showed only minor ceramic reduction in the filtered inks. Although the filter process required a substantial amount of pressure, no occlusion of the filtering took place after filtering 10 ml of sample. Consequently, the smaller PSD of the ground samples is important for the preparation of inkjet inks with high ceramic content. The preparation of the complete ink in the PBM is timesaving yet comes at the cost of viscosity increase compared to a two-step formulation approach.

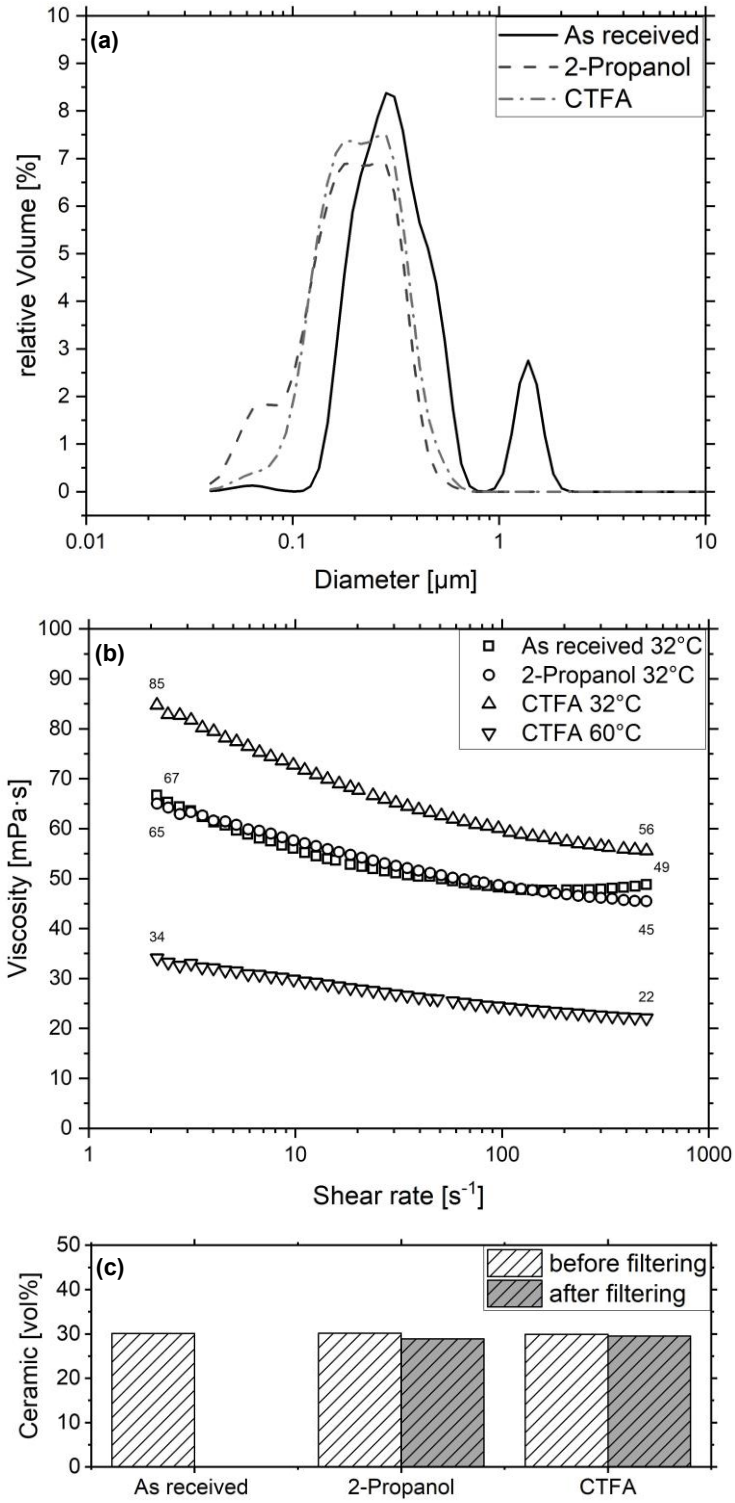

***Figure 39**: (**a**) PSD of 30 vol% A240 in CTFA with 6 mg/m² TODA as surfactant. The suspension "as received" was prepared using a hand-held power stirrer. The other samples were prepared in part or completely in the PBM, with sample "2-propanol" being ground in 2-propanol and sample "CTFA" in CTFA. (**b**) Viscosity of the said suspensions at 32°C and at 60°C in the case of "CTFA". (**c**) Ceramic content of the suspensions before and after filtration with a 5 µm PTFE filter.*

Adjusting the printing temperature to 60 °C, however, could keep the ink printable and suitable for the 3D inkjet printing.

A similar trial with a ceramic ink content of 40 vol% did not yield printable inks. Literature results, which explore highly filled ceramic inks are rare. One example shows the printing of 40 vol% ceramic embedded in a wax, which however uses a significantly larger nozzle and temperatures beyond the possible parameters of the printer used during this thesis [37]. Therefore, for further experiments, during which ink jetting was tested, the one pot preparation method in the PBM was utilized with ceramic contents of 30 vol% in the ink.

4.2.2.4. Ink Characterization

CTFA based inkjet ink with 30 vol% of TODA stabilized A240 fillers had the most suitable properties of the investigated materials. The one pot approach, during which the ink is formulated while grinding in the PBM for 8 h was deemed time efficient because it does not need further manual steps for preparation. In this subchapter, the material characterization regarding ink jetting, curing and thermal conductance took place. The preparation of testing material differed from the previous descriptions by the addition of the photo initiator TPO and thermo initiator LP. It allows the UV initiated polymerization during 3D printing and the thermal post curing after the finalization of the print. The degree of monomer to polymer conversion influences the structural as well as thermal properties of the composites and can be probed using FTIR measurement. **Figure 40a** shows the results of the polymerization degree in dependency of the UV irradiation dose and temperature. Samples irradiated just with UV light, show a steep rise in conversion until an irradiation dose of 5 J/cm². After that the conversion increased only moderately with 65 % of the monomer reacting at 30 J/cm². The subsequent thermal treatment leads to post conversion of the UV polymerized samples. It shows, that even after an UV dose of 1 J/cm² a conversion of 65 % is achievable using thermal post treatment. As a short UV exposure time can accelerate the 3D inkjet printing process, further investigations used the parameter of 1 J/cm² with a thermal post treatment for 12 h at 100 °C. Beside the polymerization properties the ability of the ink to be jetted onto the substrate with an acceptable degree of precision is of further importance for the additive process. This was investigated using the drop watcher of the inkjet printer, which enabled the monitoring of the drop

position as a function of flight time (**Figure 40b)**. It shows that after an initial formation, the ink develops a long ligament, which extends up to 800 µm. Despite the length, no observable disintegration of the ligament occurs within the timeframe of 120 µs. A disintegration could yield satellite droplets, which would worsen the print quality of a manufactured component by leading to secondary material deposition in unwanted areas of the substrate. The velocity of the drop, deduced from **Figure 40b**, is 10 m/s. As introduced in chapter 2, the value lies in an acceptable range for inkjet printing. Together with the Weber, Reynolds and Ohnesorge number of 141.2, 19.6 and 0.6, respectively, it underlines that the ink can be ejected well from the nozzle, is not too viscous, has no tendency for satellite droplets and does not form splashes upon impact onto the substrate. The droplet has a weight of 17 ng and a volume of 8.9 pl, which is also in the range typically suggested for inkjet materials. At 80 µs the trajectory of the droplet is visibly altered, which could be attributed to the high ceramic filler load and might negatively impact the printing performance. A printed demonstrator of rectangular columns on a printed base, shown in **Figure 40c**, exhibits deviations from the intended design presented in **Figure 30**. The printed columns are irregular, which might stem from the described trajectory alterations. The thermal conductivity of the material measured using the laser flash method yielded a value of 0.55 W/(m·K). The increase is roughly threefold relative to the pure polymer with a value of 0.17 W/(m·K). The result is in agreement with values from literature [228,252,253]. Higher values can be achieved, as described in subchapter 3.3.4, by increasing the ceramic content. The current results, however, hint at challenges to achieve that goal in solvent free inks. The limitations on ink viscosity and on the size of the filling material seem to be too severe. Due to the given findings, solvent-based inks are going to be investigated in the next chapter, with the aim to further increase the ceramic content in inks without compromising the requirements of inkjet printing.

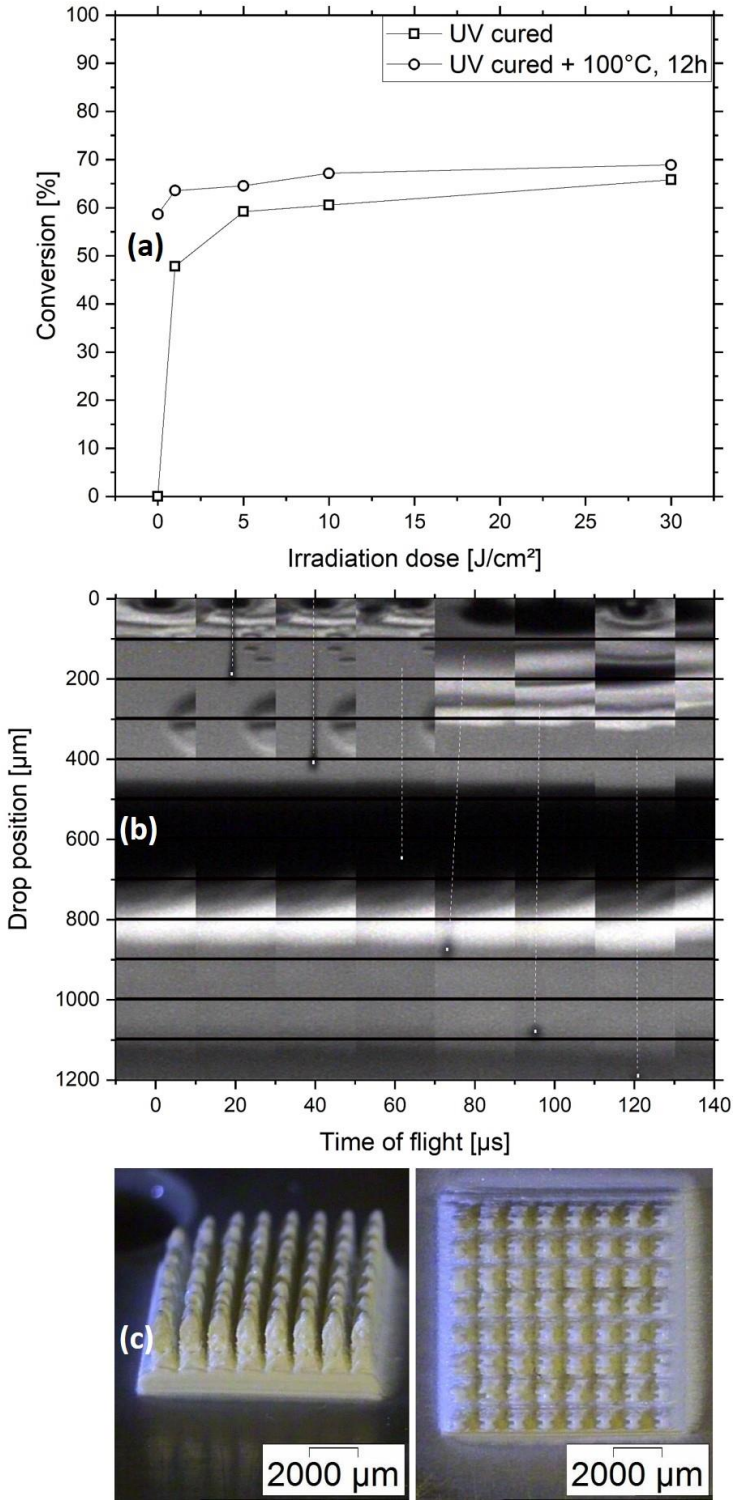

***Figure 40**: (**a**) Conversion of 30 vol% of A240 in CTFA with 6 mg/m² TODA as surfactant. The conversion is depicted as a function of the irradiation dose. The samples were either just UV cured, or UV cured and thermally treated at 100°C for 12 h. (**b**) Drop position of jetted ink as a function of the time. (**c**) Printed columns on a rectangular base resembling a heat sink for the purpose of demonstration.*

5. Solvent Based Inks

The previous section saw the investigation of solvent free ceramic inks. The presented formulations showed limitations when it came to printing thermally conductive composites. As an alternative path towards higher filling grades solvent-based inks were studied. This chapter is based, in part, on results published in [254]. The experiments included the development of an alternative way of ceramic stabilization via chemical functionalization of the particles with a silane. A selection of suitable volatile solvents allowed ink dilution. The variation of the ratio between filler and UV active components in the ink permitted the examination of the ceramic content change and its influence on the composite. Finally, the resulting ink was assessed by testing the printing properties, jetting quality and stability during usage and storage.

5.1. Experimental Section

This chapter describes the steps and parameters utilized to investigate the four topics mentioned above. It introduces the materials and follows the preparation of samples, their characterization, and the interpretation of results.

5.1.1. Materials

The materials used in this chapter are summarized in **Table 13** and **Table 14**. The SSA of the ceramic fillers was measured using the Gemini VII 2390 (Micromeritics, Norcross, Georgia, USA), which is based on the BET method introduced in subchapter 3.4.3. Thereby, degassing the sample powders to vacuum followed by nitrogen flooding enabled measurement of the adsorption/desorption isotherms for the calculation. The ceramic powders and the organic materials were used as received without further purification.

***Table 13**: Ceramic materials utilized during the experiments done in this chapter. All materials have been used as received.*

Product name	Chemical name	SSA [m²/g].	Supplier
CT3000SG (A240)	Al_2O_3	6.42	Almatis
TEC170[a]	Al_2O_3	8.71	Tecnan

[a] The product does not have a product name since it was an experimental batch produced in scope of the EU project DIMAP. The shown name is an internal designation.

***Table 14**: Organic materials utilized during the experiments done in this chapter. All materials have been used as received.*

Chemical name	CAS. No.	Supplier
3 - (trimethoxysilyl)propylmethacrylate (MPS)	2530-85-0	Merck
Ethanol	64-17-5	Carl Roth
2-propanol	67-63-0	Carl Roth
Genomer 4247	-	Rahn
Diphenyl(2,4,6-trimethylbenzoyl)phosphine oxide (TPO)	75980-60-8	TCI
Dilauroyl peroxide (LP)	105-74-8	Merck
Hexyl acetate (HexylAc)	142-92-7	Merck
Propylene glycol monomethyl ether acetate (PGMMEA)	108-65-6	Merck
Dipropylene glycol monomethyl ether (DPGMME)	34590-94-8	Merck
Diethylene glycol monoethyl ether (DEGMEE)	111-90-0	Carl Roth
Diiodomethane	75-11-6	Merck

5.1.2. Ceramic Functionalization

During grinding and homogenization of the Al_2O_3 submicron particles A240 in the PBM (PM 400, Retsch GmbH, Haan, Germany), 3 - (trimethoxysilyl)propylmethacrylate (MPS) functionalized the particles in a hydrolysis and condensation reaction. As grinding equipment two 125 ml steel beakers with $YZrO_2$ inner cladding and $YZrO_2$ grinding balls with a diameter of 2 mm were used. The mechanical treatment involved the preparation of five samples by adding 50 g of A240, 11.53 g of water, 11.53 g of ethanol, 220 g of grinding balls and a varied amount of MPS (**Table 15**) into each beaker and grinding them for 8 h at 200 rpm. As the time elapsed, the addition of another 20 g ethanol and further grinding for 5 min at 200 rpm enabled easier retrieval of the samples from the beakers. A hand-held sieve separated the homogenized suspension from the grinding balls. The samples were dried via rotary evaporation (Laborota 4003 digital, Heidolph Instruments, Schwabach, Germany) with 70 ml of sample at a time. In the beginning the bath temperature of the device was 50 °C and the pressure 200 mbar. After 100 min the pressure was changed to 30 mbar for 20 min to remove the remaining water. A mortar and pestle allowed the homogenization of each dried sample.

***Table 15**: Added amount of MPS into the PBM for functionalization and homogenization of A240, shown as absolute values and as values relative to the particle surface area.*

Sample	MPS [g]	MPS [mg/m²]
Sil0-A240	0	0
Sil1-A240	0.32	1
Sil2-A240	0.64	2
Sil4-A240	1.28	4
Sil6-A240	1.94	6

TGA measurements (DSC/TGA 400, Netzsch GmbH, Selb, Germany) of 200 mg of the powders enabled assessment of the MPS binding efficiency. The heating rate was 10 K/min, the target temperature 1200 °C, the hold time 30 min and the cooling rate 10 K/min. The minima of the resulting curves were used to calculate the amount of the attached silane according to the following:

$$MPS_{coating}[mg/m^2] = \frac{MPS_{hyd}\ [mg]}{A240\ [m^2]} \tag{53}$$

The assumption was that the MPS completely hydrolyzed ($MPS_{hyd}\ [mg]$) during the attachment so that for the computation of the attachment density the mass of the hydrolyzed molecule is divided by the surface area of the A240. Consequently, the transformation of the term enables the use of the TGA data and the SSA of the A240 being 6.4 $[m^2/g]$.

$$MPS_{coating}[mg/m^2] = \frac{MPS_{hyd}\ [wt\%] \cdot 1000\ [mg/g]}{A240\ [wt\%] \cdot\ 6.4\ [m^2/g]} \tag{54}$$

The term $MPS_{hyd}\ [wt\%]$ is the silane weight relative to the TGA measured sample weight and is described as:

$$MPS_{hyd}\ [wt\%] = Org.[wt\%] + Si\ [wt\%] \tag{55}$$

where $Org.[wt\%]$ is the weight percentage of the organic components of the silane and *Si* [*wt%*] is the weight percentage of the silicon in the molecule.

The $Org.\,[wt\%]$ term can be portrayed as follows:

$$Org.\,[wt\%] = Org.H_2O\ [wt\%]\ -\ H_2O\ [wt\%] \tag{56}$$

where $Org.H_2O\ [wt\%]$ is the weight percentage of the silane derived organic components as well as the physisorbed and chemisorbed water from the surface of the functionalized particle. It is the weight loss recorded during TGA. For the calculation an assumption was made, that the MPS bound silicon does not evaporate with the organic components during thermal degradation. Instead, for the sake of simplicity, silicon was considered to remain in elemental form at the surface of the particles, after the complete decomposition of the silane. The determination of the water amount in the loss results from measuring the PBM ground powder without MPS addition (Sil0- A240). At 1200°C the sample turns into $b{-}Al_2O_3\ [wt\%]$, which is alumina with a strongly reduced amount of surface bound water. Its density approximately resembles the density of bulk alumina. The relation between the weight of the evaporated water and the alumina is (1.11/98.89). The expectation was that this relation remains approximately constant for all silanized samples so the following equation was established:

$$H_2O\ [wt\%] = b{-}Al_2O_3\ [wt\%] \cdot \frac{1.11}{98.89} \tag{57}$$

The $b{-}Al_2O_3\ [wt\%]$ differs from $Inorg.\,[wt\%]$, which is the remaining part after the evaporation of the volatile components, by the amount of silicon:

$$b{-}Al_2O_3\ [wt\%] = Inorg.\,[wt\%] - Si\ [wt\%] \tag{58}$$

To calculate the $Si\ [wt\%]$ the relation to $Org.\,[wt\%]$ is established by:

$$Org.\,[wt\%] = \frac{169\ [g/mol]}{28\ [g/mol]} \cdot Si\ [wt\%] \tag{59}$$

where 169 [*g/mol*] is the molar mass of the organic components in the particle bound hydrolyzed MPS molecule and 28 [*g/mol*] is the molar mass of the silicon in the molecule.

The equations 57, 58 and 59 are inserted into equation 56:

$$\frac{169\ [g/mol]}{28\ [g/mol]} \cdot Si\ [wt\%] = \ Org.H_2O\ [wt\%] - (Inorg.[wt\%] - Si\ [wt\%]) \cdot \frac{1.11}{98.89} \tag{60}$$

The solution for $Si\ [wt\%]$ results in:

$$Si\ [wt\%] = \frac{Org.H_2O\ [wt\%] - \frac{1.11}{98.89} \cdot Inorg.[wt\%]}{\frac{169\ [g/mol]}{28\ [g/mol]} - \frac{1.11}{98.89}} \tag{61}$$

The insertion of equation 59 and equation 61 into equation 55 leads to:

$$MPS_{hyd}\ [wt\%] = (\frac{169\ [g/mol]}{28\ [g/mol]} + 1) \cdot \frac{Org.H_2O\ [wt\%] - \frac{1.11}{98.89} \cdot Inorg.[wt\%]}{\frac{169\ [g/mol]}{28\ [g/mol]} - \frac{1.11}{98.89}} \tag{62}$$

The values for $b - Al_2O_3\ [wt\%]$ and the water weight percentage on as received A240 describe the weight percentage of A240:

$$A240\ [wt\%] = b - Al_2O_3\ [wt\%] + b - Al_2O_3\ [wt\%] \cdot \frac{0.77}{99.23} \tag{63}$$

Equation 58 is inserted into equation 63:

$$A240\ [wt\%] = Inorg.[wt\%] - Si\ [wt\%] + (Inorg.[wt\%] - Si\ [wt\%]) \cdot \frac{0.77}{99.23} \tag{64}$$

By inserting equation 62 and equation 64 into equation 54 it was possible to calculate $MPS_{coating}[mg/m^2]$ for every sample in **Table 15** and to set it in relation to the added MPS.

Subsequently, the investigation of the silanized samples using static light scattering (LS230, Beckman Coulter, Brea, California, USA) took place to acquire the PSD. Subchapter 3.4.2 shows a description of the method. The sample preparation involved dispersion of 0.1 g of powder in 5 g 2 - propanol and ultrasonication for 15 min. Immediately after, each suspension was added drop vise into the device until the PIDS detector reached 45 % and the measurement was started.
STEM allowed the determination of A240 and silanized A240 (Sil6-A240) images using a Talos F200i S/TEM (FEI Company, Hillsboro, Oregon, USA) in imaging mode and for energy-dispersive X-ray spectroscopy (EDX) detection. The samples preparation was done by dipping a carbon coated copper grid with 400 mesh (Plano GmbH, Wetzlar, Germany) directly into the powder samples, shaking the excess material from the grid and inserting it into the device.

Dispersions of the silanized particles enabled the quality assessment of silane coating in ink. The preparation involved the mixing of diethylene glycol monoethyl ether (DEGMEE), Genomer 4247, TPO and LP according to weight percentages shown in **Table 16**. After combination of the components, homogenization with a hand-held high-power stirrer (Ultra Turrax T10, IKA-Werke, Staufen im Breisgau, Germany) took place at 14450 rpm for 5 min. Afterwards ultrasonication (Sonorex Super RK103H, Bandelin electronic GmbH and Co. KG, Berlin, Germany) further homogenized the suspension for 15 min with a power of 560 W.

Rheological characterization of the inks took place with a Bohlin CVO dynamic rheometer (Malvern Instruments, Malvern, Great Britain) using a cone plate arrangement. The utilized aluminum cone had a diameter of 60 mm and an angle of inclination of 2°. The measurement temperature was 32°C and the shear rate varied from 2 s^{-1} to 500 s^{-1}.

As a pretest for inkjet printing ceramic inks were filtered with a 5 µm PTFE filter. The as prepared and the filtered suspensions saw investigation in the TGA to assess the ceramic loss during filtration. The analysis used 20 mg of the suspensions with a rate of 10 K/min, a target temperature of 900 °C, a hold time of 15 min and a cooling rate of 10 K/min.

***Table 16**: Compositions of solvent-based materials for the investigation of the silane coating influence. The ceramic content is 20 vol% in all materials.*

Composition	M-0 [wt%]	M-1 [wt%]	M-2 [wt%]	M-4 [wt%]	M-6 [wt%]
Sil0-A240	49.2	0	0	0	0
Sil1-A240	0	49.5	0	0	0
Sil2-A240	0	0	49.6	0	0
Sil4-A240	0	0	0	49.9	0
Sil6-A240	0	0	0	0	50.5
DEGMEE	37.0	37.1	37.1	37.1	37.1
Genomer 4247	13.2	12.9	12.8	12.6	12.0
TPO	0.40	0.39	0.38	0.38	0.36
LP	0.13	0.13	0.13	0.13	0.12

5.1.3. Ink Solvent

This subchapter deals with the preparation of samples for volatile solvents investigation in ceramic inks and their influence. Since this set of experiments was done in the scope of the EU project DIMAP, the project related fillers TEC170 had to be used instead of A240. Therefore, materials were prepared composed of silanized TEC170 particles (Sil6-TEC170), MPS, hexyl acetate (HexylAc), propylene glycol monomethyl ether acetate (PGMMEA), dipropylene glycol monomethyl ether (DPGMME), DEGMEE, Genomer 4247, TPO and LP in a weight percentage given in **Table 17**. The preparation of Sil6-TEC170 happened in the same manner as Sil6-A240. The utilization of TEC170 fillers was part of the project DIMAP, which was the initiating basis for this PHD thesis. The functionalization involved the addition of 50 g of TEC170, 11.53 g ethanol, 11.53 g water, 1.94 g MPS and 221 g of $YZrO_2$ grinding balls into $YZrO_2$ clad 125 ml steel beakers and grinding the components for 8 h at 200 rpm. For better retrieval, the finished suspension was diluted with 20 g of ethanol, ground for further 5 min and separated with a sieve from the grinding balls. The drying of the samples took place in the Laborota 4003 digital rotary evaporator with a temperature of 50 °C at 200 mbar for 100 min and at 30 mbar for 20 min. The attachment efficiency analysis via TGA and the consequent calculations were done according to the description shown in the previous subchapter following the equations 53 to 64.

Table 17 shows the ceramic inks M-I to M-IV, the formulation of which involved the homogenization with the Ultra Turrax at 14450 rpm for 5 min with subsequent ultrasonication at a power of 560 W for 15 min. After preparation M-III and M-IV were filtered with a 5 µm PTFE filter. Filtering of M-I and M-II was not possible. Therefore, the samples were left standing overnight for 12 h with the additionally added MPS and filtering was done on the next day. After that, the inks, the four volatile solvents and Genomer 4247 were characterized with the dynamic rheometer at 32 °C and 60 °C with a shear rate ranging from 2 s^{-1} to 500 s^{-1}. Furthermore, surface tension measurements of the mentioned materials utilized image analysis at a pendant drop (Krüss DSA 100, KRÜSS GmbH, Hamburg, Germany). For the method, the chosen fluid density was 1.3 (g/cm^3) for all the samples. The pendant drop volume was 3 µl and the lighting adjustment of the focus assistant value was 60. The magnification of the camera pointed to the needle tip, which was one third of the whole image while the drop occupied 50 % of the total image.

***Table 17**: Compositions of solvent-based inks with the solvents HexylAc, PGMMEA, DPGMME and DEGMEE. After evaporation of the solvents the ceramic content of the remaining composites is 50 vol% for all inks.*

Composition	M-I [wt% (vol%)]	M-II [wt% (vol%)]	M-III [wt% (vol%)]	M-IV [wt% (vol%)]
Sil6-TEC170	51.0 (20.3)	51 (21.7)	51.6 (21.9)	51.6 (22.4)
MPS	1.2 (1.7)	1.2 (1.9)	0 (0)	0 (0)
HexylAc	36.4 (62.4)	0 (0)	0 (0)	0 (0)
PGMMEA	0 (0)	36.4 (59.8)	0 (0)	0 (0)
DPGMME	0 (0)	0 (0)	36.9 (61.5)	0 (0)
DEGMEE	0 (0)	0 (0)	0 (0)	36.9 (60.5)
Genomer 4247	11.0 (14.9)	11.0 (15.9)	11.1 (16.0)	11.1 (16.4)
TPO	0.33 (0.44)	0.33 (0.47)	0.33 (0.47)	0.33 (0.48)
LP	0.11 (0.18)	0.11 (0.19)	0.11 (0.19)	0.11 (0.20)

Ink jetting tests of the materials M-I to M-IV utilized a laboratory inkjet printer (DMP 2831, Fujifilm Dimatix Inc., Lebanon, New Hampshire, USA). The filtered material transfer into the ink reservoir happened via a syringe followed by attaching a 10 pl DMP print head. After the cartridge and cleaning pad installation into the printer, an initial cleaning program, consisting of 2 s of nozzle purging and 2 µs of jetting onto the pad, conditioned the nozzles for the process. The movement of the printhead onto the cleaning pad was omitted because, according to practical experience, this contributes to nozzle clogging. After the automated cleaning procedure, the cartridge

was unmounted, and the nozzles were cleaned manually with a precision tissue soaked with ethanol. Upon remounting the cartridge, the jetting tests were started, with a print head temperature of 32 °C. The printer enables the observation of the ink morphology using its drop watcher. It also allows the measurement of the ejected drop weight using a built-in software-based tool. During that, ten nozzles jet 250000 drops into a pre-weighted pan and the drop weight is divided by the total number of droplets. The tool was used for M-I to M-IV before and after a printing time of 18 min, where 4 layers of a test image (**Figure 41**) were printed onto a substrate.

The substrate wetting evaluation of the samples involved the printing of 5-layer 10 mm² square test images with a drop spacing of 20 µm onto PDMS and comparing the outcome. Furthermore, for surface energy assessment of M- II, M- III and M- IV 10 layers of the same test image were printed with a drop spacing of 40 µm onto a PDMS substrate, dried in an oven at 200 °C for 2 min and investigated via Krüss DSA100 contact angle measurement. The analysis used bare PDMS substrate as a reference. During the measurement 3 µl of water were deposited onto samples and reference. The image detection was adjusted for a sessile drop, the value of the focusing assistant was kept at about 60 and the magnification was manipulated so that the deposited drop was 50 % of the total image. For fitting of the drop shape and calculating the contact angle the tangential method was used. The same procedure was repeated with diiodomethane. The method of Fowkes allowed the surface energy calculation of both substrates. For the visualization of the changes in the wetting behavior, contact angle measurements with the ink M-IV were conducted in the same manner as for the previous two liquids whereby the fluid density was set to 1.3 g/cm³. During filtering and inkjet printing the ceramic content in the inks can decline by the interaction of the ceramic particles with the filter material or the printhead nozzle material. Therefore, TGA measurements were performed before and after filtration and after printing. During each of the steps three 20 mg subsamples of each sample were measured with a heating rate of 10 K/min, a target temperature of 900 °C a hold time of 15 min and a cooling rate of 10 K/min.

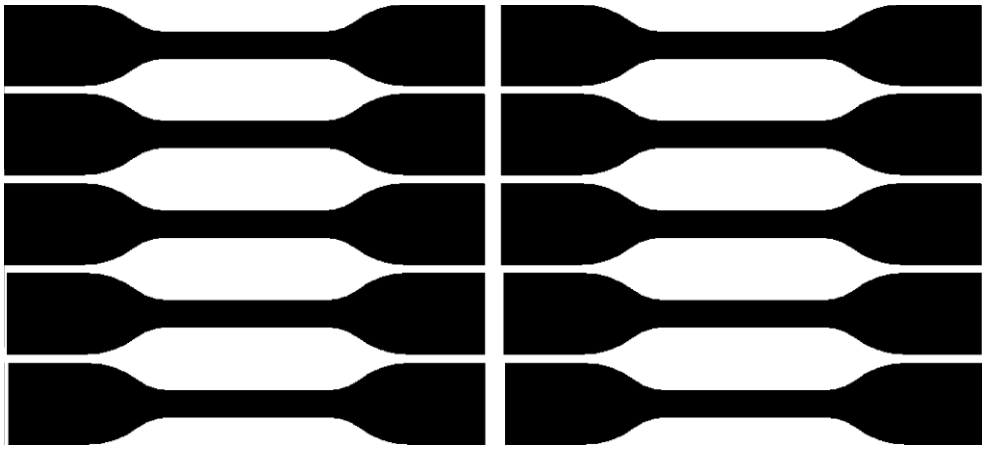

***Figure 41**: Test image for the investigation of the drop weight before and after a printing time of 18 min.*

5.1.4. Ink Ratio

The ratio between the ceramic fillers and the UV active organic component was varied in solvent-based inks which influenced the ceramic content in the final composite after evaporation of the solvent. Samples were prepared by combining the components Sil6- A240, DEGMEE, Genomer 4247, TPO and LP according to **Table 18**, homogenizing them with the hand-held power stirrer at 14450 rpm for 5 min and ultrasonicate them with a power of 560 W for 15 min. The prepared samples were filtered with a 5 µm PTFE filter. Their dynamic viscosity was investigated at 32°C and at 60°C in a shear rate range between 2 s^{-1} and 500 s^{-1}. Their surface tension was measured with the Krüss DSA100 in pended drop conformation. A fluid density of 1.3 g/cm^3 was set for all the samples. The pendant droplet was created by producing 3 µl of the liquid from the needle tip. The magnification and the focus of the camera were adjusted so that the drop occupied roughly 50 % of the image and the contours formed a sharp contrast to the illuminated background. The lighting of the device was adjusted so that the focusing assistant showed a value of 60. Afterwards, the shape of the droplet was automatically fitted, and the surface tension evaluated.

***Table 18**: Compositions of solvent-based inks with a varying ratio between Sil6- A240 and Genomer 4247. After evaporation of the solvent DEGMEE the ceramic content of the remaining composites is 50 vol% (M-7), 60 vol% (M-8), 65 vol% (M-9) and 70 vol% (M-10).*

Composition	M-7 [wt% (vol%)]	M-8 [wt% (vol%)]	M-9 [wt% (vol%)]	M-10 [wt% (vol%)]
Sil6- A240	50.9 (22.2)	51.1 (22.2)	51.22 (22.16)	51.3 (22.2)
DEGMEE	36.5 (59.5)	40.9 (66.3)	42.5 (68.8)	44.0 (71.1)
Genomer 4247	12.1 (17.6)	7.7 (11.1)	6.0 (8.7)	4.5 (6.5)
TPO	0.36 (0.52)	0.23 (0.33)	0.18 (0.26)	0.14 (0.19)
LP	0.12 (0.22)	0.08 (0.14)	0.06 (0.11)	0.05 (0.08)

For the measurement of the thermal conductance specimens have been manufactured. On the one hand, the four samples M-7 to M-10 have been printed according to the BMP template depicted in **Figure 42**. As substrate aluminum was used, which was coated with a 100 µm thick PDMS layer using a hand-held high precision film applicator and curing the PDMS for 30 min at 60 °C. After an initial 10 layers of ink with a drop spacing of 40 µm and solvent drying at 200 °C for 2 min between layers, printing was done with a drop spacing of 20 µm and drying after each second layer until a height of 1 mm was reached.

On the other hand, three samples of casted composites have been prepared using the same BMP template, height and PDMS covered substrate with a composition described in **Table 19**. This production method was faster than printing and thermal measurement values were needed for a ceramic content of 0 vol%, 10 vol% and 30 vol%.

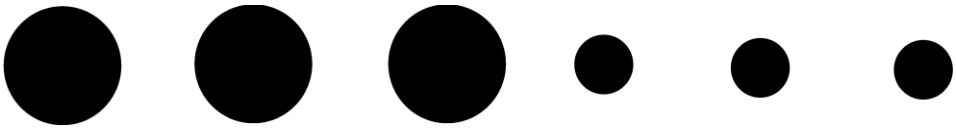

***Figure 42**: BMP template for the casting and inkjet printing of specimens for the thermal conductance measurement.*

Their manufacturing was done by producing plates in layer-by-layer fashion using a hand-held high precision film applicator. The layer thickness was 100 µm and after each layer a waiting time of 20 min was applied to let the 2-propanol evaporate from the samples until a total layer thickness of more than 1 mm was achieved. Afterwards the needed specimens were ground out of the plates using sandpaper.

The influence of the filtration and printing on the ceramic content of sample M-7 to M-10 was investigated in the TGA before and after printing the filtered inks. Three times 20 mg of the liquid not yet filtered ink and 100 mg of the solid filtered and printed ink were measured. The heating rate was 10 K/min, the target temperature 900 °C, the hold time 15 min and the cooling rate 10 K/min.

***Table 19**: Composition of the samples C-0, C-10 and C-30 for the preparation of casted composites. The ceramic content of the finished samples is 0 vol%, 10.1 vol%, 30.8 vol% and 52.0 vol%, respectively.*

Composition	C-0 [wt% (vol%)]	C-10 [wt% (vol%)]	C-30 [wt% (vol%)]
Sil6-TEC170	0.0 (0.0)	24.9 (8.4)	51.2 (25.8)
2-propanol	0.0 (0.0)	14.8 (23.7)	10.7 (23.3)
Genomer 4247	96.15 (96.01)	58.0 (65.2)	31.8 (48.8)
TPO	2.88 (2.83)	1.74 (1.94)	0.95 (1.45)
LP	0.96 (1.16)	0.58 (0.80)	0.32 (0.60)

As described in the theoretical section, for the assessment of the thermal conductance three material related values are needed, the density, the thermal capacitance, and the thermal diffusivity. The density of the samples was investigated and calculated via the Archimedes method using. Thereby the samples were weighted in air and in 2- propanol. The temperature of the 2-propanol was measured to be 22°C with a density of 0.78 g/cm³.

$$\rho\ [g/cm^3] = \frac{m_{air} \cdot \rho_{2p}}{m_{air} - m_{2p}} \tag{65}$$

The thermal capacity was measured using DSC (DSC 204 F1 Phoenix, NETZSCH-Gerätebau GmbH, Selb, Germany). Three specimens per sample have been measured. The thermal diffusivity was assessed via the LFA (LFA 447, NETZSCH-Gerätebau GmbH, Selb, Germany). In total two specimens per sample have been measured. Each measurement was repeated 7 times with a 1000 µs laser pulse.

The mechanical properties of the samples M-7 to M-10 have been investigated using the tensile test (Z010 universal testing machine, Zwick/Roell GmbH & Co. KG, Ulm, Germany). The characterization was in part conducted according to the DIN EN ISO 527-2 type A5 norm, with the exception that the thickness of the tensile specimens was

not 2 mm but 0.5 mm. The printing of the specimens was done onto an aluminum substrate which was coated with a 100 µm PDMS layer using a hand-held high precision film applicator. Prior to volumetric printing, 10 layers of ink were deposited with a drop spacing of 40 µm to increase the surface energy. Between each layer the volatile solvent was evaporated in an oven at 200°C for 2 min. Subsequently, printing was continued with a drop spacing of 20 µm whereby after two layers the volatile solvent was dried. After 80 printed layers the specimen reached a height of roughly 0.5 mm. The thickness and width in the gauge region were measured three times each with a caliper gauge. For each of the samples a minimum of three specimens was produced whereby one specimen was printed at a time using the BMP template shown in **Figure 43**. The tensile tension was applied to the specimens with an elongation rate of 1 (mm/min) until failure. The recording of the occurring forces was done with a 2.5 kN load cell.

***Figure 43**: BMP template for the inkjet printing of specimens for mechanical measurements via tensile test.*

5.1.5. Ink Characterization

This chapter should investigate proper printing parameters for ink M-7 involving UV irradiation between layers as opposed to one single thermal polymerization of the completed component at the end of printing. As template again the BMP image from **Figure 43** was chosen. Five samples were investigated, for which the printing parameters aluminum substrate and PDMS coating thickness, the drop spacing, the UV irradiation dose and irradiation time were varied according to **Table 20**. For all samples, initially 10 layers were deposited with a drop spacing of 40 µm to increase the surface energy of the substrate. The subsequent drop spacing was adjusted as shown in **Table 20**. UV irradiation was done following the drying.

***Table 20**: Samples for the investigation of curling in printed components using Ink M-7.*

Sample	Substrate thickness [mm]	PDMS [µm]	Drop spacing [µm]	Irradiation dose [J/cm²]	Irradiation time [s]
1	5	500	20	0	0
2	5	500	20	5	10
3	5	500	30	10	20
4	5	500	30	30	60
5	6	100	20	0.5	1

For the measurement of the conversion efficiency ten samples have been printed using M-7 on 10 mm² polished silicon pieces. For each sample one layer of ink has been printed with a drop spacing of 20 µm and dried at 200°C for 2 min. The samples were then UV irradiated, and/or thermally cured at 100°C for 12 h according to parameter changes depicted in **Table 21**. The conversion efficiency was measured using the FTIR (Excalibur series, Bio Rad, Hercules, California, USA). In rapid scan mode 64 scans have been conducted between 750 cm^{-1} and 4000 cm^{-1} with a sensitivity of 16. A constant nitrogen flow of 11 l/min has been kept during the measurement. As initial background measurement a bare polished silicon piece was used. As described in the theoretical section the relation between the carbonyl peak and the vinyl peak was utilized to calculate the conversion.

***Table 21**: Printed and dried samples of M-7 for conversion efficiency measurement. The samples were UV irradiated and/or thermally cured at 100°C.*

Sample	Irradiation dose [J/cm²]	Thermal curing [h]
6	0	0
7	1	0
8	5	0
9	10	0
10	30	0
11	0	12
12	1	12
13	5	12
14	10	12
15	30	12

The development of the drop morphology after ejection from the print head nozzle was examined in the drop watcher of the Dimatix inkjet printer. The stroboscope camera

was set to picture mode and the time of image recording was changed from 0 to 140 µs in 20 µs intervals.

The drop weight of the ink was investigated in dependency of the idle time at 0 min, 1 min, 5 min, 10 min and 20 min by using the printer-based function of drop weight assessment. Thereby, 200000 drops are jetted into a pan of known weight to calculate the average drop weight. Similarly, the average drop weight was measured in dependency of the print head temperature which was set to be 32 °C, 40 °C, 50 °C and 60 °C.

Investigations of the ink stability were done in dependency of the storage time which was chosen to be 1 d, 3 d, 7 d and 14 d. After the said intervals, the ink was redispersed by vigorously shaking. A 20 mg subsample was then examined for its ceramic content in the TGA.

Finally, a demonstrator was printed with a square base of 1 mm in height and columns on top of it with the same height (**Figure 44**). For the printing, again 10 ground layers with a drop spacing of 40 µm have been printed to increase the surface energy of the substrate. After each layer, the solvent was evaporated at 200 °C for 2 min. Afterwards, volumetric printing was conducted by printing layers with a drop spacing of 20 µm. After every second layer the solvent was evaporated in the described manner.

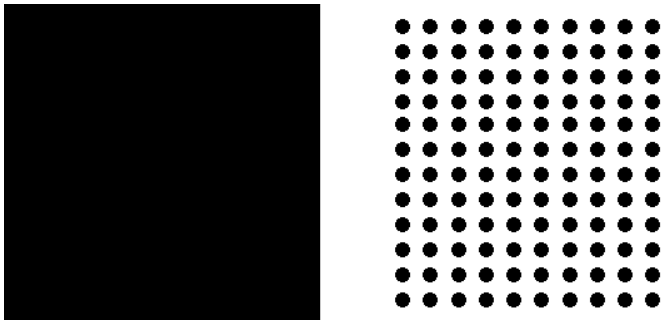

***Figure 44**: BMP template for the inkjet printing of a heat sink as a demonstrator. On the left the square base is depicted. On the right are the columns situated on top of the base.*

5.2. Results and Discussion

The chapter 4 dealt with solvent free ceramic inks for 3D inkjet printing. Among others the goal was the formulation of an ink for the printing of thermally conductive composites. Yet, the ceramic content could not be increased to significantly more than 30 vol%, which did not allow the thermal conductivity to exceed 0.55 W/(m·K). This subchapter shows the results of experiments, introduced in 5.1, which increases the ceramic content of printed composites relative to the solvent free inks by employing volatile solvents. The investigation results are presented in the four subordinate subchapters “Ceramic Functionalization”, “Ink Solvent”, “Ink Ratio” and “Ink Jetting”.

“Ceramic Functionalization” examines the chemical binding of the small molecule MPS on the surface of A240 Al_2O_3 submicron particles. It answers the question, which quantity of MPS is necessary to stabilize the ceramic in the solvent-based matrix. “Ink solvent” investigates the suitability of four volatile solvents to supplement the stabilization properties of MPS and enable sufficient inkjet capabilities. “Ink Ratio” adjusts the Genomer 4247 concentration relative to the ceramic content, which yields different filling grades in the inkjet-printed composites, once the solvent is evaporated and the ink cured. It should show, what is the maximum viable ceramic concentration in 3D inkjet-printed composites. When the optimum ink composition is found “Ink Jetting” shows the ink performance during printing tests, which culminates in the printing of patterns and objects for demonstration. The subchapter describes samples, introduced in 5.1, which are summarized in the following **Table 22** to allow a better overview.

***Table 22**: Overview of all prepared solvent-based inks and casting composites M-0 to C-30.*

Composition	M-0 [wt%]	M-1 [wt%]	M-2 [wt%]	M-4 [wt%]	M-6 [wt%]
Sil0-A240	49.2	0	0	0	0
Sil1-A240	0	49.5	0	0	0
Sil2-A240	0	0	49.6	0	0
Sil4-A240	0	0	0	49.9	0
Sil6-A240	0	0	0	0	50.5
DEGMEE	37.0	37.1	37.1	37.1	37.1
Genomer 4247	13.2	12.9	12.8	12.6	12.0
TPO	0.40	0.39	0.38	0.38	0.36
LP	0.13	0.13	0.13	0.13	0.12

Composition	M-I [wt% (vol%)]	M-II [wt% (vol%)]	M-III [wt% (vol%)]	M-IV [wt% (vol%)]
Sil6-TEC170	51.0 (20.3)	51 (21.7)	51.6 (21.9)	51.6 (22.4)
MPS	1.2 (1.7)	1.2 (1.9)	0 (0)	0 (0)
HexylAc	36.4 (62.4)	0 (0)	0 (0)	0 (0)
PGMMEA	0 (0)	36.4 (59.8)	0 (0)	0 (0)
DPGMME	0 (0)	0 (0)	36.9 (61.5)	0 (0)
DEGMEE	0 (0)	0 (0)	0 (0)	36.9 (60.5)
Genomer 4247	11.0 (14.9)	11.0 (15.9)	11.1 (16.0)	11.1 (16.4)
TPO	0.33 (0.44)	0.33 (0.47)	0.33 (0.47)	0.33 (0.48)
LP	0.11 (0.18)	0.11 (0.19)	0.11 (0.19)	0.11 (0.20)

Composition	M-7 [wt% (vol%)]	M-8 [wt% (vol%)]	M-9 [wt% (vol%)]	M-10 [wt% (vol%)]
Sil6-A240	50.9 (22.2)	51.1 (22.2)	51.22 (22.16)	51.3 (22.2)
DEGMEE	36.5 (59.5)	40.9 (66.3)	42.5 (68.8)	44.0 (71.1)
Genomer 4247	12.1 (17.6)	7.7 (11.1)	6.0 (8.7)	4.5 (6.5)
TPO	0.36 (0.52)	0.23 (0.33)	0.18 (0.26)	0.14 (0.19)
LP	0.12 (0.22)	0.08 (0.14)	0.06 (0.11)	0.05 (0.08)

Composition	C-0 [wt% (vol%)]	C-10 [wt% (vol%)]	C-30 [wt% (vol%)]
Sil6-TEC170	0.0 (0.0)	24.9 (8.4)	51.2 (25.8)
2-propanol	0.0 (0.0)	14.8 (23.7)	10.7 (23.3)
Genomer 4247	96.15 (96.01)	58.0 (65.2)	31.8 (48.8)
TPO	2.88 (2.83)	1.74 (1.94)	0.95 (1.45)
LP	0.96 (1.16)	0.58 (0.80)	0.32 (0.60)

5.2.1. Ceramic Functionalization

The inkjet printing of particulate ceramic suspensions with a filler content of 20 vol% requires a coating of the particles to prevent them from agglomeration and clogging the nozzles. This was done by functionalization of their surfaces with MPS while grinding them in the PBM. After the mechanical treatment, the particles were dried in a rotary evaporator. The MPS amount, which remained on the particle surface was measured via TGA. **Figure 45a** shows the weight loss of the particles as received, ground without MPS (Sil0-A240) and ground with MPS (Sil6-A240). The as received sample experiences a weight loss of 0.77 wt%, which is caused by the removal of surface bound water. The same is true for Sil0-A240 where, however, the weight loss of 1.11 wt% is more pronounced. On the one hand, this is presumably due to the higher surface area created during the grinding of the powder. This exposes more hydroxyl groups, which in turn bind water onto the ceramic surface. On the other hand, the ball milling of Al_2O_3 powders in an aqueous environment has been shown to further increase the amount of water on the already exposed surfaces. The binding of the H_2O happens in the first place by chemisorption of hydroxyl groups onto which, in a consequent step, water molecules attach via physisorption. This increase in OH-groups is advantageous for the coating with MPS since they function as anchoring points for the silane. With 2.86 wt% the sample Sil6-A240 has the highest weight reduction due to the highest added amount of MPS. The weight reductions of the samples Sil1-A240, Sil2-A240 and Sil4-A240 are summarized in **Figure A7**. The results gained from the TGA analysis were used to calculate the amount of MPS per square meter as can be seen in **Figure 45b**. The graph demonstrates the relationship between the MPS on the particles to the initially added amount of the silane. It shows that the addition of 1 mg/m² to 6 mg/m² of the molecules resulted in 0.36 mg/m² to 1.42 mg/m² of attached MPS. The difference can be explained by a loss of silane, which probably occurred during the drying in the rotary evaporator where weakly bound molecules detached from the particles. Presumably, the remaining silane is composed of covalently bonded molecules and physically attached oligo molecules.

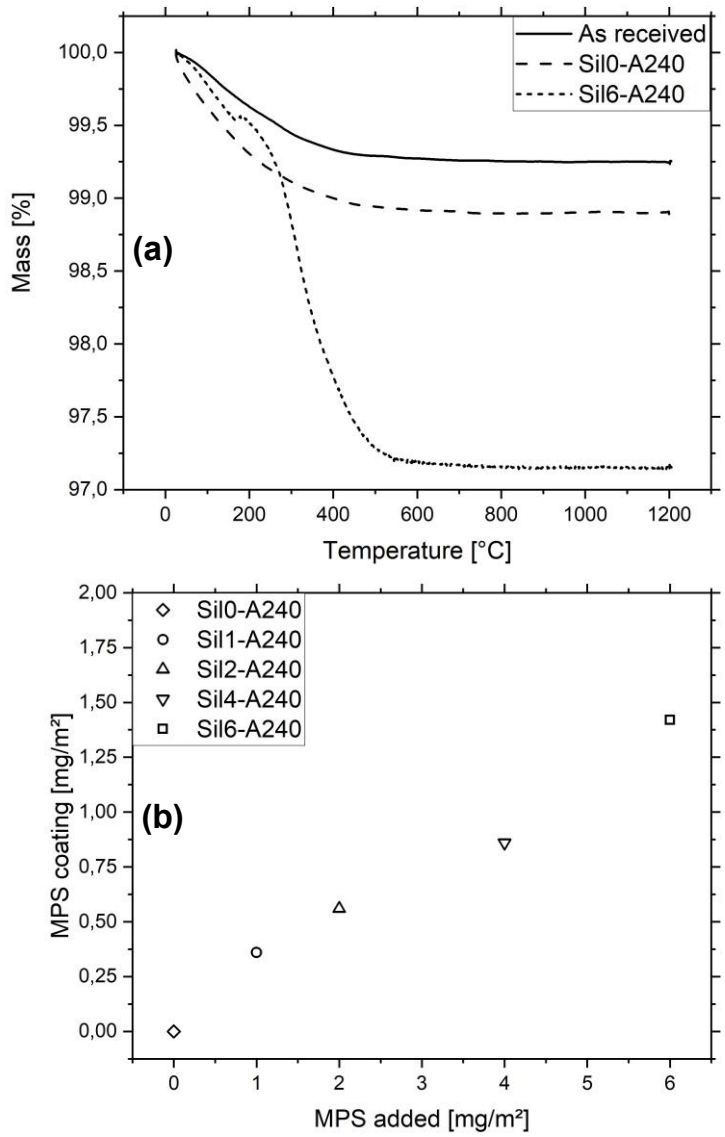

***Figure 45**: (**a**) TGA curve of A240 as received, Sil0- A240, Sil6- A240. (**b**) Total amount of hydrolyzed MPS in the coating in dependency of the added MPS for Sil0- A240, Sil1- A240, Sil2- A240, Sil4- A240 and Sil6- A240.*

Figure 46a shows the results of the static light scatting (SLSC) measurement of the samples Sil0- A240, Sil1- A240, Sil2- A240, Sil4- A240 and Sil6- A240 (**Table 15**) suspended and ultrasonicated in 2-propanol. The diameters are demonstrated as D10, D50 and D90 values to visualize the improving stability of the fillers. With an increasing amount of MPS the size of the particles decreases due to a denser MPS coating with Sil6-A240 having the best results. The particle size distribution (PSD) of the sample can be seen in **Figure 46b**. The PSD influences the rheological properties of a suspension and is important for the packing density in the composites. The material is monomodal with the peak being around 0.31 µm and the distribution

ranging from about 0.05 µm to 0.99 µm. The distribution is typical for ceramic fillers produced on a large scale as opposed to wet chemically synthesized particles, which often show very narrow PSDs.

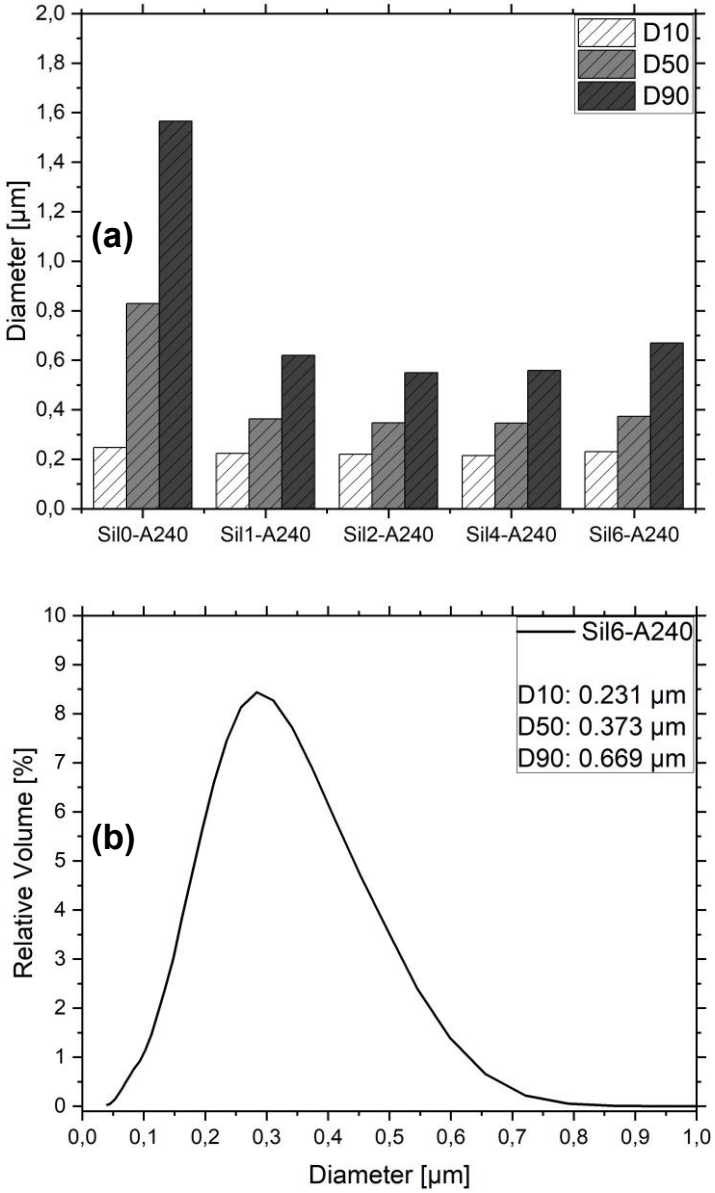

***Figure 46**: (**a**) Particle diameter of Sil0-A240, Sil1-A240, Sil2-A240, Sil4-A240 and Sil6-A240 expressed in D10, D50 and D90 values. (**b**) PSD of Sil6-A240.*

In addition to that, Sil6-A240 was investigated via STEM to characterize the thickness of the MPS coating. **Figure 47a** shows the irregular morphology of the sample, which as it was seen in the PSD, differs in size. The MPS shell was not visible by observation in the TEM mode (**Figure A8**). Therefore, the EDX sensor of the device was used (**Figure 47b**) in a close-up of a single particle. It revealed an increased silicon

concentration at the surface of the particle relative to its surrounding. The results suggest that in comparison to literature values, where MPS coatings of several nanometers in thickness [255], Sil6-A240 only has a very thin coating. The stability might be worse than for comparable samples with a thicker coating. However, when it comes to thermal conductance the coating shows an adverse effect with increasing thickness [174].

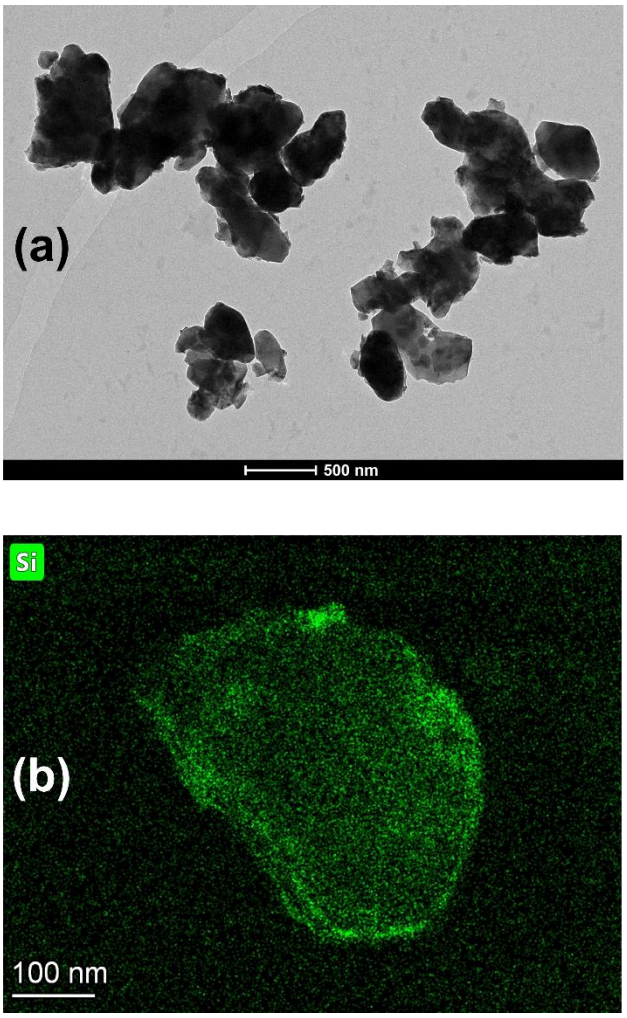

***Figure 47**: (**a**) TEM image of Sil6-A240. (**b**) TEM image of a Sil6-A240 particle with an overlayed EDX image.*

In order to investigate the interaction of the silanized ceramic in suspension, rheological measurements have been conducted. **Figure 48a** demonstrates the viscosity of the inks M-0, M-1, M-2, M-4 and M-6 at 32°C, summarized in **Table 23**. M-0 exhibits a shear thinning behavior with an initial viscosity drop from 1641.6 mPa·s to 41.8 mPa·s. The introduction of MPS coating onto the particle leads

to a marked decrease in the shear dependency compared to M-0. At low shear rates the viscosities are between 24.2 mPa·s and 20.6 mPa·s. At a shear rate of 500 s^{-1} the values range from 18.4 mPa·s to 17.8 mPa·s. Although the differences are small, a trend to a further decrease of the viscosity can be observed with increasing MPS content which has its low with M-4. For M-6 the values rise again which, however, is attributed to parameter variations during the preparation of the sample. The reduction in interaction can be explained by the weakening of the Van-der-Waals forces of the particle surfaces through their covering with organic moieties. This is true until a plateau is reached, and no further improvement can be observed at the given particle concentration of 20 vol%. A low interaction between the particles is important for inkjet printing since it reduces the risk of nozzle clogging. Filtering a suspension with a 5 µm filter is a standard procedure before printing. It is not possible to filter the samples M-0 and M- 1. The sample M-2 allows limited filtering whereby the filter occludes during the procedure. In turn, the filtering of M-4 and M-6 was possible. **Figure 48b** shows the ceramic concentration after the filtering. For M-2 the ceramic concentration is significantly lower than in the initial sample. In M-4 the reduction is 2.4 vol% and for M-6 no reduction could be measured. Hence, the potential to filter the material increases with the increasing MPS proportion, which is again probably due to reduced Van-der-Waals forces. This is in line with established literature results [178,187].

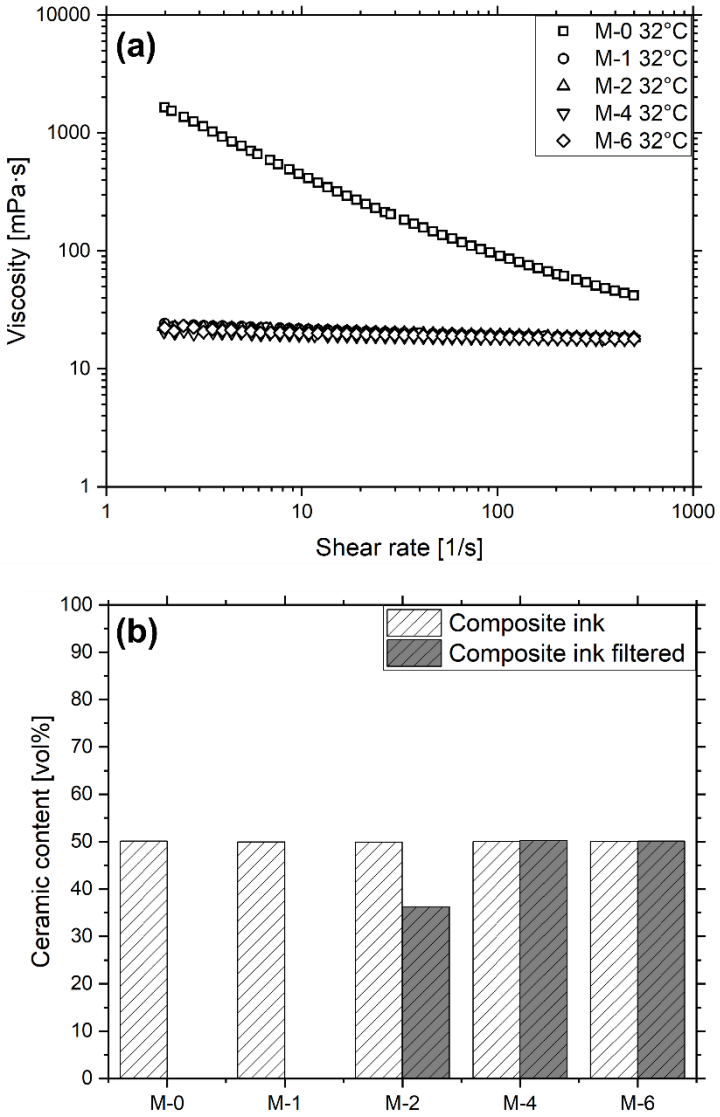

***Figure 48**: (**a**) Viscosity in dependency of the shear rate of M-0, M-1, M-2, M-4, M-6 at a temperature of 32°C. (**b**) Ceramic content of the materials upon solvent evaporation before and after filtration.*

5.2.2. Ink Solvent

The influence of the solvents was investigated for the inks M-I, M-II, M-III and M-IV containing Sil6-TEC170 and summarized in **Table 22**. **Figure 49** shows the rheology of the materials at 32°C. M-I, M-II and M-III exhibit shear thinning, while in comparison M-IV reveals only a minor viscosity reduction at elevated shear rates. With the increasing polarity of the solvents HexylAc, PGMMEA, DPGMME and DEGMEE the interaction of the particles with each other declines. At higher shear forces the influence of the solvent is smaller than for shear rates near 0 s^{-1} so that the difference in viscosity decreases. At the shear rate 500 s^{-1} the viscosity of M-II sinks

relative to M-I from 27.9 mPa·s to 18.3 mPa·s. A similar reduction is seen for M-III and M-IV where the viscosity sinks from 28.1 mPa·s to 18.4 mPa·s. M-I and M-II contain an additional amount of MPS because filtering was initially not possible.

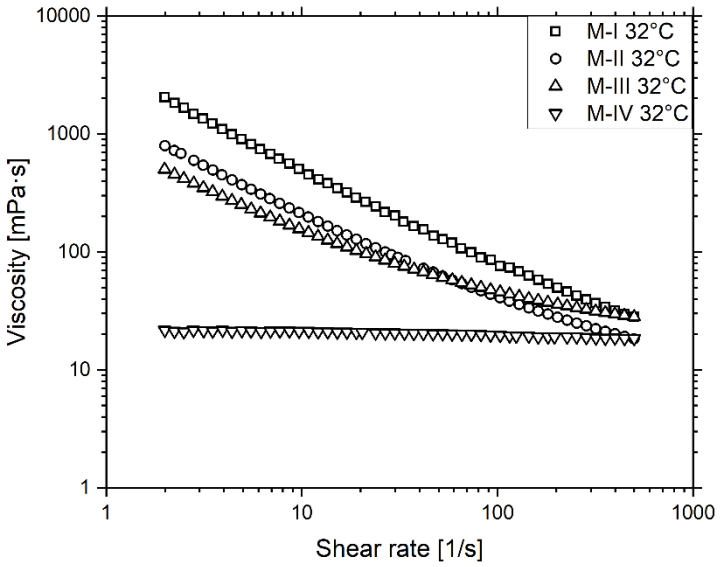

***Figure 49**: Viscosity of the filtered inks M-I, M-II, M-III and M-IV after filtration in dependency of the shear rate at a temperature of 32°C.*

Table 23 shows the surface tensions and viscosities of M-I, M-II, M-III and M-IV in comparison to the solvents and Genomer 4247 at the shear rate of 500 s^{-1} and the temperatures of 32°C and 60°C. The surface tension and viscosity of Genomer 4247 are the highest of all the materials due to its high molecular weight and its high number of polar segments. The solvents HexylAc, PGMMEA, DPGMME and DEGMEE as well as the materials M-I, M-II, M-III and M-IV display higher values with increasing permittivity. Except for M-II, all materials have decreased viscosities at 60°C compared to 32°C. The low decrease in M-I and a slight increase in M-II can be explained by the added MPS molecules, which still have not reacted and now start to link onto the particles and with each other at elevated temperatures.

***Table 23**: Surface tension and viscosity at 32°C and 60°C of the materials M-I, M-II, M-III and M-IV as well as the values for the used volatile solvents and the oligomer Genomer 4247. The viscosity was measured at a shear rate of 500 s^{-1}.*

	Surface tension [mN/m]	Viscosity at 32°C [mPa·s]	Viscosity at 60°C [mPa·s]
Genomer 4247	38.4 ± 1.6	3991.7 ± 187.4	325.1 ± 137.5
HexylAc	24.6 ± 0.4	1.4 ± 0.1	1.1 ± 0.0
PGMMEA	28.1 ± 1.3	1.7 ± 0.0	1.2 ± 0.1
DPGMME	30.3 ± 0.1	3.6 ± 0.0	2.0 ± 0.0
DEGMEE	34.8 ± 1.3	4.2 ± 0.1	2.3 ± 0.1
M-I	16.1 ± 0.8	27.9 ± 2.1	24.2 ± 2.4
M-II	27.9 ± 1.9	18.3 ± 1.8	18.4 ± 0.7
M-III	30.1 ± 0.9	28.1 ± 0.6	18.8 ± 1.2
M-IV	31.7 ± 0.2	18.4 ± 0.1	9.0 ± 0.1

Figure 50a shows the formation of droplets in the drop watcher of the inkjet printer. This image is representative for the initial printing of M-I, M-II, M-III and M-IV where no occlusion of the nozzles takes place. **Figure 50b** illustrates the drop weight of the materials after a jetting time of 0 min and 18 min, printing a test image (**Figure A9**). The drop weight for M-I is initially 6 ng and sinks further to 2 ng. Similarly, the drop weight for M-II sinks from 13 ng to 9 ng. This reduction is caused by the evaporation of the solvents due to high vapor pressure. So that only frequent cleaning cycles can keep the materials in an operational state during printing. On the contrary, M-III and M-IV do not indicate significant weight reduction, which means that the nozzles stay functional for a longer time.

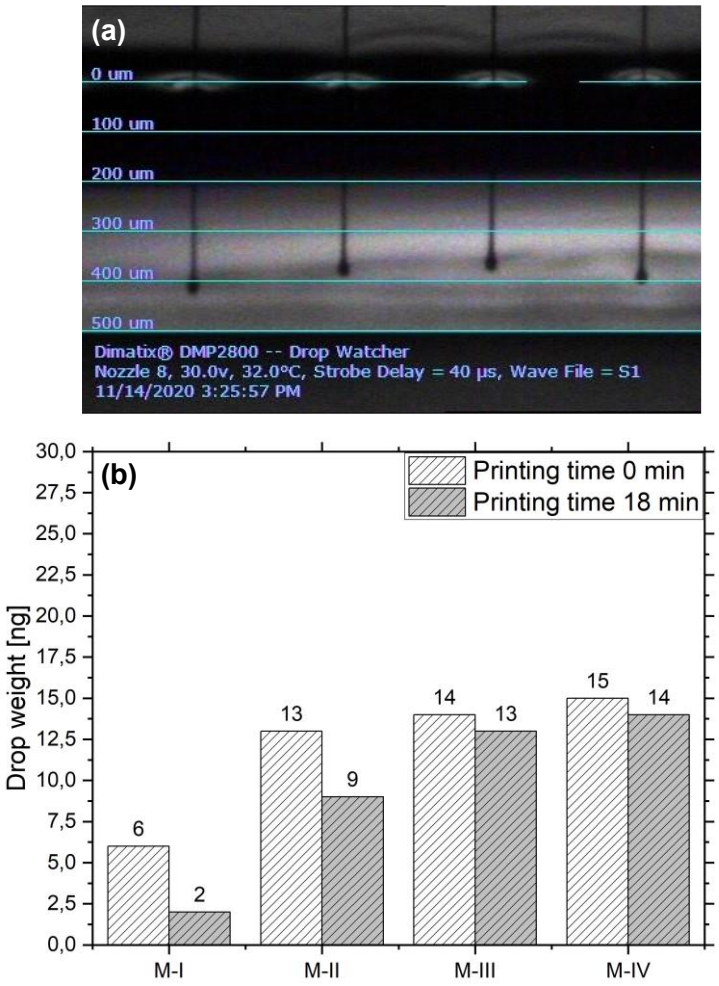

***Figure 50**: (**a**) M-IV ink during jetting in the drop watcher. (**b**) Measurement of the average drop weight of M-I, M-II, M-III and M-IV with 10 nozzles at 32°C before and after the printing of a four-layer test image.*

Figure 51a to **Figure 51d** demonstrate the deposition of the four materials with a drop spacing of 20 µm onto a PDMS coated aluminum substrate. For M-I the image indicates good wetting with a homogeneous covering of the substrate, which is caused by their comparatively low surface tensions of 16.10 ± 0.75 mN/m relative to the surface energy of PDMS which is 21.0 ± 0.80 mJ/m². The deposition of M-II, M-III and M-IV leads to large drop formations due to their high surface tensions of 27.92 ± 1.89 mN/m, 30.06 ± 0.86 mN/m and 31.72 ± 0.24 mN/m, respectively. To improve the wetting for materials with respective surface tensions 10 layers were printed with a drop spacing of 40 µm to form a film with a surface energy of 34.4 ± 0.80 mJ/m² onto which normal printing was possible with significantly better wetting. **Figure 51e** and **Figure 51f** illustrate the difference, where at first a drop of M-IV is deposited on PDMS, having a contact angle of 57.4 ± 0.80°, and then the same

drop is deposited onto the ground layers which leads to a lower contact angle of 29.1 ± 0.81°.

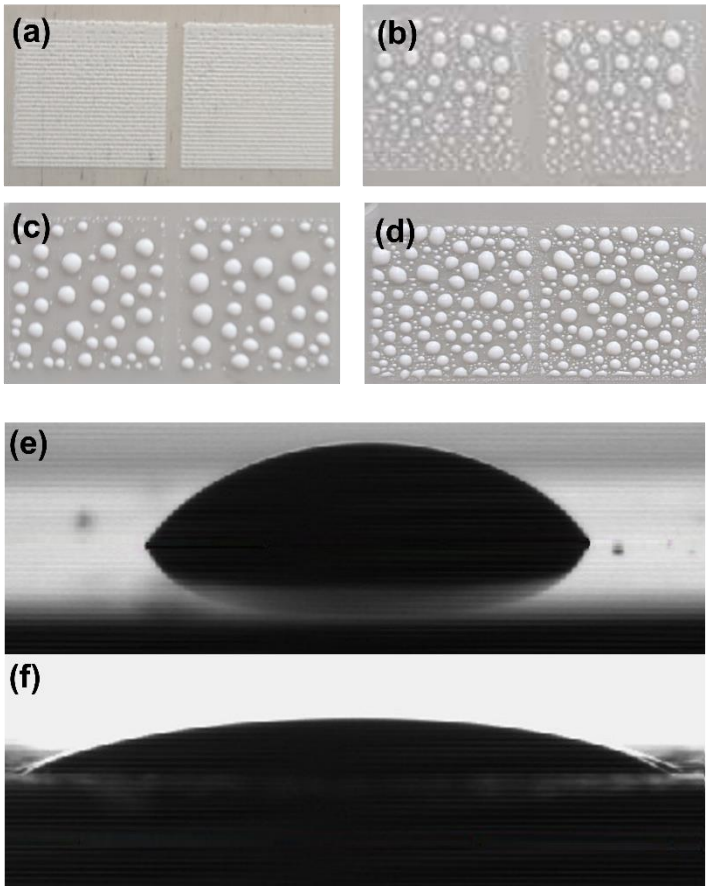

Figure 51*: (a) M-I, (b) M-II, (c) M-III and (d) M-IV inkjet-printed onto PDMS with a drop spacing of 20 µm. (e) Drops of the material M-IV on PDMS and (f) on previously printed ground layers of the composite ink.*

Figure 52 displays the ceramic content of the materials before and after filtering, as well as after printing. It shows that during the processing of the material no relevant amounts of ceramic were lost, which underlines the good stabilization of the particles inside the inks.

With regular cleaning cycles all inks have shown to be suitable for composite deposition. However, due to economic reasons the reduction of cleanings cycles is likely to be important for volumetric printing. In this regard, the solvents HexylAc and PGMMEA are less suitable for the printing of concentrated ceramic suspensions due to their inferior stabilizing properties when compared to the other two solvents and due to their high vapor pressure. Both factors lead to a fast occlusion of the nozzles. DPGMME and DEGMEE combine good stabilizing characteristics with a high vapor

pressure. The latter, however, offers overall the best results and is therefore chosen for further experiments.

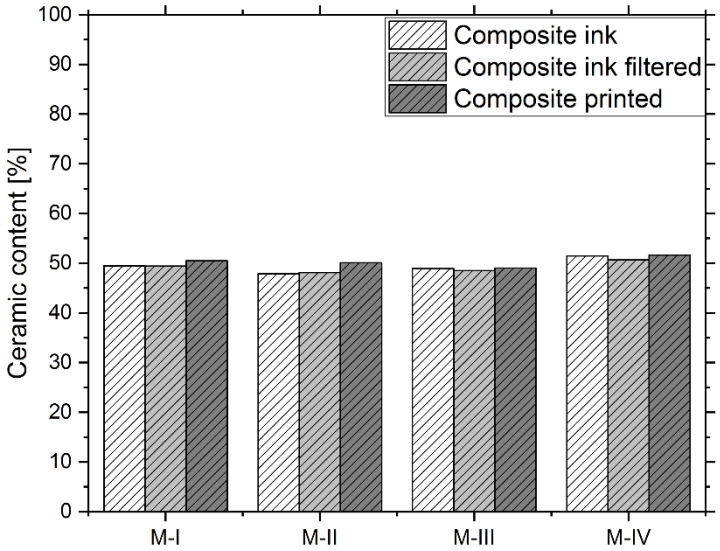

***Figure 52**: Ceramic content of the composite ink before and after filtration, as well as after printing.*

5.2.3. Ink Ratio

The adjustment of the ceramic to organic ratio in the ink aims at increasing the ceramic content and thermal conductance in the final composite. Furthermore, changes in components ratio influence ink properties like viscosity and surface tension, which requires experimental review. **Figure 53** shows the viscosity of M-7 to M-10 at 32°C in dependency of the shear rate. The composition of the inks is summarized in **Table 22** with Sil6-A240 being the coated ceramic filler. Just like M-IV, the materials exhibit negligible shear thinning. The influence of Genomer 4247 is noticeable and declines from sample M-7 to M-10, where the viscosity at 500 s^{-1} drops from 15.7 mPa·s to 11.0 mPa·s. **Table A4** in the appendix indicates that the viscosities also decrease with temperature elevation to 60°C. The surface tensions of the materials, also shown in **Table A4**, stay approximately the same with values ranging between 31.1 mN/m and 33.0 mN/m. This requires the deposition of ground layers prior to the volumetric printing for better wetting on PDMS. The siloxane was chosen as substrate due to its resistance to temperatures up to around 200°C, and its low surface energy allowing the retrieval of the samples from the substrate after printing. **Figure A10** repeats the observation that the DEGMEE based inks do not show signs of solvent

evaporation during a printing time of 18 minutes, which is reflected in the steady drop weight of the inks independent of ink ratio.

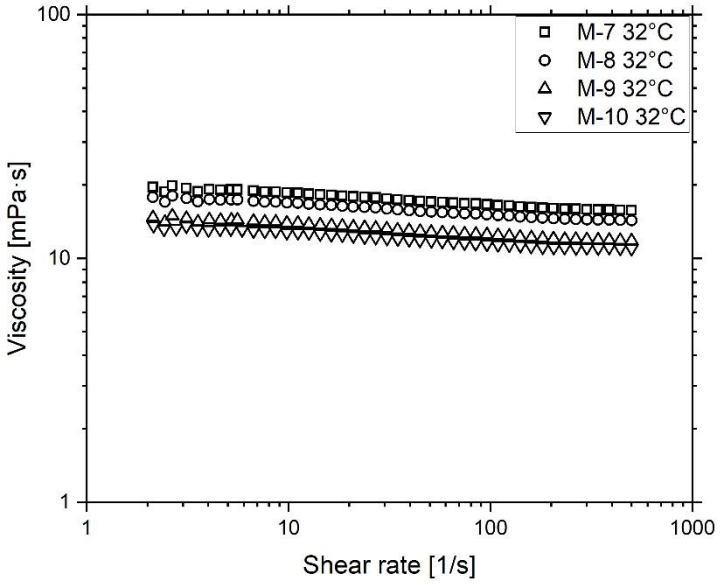

***Figure 53**: Viscosity of the inks M-7 to M-10 in dependency of the shear rate at a temperature of 32°C.*

Altering the ink composition might also have an influence on its stability and potentially lead to increased interaction with other surfaces fostering agglomeration, ceramic reduction and nozzle clogging during printing. Therefore, **Figure 54a** shows the ceramic content of M-7 to M-10 as composite inks prior to filtering and as printed composites. The ceramic content does not decrease relative to the organic components after filtering and printing. Since interaction with the filter and nozzle material may lead to retention of the ceramic, an unchanged composition hints at the stability of the fillers in the inks. Consequently, the ceramic content increases from 50 vol% to 70 vol% in the samples M-7 to M-10, according to the TGA measurement. The density of the composites partly reflects this trend in **Figure 54b.** Except for M-10, the densities of the casted composites C-0 to C-30, summarized in **Table 23**, as well as of the printed M-7 to M-9 increase following a linear trend. The deviation of M-10 might be the consequence of air inclusions in the composite due to a reduced packing density. The finding does not contradict the previously shown thermogravimetric results, as the TGA visualizes the ratio of the organic and inorganic components and cannot detect vacancies.

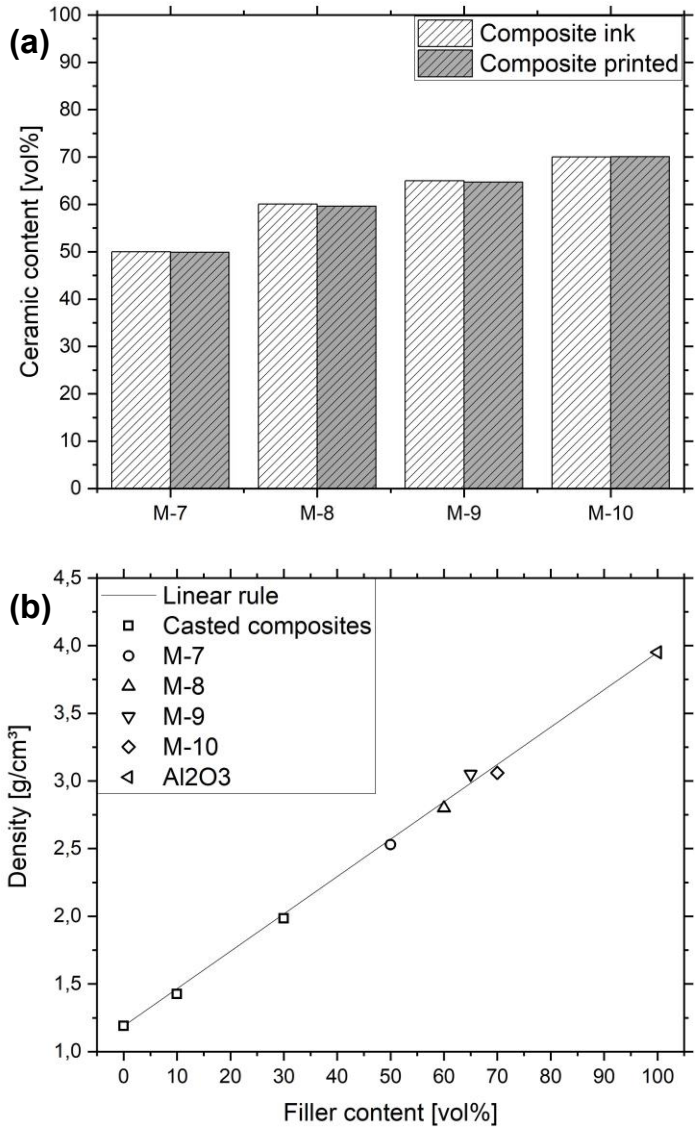

***Figure 54**: (**a**) Ceramic content of the inks M-7 to M-10 and of the respective printed composites. (**b**) Density of the printed composites M-7 to M-10, as well as of casted composites C-0 to C-30 in dependency of the ceramic content.*

After the preliminary analysis, the printed samples M-7 to M-10 as well as the casted composites allowed the assessment of their thermal conductivity using the laser flash method. **Figure 55** displays the result of the measurement alongside the Bruggemann model. The values are in the range of 0.21 W/(m·K) to 1.86 W/(m·K). The sample M- 10 deviates from the model. An explanation for that might be the inclusion of thermally insulating air due to excession of the maximally possible filling grade, which leads to an effective decrease of the ceramic content. The Bruggemann model was adjusted for a filler thermal conductivity of 30 W/(m·K) with the empirical prefactor k, introduced in 3.3.4, being 0.2. Under omittance of the value for M-10, the adjusted

model has a high correlation with the measurement results, being reflected in the coefficient of determination R^2=1.0. Contrary to that, the Bruggeman model without the prefactor does not match the results in a meaningful way. One explanation for that is the large proportion of small particles in the PSD, which increases the interfacial thermal resistance in the composite. At the Kapitza radius, also introduced in subchapter 3.3.4, the thermal resistance of the particles completely mitigates the higher thermal conductivity of the ceramic. Examples of the test specimens employed in the laser flash method are shown in **Figure A12**.

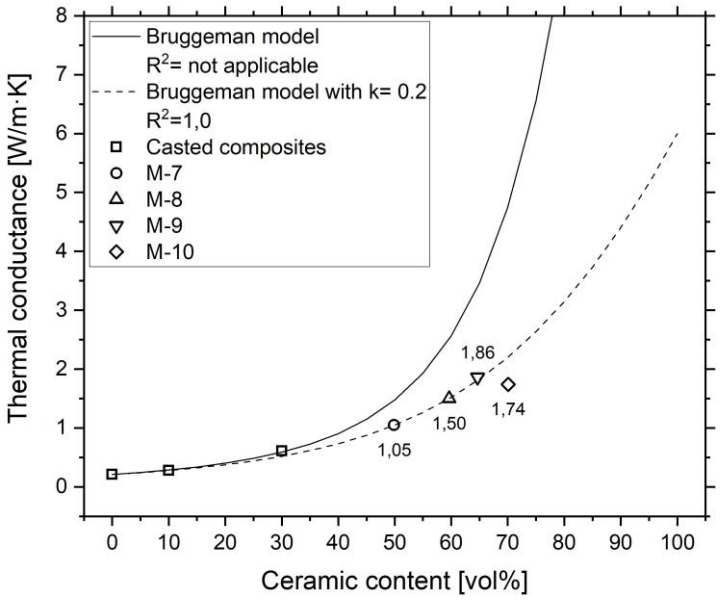

***Figure 55**: Thermal conductance in dependency of the ceramic content using the casted composites C-0 to C-30 as well as the printed composites M-7 to M-10.*

In addition to the thermal properties, the mechanical properties of the printed composites M-7 to M-10 were of interest. The structural integrity of 3D inkjet-printed components is important for their deployment. Tensile tests allowed the estimation of these properties (**Figure A13**). **Figure 56a** shows the Young's modulus and the elongation at break for the printed Genomer 4247 and M-7. The values for the stiffness are 702 MPa and 1537 MPa, respectively. As introduced in subchapter 3.3.3, the addition of ceramic is known to decrease the ductility in composites. The values for the elongation at break decreased from 6.7 % to 3.0 %, respectively. This trend is caused by the low elasticity of the ceramic fillers. **Figure 56b** shows the ultimate tensile strength and tensile toughness of the materials. The values for the UTS are 46.5 MPa and 43.0 MPa for Genomer 4247 and M-7, respectively. As introduced in

subchapter 3.3.3, the decline of the UTS upon ceramic addition is often caused by the fillers acting as defects and filler heterogeneity induced stress peaks. Similarly, U_T decreases due to the decline of UTS and ε_{max} with the values for the toughness being 1.6 J/m³ and 0.6 J/m³, respectively. Yet, the testing of M-8 to M-10 was not possible, as the specimens broke during printing (**Figure A11a)**. A possible explanation might be the material shrinkage during printing and curing in combination with filler inhomogeneity. Examples of successfully printed specimens are depicted in **Figure A11b**.

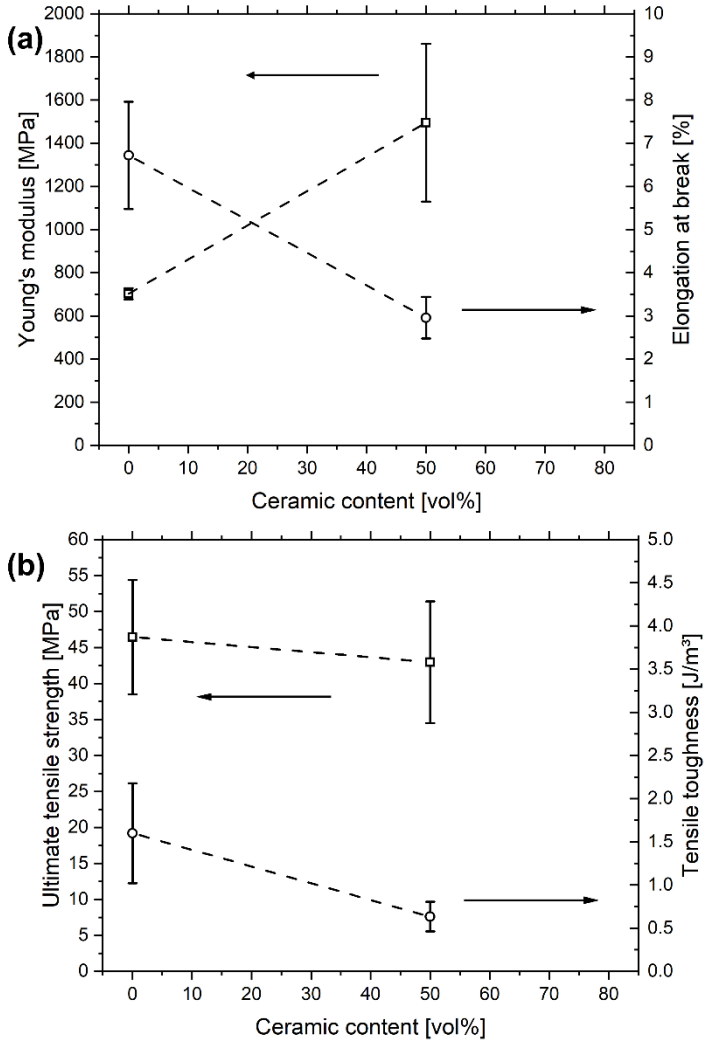

***Figure 56**: **(a)** Tensile modulus and the elongation at break in dependency of the ceramic content for printed Genomer 4247 and M-7, **(b)** Ultimate tensile strength and tensile toughness as a function of the ceramic content for the tested materials.*

The quality of the results regarding the thermal conductance is confirmed by experimental values in [228,252,253]. The lack of respective publications on the

mechanical properties of the investigated material systems does not allow relevant comparison. To sum up, the aim to modify the thermal conductance by increasing the ceramic content in the composite is possible up to a filling grade of 65 vol%. The increase, however, comes with the drawback of a decline in the materials UTS, ε_{max} and toughness. Therefore, to ensure the structural integrity of the material, the ceramic content was limited to 50 vol% for further investigations.

5.2.4. Ink Jetting

The previous subchapter presented the manufacturing of samples for thermal and mechanical analysis. These were produced layer-by-layer with solvent evaporation steps in between. The polymerization of the oligomer Genomer 4247, however, took place after the finalization of the print. Although, the ceramic loading offers structural integrity for single material prints of low height, further layer-by-layer polymerization might be needed in larger prints and multi material components. This was done by additional UV irradiation between layer deposition after solvent evaporation. It increased the polymerization degree of each layer compared to just solvent evaporation, yet it also causes the early onset of samples curling and detachment. To solve that, M-7 samples were printed while adjusting parameters (**Table 24**), which were observed to be of influence in preliminary trials. These parameters are “aluminum substrate thickness”, “PDMS thickness on aluminum substrate”, “drop spacing”, “irradiation dose” and “irradiation time”. In samples 1 to 4 the irradiation dose was changed with time. **Figure A14** shows the result, where the samples curl and detach from the surface after 14 to 20 deposited layers. It is likely that the curling occurs due to differences in the polymerization degree of the upper and the lower sample layers. The temperature and the UV intensity are higher at the top than at the bottom due to the thermal isolation of the 500 µm thick PDMS for the former and particle scattering for the latter. The intention to completely polymerize the deposited layers by UV irradiation and therefore prevent the difference in the polymerization degree failed. As samples 2 to 4 show in **Table 24**, the delamination happens faster than in sample 1 with no UV irradiation.

***Table 24**: Samples for the investigation of specimen curling during 3D printing.*

Sample	Substrate thickness [mm]	PDMS thickness [µm]	Drop spacing [µm]	Irradiation dose [J/m²]	Irradiation time [s]	Curling after layer number
1	5	500	20	0	0	20
2	5	500	20	5	10	15
3	5	500	30	10	20	15
4	5	500	30	30	60	14
5	6	100	20	0.5	1	80

This finding was confirmed by FTIR, shown in **Figure 57**, where the conversion of samples, introduced in **Table 24**, was higher for samples 2 to 4 relative to sample 1, yet still not complete. Only after a heat treatment at 100°C for 12 h polymerization of nearly 60 % could be achieved. For sample 5, it was possible to delay curling until layer 80 by increasing the aluminum substrate thickness to 6 mm, reducing the PDMS thickness to 100 µm and UV irradiate the sample with a lower dose of 0.5 J/cm². After the establishment of the curing parameters the ink itself was characterized.

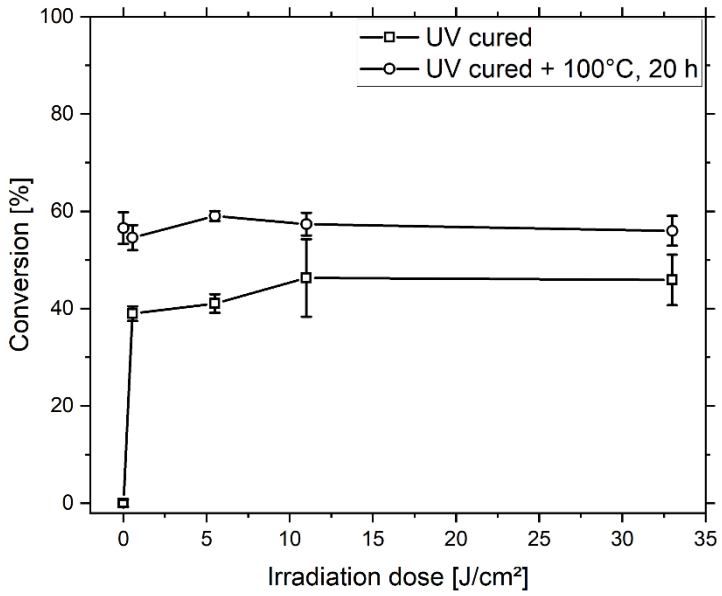

***Figure 57**: Conversion as function of the UV irradiation dose for printed and dried ink M-7, as well as for printed and dried ink M-7, which was thermally treated in an oven at 100°C for 12 h.*

For successful jetting and deposition, the ink drop must detach from the ink bulk and exit the print head, yet it should keep its coherence during flight. Moreover, upon impact on the substrate it should form a regular drop pattern. To test for that,

Figure 58a shows the drop position as a function of the time during the ejection from the nozzle. The drop velocity is 11 m/s, which is in the allowed range according to chapter 2. The impact of the drop onto the substrate is not likely to result in splashing and the formation of an irregular drop pattern on the substrate. The Weber, the Reynolds and the Ohnesorge numbers support this finding. Their values are 159.2, 20.8 and 0.6, respectively. Furthermore, the numbers hint at a sufficient balance of the ink to form droplets, which then do not disintegrate to form satellites during flight. Instead, the drops show ligaments, which extends for up to 800 µm probably due to the high surface tension of the ink (**Table A4**). Weighting the droplets shows an average drop mass of 14 ng with a volume of 9 pl, which is normal for inkjet printing. However, depending on the process parameters, the weight can change. **Figure 58b** exhibits the average drop weights of the ink, which decrease as a function of the idle time and increases as a function of the print head temperature. In the cases of the former, the decline is possibly caused by evaporation of the solvent, which leads to an increase of the particle and oligomer concentration relative to the total volume. At elevated concentrations, the ink viscosity increases and occludes the nozzles. In the case of the latter, the temperature increase probably reduces the viscosity of the ink, allowing the formation of heavier droplets.

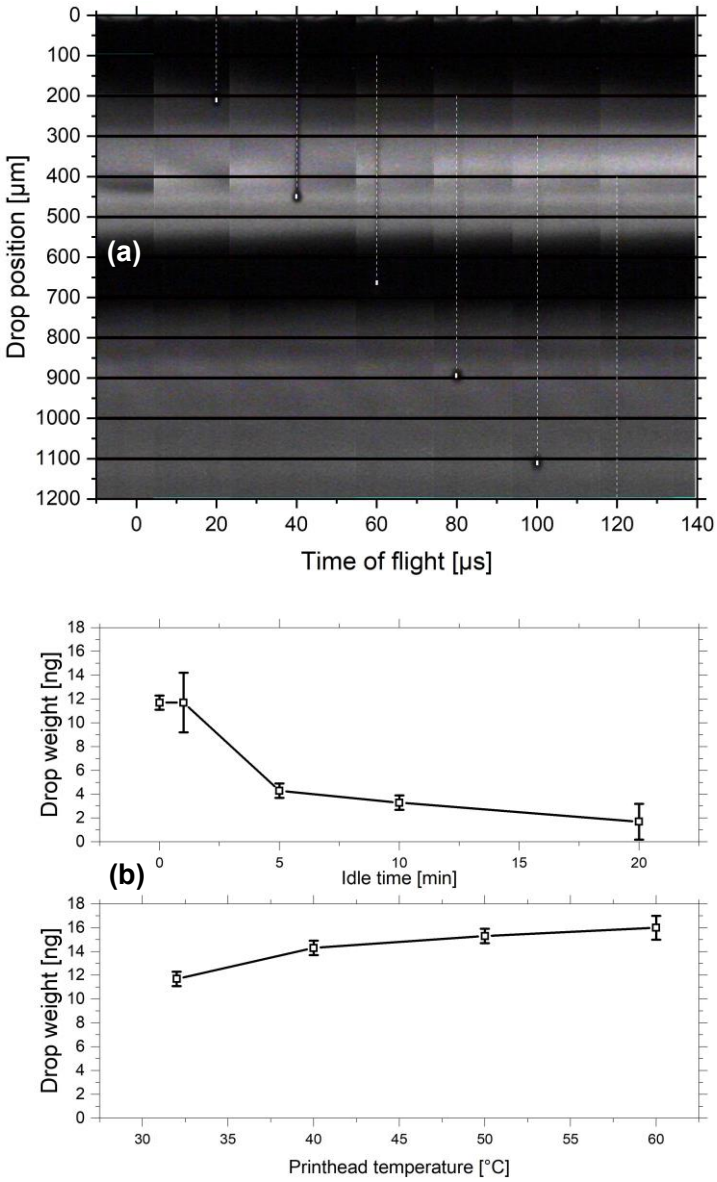

***Figure 58**: (**a**) Drop procession during jetting observed over a timeframe of 120 µs. (**b**) Drop weight of the ink measured as a function of the idle time at 32°C and as a function of the print head temperature at the idle time as well as at the printing time of 0 min.*

The acquired information on the inkjet printing of the ink M-7 enabled the printing of components and patterns for the purpose of demonstration. **Figure 59a** shows a printed rectangular base with protruding columns from its top side resembling a heat sink. The total height of the structure is 2 mm. The columns have a diameter of around 500 µm. **Figure 59b** exhibits the printed Sigillum of the University of Freiburg. The left image depicts one printed and dried layer of ink, while the right image shows 10 printed layers. As opposed to **Figure 59a**, only one nozzle was used to achieve a higher resolution and prevent drop misplacement. To demonstrate the ability to print

macroscopic components **Figure 59c** shows a 3D inkjet printed wrench. The structure has a thickness of 1 mm. These results resemble a novelty, since, according to our knowledge, no material with such characteristics was published so far.

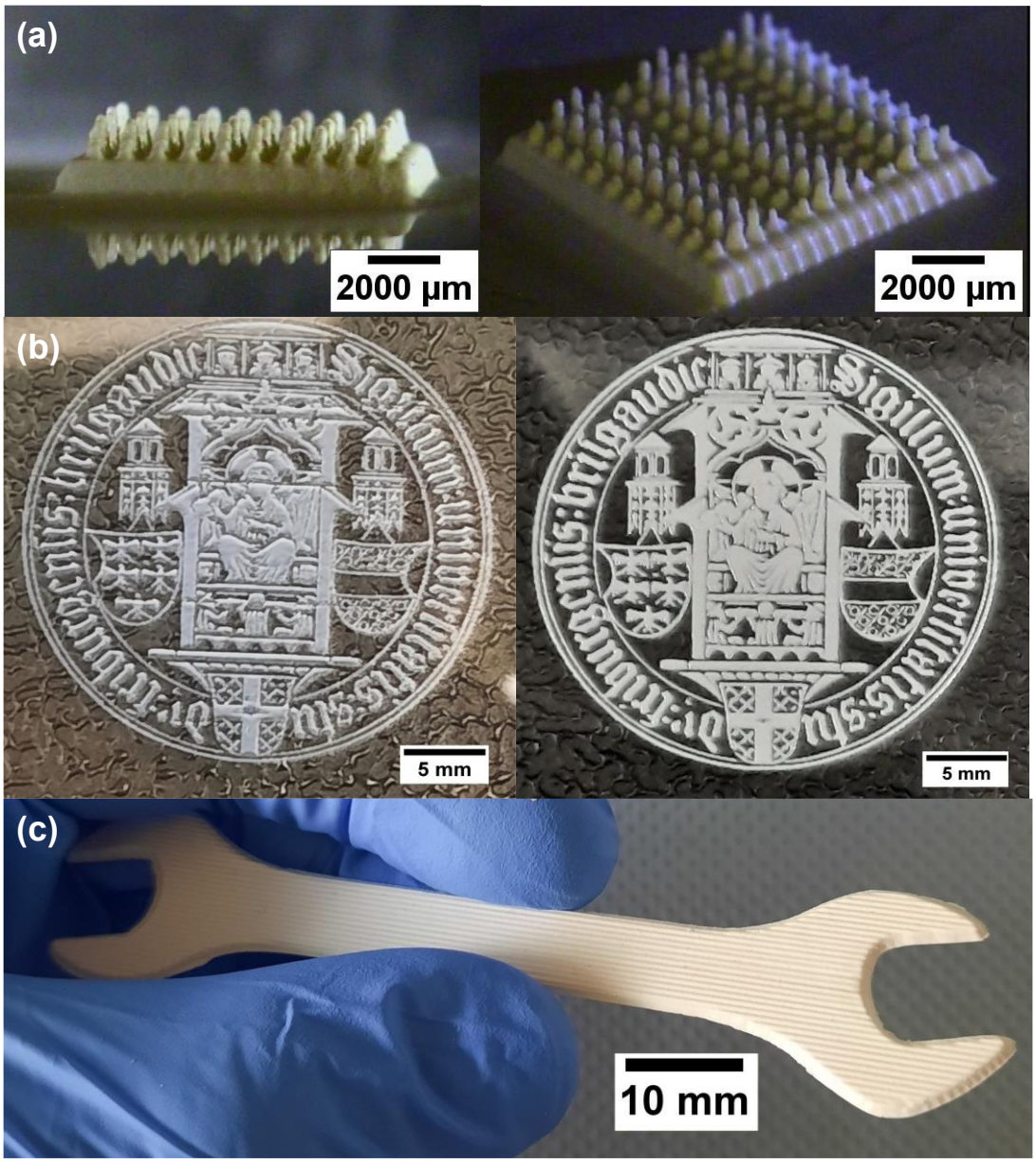

***Figure 59**: Inkjet-printed structures and components for the purpose of demonstration. (**a**) Heat sink with a rectangular base and round columns on top. (**b**) Sigillum of the University of Freiburg. The left image was printed as one layer, while on the right image are 10 layers printed over each other. (**c**) Printed wrench with a thickness of 1 mm.*

6. Conclusion and Outlook

This thesis dealt with the investigation of new ceramic inks for the 3D inkjet printing of polymer-ceramic composites for structural and thermal purposes. In the case of the latter, for the first time, it was possible to produce inks suitable for multi-material deposition with properties approaching commercial thermally conductive pastes. Furthermore, the ink production involved methods, which allow the preparation of large ink quantities.

The experiments encompassed three kinds of inks, first "solvent free inks for structural composites", second "solvent free inks for thermally conductive composites" and third "solvent-based inks for thermally conductive composites".

The investigation of "solvent free inks for structural composites" sought to develop materials, which utilize micro and nano mechanism to increase the tensile toughness and elongation at break of otherwise brittle photopolymers. Three particle sizes, 14 nm, 50 nm and 170 nm were tested for their suitability to initiate respective mechanisms. Tensile tests did not show that filler addition significantly changes the tensile toughness and elongation at break relative to the unfilled matrix, the values of which were 1.1 J/m² and 6 %. Instead, the results gave possible evidence that particle scattering related decrease of polymerization could have an adverse effect on the toughness, as well as on the Young's modulus and ultimate tensile strength.

As an outlook, possible next steps towards the development of tough structural composites for 3D inkjet printing might be the further refinement of the grinding process to achieve smaller particle sizes. Furthermore, additional post polymerization by heat may counter the scattering of particles. Finally, examinations of the composite matrix could be done to improve the polymer network heterogeneity.

The investigation of "solvent free inks for thermally conductive composites" for 3D inkjet printing introduced UV curable materials filled with the 240 nm sized submicron particles A240. Examinations of the maximally possible ceramic concentration in inks, using viscosity measurements, showed **30 vol%** to be the furthest possible value. The juxtaposition with the empirical Krieger and Dougherty model gave hints at possible interparticle force influence as a reason for this limitation. Thermal conductivity assessment of printed specimens showed a value of **0.6 W/(m·K)**. A further increase

necessitated a higher ceramic content, the realization of which however is aggravated by the limitations of the inkjet printing technology.

The formulation of "solvent-based inks for thermally conductive composites" could help to solve the challenge. It allows inks with a tolerable ceramic concentration, which however increases upon evaporation of a volatile solvent. This way the investigation yielded composites with ceramic contents of **50 vol%** to **65 vol%**. The materials had a thermal conductivity of 1.0 W/(m·K) to 1.9 W/(m·K). This is a more than **tenfold** increase relative to the unfilled organic matrix. However, only composites with 50 vol% ceramic content were deemed mechanically sufficiently stable. Their tensile properties showed an increase of the Young's modulus by **92 %** relative to the unfilled Genomer 4247 matrix. Opposed to that, the ultimate tensile strength, the elongation at break and the tensile toughness decreased by 7 %, 64 % and 32 %, respectively. The material allowed the printing of structures and components, which demonstrated its performance and suitability for multi-material deposition.

As an outlook on further improvement possibilities, the reduction of the organic matrix shrinkage is to be mentioned. This could allow a higher ceramic filling grade in the resulting composites without causing the material to break. Also, larger ceramic fillers could be investigated to reduce the influence of the thermal resistivity of particle surfaces. Moreover, other functional ceramics could be worked into inks in a similar manner to serve purposes like the adjustment of magnetic or dielectric properties. Finally, the developed composite is suitable to produce custom ceramic parts as well. First debinding and sintering trials conducted as proof of concept, led to crack-free pieces, shown in **Figure 60**, with a density of 3.95 g/cm³, being the value for bulk Al_2O_3.

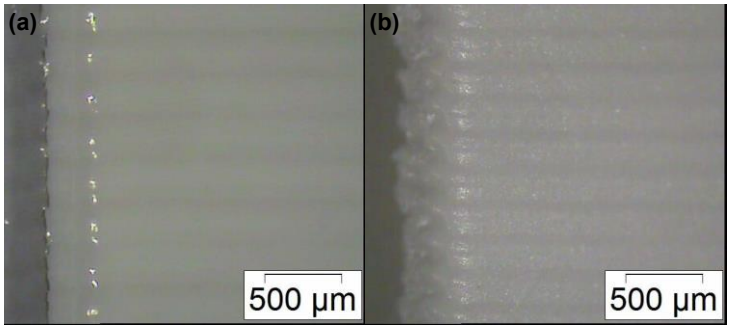

***Figure 60**: Printed structure with the dimensions of 10x10x0.5 m³ using the ink M-7 (**a**) before debinding and sintering as well as (**b**) after debinding and sintering.*

Bibliography

1. Efstathiou, S. Is It Possible to Give Scientific Solutions to Grand Challenges? On the Idea of Grand Challenges for Life Science Research. *Studies in History and Philosophy of Science Part C :Studies in History and Philosophy of Biological and Biomedical Sciences* **2016**, *56*, 48–61, doi:10.1016/J.SHPSC.2015.10.009.
2. Kaldewey, D. The Grand Challenges Discourse: Transforming Identity Work in Science and Science Policy. *Minerva* **2018**, *56*, 161–182, doi:10.1007/S11024-017-9332-2.
3. Ludwig, D.; Blok, V.; Garnier, M.; Macnaghten, P.; Pols, A. What's Wrong with Global Challenges? *Journal of Responsible Innovation* **2021**, *0*, 1–22, doi:10.1080/23299460.2021.2000130.
4. Molina, A.; Rodriguez, C.A.; Ahuett, H.; Cortés, J.A.; Ramírez, M.; Jiménez, G.; Martinez, S. Next-Generation Manufacturing Systems: Key Research Issues in Developing and Integrating Reconfigurable and Intelligent Machines. *International Journal of Computer Integrated Manufacturing* **2005**, *18*, 525–536, doi:10.1080/09511920500069622.
5. Esmaeilian, B.; Behdad, S.; Wang, B. The Evolution and Future of Manufacturing: A Review. *Journal of Manufacturing Systems* **2016**, *39*, 79–100, doi:10.1016/J.JMSY.2016.03.001.
6. Sun, C.; Wang, Y.; McMurtrey, M.D.; Jerred, N.D.; Liou, F.; Li, J. Additive Manufacturing for Energy: A Review. *Applied Energy* **2021**, *282*, doi:10.1016/J.APENERGY.2020.116041.
7. Ngo, T.D.; Kashani, A.; Imbalzano, G.; Nguyen, K.T.Q.; Hui, D. Additive Manufacturing (3D Printing): A Review of Materials, Methods, Applications and Challenges. *Composites Part B: Engineering* **2018**, *143*, 172–196, doi:10.1016/J.COMPOSITESB.2018.02.012.
8. Bose, S.; Bandyopadhyay, A. Additive Manufacturing : The Future of Manufacturing in a Flat World. *Additive Manufacturing* **2019**, 451–461, doi:10.1201/9780429466236-15.

9. Ligon, S.C.; Liska, R.; Stampfl, J.; Gurr, M.; Mülhaupt, R. Polymers for 3D Printing and Customized Additive Manufacturing. *Chemical Reviews* **2017**, *117*, 10212–10290, doi:10.1021/acs.chemrev.7b00074.
10. Gebhardt, A. *Rapid Prototyping*; Carl Hanser Verlag GmbH & Co. KG: München, 2003; ISBN 978-3-446-21259-6.
11. Jacobs, P.F. *Stereolithography and Other RP & M Technologies: From Rapid Prototyping to Rapid Tooling*; Society of Manufacturing Engineers in cooperation with the Rapid Prototyping Association of SME; ASME Press, 1996; ISBN 9780872634671.
12. Wendel, B.; Rietzel, D.; Kühnlein, F.; Feulner, R.; Hülder, G.; Schmachtenberg, E. Additive Processing of Polymers. *Macromolecular Materials and Engineering* **2008**, *293*, 799–809, doi:10.1002/MAME.200800121.
13. Stansbury, J.W.; Idacavage, M.J. 3D Printing with Polymers: Challenges among Expanding Options and Opportunities. *Dental Materials* **2016**, *32*, 54–64, doi:10.1016/j.dental.2015.09.018.
14. Boton, C.; Rivest, L.; Ghnaya, O.; Chouchen, M. What Is at the Root of Construction 4.0: A Systematic Review of the Recent Research Effort. *Archives of Computational Methods in Engineering* **2021**, *28*, 2331–2350, doi:10.1007/S11831-020-09457-7.
15. Elbadawi, M.; McCoubrey, L.E.; Gavins, F.K.H.; Ong, J.J.; Goyanes, A.; Gaisford, S.; Basit, A.W. Harnessing Artificial Intelligence for the next Generation of 3D Printed Medicines. *Advanced Drug Delivery Reviews* **2021**, *175*, doi:10.1016/J.ADDR.2021.05.015.
16. Bueno, A.; Godinho Filho, M.; Frank, A.G. Smart Production Planning and Control in the Industry 4.0 Context: A Systematic Literature Review. *Computers and Industrial Engineering* **2020**, *149*, doi:10.1016/J.CIE.2020.106774.
17. Bonnard, R.; Hascoët, J.Y.; Mognol, P.; Stroud, I. STEP-NC Digital Thread for Additive Manufacturing: Data Model, Implementation and Validation. *International Journal of Computer Integrated Manufacturing* **2018**, *31*, 1141–1160, doi:10.1080/0951192X.2018.1509130.
18. Silva, N.R.F.A.; Witek, L.; Coelho, P.G.; Thompson, V.P.; Rekow, E.D.; Smay, J. Additive CAD/CAM Process for Dental Prostheses. *Journal of Prosthodontics* **2011**, *20*, 93–96, doi:10.1111/J.1532-849X.2010.00623.X.

19. Mendes-Felipe, C.; Oliveira, J.; Etxebarria, I.; Vilas-Vilela, J.L.; Lanceros-Mendez, S. State-of-the-Art and Future Challenges of UV Curable Polymer-Based Smart Materials for Printing Technologies. *Advanced Materials Technologies* **2019**, *4*, doi:10.1002/ADMT.201800618.
20. Kuang, X.; Roach, D.J.; Wu, J.; Hamel, C.M.; Ding, Z.; Wang, T.; Dunn, M.L.; Qi, H.J. Advances in 4D Printing: Materials and Applications. *Advanced Functional Materials* **2019**, *29*, doi:10.1002/ADFM.201805290.
21. Ngo, T.D.; Kashani, A.; Imbalzano, G.; Nguyen, K.T.Q.; Hui, D. Additive Manufacturing (3D Printing): A Review of Materials, Methods, Applications and Challenges. *Composites Part B: Engineering* **2018**, *143*, 172–196, doi:10.1016/J.COMPOSITESB.2018.02.012.
22. Standard Terminology for Additive Manufacturing Technologies, Available online: https://www.astm.org/f2792-12.html (accessed on 15 February 2022).
23. ASTM International - Standards Worldwide Available online: https://www.astm.org/ (accessed on 15 February 2022).
24. Nandwana, P.; Elliott, A.M.; Siddel, D.; Merriman, A.; Peter, W.H.; Babu, S.S. Powder Bed Binder Jet 3D Printing of Inconel 718: Densification, Microstructural Evolution and Challenges. *Current Opinion in Solid State and Materials Science* **2017**, *21*, 207–218, doi:10.1016/J.COSSMS.2016.12.002.
25. Naghieh, S.; Sarker, M.D.; Karamooz-Ravari, M.R.; McInnes, A.D.; Chen, X. Modeling of the Mechanical Behavior of 3D Bioplotted Scaffolds Considering the Penetration in Interlocked Strands. *Applied Sciences* **2018**, *8*, doi:10.3390/app8091422.
26. Mason, M.; Huang, T.; Landers, R.; Leu, M.; Hilmas, G. Freeform Extrusion of High Solids Loading Ceramic Slurries. Part 1: Extrusion Process Modeling. **2006**, 16.
27. Cazón, A.; Morer, P.; Matey, L. PolyJet Technology for Product Prototyping: Tensile Strength and Surface Roughness Properties. *Proceedings of the Institution of Mechanical Engineers, Part B: Journal of Engineering Manufacture* **2014**, *228*, 1664–1675, doi:10.1177/0954405413518515.
28. Lumpe, T.S.; Mueller, J.; Shea, K. Tensile Properties of Multi-Material Interfaces in 3D Printed Parts. *Materials & Design* **2019**, *162*, 1–9, doi:10.1016/J.MATDES.2018.11.024.

29. Gülcan, O.; Günaydın, K.; Tamer, A. The State of the Art of Material Jetting—A Critical Review. *Polymers (Basel)* **2021**, *13*, doi:10.3390/POLYM13162829.
30. Dämmer, G.; Gablenz, S.; Hildebrandt, A.; Major, Z. PolyJet-Printed Bellows Actuators: Design, Structural Optimization, and Experimental Investigation. *Frontiers in Robotics and AI* **2019**, *6*, doi:10.3389/frobt.2019.00034.
31. Dämmer, G.; Gablenz, S.; Hildebrandt, A.; Major, Z. Design of an Additively Manufacturable Multi-Material Light-Weight Gripper with Integrated Bellows Actuators. *Advances in Science, Technology and Engineering Systems Journal* **2019**, *4*, doi:10.25046/aj040204.
32. Tappa, K.; Jammalamadaka, U. Novel Biomaterials Used in Medical 3D Printing Techniques. *Journal of Functional Biomaterials* **2018**, *9*, doi:10.3390/JFB9010017.
33. Silva, M.R.; Pereira, A.M.; Sampaio, Á.M.; Pontes, A.J. Assessment of the Dimensional and Geometric Precision of Micro-Details Produced by Material Jetting. *Materials* **2021**, *14*, doi:10.3390/MA14081989.
34. Hanemann, T.; Bauer, W.; Knitter, R.; Woias, P. Rapid Prototyping and Rapid Tooling Techniques for the Manufacturing of Silicon, Polymer, Metal and Ceramic Microdevices. *MEMS/NEMS* **2007**, 801–869, doi:10.1007/0-387-25786-1_20.
35. Magdassi, S. *The Chemistry of Inkjet Inks*; Magdassi, S., Ed.; World Scientific Publishing: Singapore, 2010; ISBN 9789812818218 9812818219.
36. Revilla-León, M.; Özcan, M. Additive Manufacturing Technologies Used for Processing Polymers: Current Status and Potential Application in Prosthetic Dentistry. *Journal of Prosthodontics* **2019**, *28*, 146–158, doi:10.1111/JOPR.12801.
37. Derby, B.; Reis, N. Inkjet Printing of Highly Loaded Particulate Suspensions. *MRS Bulletin* **2003**, *28*, 815–818, doi:10.1557/MRS2003.230.
38. Vaezi, M.; Seitz, H.; Yang, S. A Review on 3D Micro-Additive Manufacturing Technologies. *The International Journal of Advanced Manufacturing Technology* **2013**, *67*, 1721–1754, doi:10.1007/s00170-012-4605-2.
39. Derby, B. Inkjet Printing Ceramics: From Drops to Solid. *J Eur Ceram Soc* **2011**, *31*, 2543–2550, doi:10.1016/j.jeurceramsoc.2011.01.016.
40. Zammit, D.; Safran, T.; Ponnudurai, N.; Jaberi, M.; Chen, L.; Noel, G.; Gilardino, M. Step-Specific Simulation: The Utility of 3D Printing for the

Fabrication of a Low-Cost, Learning Needs-Based Rhinoplasty Simulator. *Aesthetic Surgery Journal* **2020**, *40*, doi:10.1093/asj/sjaa048.

41. Mendible, G.A.; Rulander, J.A.; Johnston, S.P. Comparative Study of Rapid and Conventional Tooling for Plastics Injection Molding. *Rapid Prototyping Journal* **2017**, *23*, 344–352, doi:10.1108/RPJ-01-2016-0013.
42. Eufracio Aguilera, A.F.; Nagarajan, B.; Fleck, B.A.; Qureshi, A.J. Ferromagnetic Particle Structuring in Material Jetting - Manufacturing Control System and Software Development. **2019**, *34*, 545–551, doi:10.1016/J.PROMFG.2019.06.218.
43. Kamyshny, A.; Magdassi, S. Conductive Nanomaterials for Printed Electronics. *Small* **2014**, *10*, doi:10.1002/smll.201303000.
44. Gouzman, I.; Grossman, E.; Verker, R.; Atar, N.; Bolker, A.; Eliaz, N. Advances in Polyimide-Based Materials for Space Applications. *Advanced Materials* **2019**, *31*, 1807738, doi:10.1002/adma.201807738.
45. Zhang, F.; Saleh, E.; Vaithilingam, J.; Li, Y.; Tuck, C.J.; Hague, R.J.M.; Wildman, R.D.; He, Y. Reactive Material Jetting of Polyimide Insulators for Complex Circuit Board Design. *Additive Manufacturing* **2019**, *25*, 477–484, doi:10.1016/j.addma.2018.11.017.
46. Saleh, E.; Zhang, F.; He, Y.; Vaithilingam, J.; Fernandez, J.L.; Wildman, R.; Ashcroft, I.; Hague, R.; Dickens, P.; Tuck, C. 3D Inkjet Printing of Electronics Using UV Conversion. *Advanced Materials Technologies* **2017**, *2*, 1700134, doi:10.1002/admt.201700134.
47. Balandin, A.A.; Ghosh, S.; Bao, W.; Calizo, I.; Teweldebrhan, D.; Miao, F.; Lau, C.N. Superior Thermal Conductivity of Single-Layer Graphene. *Nano Letters* **2008**, *8*, 902–907, doi:10.1021/nl0731872.
48. MacDonald, E.; Wicker, R. Multiprocess 3D Printing for Increasing Component Functionality. *Science (1979)* **2016**, *353*, doi:10.1126/science.aaf2093.
49. Lu, L.; Zhang, Z.; Xu, J.; Pan, Y. 3D-Printed Polymer Composites with Acoustically Assembled Multidimensional Filler Networks for Accelerated Heat Dissipation. *Composites Part B: Engineering* **2019**, *174*, 106991, doi:10.1016/j.compositesb.2019.106991.
50. Bordia, R.K.; Kang, S.-J.L.; Olevsky, E.A. Current Understanding and Future Research Directions at the Onset of the next Century of Sintering Science and

Technology. *Journal of the American Ceramic Society* **2017**, *100*, 2314–2352, doi:10.1111/jace.14919.

51. Quill, T.J.; Smith, M.K.; Zhou, T.; Baioumy, M.G.S.; Berenguer, J.P.; Cola, B.A.; Kalaitzidou, K.; Bougher, T.L. Thermal and Mechanical Properties of 3D Printed Boron Nitride – ABS Composites. *Applied Composite Materials* **2018**, *25*, 1205–1217, doi:10.1007/s10443-017-9661-1.
52. Chen, H.; Ginzburg, V. v; Yang, J.; Yang, Y.; Liu, W.; Huang, Y.; Du, L.; Chen, B. Thermal Conductivity of Polymer-Based Composites: Fundamentals and Applications. *Progress in Polymer Science* **2016**, *59*, 41–85, doi:10.1016/j.progpolymsci.2016.03.001.
53. Check, C.; Chartoff, R.; Chang, S. Inkjet Printing of 3D Nano-Composites Formed by Photopolymerization of an Acrylate Monomer. *Reactive and Functional Polymers* **2015**, *97*, 116–122, doi:10.1016/J.REACTFUNCTPOLYM.2015.09.009.
54. Saleh, E.; Woolliams, P.; Clarke, B.; Gregory, A.; Greedy, S.; Smartt, C.; Wildman, R.; Ashcroft, I.; Hague, R.; Dickens, P.; et al. 3D Inkjet-Printed UV-Curable Inks for Multi-Functional Electromagnetic Applications. *Additive Manufacturing* **2017**, *13*, 143–148, doi:10.1016/j.addma.2016.10.002.
55. Danu, S.; Darsono; Marsongko UV-Curing of Titanium Dioxide Pigmented Epoxy Acrylate Coating on Ceramic Tiles. *Journal of the Ceramic Society of Japan* **2008**, *116*, 896–903, doi:10.2109/jcersj2.116.896.
56. Derby, B.; Reis, N. Inkjet Printing of Highly Loaded Particulate Suspensions. *MRS Bulletin* **2003**, *28*, 815–818, doi:10.1557/MRS2003.230.
57. DIMAP: DIMAP Available online: http://www.dimap-project.eu/ (accessed on 14 April 2022).
58. Ionita, C.N.; Mokin, M.; Varble, N.; Bednarek, D.R.; Xiang, J.; Snyder, K. v; Siddiqui, A.H.; Levy, E.I.; Meng, H.; Rudin, S. Challenges and Limitations of Patient-Specific Vascular Phantom Fabrication Using 3D Polyjet Printing. *Proc SPIE Int Soc Opt Eng* **2014**, *9038*, 90380M-90380M, doi:10.1117/12.2042266.
59. Gouzman, I.; Atar, N.; Grossman, E.; Verker, R.; Bolker, A.; Pokrass, M.; Sultan, S.; Sinwani, O.; Wagner, A.; Lück, T.; et al. 3D Printing of Bismaleimides: From New Ink Formulation to Printed Thermosetting Polymer Objects. *Advanced Materials Technologies* **2019**, *4*, 1900368, doi:10.1002/ADMT.201900368.

60. Wei, X.; Thakare, K.; Zeng, L.; Pei, Z.J. Experimental Investigation of Stratasys J750 PolyJet Printer: Effects of Finish Type and Shore Hardness on Dimensional Accuracy. In Proceedings of the ASME 2019 14th International Manufacturing Science and Engineering Conference; June 11 2019.
61. Derby, B. Additive Manufacture of Ceramics Components by Inkjet Printing. *Engineering* **2015**, *1*, 113–123, doi:10.15302/J-ENG-2015014.
62. Derby, B. Inkjet Printing Ceramics: From Drops to Solid. *J Eur Ceram Soc* **2011**, *31*, 2543–2550, doi:https://doi.org/10.1016/j.jeurceramsoc.2011.01.016.
63. Dimatix Material-Drucker DMP-2850 | Fujifilm [Deutschland] Available online: https://www.fujifilm.com/de/de/business/inkjet-solutions/inkjet-technology-integration/dmp-2850 (accessed on 29 March 2022).
64. Dimatix Materials Cartridge | Fujifilm [United States] Available online: https://www.fujifilm.com/us/en/business/inkjet-solutions/inkjet-technology-integration/materials-cartridge (accessed on 29 March 2022).
65. Fayazfar, H.; Liravi, F.; Ali, U.; Toyserkani, E. Additive Manufacturing of High Loading Concentration Zirconia Using High-Speed Drop-on-Demand Material Jetting. *The International Journal of Advanced Manufacturing Technology* **2020**, *109*, 2733–2746, doi:10.1007/s00170-020-05829-2.
66. Monne, M.A.; Grubb, P.M.; Stern, H.; Subbaraman, H.; Chen, R.T.; Chen, M.Y. Inkjet-Printed Graphene-Based 1 × 2 Phased Array Antenna. *Micromachines 2020, Vol. 11, Page 863* **2020**, *11*, 863, doi:10.3390/MI11090863.
67. Wijshoff, H. The Dynamics of the Piezo Inkjet Printhead Operation. *Physics Reports* **2010**, *491*, 77–177, doi:10.1016/J.PHYSREP.2010.03.003.
68. Martin, G.D.; Hoath, S.D.; Hutchings, I.M. Inkjet Printing - the Physics of Manipulating Liquid Jets and Drops. *Journal of Physics: Conference Series* **2008**, *105*, 012001, doi:10.1088/1742-6596/105/1/012001.
69. Derby, B. Inkjet Printing of Functional and Structural Materials: Fluid Property Requirements, Feature Stability, and Resolution. *40*, 395–414, doi:10.1146/annurev-matsci-070909-104502.
70. Fromm, J.E. Numerical Calculation of the Fluid Dynamics of Drop-on-Demand Jets. *IBM Journal of Research and Development* **1984**, *28*, 322–333, doi:10.1147/RD.283.0322.

71. Reis, N.; Derby, B. Ink Jet Deposition of Ceramic Suspensions: Modeling and Experiments of Droplet Formation. *MRS Online Proceedings Library (OPL)* **2000**, *625*, 65–70, doi:10.1557/PROC-625-117.

72. Derby, B. Inkjet Printing Ceramics: From Drops to Solid. *J Eur Ceram Soc* **2011**, *31*, 2543–2550, doi:10.1016/J.JEURCERAMSOC.2011.01.016.

73. Jo, B.W.; Lee, A.; Ahn, K.H.; Lee, S.J. Evaluation of Jet Performance in Drop-on-Demand (DOD) Inkjet Printing. *Korean Journal of Chemical Engineering* **2009**, *26*, 339–348, doi:10.1007/S11814-009-0057-2.

74. Duineveld, P.C.; de Kok, M.M.; Buechel, M.; Sempel, A.; Mutsaers, K.A.H.; van de Weijer, P.; Camps, I.G.J.; van de Biggelaar, T.; Rubingh, J.-E.J.M.; Haskal, E.I. Ink-Jet Printing of Polymer Light-Emitting Devices. *Organic Light-Emitting Materials and Devices V* **2002**, *4464*, 59, doi:10.1117/12.457460.

75. Field, A.D. An Experimental Investigation of Fluid Flow Resulting from the Impact of a Water Drop with an Unyielding Dry Surface. *Proceedings of the Royal Society of London. A. Mathematical and Physical Sciences* **1981**, *373*, 419–441, doi:10.1098/RSPA.1981.0002.

76. Bhola, R.; Chandra, S. Parameters Controlling Solidification of Molten Wax Droplets Falling on a Solid Surface. *Journal of Materials Science* **1999**, *34*, 4883–4894, doi:10.1023/A:1004680315199.

77. Haskal, E.I.; Buechel, M.; Dijksman, J.F.; Duineveld, P.C.; Meulenkamp, E.A.; Mutsaers, C.A.H.A.; Sempel, A.; Snijder, P.; Vulto, S.I.E.; van de Weijer, P.; et al. 21.1: Ink Jet Printing of Passive-Matrix Polymer Light Emitting Displays. *SID Symposium Digest of Technical Papers* **2002**, *33*, 776, doi:10.1889/1.1830897.

78. Xu, D.; Sanchez-Romaguera, V.; Barbosa, S.; Travis, W.; de Wit, J.; Swan, P.; Yeates, S.G. Inkjet Printing of Polymer Solutions and the Role of Chain Entanglement. *Journal of Materials Chemistry* **2007**, *17*, 4902–4907, doi:10.1039/B710879F.

79. Reis, N.; Ainsley, C.; Derby, B. Ink-Jet Delivery of Particle Suspensions by Piezoelectric Droplet Ejectors. *Journal of Applied Physics* **2005**, *97*, doi:10.1063/1.1888026.

80. Reis, N.; Ainsley, C.; Derby, B. Viscosity and Acoustic Behavior of Ceramic Suspensions Optimized for Phase-Change Ink-Jet Printing. *Journal of the*

American Ceramic Society **2005**, *88*, 802–808, doi:10.1111/J.1551-2916.2005.00138.X.

81. Antohe, B.; Wallace, D.B. Acoustic Phenomena in a Demand-Mode Piezoelectric Ink-Jet Printer. *Journal of Imaging Science and Technology* **2002**, *46*, 409–414.
82. Yarin, A.L. Drop Impact Dynamics: Splashing, Spreading, Receding, Bouncing.. *Annual Review of Fluid Mechanics* **2006**, *38*, 159–192, doi:10.1146/ANNUREV.FLUID.38.050304.092144.
83. Shi, Q.; Yu, K.; Kuang, X.; Mu, X.; Dunn, C.K.; Dunn, M.L.; Wang, T.; Jerry Qi, H. Recyclable 3D Printing of Vitrimer Epoxy. *Materials Horizons* **2017**, *4*, 598–607, doi:10.1039/C7MH00043J.
84. Robertson, I.D.; Yourdkhani, M.; Centellas, P.J.; Aw, J.E.; Ivanoff, D.G.; Goli, E.; Lloyd, E.M.; Dean, L.M.; Sottos, N.R.; Geubelle, P.H.; et al. Rapid Energy-Efficient Manufacturing of Polymers and Composites via Frontal Polymerization. *Nature 2018 557:7704* **2018**, *557*, 223–227, doi:10.1038/s41586-018-0054-x.
85. Rodriguez, J.N.; Zhu, C.; Duoss, E.B.; Wilson, T.S.; Spadaccini, C.M.; Lewicki, J.P. Shape-Morphing Composites with Designed Micro-Architectures. *Scientific Reports 2016 6:1* **2016**, *6*, 1–10, doi:10.1038/srep27933.
86. Baekeland, L.H. The Synthesis, Constitution, and Uses of Bakelite. *Industrial and Engineering Chemistry* **2002**, *1*, 149–161, doi:10.1021/IE50003A004.
87. Bryce, D. *Plastic Injection Molding: Manufacturing Process Fundamentals*; Society of manufacturing engineers: Dearborn, 1996;
88. Broutman, L.; Agarwal, B. *Analysis and Performance of Fiber Composites*; Wiley: Hoboken, 1980; ISBN 978-1-119-38998-9.
89. Advani, S.; Hsiao, K. *Manufacturing Techniques for Polymer Matrix Composites (PMCs)*; Woodhead Publishing: Cambridge, 2012; ISBN 978-0-85709-625-8.
90. Rouison, D.; Sain, M.; Couturier, M. Resin Transfer Molding of Natural Fiber Reinforced Composites: Cure Simulation. *Composites Science and Technology* **2004**, *64*, 629–644, doi:10.1016/j.compscitech.2003.06.001.
91. Kuang, X.; Zhao, Z.; Chen, K.; Fang, D.; Kang, G.; Jerry Qi, H.; Kuang, X.; Zhao, Z.; Chen, K.; Qi, H.J.; et al. High-speed 3D Printing of High-performance

Thermosetting Polymers via Two-stage Curing. *Wiley Online Library* **2018**, *39*, doi:10.1002/marc.201700809.

92. Fette, M.; Sander, P.; Wulfsberg, J.; Zierk, H.; Herrmann, A.; Stoess, N. Optimized and Cost-Efficient Compression Molds Manufactured by Selective Laser Melting for the Production of Thermoset Fiber Reinforced Plastic Aircraft Components. *Procedia CIRP* **2015**, *35*, 25–30, doi:10.1016/j.procir.2015.08.082.
93. Chandrasekaran, S.; Duoss, E.B.; Worsley, M.A.; Lewicki, J.P. 3D Printing of High Performance Cyanate Ester Thermoset Polymers. *J. Mater. Chem. A* **2018**, *6*, 853–858, doi:10.1039/C7TA09466C.
94. Taormina, G.; Sciancalepore, C.; Bondioli, F.; Messori, M. Special Resins for Stereolithography: In Situ Generation of Silver Nanoparticles. *Polymers (Basel)* **2018**, *10*, doi:10.3390/polym10020212.
95. Lewicki, J.P.; Rodriguez, J.N.; Zhu, C.; Worsley, M.A.; Wu, A.S.; Kanarska, Y.; Horn, J.D.; Duoss, E.B.; Ortega, J.M.; Elmer, W.; et al. 3D-Printing of Meso-Structurally Ordered Carbon Fiber/Polymer Composites with Unprecedented Orthotropic Physical Properties. *Scientific Reports* **2017**, *7*, 43401, doi:10.1038/srep43401.
96. Anseth, K.S.; Newman, S.M.; Bowman, C.N. Polymeric Dental Composites: Properties and Reaction Behavior of Multimethacrylate Dental Restorations. *Advances in Polymer Science* **1995**, *122*, 176–217, doi:10.1007/3540587888_16.
97. Hutchison, J.B.; Haraldsson, K.T.; Good, B.T.; Sebra, R.P.; Luo, N.; Anseth, K.S.; Bowman, C.N. Robust Polymer Microfluidic Device Fabrication via Contact Liquid Photolithographic Polymerization (CLiPP). *Lab Chip* **2004**, *4*, 658–662, doi:10.1039/B405985A.
98. Berchtold, K.A.; Nie, J.; Stansbury, J.W.; Hacioğlu, B.; Beckel, E.R.; Bowman, C.N. Novel Monovinyl Methacrylic Monomers Containing Secondary Functionality for Ultrarapid Polymerization: Steady-State Evaluation. *Macromolecules* **2004**, *37*, 3165–3179, doi:10.1021/ma035862+.
99. McMahon, T.T.; Zadnik, K. Twenty-Five Years of Contact Lenses: The Impact on the Cornea and Ophthalmic Practice. *Cornea* **2000**, *19*, doi:10.1097/00003226-200009000-00018.

100. Anseth, K.S.; Metters, A.T.; Bryant, S.J.; Martens, P.J.; Elisseeff, J.H.; Bowman, C.N. In Situ Forming Degradable Networks and Their Application in Tissue Engineering and Drug Delivery. *Journal of Controlled Release* **2002**, *78*, 199–209, doi:10.1016/S0168-3659(01)00500-4.
101. Willson, C.G.; Trinque, B.C. The Evolution of Materials for the Photolithographic Process. *Journal of Photopolymer Science and Technology* **2003**, *16*, 621–627, doi:10.2494/photopolymer.16.621.
102. Khire, V.S.; Lee, T.Y.; Bowman, C.N. Surface Modification Using Thiol−Acrylate Conjugate Addition Reactions. *Macromolecules* **2007**, *40*, 5669–5677, doi:10.1021/ma070146j.
103. Francis, L.F.; McCormick, A. v.; Vaessen, D.M.; Payne, J.A. Development and Measurement of Stress in Polymer Coatings. *Journal of Materials Science* **2002**, *37*, 4717–4731, doi:10.1023/A:1020886802632.
104. Bowman, C.N.; Peppas, N.A. Coupling of Kinetics and Volume Relaxation during Polymerizations of Multiacrylates and Multimethacrylates. *Macromolecules* **1991**, *24*, 1914–1920, doi:10.1021/MA00008A032.
105. O'Brien, A.K.; Bowman, C.N. Impact of Oxygen on Photopolymerization Kinetics and Polymer Structure. *Macromolecules* **2006**, *39*, 2501–2506, doi:10.1021/ma051863l.
106. Ligon-Auer, S.C.; Schwentenwein, M.; Gorsche, C.; Stampfl, J.; Liska, R. Toughening of Photo-Curable Polymer Networks: A Review. *Polymer Chemistry* **2016**, *7*, 257–286, doi:10.1039/C5PY01631B.
107. Bowman, C.N.; Kloxin, C.J. Toward an Enhanced Understanding and Implementation of Photopolymerization Reactions. *AIChE Journal* **2008**, *54*, 2775–2795, doi:10.1002/aic.11678.
108. Anseth, K.S.; Rothenberg, M.D.; Bowman, C.N. A Photochromic Technique To Study Polymer Network Volume Distributions and Microstructure during Photopolymerizations. *Macromolecules* **1994**, *27*, 2890–2892, doi:10.1021/MA00088A034.
109. Kannurpatti, A.R.; Anseth, J.W.; Bowman, C.N. A Study of the Evolution of Mechanical Properties and Structural Heterogeneity of Polymer Networks Formed by Photopolymerizations of Multifunctional (Meth)Acrylates. *Polymer (Guildf)* **1998**, *39*, 2507–2513, doi:10.1016/S0032-3861(97)00585-5.

110. Goodner, M.D.; Bowman, C.N. Development of a Comprehensive Free Radical Photopolymerization Model Incorporating Heat and Mass Transfer Effects in Thick Films. *Chemical Engineering Science* **2002**, *57*, 887–900, doi:10.1016/S0009-2509(01)00287-1.
111. O'Neil, G.A.; Torkelson, J.M. Modeling Insight into the Diffusion-Limited Cause of the Gel Effect in Free Radical Polymerization. *Macromolecules* **1999**, *32*, 411–422, doi:10.1021/ma9811324.
112. Fouassier, J.; Rabek, J. *Radiation Curing in Polymer Science and Technology: Practical Aspects and Applications*; Springer Dordrecht, 1993; ISBN 978-1851669387.
113. Hoyle, C.E.; Lee, T.Y.; Roper, T. Thiol–Enes: Chemistry of the Past with Promise for the Future. *Journal of Polymer Science Part A: Polymer Chemistry* **2004**, *42*, 5301–5338, doi:10.1002/pola.20366.
114. Cantó-Mirapeix, A.; Herrero-Martínez, J.M.; Mongay-Fernández, C.; Simó-Alfonso, E.F. Lauroyl Peroxide as Thermal Initiator of Lauryl Methacrylate Monolithic Columns for CEC. *ELECTROPHORESIS* **2008**, *29*, 4399–4406, doi:10.1002/ELPS.200800317.
115. Bowman, C.; Journal, C.K.-Aic.; 2008, undefined Toward an Enhanced Understanding and Implementation of Photopolymerization Reactions. *Wiley Online Library* **2007**, *54*, 2775–2795, doi:10.1002/aic.11678.
116. Miller, G.A.; Gou, L.; Narayanan, V.; Scranton, A.B. Modeling of Photobleaching for the Photoinitiation of Thick Polymerization Systems. *Journal of Polymer Science, Part A: Polymer Chemistry* **2002**, *40*, 793–808, doi:10.1002/POLA.10162.
117. Kurdikar, D.L.; Peppas, N.A. Method of Determination of Initiator Efficiency: Application to UV Polymerizations Using 2,2-Dimethoxy-2-Phenylacetophenone. *Macromolecules* **1994**, *27*, 733–738, doi:10.1021/MA00081A017.
118. Goodner, M.D.; Bowman, C.N. Modeling Primary Radical Termination and Its Effects on Autoacceleration in Photopolymerization Kinetics. *Macromolecules* **1999**, *32*, 6552–6559, doi:10.1021/ma9901947.
119. Buback, M.; Gilbert, R.G.; Russell, G.T.; Hill, D.J.T.; Moad, G.; O'Driscoll, K.F.; Shen, J.; Winnik, M.A. Consistent Values of Rate Parameters in Free Radical Polymerization Systems. II. Outstanding Dilemmas and

Recommendations. *Journal of Polymer Science Part A: Polymer Chemistry* **1992**, *30*, 851–863, doi:10.1002/POLA.1992.080300516.

120. Russell, G.T.; Gilbert, R.G.; Napper, D.H. Chain-Length-Dependent Termination Rate Processes in Free-Radical Polymerizations. 1. Theory. *Macromolecules* **1992**, *25*, 2459–2469, doi:10.1021/MA00035A026.
121. Berchtold, K.A.; Randolph, T.W.; Bowman, C.N. Propagation and Termination Kinetics of Cross-Linking Photopolymerizations Studied Using Electron Paramagnetic Resonance Spectroscopy in Conjunction with Near IR Spectroscopy. *Macromolecules* **2005**, *38*, 6954–6964, doi:10.1021/ma0506482.
122. Elliott, J.E.; Macdonald, M.; Nie, J.; Bowman, C.N. Structure and Swelling of Poly(Acrylic Acid) Hydrogels: Effect of PH, Ionic Strength, and Dilution on the Crosslinked Polymer Structure. *Polymer (Guildf)* **2004**, *45*, 1503–1510, doi:10.1016/j.polymer.2003.12.040.
123. Zhu, S.; Hamielec, A.E. Chain-Length-Dependent Termination for Free Radical Polymerization. *Macromolecules* **1989**, *22*, 3093–3098, doi:10.1021/MA00197A033.
124. Buback, M.; Gilbert, R.G.; Russell, G.T.; Hill, D.J.T.; Moad, G.; O'Driscoll, K.F.; Shen, J.; Winnik, M.A. Consistent Values of Rate Parameters in Free Radical Polymerization Systems. II. Outstanding Dilemmas and Recommendations. *Journal of Polymer Science Part A: Polymer Chemistry* **1992**, *30*, 851–863, doi:10.1002/POLA.1992.080300516.
125. Gou, L.; Opheim, B.; Coretsopoulos, C.N.; Scranton, A.B. Consumption of the Molecular Oxygen in Polymerization Systems Using Photosensitized Oxidation of Dimethylanthracene. *Chemical Engineering Communications* **2006**, *193*, 620–627, doi:10.1080/00986440500193921.
126. O'Brien, A.K.; Cramer, N.B.; Bowman, C.N. Oxygen Inhibition in Thiol–Acrylate Photopolymerizations. *Journal of Polymer Science Part A: Polymer Chemistry* **2006**, *44*, 2007–2014, doi:10.1002/pola.21304.
127. Kannurpatti, A.R.; Anderson, K.J.; Anseth, J.W.; Bowman, C.N. Use of "'Living'" Radical Polymerizations to Study the Structural Evolution and Properties of Highly Crosslinked Polymer Networks. *J Polym Sci B: Polym Phys* **1997**, *35*, 2297–2307, doi:10.1002/(SICI)1099-0488(199710)35:14.

128. Lovell, L.G.; Lu, H.; Elliott, J.E.; Stansbury, J.W.; Bowman, C.N. The Effect of Cure Rate on the Mechanical Properties of Dental Resins. *Dental Materials* **2001**, *17*, 504–511, doi:10.1016/S0109-5641(01)00010-0.
129. Kloosterboer, J.G. Network Formation by Chain Crosslinking Photopolymerization and Its Applications in Electronics. *Electronic Applications* **2005**, 1–61, doi:10.1007/BFB0025902.
130. Hutchison, J.B.; Lindquist, A.S.; Anseth, K.S. Experimental Characterization of Structural Features during Radical Chain Homopolymerization of Multifunctional Monomers Prior to Macroscopic Gelation. *Macromolecules* **2004**, *37*, 3823–3831, doi:10.1021/ma035400w.
131. Asif, A.; Shi, W.; Shen, X.; Nie, K. Physical and Thermal Properties of UV Curable Waterborne Polyurethane Dispersions Incorporating Hyperbranched Aliphatic Polyester of Varying Generation Number. *Polymer (Guildf)* **2005**, *46*, 11066–11078, doi:10.1016/J.POLYMER.2005.09.046.
132. Miklečić, J.; Blagojević, S.L.; Petrič, M.; Jirouš-Rajković, V. Influence of TiO2 and ZnO Nanoparticles on Properties of Waterborne Polyacrylate Coating Exposed to Outdoor Conditions. *Progress in Organic Coatings* **2015**, *89*, 67–74, doi:10.1016/J.PORGCOAT.2015.07.016.
133. Ngan, C.G.Y.; O'Connell, C.D.; Blanchard, R.; Boyd-Moss, M.; Williams, R.J.; Bourke, J.; Quigley, A.; McKelvie, P.; Kapsa, R.M.I.; Choong, P.F.M. Optimising the Biocompatibility of 3D Printed Photopolymer Constructs in Vitro and in Vivo. *Biomedical Materials* **2019**, *14*, 035007, doi:10.1088/1748-605X/AB09C4.
134. Dorfinger, P.; Stampfl, J.; Liska, R. Toughening of Photopolymers for Stereolithography (SL). *Materials Science Forum* **2015**, *825–826*, 53–59, doi:10.4028/www.scientific.net/MSF.825-826.53.
135. Boots, H.M.J.; Kloosterboer, J.G.; van de Hei, G.M.M.; Pandey, R.B. Inhomogeneity during the Bulk Polymerisation of Divinyl Compounds: Differential Scanning Calorimetry Experiments and Percolation Theory. *British Polymer Journal* **1985**, *17*, 219–223, doi:10.1002/PI.4980170224.
136. Brian Hutchison, J.; Lindquist, A.S.; Anseth, K.S. Experimental Characterization of Structural Features during Radical Chain Homopolymerization of Multifunctional Monomers Prior to Macroscopic Gelation. *Macromolecules* **2004**, *37*, 3823–3831, doi:10.1021/MA035400W.

137. Aktuelles - Rahn AG Available online: https://www.rahn-group.com/de/energycuring/aktuell/ (accessed on 19 February 2022).
138. Oldring, P.K.T.Peter. *Chemistry & Technology of UV & EB Formulation for Coatings, Inks & Paints*; SITA Technology: Leipzig, 1991; ISBN 978-0947798109.
139. Gibson, I.; Rosen, D.; Stucker, B.; Khorasani, M. Material Jetting. *Additive Manufacturing Technologies* **2021**, 203–235, doi:10.1007/978-3-030-56127-7_7.
140. Xu, P.; Ruatta, S.; Schmidt, K.; VA Doan Phase Change Support Material Composition. *Google Patents* 2007.
141. KA Schmidt Selective Deposition Modeling with Curable Phase Change Materials. *Google Patents* 2005.
142. ProJet MJP 5600 – 3D Drucker | 3D Systems Available online: https://de.3dsystems.com/3d-printers/projet-mjp-5600 (accessed on 19 February 2022).
143. PolyJet 3D-Druckverfahren | Stratasys Available online: https://www.stratasys.com/de/polyjet-technology (accessed on 19 February 2022).
144. Dodiuk, H.; Goodman, S.H. Handbook of Thermoset Plastics. In *Handbook of Thermoset Plastics (Third Edition)*; Dodiuk, H., Goodman, S.H., Eds.; William Andrew Publishing: Boston, 2014; pp. 1–12 ISBN 978-1-4557-3107-7.
145. Asif, A.; Shi, W.; Shen, X.; Nie, K. Physical and Thermal Properties of UV Curable Waterborne Polyurethane Dispersions Incorporating Hyperbranched Aliphatic Polyester of Varying Generation Number. *Polymer (Guildf)* **2005**, *46*, 11066–11078, doi:10.1016/J.POLYMER.2005.09.046.
146. Digital ABS Plus - 3DDrucker.De Available online: https://3ddrucker.de/materialien/polyjet-materialien/digital-abs/ (accessed on 19 February 2022).
147. VisiJet M2R-CL (MJP) | 3D Systems Available online: https://de.3dsystems.com/materials/visijet-m2r-cl-mjp (accessed on 19 February 2022).
148. VisiJet M2S-HT90 Hochtemperaturbeständiger Kunststoff l 3D Systems Available online: https://de.3dsystems.com/materials/visijet-m2s-ht90-mjp (accessed on 19 February 2022).

149. Ebadi-Dehaghani, H.; Nazempour, M. *Thermal Conductivity of Nanoparticles Filled Polymers*; InTech: Rijeka, 2012; ISBN 978-953-51-0500-8.
150. Kovacs, J.G.; Kortelyesi, G.; Kovacs, N.K.; Suplicz, A. Evaluation of Measured and Calculated Thermal Parameters of a Photopolymer. *International Communications in Heat and Mass Transfer* **2011**, *38*, 863–867, doi:10.1016/J.ICHEATMASSTRANSFER.2011.04.001.
151. Goldin, N.; Dodiuk, H.; Lewitus, D. Enhanced Thermal Conductivity of Photopolymerizable Composites Using Surface Modified Hexagonal Boron Nitride Fillers. *Composites Science and Technology* **2017**, *152*, 36–45, doi:10.1016/J.COMPSCITECH.2017.09.001.
152. Shi, F. *Ceramic Materials Progress in Modern Ceramics.*; InTech: Rijeka, 2012; ISBN 978-953-51-0476-6.
153. Tong, X.C. Advanced Materials for Thermal Management of Electronic Packaging. **2011**, *30*, doi:10.1007/978-1-4419-7759-5.
154. Kurian, M.; Thankachan, S.; Nair, S.S. *Ceramic Catalysts: Materials, Synthesis, and Applications.*; Elsevier Science: Amsterdam, 2022; ISBN 0323857469.
155. Lakshmanan, A. *Sintering of Ceramics: New Emerging Techniques*; Intech: Rijeka, 2012; ISBN 978-953-51-0017-1.
156. Jaffe, B.; Cook, W.R.; Jaffe, H. Piezoelectric Ceramics. In *Piezoelectric Ceramics*; JAFFE, B., COOK, W.R., JAFFE, H., Eds.; Academic Press, 1971; pp. 1–5 ISBN 978-0-12-379550-2.
157. Schadler, L.S.; Kumar, S.K.; Benicewicz, B.C.; Lewis, S.L.; Harton, S.E. Designed Interfaces in Polymer Nanocomposites: A Fundamental Viewpoint. *MRS Bulletin* **2007**, *32*, 335–340, doi:10.1557/mrs2007.232.
158. Chen, L.; Qian, L. Role of Interfacial Water in Adhesion, Friction, and Wear—A Critical Review. *Friction* **2021**, *9*, doi:10.1007/S40544-020-0425-4.
159. Acikgoz, M.; Harrell, J.; Pavanello, M. Seeking a Structure-Function Relationship for γ-Al2O3 Surfaces. *Journal of Physical Chemistry C* **2018**, *122*, 25314–25330, doi:10.1021/ACS.JPCC.8B06506.
160. Baumgarten, E.; Wagner, R.; Lentes-Wagner, C. Quantitative Determination of Hydroxyl Groups on Alumina by IR Spectroscopy. *Fresenius' Zeitschrift für Analytische Chemie* **1989**, *334*, 246–251, doi:10.1007/BF00497251.

161. Koga, N.; Fukagawa, T.; Tanaka, H. Preparation and Thermal Decomposition of Synthetic Bayerite. *Journal of Thermal Analysis and Calorimetry* **2001**, *64*, 965–972, doi:10.1023/A:1011531215596.

162. Bauer, J.; Hengsbach, S.; Tesari, I.; Schwaiger, R.; Kraft, O. High-Strength Cellular Ceramic Composites with 3D Microarchitecture. *Proc Natl Acad Sci U S A* **2014**, *111*, 2453–2458, doi:10.1073/PNAS.1315147111/-/DCSUPPLEMENTAL/SM03.MP4.

163. Dörre, E.; Hübner, H. *Alumina : Processing, Properties, and Applications*; Springer-Verlag: Berlin, 1984; ISBN 3540135766.

164. Stuart, J.T. Thermal Conduction in Artificial Sapphire Crystals at Low Temperatures I. Nearly Perfect Crystals. *Proceedings of the Royal Society of London. Series A. Mathematical and Physical Sciences* **1955**, *231*, 130–144, doi:10.1098/RSPA.1955.0161.

165. Sato, T. Thermal Decomposition of Aluminium Hydroxides. *Journal of Thermal Analysis* **1987**, *32*, 61–70, doi:10.1007/BF01914548.

166. Morterra, C.; Magnacca, G. A Case Study: Surface Chemistry and Surface Structure of Catalytic Aluminas, as Studied by Vibrational Spectroscopy of Adsorbed Species. *Catalysis Today* **1996**, *27*, 497–532, doi:https://doi.org/10.1016/0920-5861(95)00163-8.

167. Calvin, J.J.; Rosen, P.F.; Ross, N.L.; Navrotsky, A.; Woodfield, B.F. Review of Surface Water Interactions with Metal Oxide Nanoparticles. *Journal of Materials Research* **2019**, *34*, 416–427, doi:10.1557/JMR.2019.33.

168. McHale, J.M.; Auroux, A.; Perrotta, A.J.; Navrotsky, A. Surface Energies and Thermodynamic Phase Stability in Nanocrystalline Aluminas. *Science (1979)* **1997**, *277*, 788–789, doi:10.1126/SCIENCE.277.5327.788.

169. Navrotsky, A. Energetics of Nanoparticle Oxides: Interplay between Surface Energy and Polymorphism†. *Geochemical Transactions* **2003**, *4*, doi:10.1186/1467-4866-4-34.

170. Hanemann, T.; Szabó, D.V. Polymer-Nanoparticle Composites: From Synthesis to Modern Applications. *Materials* 2010, *3*.

171. Bourgeat-Lami, E.; Lang, J. Encapsulation of Inorganic Particles by Dispersion Polymerization in Polar Media: 1. Silica Nanoparticles Encapsulated by Polystyrene. *Journal of Colloid and Interface Science* **1998**, *197*, 293–308, doi:10.1006/jcis.1997.5265.

172. Fu, S.-Y.; Feng, X.-Q.; Lauke, B.; Mai, Y.-W. Effects of Particle Size, Particle/Matrix Interface Adhesion and Particle Loading on Mechanical Properties of Particulate–Polymer Composites. *Composites Part B: Engineering* **2008**, *39*, 933–961, doi:10.1016/J.COMPOSITESB.2008.01.002.
173. Consiglio, R.; Baker, D.R.; Paul, G.; Stanley, H.E. Continuum Percolation Thresholds for Mixtures of Spheres of Different Sizes. *Physica A: Statistical Mechanics and its Applications* **2003**, *319*, 49–55, doi:10.1016/S0378-4371(02)01501-7.
174. Burger, N.; Laachachi, A.; Ferriol, M.; Lutz, M.; Toniazzo, V.; Ruch, D. Review of Thermal Conductivity in Composites: Mechanisms, Parameters and Theory. *Progress in Polymer Science* **2016**, *61*, 1–28, doi:10.1016/j.progpolymsci.2016.05.001.
175. Vollath, D.; Fischer, F.D.; Holec, D. Surface Energy of Nanoparticles – Influence of Particle Size and Structure. *Beilstein Journal of Nanotechnology* **2018**, *9*, 2265–2276.
176. Mittal, K.L. *Acid-Base Interactions Relevance to Adhesion Science and Technology*; VSP Publishing: Zeist, 2000; ISBN 978-9-06-764325-2.
177. Goniakowski, J.; Finocchi, F.; Noguera, C. Polarity of Oxide Surfaces and Nanostructures. *Reports on Progress in Physics* **2007**, *71*, 16501, doi:10.1088/0034-4885/71/1/016501.
178. Israelachvili, J.N. *Intermolecular and Surface Forces*; Third Edition.; Academic Press: San Diego, 2011; ISBN 978-0-12-375182-9.
179. Verwey, E.J.W. Theory of the Stability of Lyophobic Colloids. *Journal of Physical and Colloid Chemistry* **2002**, *51*, 631–636, doi:10.1021/J150453A001.
180. Derjaguin, B.; Landau, L. Theory of the Stability of Strongly Charged Lyophobic Sols and of the Adhesion of Strongly Charged Particles in Solutions of Electrolytes. *Progress in Surface Science* **1993**, *43*, 30–59, doi:10.1016/0079-6816(93)90013-L.
181. van Oss, C.J.; Giese, R.F.; Costanzo, P.M. DLVO and Non-DLVO Interactions in Hectorite. *Clays and Clay Minerals* **1990**, *38*, 151–159, doi:10.1346/CCMN.1990.0380206.
182. Park, S.-J.; Seo, M.-K. *Interface Science and Composites*; Academic Press: Cambridge, 2011; ISBN 9780080963488.

183. Park, S.J.; Seo, M.K. Intermolecular Force. *Interface Science and Technology* **2011**, *18*, 1–57, doi:10.1016/B978-0-12-375049-5.00001-3.

184. van Oss, C.J.; Chaudhury, M.K.; Good, R.J. Interfacial Lifshitz-van Der Waals and Polar Interactions in Macroscopic Systems. *Chemical Reviews* **2002**, *88*, 927–941, doi:10.1021/CR00088A006.

185. Fowkes, F.M. Additivity of Intermolecular Forces at Interfaces. I. Determination of the Contribution to Surface and Interfacial Tensions of Dispersion Forces in Various Liquids 1. *The Journal of Physical Chemistry* **2002**, *67*, 2538–2541, doi:10.1021/J100806A008.

186. Chaudhury, M.Kumar.; Pocius, A. v. *Surfaces, Chemistry and Applications*; Elsevier Science: Amsterdam, 2002; ISBN 9780080525983.

187. Horn, R.G. Surface Forces and Their Action in Ceramic Materials. *Journal of the American Ceramic Society* **1990**, *73*, 1117–1135, doi:10.1111/J.1151-2916.1990.TB05168.X.

188. Lewis, J.A. Colloidal Processing of Ceramics. *Journal of the American Ceramic Society* **2000**, *83*, 2341–2359, doi:10.1111/J.1151-2916.2000.TB01560.X.

189. Kerkar, A. v.; Henderson, R.J.M.; Feke, D.L. Steric Stabilization of Nonaqueous Silicon Slips: I, Control of Particle Agglomeration and Packing. *Journal of the American Ceramic Society* **1990**, *73*, 2879–2885, doi:10.1111/J.1151-2916.1990.TB06689.X.

190. Pashley, R.M.; Israelachvili, J.N. A Comparison of Surface Forces and Interfacial Properties of Mica in Purified Surfactant Solutions. *Colloids and Surfaces* **1981**, *2*, 169–187, doi:10.1016/0166-6622(81)80006-6.

191. Patel, S.S.; Tirrell, M. Measurement of Forces Between Surfaces in Polymer Fluids. *https://doi.org/10.1146/annurev.pc.40.100189.003121* **2003**, *40*, 597–635, doi:10.1146/ANNUREV.PC.40.100189.003121.

192. Napper, D.H. The Role of Polymers in the Stabilization of Disperse Systems. *Chem and Technol of Water-Soluble Polym* **1983**, 233–248, doi:10.1007/978-1-4757-9661-2_14.

193. Russel, W.B.; Saville, D.A.; Schowalter, W.R. Polymeric Stabilization. *Colloidal Dispersions* **1989**, 310–328, doi:10.1017/CBO9780511608810.012.

194. Vincent, B.; Edwards, J.; Emmett, S.; Jones, A. Depletion Flocculation in Dispersions of Sterically-Stabilised Particles ("Soft Spheres"). *Colloids and Surfaces* **1986**, *18*, 261–281, doi:10.1016/0166-6622(86)80317-1.

195. Bergström, L. Rheology of Concentrated Suspensions. In *Surface and Colloid Chemistry in Advanced Ceramics Processing*; Marcel Dekker: New York, 1994; pp. 193–239 ISBN 0-8247-9098-7.
196. Mewis, J.; Frith, W.J.; Strivens, T.A.; Russel, W.B. The Rheology of Suspensions Containing Polymerically Stabilized Particles. *AIChE Journal* **1989**, *35*, 415–422, doi:10.1002/AIC.690350309.
197. de Hek, H.; Vrij, A. Interactions in Mixtures of Colloidal Silica Spheres and Polystyrene Molecules in Cyclohexane: I. Phase Separations. *Journal of Colloid and Interface Science* **1981**, *84*, 409–422, doi:10.1016/0021-9797(81)90232-0.
198. Marra, J.; Israelachvili, J. Direct Measurements of Forces between Phosphatidylcholine and Phosphatidylethanolamine Bilayers in Aqueous Electrolyte Solutions. *Biochemistry* **2002**, *24*, 4608–4618, doi:10.1021/BI00338A020.
199. Krieger, I.M. Rheology of Monodisperse Latices. *Advances in Colloid and Interface Science* **1972**, *3*, 111–136, doi:10.1016/0001-8686(72)80001-0.
200. Bender, J.; Wagner, N.J. Reversible Shear Thickening in Monodisperse and Bidisperse Colloidal Dispersions. *Journal of Rheology* **1998**, *40*, 899, doi:10.1122/1.550767.
201. Marshall, L.; Zukoski IV, C.F. Experimental Studies on the Rheology of Hard-Sphere Suspensions near the Glass Transition. *Journal of Physical Chemistry* **1990**, *94*, 1164–1171, doi:10.1021/J100366A030.
202. Schadler, L.S.; Brinson, L.C.; Sawyer, W.G. Polymer Nanocomposites: A Small Part of the Story. *JOM* **2007**, *59*, 53–60, doi:10.1007/s11837-007-0040-5.
203. Voigt, W. *Lehrbuch Der Kristallphysik*; Vieweg+Teubner Verlag: Berlin, 1966;
204. Hashin, Z.; Shtrikman, S. A Variational Approach to the Theory of the Elastic Behaviour of Multiphase Materials. *Journal of the Mechanics and Physics of Solids* **1963**, *11*, 127–140, doi:10.1016/0022-5096(63)90060-7.
205. Christensen, R.M. A Critical Evaluation for a Class of Micro-Mechanics Models. *Journal of the Mechanics and Physics of Solids* **1990**, *38*, 379–404, doi:10.1016/0022-5096(90)90005-O.
206. Pal, R. New Models for Effective Young's Modulus of Particulate Composites. *Composites Part B: Engineering* **2005**, *36*, 513–523, doi:10.1016/J.COMPOSITESB.2005.02.003.

207. Dittanet, P.; Pearson, R.A. Effect of Silica Nanoparticle Size on Toughening Mechanisms of Filled Epoxy. *Polymer (Guildf)* **2012**, *53*, 1890–1905, doi:10.1016/J.POLYMER.2012.02.052.

208. Sprenger, S. Epoxy Resin Composites with Surface-Modified Silicon Dioxide Nanoparticles: A Review. *Journal of Applied Polymer Science* **2013**, *130*, 1421–1428, doi:10.1002/APP.39208.

209. Sudduth, R. Analysis of the Maximum Tensile Strength of a Composite with Spherical Particulates. *Journal of Composite Materials* **2006**, *40*, 301–331, doi:10.1177/0021998305055188.

210. Zhao, S.; Schadler, L.S.; Duncan, R.; Hillborg, H.; Auletta, T. Mechanisms Leading to Improved Mechanical Performance in Nanoscale Alumina Filled Epoxy. *Composites Science and Technology* **2008**, *68*, 2965–2975, doi:10.1016/J.COMPSCITECH.2008.01.009.

211. Schaefer, D.W.; Justice, R.S. How Nano Are Nanocomposites? *Macromolecules* **2007**, *40*, 8501–8517, doi:10.1021/ma070356w.

212. Crosby, A.J.; Lee, J. Polymer Nanocomposites: The "Nano" Effect on Mechanical Properties. *Polymer Reviews* **2007**, *47*, 217–229, doi:10.1080/15583720701271278.

213. Peters, R.; Litvinov, V.M.; Steeman, P.; Dias, A.A.; Mengerink, Y.; van Benthem, R.; de Koster, C.G.; van der Wal, S.; Schoenmakers, P. Characterisation of UV-Cured Acrylate Networks by Means of Hydrolysis Followed by Aqueous Size-Exclusion Combined with Reversed-Phase Chromatography. *J Chromatogr A* **2007**, *1156*, 111–123, doi:10.1016/J.CHROMA.2006.10.071.

214. Liang, Y.L.; Pearson, R.A. Toughening Mechanisms in Epoxy–Silica Nanocomposites (ESNs). *Polymer (Guildf)* **2009**, *50*, 4895–4905, doi:10.1016/J.POLYMER.2009.08.014.

215. Johnsen, B.B.; Kinloch, A.J.; Mohammed, R.D.; Taylor, A.C.; Sprenger, S. Toughening Mechanisms of Nanoparticle-Modified Epoxy Polymers. *Polymer (Guildf)* **2007**, *48*, 530–541, doi:10.1016/J.POLYMER.2006.11.038.

216. Fu, S.Y.; Feng, X.Q.; Lauke, B.; Mai, Y.W. Effects of Particle Size, Particle/Matrix Interface Adhesion and Particle Loading on Mechanical Properties of Particulate–Polymer Composites. *Composites Part B: Engineering* **2008**, *39*, 933–961, doi:10.1016/J.COMPOSITESB.2008.01.002.

217. Ash, B.J.; Siegel, R.W.; Schadler, L.S. Mechanical Behavior of Alumina/Poly(Methyl Methacrylate) Nanocomposites. *Macromolecules* **2004**, *37*, 1358–1369, doi:10.1021/ma0354400.

218. Gurr, M.; Hofmann, D.; Ehm, M.; Thomann, Y.; Kübler, R.; Mülhaupt, R. Acrylic Nanocomposite Resins for Use in Stereolithography and Structural Light Modulation Based Rapid Prototyping and Rapid Manufacturing Technologies. *Advanced Functional Materials* **2008**, *18*, 2390–2397, doi:10.1002/adfm.200800344.

219. Wang, Z.L.; Mu, H.T.; Liang, J.G.; Tang, D.W. Thermal Boundary Resistance and Temperature Dependent Phonon Conduction in CNT Array Multilayer Structure. *International Journal of Thermal Sciences* **2013**, *74*, 53–62, doi:10.1016/J.IJTHERMALSCI.2013.07.006.

220. Callister, W.; Rethwisch, D. *Materials Science and Engineering: An Introduction*; Wiley New York, 2018; ISBN 9781119405498.

221. Huang, X.; Jiang, P.; Tanaka, T. A Review of Dielectric Polymer Composites with High Thermal Conductivity. *IEEE Electrical Insulation Magazine* **2011**, *27*, 8–16, doi:10.1109/MEI.2011.5954064.

222. Shindé, S.; Goela, J. *High Thermal Conductivity Materials*; Springer: New York, 2006; ISBN 978-0387220215.

223. Usman, C.; Mabrouk, A.; Abdala, A. Enhanced Thermal Conductivity of Polyethylene Nanocomposites with Graphene, Granulated Graphene, Graphene Nanoplatelet, and Their Hybrids. *International Journal of Energy Research* **2021**, doi:10.1002/ER.7147.

224. Consiglio, R.; Baker, D.; Paul, G.; Stanley, H. Continuum Percolation Thresholds for Mixtures of Spheres of Different Sizes. *Physica A: Statistical Mechanics and its Applications* **2003**, *319*, 49–55, doi:10.1016/S0378-4371(02)01501-7.

225. Bruggeman, D.A.G. Berechnung Verschiedener Physikalischer Konstanten von Heterogenen Substanzen. I. Dielektrizitätskonstanten Und Leitfähigkeiten Der Mischkörper Aus Isotropen Substanzen. *Ann Phys* **1935**, *416*, 636–664, doi:10.1002/andp.19354160705.

226. Liu, Y.; Chen, Z.; Qin, Y.; Shen, Y.; Zhou, Y.; Wang, D.; Hu, J.; Feng, W. Silicone Resin-Based Composite Materials for High Thermal Stability and

Thermal Conductivity. *Journal of Electronic Materials* **2020**, *49*, 4379–4384, doi:10.1007/S11664-020-08194-8.

227. Garrett, K.W.; Rosenberg, H.M. The Thermal Conductivity of Epoxy-Resin / Powder Composite Materials. *Journal of Physics D: Applied Physics* **1974**, *7*, 1247, doi:10.1088/0022-3727/7/9/311.
228. Bigg, D.M. Thermally Conductive Polymer Compositions. *Polymer Composites* **1986**, *7*, 125–140, doi:10.1002/PC.750070302.
229. Abbe, E. Beiträge Zur Theorie Des Mikroskops Und Der Mikroskopischen Wahrnehmung: I. Die Construction von Mikroskopen Auf Grund Der Theorie. *Archiv für mikroskopische Anatomie* **1873**, *9*, 413–418, doi:10.1007/BF02956173.
230. Kohl, H.; Reimer, L. *Transmission Electron Microscopy*; Springer Series in Optical Sciences; Springer New York: New York, NY, 2008; ISBN 978-0-387-40093-8.
231. Prandtl - Führer Durch Die Strömungslehre. *Prandtl - Führer durch die Strömungslehre* **2012**, doi:10.1007/978-3-8348-2315-1.
232. PIDS Technologie Für Nanopartikelanalyse - Beckman Coulter Available online: https://www.beckman.de/resources/technologies/laser-diffraction/pids (accessed on 20 February 2022).
233. Wriedt, T. Mie Theory: A Review. *Springer Series in Optical Sciences* **2012**, *169*, 53–71, doi:10.1007/978-3-642-28738-1_2.
234. Minton, A.P. Recent Applications of Light Scattering Measurement in the Biological and Biopharmaceutical Sciences. *Analytical Biochemistry* **2016**, *501*, 4–22, doi:10.1016/J.AB.2016.02.007.
235. Brunauer, S.; Emmett, P.H.; Teller, E. Adsorption of Gases in Multimolecular Layers. *J Am Chem Soc* **2002**, *60*, 309–319, doi:10.1021/JA01269A023.
236. Sukanto; Soenoko, R.; Suprapto, W.; Irawan, Y.S. Parameter Optimization of Ball Milling Process for Silica Sand Tailing. *IOP Conference Series: Materials Science and Engineering* **2019**, *494*, doi:10.1088/1757-899X/494/1/012073.
237. Munkhbayar, B.; Nine, M.J.; Jeoun, J.; Bat-Erdene, M.; Chung, H.; Jeong, H. Influence of Dry and Wet Ball Milling on Dispersion Characteristics of the Multi-Walled Carbon Nanotubes in Aqueous Solution with and without Surfactant. *Powder Technology* **2013**, *234*, 132–140, doi:10.1016/J.POWTEC.2012.09.045.

238. Zhang, D.L. Processing of Advanced Materials Using High-Energy Mechanical Milling. *Progress in Materials Science* **2004**, *49*, 537–560, doi:10.1016/S0079-6425(03)00034-3.

239. Lu, Y.; Guan, S.; Hao, L.; Yoshida, H. Review on the Photocatalyst Coatings of TiO2: Fabrication by Mechanical Coating Technique and Its Application. *Coatings 2015, Vol. 5, Pages 425-464* **2015**, *5*, 425–464, doi:10.3390/COATINGS5030425.

240. Burmeister, C.F.; Kwade, A. Process Engineering with Planetary Ball Mills. *Chemical Society Reviews* **2013**, *42*, 7660–7667, doi:10.1039/C3CS35455E.

241. Rothstein, J.P.; McKinley, G.H. Non-Isothermal Modification of Purely Elastic Flow Instabilities in Torsional Flows of Polymeric Fluids. *Physics of Fluids* **2001**, *13*, 382–396, doi:10.1063/1.1338540.

242. Ström, G.; Fredriksson, M.; Stenius, P. Contact Angles, Work of Adhesion, and Interfacial Tensions at a Dissolving Hydrocarbon Surface. *Journal of Colloid and Interface Science* **1987**, *119*, 352–361, doi:10.1016/0021-9797(87)90280-3.

243. Wenning, M.; Seiler, H.; Scherer, S. Fourier-Transform Infrared Microspectroscopy, a Novel and Rapid Tool for Identification of Yeasts. *Appl Environ Microbiol* **2002**, *68*, 4717–4721, doi:10.1128/AEM.68.10.4717-4721.2002.

244. Wu, J.; Zhao, Z.; Hamel, C.M.; Mu, X.; Kuang, X.; Guo, Z.; Qi, H.J. Evolution of Material Properties during Free Radical Photopolymerization. *Journal of the Mechanics and Physics of Solids* **2018**, *112*, 25–49, doi:10.1016/J.JMPS.2017.11.018.

245. File:Ftir-Interferogram.Png - Wikimedia Commons Available online: https://commons.wikimedia.org/wiki/File:Ftir-interferogram.png (accessed on 4 March 2022).

246. Scowen, I.J.; Telford, R. *Principles of Thermal Analysis and Calorimetry*; Gaisford, S., Kett, V., Haines, P.J., Eds.; 2nd ed.; Royal Society of Chemistry: Cambridge, 2016; ISBN 978-1-78262-051-8.

247. Spierings, A.B.; Schneider, M.; Eggenberger, R. Comparison of Density Measurement Techniques for Additive Manufactured Metallic Parts. *Rapid Prototyping Journal* **2011**, *17*, 380–386, doi:10.1108/13552541111156504/FULL/PDF.

248. Hay, B.; Filtz, J.R.; Hameury, J.; Rongione, L. Uncertainty of Thermal Diffusivity Measurements by Laser Flash Method. *International Journal of Thermophysics 2005 26:6* **2005**, *26*, 1883–1898, doi:10.1007/S10765-005-8603-6.

249. DLR - Institut Für Werkstoff-Forschung - Laser-Flash-Anlage Zur Bestimmung Der Thermischen Diffusivität Available online: https://www.dlr.de/wf/desktopdefault.aspx/tabid-2191/3208_read-4841/ (accessed on 4 May 2022).

250. Pelleg, J. Mechanical Properties of Materials. *Solid Mechanics and its Applications* **2013**, *190*, 1–634, doi:10.1007/978-94-007-4342-7.

251. Graf, D.; Qazzazie, A.; Materials, T.H.-; 2020, undefined Investigations on the Processing of Ceramic Filled Inks for 3D InkJet Printing. *mdpi.com*, doi:10.3390/ma13112587.

252. Huang, C.; Qian, X.; Yang, R. Thermal Conductivity of Polymers and Polymer Nanocomposites. *Materials Science and Engineering: R: Reports* **2018**, *132*, 1–22, doi:https://doi.org/10.1016/j.mser.2018.06.002.

253. Fu, J.; Shi, L.; Zhang, D.; Zhong, Q.; Chen, Y. Effect of Nanoparticles on the Performance of Thermally Conductive Epoxy Adhesives. *Polymer Engineering & Science* **2010**, *50*, 1809–1819, doi:10.1002/pen.21705.

254. Graf, D.; Jung, J.; Hanemann, T. Formulation of a Ceramic Ink for 3D Inkjet Printing. *Micromachines 2021, Vol. 12, Page 1136* **2021**, *12*, 1136, doi:10.3390/MI12091136.

255. Yun, J.S.; Park, T.-W.; Jeong, Y.H.; Cho, J.H. Development of Ceramic-Reinforced Photopolymers for SLA 3D Printing Technology. *Applied Physics A* **2016**, *122*, 629, doi:10.1007/s00339-016-0157-x.

256. Faber, K.T.; Evans, A.G. Crack Deflection Processes-II. Experiment. *Acta Metallurgica* **1983**, *31*, 577–584, doi:10.1016/0001-6160(83)90047-0.

257. Faber, K.T.; Evans, A.G. Crack Deflection Processes-I. Theory. *Acta Metallurgica* **1983**, *31*, 565–576, doi:10.1016/0001-6160(83)90046-9.

258. Hull, D. *Fractography: Observing, Measuring, and Interpreting Fracture Surface Topography*; Cambridge University Press: Cambridge, 1999; ISBN 978-0521646840.

259. Kinloch, A.J.; Young, R.J. Fracture Behaviour of Polymers. *Fracture Behaviour of Polymers* **1995**, doi:10.1007/978-94-017-1594-2.

260. Lange, F.F. The Interaction of a Crack Front with a Second-Phase Dispersion. *The Philosophical Magazine: A Journal of Theoretical Experimental and Applied Physics* **1970**, *22*, 983–992, doi:10.1080/14786437008221068.

261. Evans, A.G. The Strength of Brittle Materials Containing Second Phase Dispersions. *The Philosophical Magazine: A Journal of Theoretical Experimental and Applied Physics* **1972**, *26*, 1327–1344, doi:10.1080/14786437208220346.

262. Azimi, H.R.; Pearson, R.A.; Hertzberg, R.W. Fatigue of Hybrid Epoxy Composites: Epoxies Containing Rubber and Hollow Glass Spheres. *Polymer Engineering and Science* **1996**, *36*, 2352–2365, doi:10.1002/PEN.10633.

263. Huang, Y.; Kinloch, A.J. Modelling of the Toughening Mechanisms in Rubber-Modified Epoxy Polymers. *Journal of Materials Science* **1992**, *27*, 2753–2762, doi:10.1007/BF00540703.

264. Evans, A.G.; Williams, S.; Beaumont, P.W.R. On the Toughness of Particulate Filled Polymers. *Journal of Materials Science 1985 20:10* **1985**, *20*, 3668–3674, doi:10.1007/BF01113774.

265. Daniel, I.; Ishai, O. *Basic Concepts, Materials, Processes and Characteristics*; Oxford University Press: New York, 2006; ISBN 9780195150971.

266. Bray, D.J.; Dittanet, P.; Guild, F.J.; Kinloch, A.J.; Masania, K.; Pearson, R.A.; Taylor, A.C. The Modelling of the Toughening of Epoxy Polymers via Silica Nanoparticles: The Effects of Volume Fraction and Particle Size. *Polymer (Guildf)* **2013**, *54*, 7022–7032, doi:10.1016/J.POLYMER.2013.10.034.

267. Hsieh, T.H.; Kinloch, A. j.; Masania, K.; Sohn Lee, J.; Taylor, A.C.; Sprenger, S. The Toughness of Epoxy Polymers and Fibre Composites Modified with Rubber Microparticles and Silica Nanoparticles. *Journal of Materials Science* **2010**, *45*, 1193–1210, doi:10.1007/s10853-009-4064-9.

268. Hsieh, T.H.; Kinloch, A.J.; Masania, K.; Taylor, A.C.; Sprenger, S. The Mechanisms and Mechanics of the Toughening of Epoxy Polymers Modified with Silica Nanoparticles. *Polymer (Guildf)* **2010**, *51*, 6284–6294, doi:10.1016/J.POLYMER.2010.10.048.

A. Appendix

A.1. Stabilization

A.1.1. Electrostatic Forces

During electrophoresis the velocity U_{ES} of a particle in a liquid is measured while an electric field is applied. Under the assumption that under optimal conditions the particle diameter a is significantly larger than the thickness of the double layer, $\kappa a > 100$ and that $\zeta \leq 50$ mV, the Helmholtz-Smoluchowski equation can be used to calculate the Zeta potential:

$$U_{ES} = \frac{\varepsilon \zeta E}{4\pi\eta}, \tag{a1}$$

with κ being the inverse of the Debye length, which corresponds to the double layer thickness, ε the dielectric constant of the solvent, E the applied field strength and η the viscosity of the solvent. Here, the Zeta potential is the median in the Gaussian distribution of a set of particles. The values differ with particles size whereby very small particles have a ζ of 20 % larger than the median. The following equation allows the determination of the surface potential ψ_0 for small ζ:

$$\psi_0 = \zeta(1 + z/\alpha)e^{\kappa z}, \tag{a2}$$

with z being the distance between the slipping plane and the surface of the charged particle. Usually, a value of 5 Å is assumed for the distance. The value α is the Stokes radius. The inverse Debye length κ can be expressed in the following equation:

$$\kappa = \sqrt{4\pi e^2 \sum v_i^2 \eta_i^2 / \epsilon k T}, \tag{a3}$$

with e being the electron charge $1.6 \cdot 10^{-19}$ C, v_i the valency of each ionic species, η_i the number of ions of each species per cubic centimeter of the bulk fluid. k is Boltzmann's constant $1.38 \cdot 10^{-23}$ J/K and T is the absolute temperature in K.

A.1.2. Dispersive Forces

Assuming the presence of only vdW forces A can be calculated by:

$$2\gamma^{vdW} = -\Delta G_{l_0}^{vdW} = A/12\pi l_0^2, \tag{a4}$$

if the nonpolar surface tension or surface energy γ^{vdW} of the condensed material is known. The Hamaker constant describes all of the three electrodynamic interactions dispersion, orientation and induction force. However, in condensed media the dispersion force dominates and $A_{dispersion}$ is the main term [184]. Although, the vdW forces are mostly attractive, dissimilar materials suspended in certain liquids show repulsion.

It is possible to calculate the vdW interaction between two materials 1 and 2. In case these materials are solid and liquid, the non-polar surface energy γ_s^{vdW} of the solid can be calculated using the Young-Good-Girifalco Fowkes equation if the only other force present is ES in nature [184]:

$$1 + \cos\theta = 2\sqrt{\gamma_s^{vdW}/\gamma_l}, \tag{a5}$$

with θ being the contact angle of a nonpolar liquid on the solid surface.

A.1.3. Polar Forces

The total surface tension or surface energy can be expressed by:

$$\gamma = \gamma^{vdW} + \gamma^{AB}, \tag{a6}$$

and due to the asymmetry of the AB forces γ^{AB} is expressed by the non-additive parameters γ^+ for electron-acceptance and γ^- for electron-donation:

$$\gamma_i^{AB} = 2\sqrt{\gamma_i^+\gamma_i^-}, \tag{a7}$$

with i being material 1 or 2 the following equation can be written:

$$(1+\cos\theta)\gamma_L = 2\left(\sqrt{\gamma_S^{vdW}\gamma_L^{vdW}} + \sqrt{\gamma_S^{+}\gamma_L^{-}} + \sqrt{\gamma_S^{-}\gamma_L^{+}}\right). \quad \text{(a8)}$$

To obtain the parameters γ_S^{vdW}, γ_S^{+} and γ_S^{-} of the solid, contact angles must be determined with at least three liquids, of which two must be polar [184].

A.2. Mechanical Properties

Crack deflection initiates toughening by increasing the total fracture surface area, which absorbs more deformation energy than the unfilled matrices [256–258]. The mechanism depends on the particle radius R and the center-to-center interparticle distance h, which in turn depends on R and the volume fraction of the filler φ:

$$\frac{G_{Ic}}{G_{Ic,m}} = \frac{1}{2}\left(1 + \frac{\sqrt{(h/2)^2 + R^2}}{(h/2)}\right), \quad \text{(a9)}$$

with G_{Ic} being the fracture energy of the composite and $G_{Ic,m}$ the respective value for the matrix.

In addition to the surface increase, crack deflection causes local growth of tilted and twisted cracks. The angle of respective direction alterations α_{max} is dependent on h and R:

$$\alpha_{max} = sin^{-1}(2R/h). \quad \text{(a10)}$$

The mechanism of crack pinning absorbs energy by effectively binding a proceeding crack and forcing it to form secondary cracks [259–261]. The stress needed to overcome this mechanism in the composite in comparison to the unfilled matrix is summarized as:

$$\frac{\sigma_c}{\sigma_m} = \sqrt{\frac{E_c G_{Ic}}{E_m G_{Ic,m}}}. \quad \text{(a11)}$$

The term is dependent on h and R.

The mechanisms of particle pullout and micro-cracking interact with the previous mechanisms. During these processes, the propagating crack sprouts further smaller micro-cracks near the particles, which leads to further energy dissipation [262].

In case of nanoparticles, the mechanisms of particle debonding, plastic void growth and shear banding scatter energy by desorption of the particulate filler from the matrix under the formation of cavities and adjacent polymer deformation [208,263–265]. Essential for the processes is the interface between the two components. A strong interface can prevent the mechanism from occurring leading to a yield in the matrix, which is otherwise independent from the particle content φ. Therefore, an interface is needed, which is weaker than the matrix to initiate linearly elastic deformations and which takes place only at the tip of a propagating crack [266–268]. The following equation describes the total absorbed energy by the mechanisms in relation to the absorbed energy of the pure matrix:

$$\frac{G_{IC}}{G_{IC,m}} = \frac{G_{IC,m} + G_{IC,S} + 0.143 G_{IC,V}}{G_{IC,m}}, \tag{a12}$$

with the terms $G_{IC,S}$ and $G_{IC,V}$ being the fracture energies of the shear banding and the void growth, respectively. Since only every seventh nanoparticle triggers the formation of voids the factor 0.143 is used in the equation. Furthermore, no term for the particle debonding is added because it was shown that its contribution is not an energetic one, but rather a prerequisite for void formation.

$$G_{IC,S} = 0.5 \varphi \sigma_{yc} \gamma_f F'(r_y)\,. \tag{a13}$$

σ_{yc} is the plane-strain compressive true yield stress, γ_f is the true fracture strain of the unmodified matrix and $F'(r_y)$ is a model related term. Thereby, r_y is the radius of the plane-strain plastic zone at the crack tip of the fracture in the nanoparticle laden matrix.

$$G_{IC,V} = \left(1 - \frac{\mu_m^2}{3}\right)(\varphi_v - \varphi)\sigma_{yc} r_{pz} K_v^2\,, \tag{a14}$$

In this equation μ_m is a material constant visualizing the pressure-dependency of yield stress. φ_v is the volume fraction of the voids and r_{pz} is the radius of the plane-strain plastic zone at the crack tip of the fracture in the unmodified matrix. K_v is the von Mises stress concentration factor.

A.3. Wetting Behavior

Utilizing the Young equation, its dispersive part transforms into:

$$\cos\varphi = 2\sqrt{\gamma_s^{vdW}} \cdot \frac{1}{\sqrt{\gamma_l^{vdW}}} - 1\,, \tag{a15}$$

with φ being the contact angle between the vectors γ_l and γ_{sl}. Plotting the equation in the form of a straight line $y = mx + b$ and measuring the slope of the regression line allows the calculation of γ_s^{vdW}.
Further transformations using the equations of Young and Dupré yield the following form:

$$W_{sl}^{AB} = 2\sqrt{\gamma_l^{AB}} \cdot \sqrt{\gamma_s^{AB}}, \tag{a16}$$

with W_{sl}^{AB} being the polar part of the work of adhesion. The plotting of the equation as a straight line allows the deduction of γ_s^{AB} from the slope of the regression line. The addition of the dispersive and polar part of the solid surface energy results in γ_s.

A.4. Solvent Free Inks

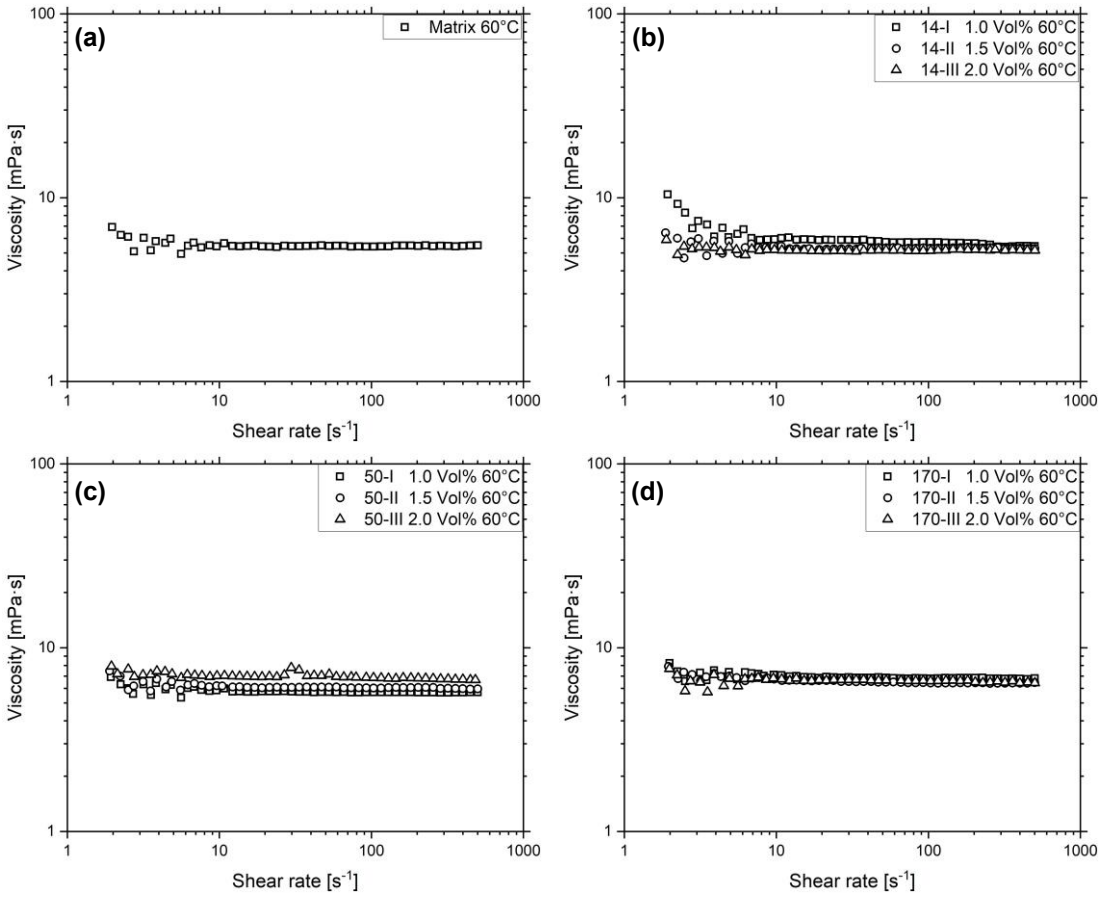

Figure A1*: Viscosity of solvent free inks 14-I to 170-III and the pure matrix as reference*

Table A1*: Viscosity at 60°C and surface tension at 25°C of the solvent free inks 14-I to 170-III and the pure matrix as reference. The viscosity values were taken at 500 s^{-1}.*

	Viscosity at 60°C [mPa·s]	Surface tension [mN/m]
Matrix	5.5 ± 0.2	27.3 ± 1.5
14-I	6.2 ± 0.0	30.0 ± 2.4
14-II	6.7 ± 0.1	32.5 ± 2.1
14-III	7.1 ± 0.1	30.3 ± 2.4
50-I	5.7 ± 0.2	27.2 ± 1.3
50-II	5.9 ± 0.0	32.0 ± 2.4
50-III	6.7 ± 0.1	29.7 ± 2.3
170-I	6.3 ± 0.1	30.0 ± 2.9
170-II	6.4 ± 0.0	30.4 ± 1.9
170-III	6.8 ± 0.1	31.9 ± 1.2

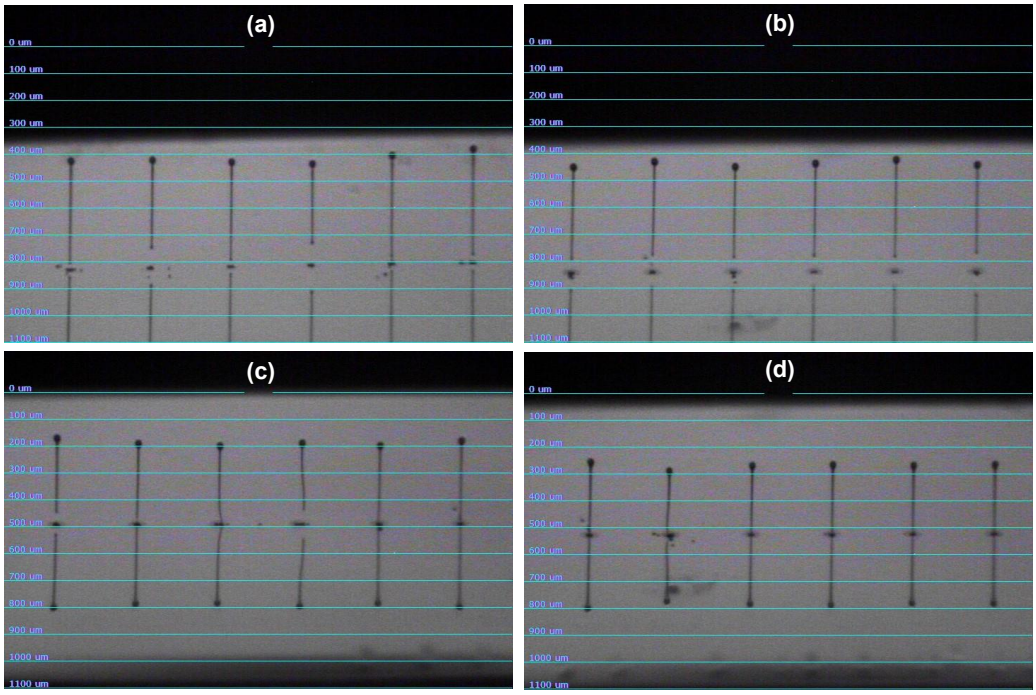

***Figure A2**: Jetting tests of (**a**) the pure matrix material, (**b**) 14-III, (**c**) 50-III and (**d**) 170-III.*

***Table A2**: Ink Jetting characteristics of the matrix and the inks 14- III, 50- III and 170- III.*

Samples	Drop Velocity [m/s]	Drop Volume [pl]	Drop Weight [ng]	Jetting Time [s]
Matrix	11.5	7.8	8.0	> 600
14- III	10	10.0	11.0	> 600
50- III	9	8.2	9.0	> 600
170- III	8	7.3	8.0	> 600

***Table A3**: Number of cured layers, which were necessary to fill the PDMS mold during printing.*

Sample	Matrix	14-I	14-II	14-III	50-I	50-II	50-III	170-I	170-II	170-III
Layer number	71	58	60	76	61	73	80	150	180	107

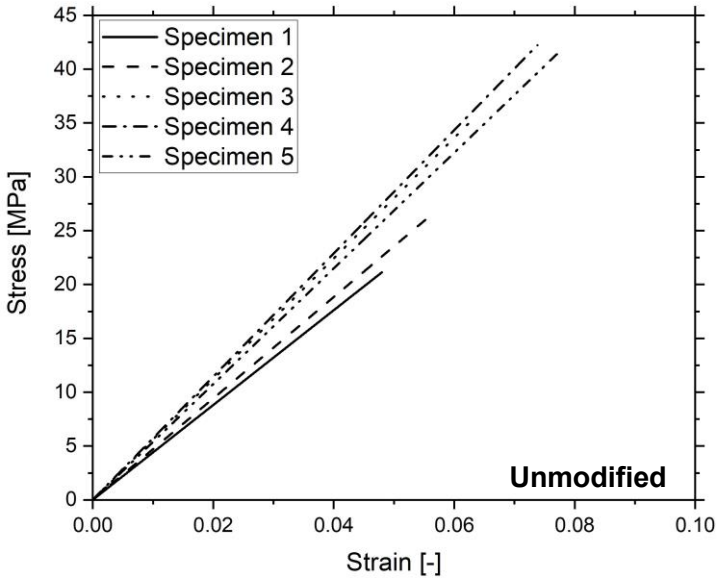

***Figure A3**: Tensile test results of 3D inkjet-printed specimens of the unmodified matrix material.*

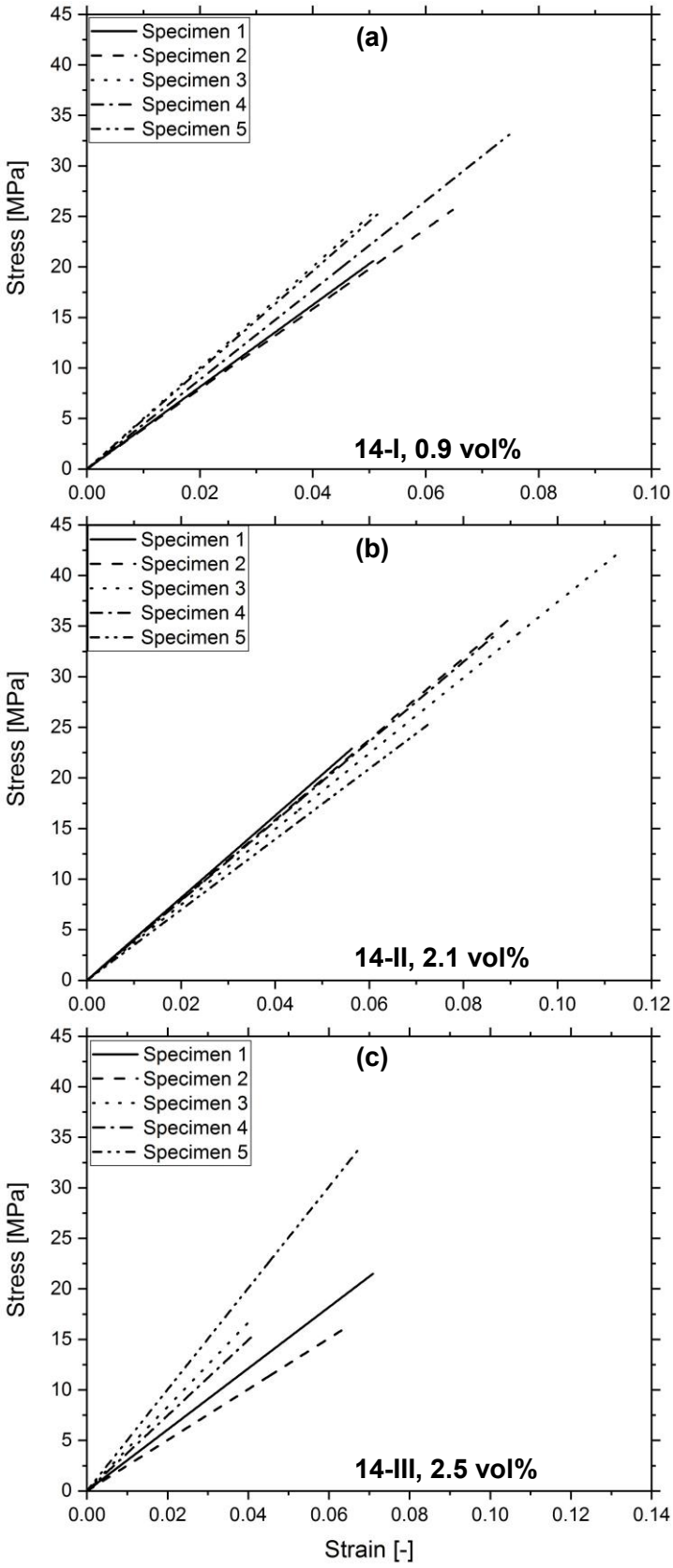

***Figure A4**: Tensile test results for 3D inkjet-printed specimens of 14- I, 14- II and 14- III*

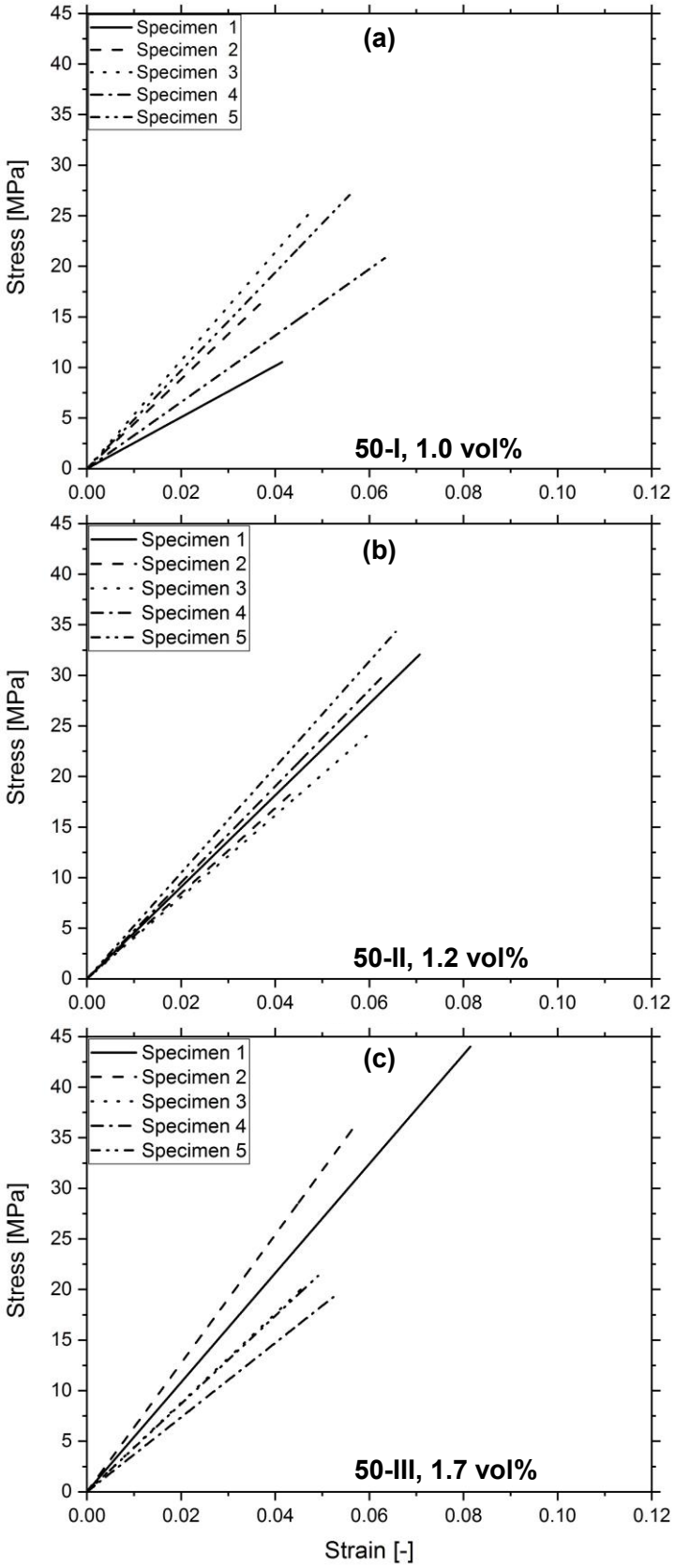

Figure A5*: Tensile test results of 3D inkjet-printed specimens of 50- I, 50- II and 50- III.*

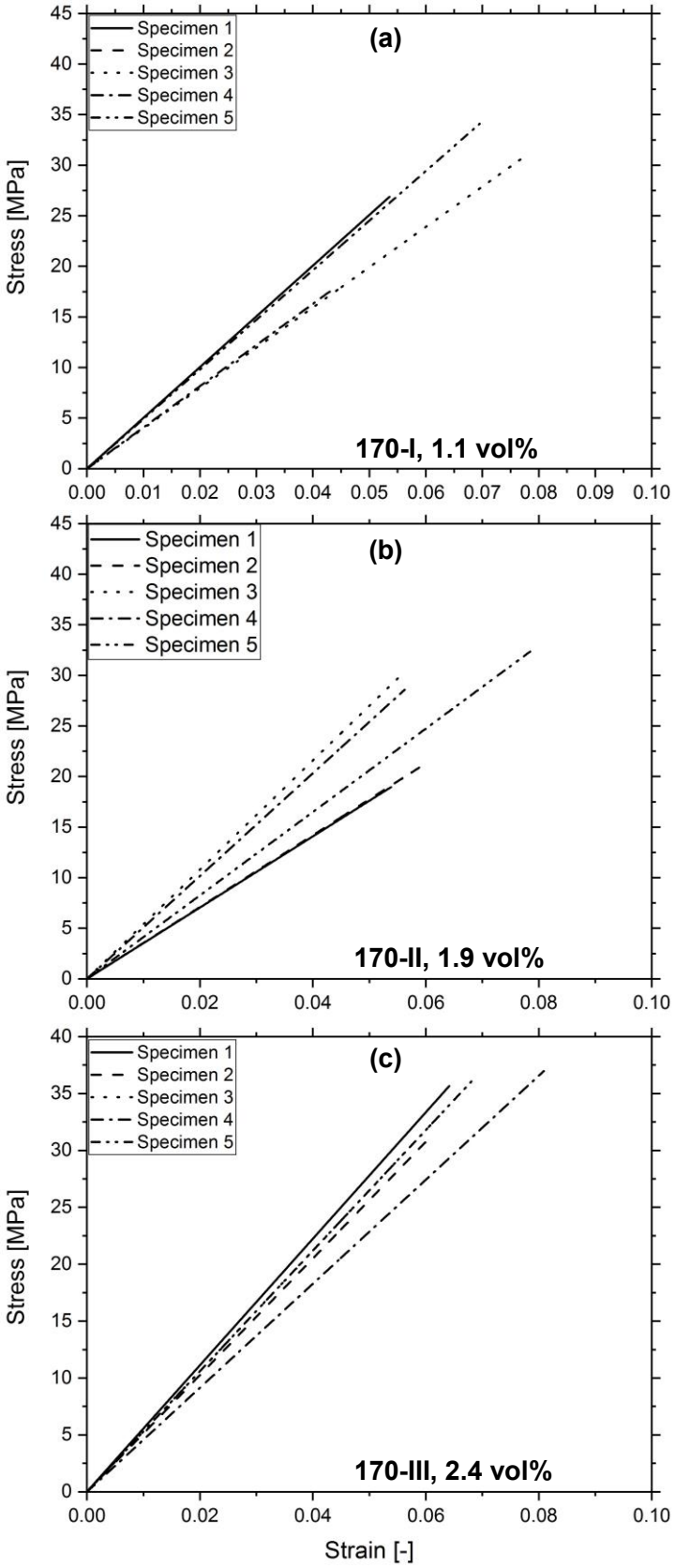

***Figure A6**: Tensile test results for 3D inkjet-printed specimens of 170-I, 170-II and 170-III.*

A.5. Solvent Based Inks

A.5.1. Ceramic Functionalization

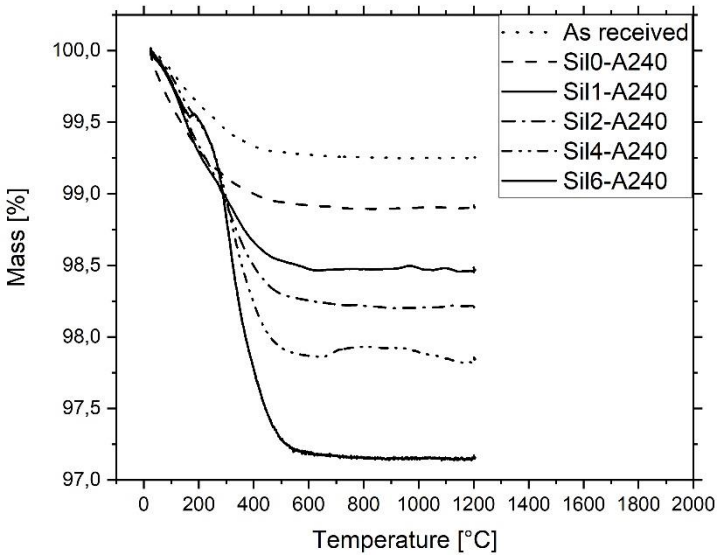

Figure A7*: TGA curves of A240 as received, Sil0- A240, Sil1- A240, Sil2- A240, Sil4- A240, Sil6- A240.*

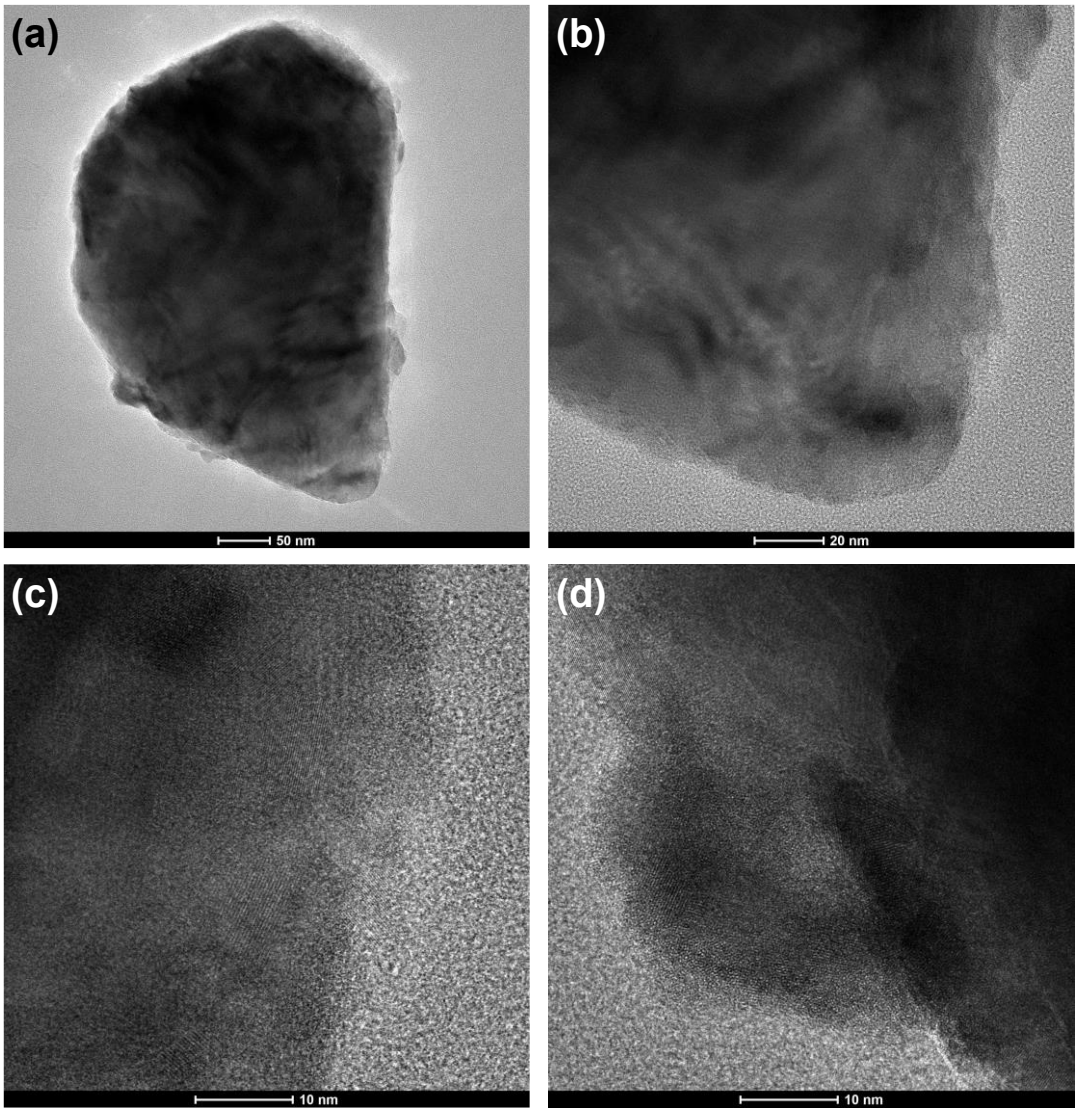

***Figure A8**: TEM images of Sil6-A240 with increasing close-up to the particle surface.*

A.5.2. Solvent Selection

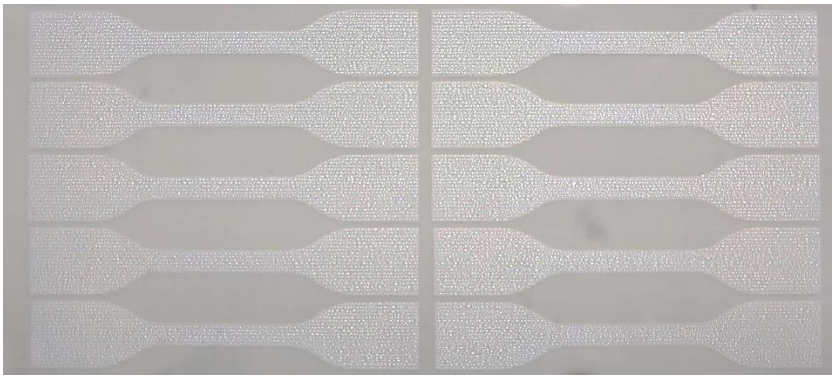

***Figure A9**: Tensile specimen shaped test image printed with 4 layers of ink using a drop spacing of 40 µm for the assessment of the ink deposition quantity before and after the printing.*

A.5.3. Ink Ratio

***Table A4**: Surface tension as well as viscosity at 32°C and 60°C of samples M- 7 to M- 10. The viscosity values were taken at 500 s^{-1}.*

	Surface tension [mN/m]	Viscosity at 32°C [mPa·s]	Viscosity at 60°C [mPa·s]
M-7	31.1 ± 0.2	15.7 ± 0.1	7.7 ± 0.0
M-8	32.3 ± 0.5	14.3 ± 0.1	7.0 ± 0.1
M-9	33.0 ± 0.1	11.8 ± 0.1	6.4 ± 0.1
M-10	32.3 ± 0.2	11.0 ± 0.0	5.9 ± 0.0

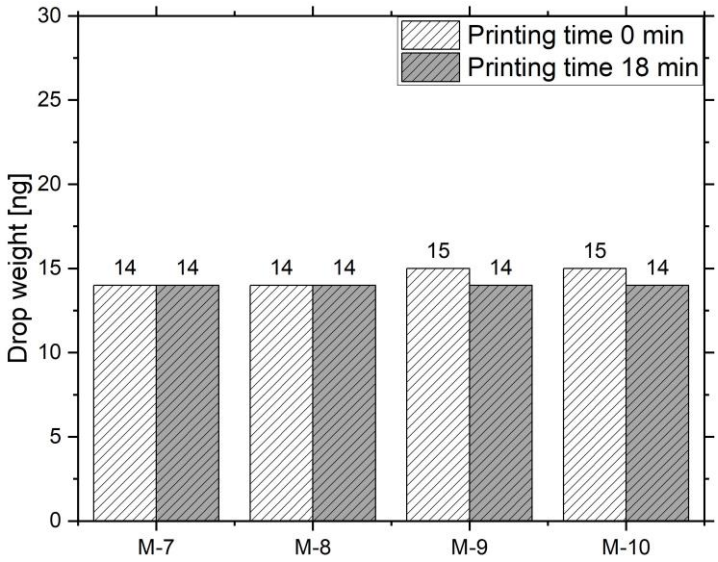

***Figure A10**: Measurement of the average drop weight of M-7 to M-10 with 10 nozzles at 32°C before and after the printing of a four-layer test image.*

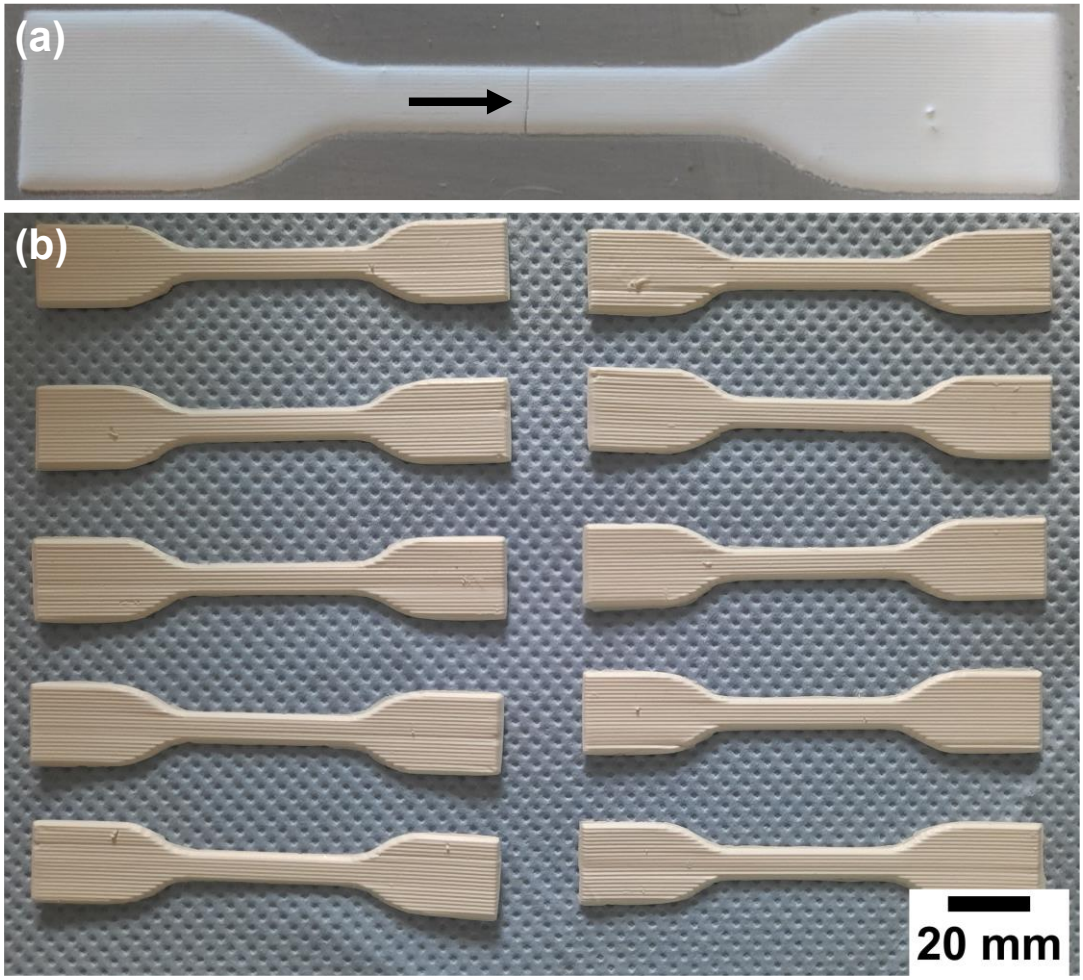

***Figure A11**: (**a**) Broken specimen during 3D inkjet-printing of Ink M-8. (**b**) Successfully 3D inkjet-printed specimens using the ink M-7.*

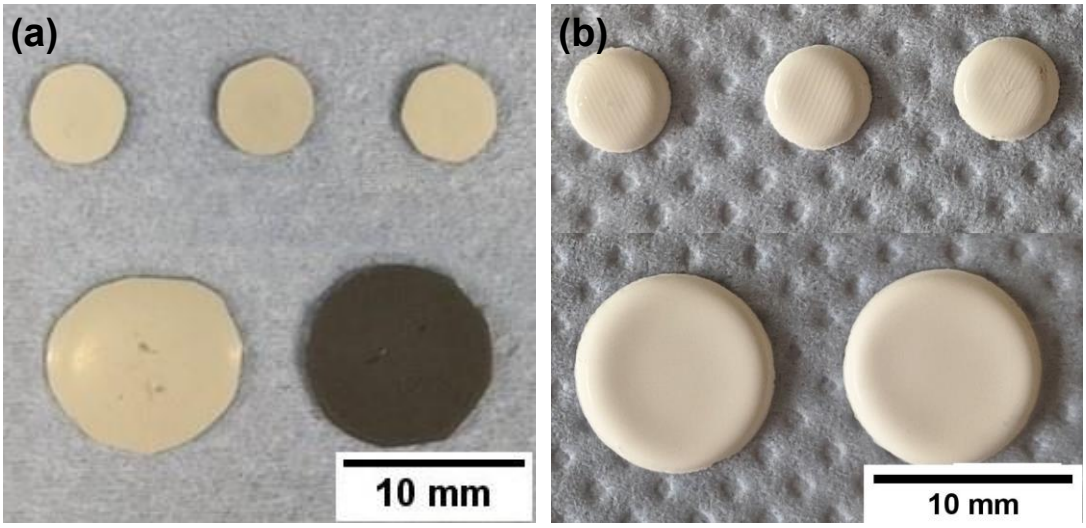

***Figure A12**: Specimens for thermal conductance assessment. Small specimens are analyzed using the DSC and large specimens are measured using the laser flash method. (**a**) Sample C-30 was produced by casting. The black color of one specimen is graphite applied for the measurement. (**b**) Sample M-10 was 3D inkjet-printed.*

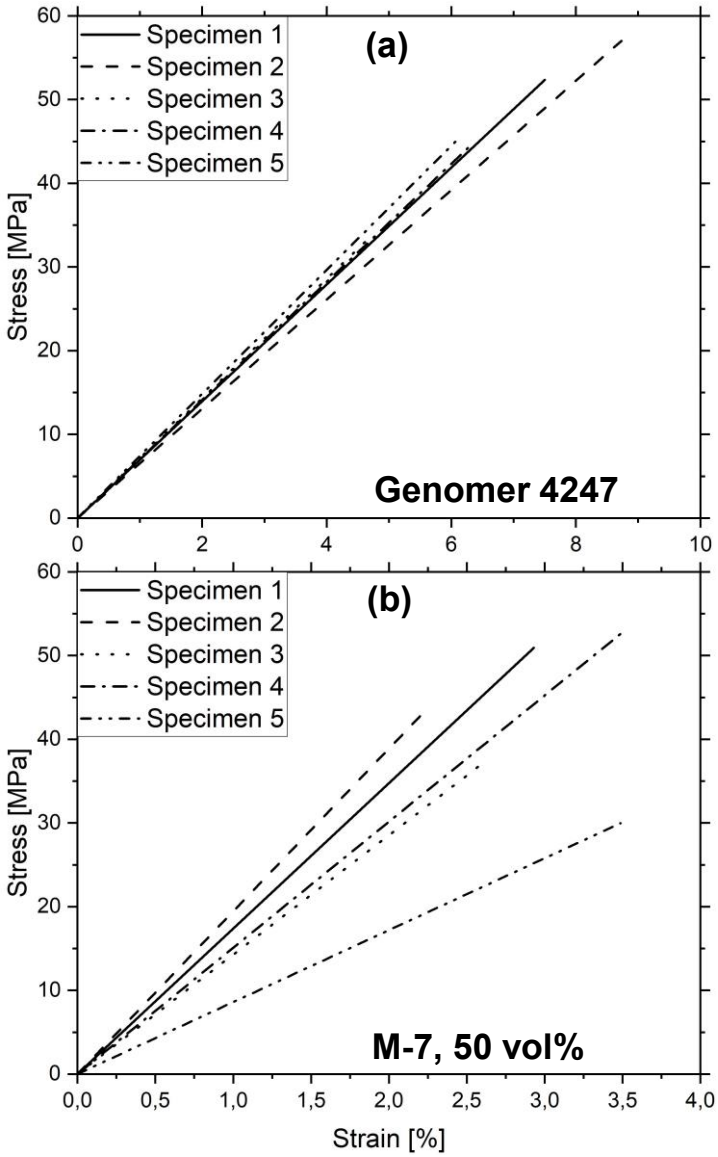

***Figure A13**: Tensile test results for casted specimens of cured Genomer 4247 and 3D inkjet-printed specimens of ink M-7.*

A.5.4. Printing Tests

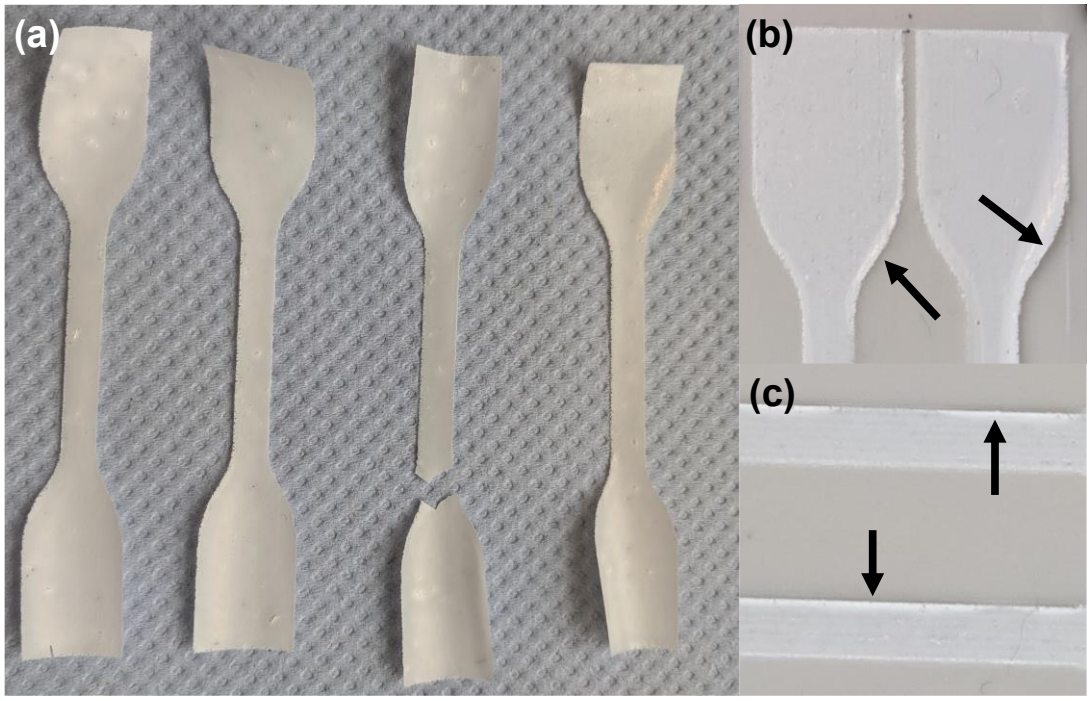

***Figure A14**: (**a**) Printed, oven-dried and UV cured samples 1 to 4 after detachment from the PDMS surface due to curling. (**b**), (**c**) Material detachment from the PDMS substrate during samples production.*

List of Figures

List of Tables

Publications

Journal articles

1. N. Rostami, D. Graf, L. Schranzhofer, S. Hild, and T. Hanemann, "Overcoming oxygen inhibition effect by TODA in acrylate-based ceramic-filled inks," *Progress in Organic Coatings*, vol. 130, pp. 221–225, **2019**, doi: 10.1016/J.PORGCOAT.2019.01.048.

2. D. Graf *et al.*, "Influence of Al_2O_3 Nanoparticle Addition on a UV Cured Polyacrylate for 3D Inkjet Printing," *Polymers 2019, Vol. 11, Page 633*, vol. 11, no. 4, p. 633, **2019**, doi: 10.3390/POLYM11040633.

3. D. Graf, A. Qazzazie, and T. Hanemann, "Investigations on the Processing of Ceramic Filled Inks for 3D InkJet Printing," *Materials*, vol. 13, no. 11, **2020**, doi: 10.3390/ma13112587.

4. D. Graf, J. Jung, and T. Hanemann, "Formulation of a Ceramic Ink for 3D Inkjet Printing," *Micromachines 2021, Vol. 12, Page 1136*, vol. 12, no. 9, p. 1136, **2021**, doi: 10.3390/MI12091136.

Conference contributions

1. D. Graf et al., "Polymer-ceramic-composites for 3D inkjet printing," *MST Kongress 2017 (Munich, Germany), 24.10.2017*, poster presentation.

2. D. Graf, "UV curable ceramic inks for 3D inkjet printing," *Addit 2017 (Steyr, Austria), 28.09.2017*, oral presentation.

3. D. Graf, S. Burchard, T. Hanemann, "Stabilization of Al_2O_3 nanoparticles via 3 - (trimethoxysilyl)propyl methacrylate in UV curable ink for 3D inkjet printing," *Particle-Based Materials Symposium 2017 (Saarbrücken, Germany), 09.11.2017*, poster presentation.

4. D. Graf, T. Hanemann, "New nanoparticle-reinforced polyacrylates fabricated by 3D inkjet printing and UV-curing," *Cimtec 2018 (Perugia, Italy), 08.06.2018*, poster presentation.

5. D. Graf *et al.*, "3D inkjet printable ceramic inks for components with enhanced mechanical or thermal properties," *MSE Congress 2018 (Darmstadt, Germany), 27.09.2018*, oral poster presentation.

6. D. Graf, J. Jung, T. Hanemann, "Thermisch leitfähige Polymer-Keramik-Komposite für den Tintenstrahldruck," *MST Kongress 2021 (Ludwigsburg, Germany), 09.11.2021*, poster presentation.

Supervised Theses

1. S. Burchard, "Keramische Tinten für den 3D-Inkjet-Druck für die Verbesserung der mechanischen Eigenschaften von Komponenten," *Bachelor thesis*, Department of materials processing, IMTEK-University of Freiburg, 2017.

2. H. Nguyen, "Keramische Tinten für den 3D-Inkjet-Druck thermisch leitender Komponenten," *Bachelor thesis*, Department of materials processing, IMTEK-University of Freiburg, 2017.

3. P. Geiping, “Stabilisierung von Al_2O_3 - Nanopartikeln für die Herstellung 3D - inkjetdruckbarer Tinten,” *Bachelor thesis,* Department of materials processing, IMTEK-University of Freiburg, 2019.

4. A. Qazzazie, “Development of 3D inkjet printable ceramic-polymer inks for components with adjusted mechanical properties,” *Master thesis,* Department of materials processing, IMTEK-University of Freiburg, 2019.

5. S. Burchard, “Entwicklung und Charakterisierung einer keramisch gefüllten Tinte für den 3D-Inkjet-Druck zur Verbesserung der thermischen Eigenschaften,” *Master thesis,* Department of materials processing, IMTEK-University of Freiburg, 2019.

Acknowledgements

First of all, I would like to thank Prof. Dr. Thomas Hanemann, my doctoral supervisor, for the supervision of this work, the friendly help and the manifold ideas that opened up a critical approach to this topic for me. The numerous conversations on an intellectual and personal level will always remain in my memory as enriching and constructive exchanges. I have always found our dialogues to be encouraging and motivating. I would also like to thank Prof. Dr. Margit Zacharias for her helpful and scientific support as a second reviewer. Furthermore, I would like to thank Prof. Dr. Jürgen Wilde and Prof. Dr. Jürgen Wöllenstein for their agreement to be part of the examination board.

Moreover, I would like to express my special thanks to the following people, without whose assistance the preparation of this dissertation would never have been possible:

Dr. Thomas Eiselt for his kind introduction to the working practices of the Materials Process Engineering group.

Uwe Gleißner for the detailed introduction to the equipment of the working group and the stimulating discussions.

Markus Mauck for the help in dealing with difficult technical issues.

Dr. Bilal Khatri for reading through manuscripts and introducing stereolithography.

Dr. Christof Megnin for creating milling programs and making milled parts.

Marco Frey for sound advice, stimulating discussions and critical questions around the lab work, as well as reading through the PhD thesis.

Afnan Qazzazie-Hauser for energetic support in the context of her master thesis, for complimentary discussions on chemical issues, and for reading through the doctoral thesis.

Dr. Kirsten Honnef for help with project-related concerns and organizational issues, as well as reading through the doctoral thesis.

Dr. Christoph Pfeiffer for active support in project-related work and critical reading of the doctoral thesis.

Judith Jung for carrying out and evaluating the thermal conductivity analysis.

Dr. Steffen Scholz for enabling my participation in the EU project DIMAP.

Dr. Tobias Müller for the organizational support around the DIMAP project.

The consortium of the EU project DIMAP, for laying the foundation of my doctoral thesis.

Dr. Andreas Hoffmann for the technical support and instruction in the flash point measurement.

Dorit Nötzel for the organizational help.

Anna Medesi for the technical support in chemical questions.

Karin Seitz for the great help in matters of KIT-internal bureaucracy.

The Professorship of Chemistry and Physics of Interfaces, especially Dr. Oswald Prucker, Natalia Schatz, Daniela Mössner and Martin Schönstein for instruction in chemical equipment and advice on chemical reagents.

Professor Jürgen Wilde for allowing us to use equipment of his working group.

The Professorship of Packaging and Interconnection, especially Fabian Kohler, Markus Feißt, Nilavzhagan Subbiah and Alexander Schiffmacher for the instruction in the tensile testing machine.

Sven Burchard, Hien Nguyen, Philipp Geiping for the support of the doctorate in the context of their bachelor and master theses.

Emine Cimen and Heeji Yoo for supporting my work as research assistants.

Besides the colleagues mentioned above, I also wanted to thank Yusi Wen, Chao Hui Liu, Diana Syperek, Edgar Cruz, Lars Hüttenes, and Konstantin Gradwohl for making my workday livelier and more interesting.

Finally, I wanted to thank my parents and grandparents for always believing in me and supporting me. Thank you for always keeping me on the right track.